Imaging Cerebrovascular Health using 7T MRI

Matthijs H.S. de Buck

St Hugh's College

University of Oxford

A thesis submitted for the degree of Doctor of Philosophy

Trinity Term 2023

Acknowledgements

This thesis marks the end of a wonderful period in Oxford. Although the thesis only discusses what I've worked on during that time, it was the many great and lovely people around me that made my period in Oxford deserve the adjective 'wonderful'.

Firstly, I want to express my gratitude to my supervisors, Peter Jezzard and Aaron Hess. If it wasn't for you, I would probably not even have pursued a PhD in the first place. Since first working under your supervision during my Master's, I have been amazed by the amount of time, care, and attention with which you have always supported me. You have not just been fantastic supervisors, but also fantastic mentors. Your advice has been invaluable throughout, from preparing for my DPhil interviews at the start to finding my next career steps at the end. And whether I had to move to a new house, had to self-isolate for a while, or even needed a hospital pick-up from Banbury, you were always the first to offer help (despite having incredibly busy lives, with young families and less-than-well-behaved dogs). It has been an absolute pleasure, and I will miss our weekly meetings.

I also want to thank my friends and colleagues at FMRIB. FMRIB wouldn't be the welcoming and inspiring place that it is without all its students and staff, but there are too many people to name everyone individually. However, I want to especially thank my DPhil cohort, who have been on their entire DPhil journeys alongside me. Daniel, Xi, Cristiana, and James, it has been a pleasure to spend time with you - from the lab to the pub, and from board game nights to conference hotel rooms.

My time in Oxford would not have been the same without all my friends in the St Hugh's Boat Club and the St Hugh's MCR. I don't know whether the early nights before 6am outings or wine-filled formals have positively contributed to my work, but they have most certainly made my time in Oxford more enjoyable. There are, again, too many people to name everyone individually, but I would like to especially thank Adomas, Ben, Billy, Boris, James, Kiana, Ollie, Sandra, and Sascha for their friendship throughout the years.

To my Dutch friends in Oxford, Nina, Jakob, and Joost, thank you for the wonderful memories at dinners, pubs, and football games in Oxford and beyond. And thanks to Vince, Tom, and Chris, who were some of the first people I met in Oxford, and with whom I greatly enjoyed exploring as much of England as we could within the very few months that they were here.

Thanks to many friends from Leiden and Dordrecht for either crossing the Channel to visit me in Oxford or for making time for me when I was back in the Netherlands. I look forward to being able to see all of you more frequently again now that I am coming back to the Netherlands.

The same goes for my family, and especially mam, pap, Dagmar, Wietse, and opa. Thank you for supporting me, for coming to visit various times, and being there for me and for each other, through joyful and challenging times alike.

Finally, last yet everything but least, thank you Nicole. At the start of my DPhil, three and a half years sounded like an impossibly long time of being apart, yet it has felt like you were always by my side. Thank you for sharing your room with me for many months during the first lockdown, and thank you for coming to Oxford to literally be at my side day and night after I broke my arms. This thesis would not be here without your help at those times. Thank you for tackling challenges and celebrating successes together. Now that I am coming back, I look forward to going on my next adventure with you.

Abstract

Magnetic resonance imaging is a valuable clinical tool for the visualization of intracranial vasculature. Without exposing patients to ionizing radiation or intravenous contrasts, it can provide multi-modal structural information about the shape, structure, and function of the various vessels involved in stroke and dementia. However, imaging methods are limited by the achieved contrasts and resolutions, as well as the required scan times.

Ultra-high field 7T MRI offers increased signal-to-noise ratio and desirable changes in relaxation parameters, therefore promising substantial improvements to existing neurovascular MRI approaches such as MR angiography (MRA) and MR vessel wall imaging (VWI). However, 7T MRI also introduces increased specific absorption rates and reduced homogeneity and extent of the transmit B1 field. Because of the latter, the first research chapter in this thesis (Chapter 3) studies the possibility to increase the extent of this 7T $B1^+$ field into the feeding arteries in the neck using parallel transmission (pTx).

The second research chapter (Chapter 4) aims to improve the accelerated acquisition of high-resolution MRA using compressed sensing reconstruction. This facilitates the visualization of the small intracranial arteries which are involved in lacunar infarcts and vascular dementia, which can be achieved within clinical scan times.

The final parts of this thesis (Chapters 5-7) focus on a specific intracranial VWI sequence called DANTE-SPACE. A simulation framework for the sequence is first presented in Chapter 5. This framework includes various additional processes such as (pulsatile) tissue motion and $B1^+$ variations to accurately represent the intra- and extra-vascular contrast mechanisms. The simulations are then used for the optimization and comparison of the T2-weighted DANTE-SPACE sequence at 3T, 7T without pTx, and 7T with pTx. The optimizations aim to maximize the contrast between both the blood within and the cerebrospinal fluid surrounding intracranial vessel walls, and the comparison between different field strengths provides a first quantitative indication of the added value of ultra-high field MRI for the DANTE-SPACE sequence.

Contents

Publications Related to This Thesis

Journal articles

de Buck MHS, Jezzard P, Hess AT. "Optimization of undersampling parameters for 3D intracranial compressed sensing MR angiography at 7T". Magnetic Resonance in Medicine 88(2), 880-889, 2022.

Ji Y, Wu W, **de Buck MHS**, Okell T, Jezzard P. "Highly accelerated intracranial time-of-flight magnetic resonance angiography using wave-encoding". Magnetic Resonance in Medicine (in press), 2023.

de Buck MHS, Jezzard P, Frost R, Randell C, Hurst K, Choudhury RC, Robson MD, Biasiolli L. "10-channel phased-array coil design for carotid wall MRI at 3T". PLOS One (in press), 2023.

de Buck MHS, Kent JL, Jezzard P, Hess AT. "Head-and-neck multi-channel $B1^+$ mapping and RF shimming of the carotid arteries using a 7T parallel transmit head coil". Under review (first revision) at Magnetic Resonance in Medicine.

de Buck MHS, Jezzard P, Hess AT. "An Extended Phase Graph-based framework for DANTE-SPACE simulations including physiological, temporal, and spatial variations". In preparation.

de Buck MHS, Hess AT, Jezzard P. "Optimization and comparison of intracranial T2-weighted DANTE-SPACE vessel wall imaging at 3T and 7T". In preparation.

Kent JL, **de Buck MHS**, Dragonu I, Chiew M, Valkovič L, Hess AT. "Single Breath-hold Accelerated 3D Multi-Channel $B1^+$ Mapping at 7T for the Brain and Heart". In preparation.

Conference proceedings

de Buck MHS, Jezzard P, Hess AT. "An investigation into the optimal undersampling parameters for 3D TOF MRA at 7T using compressed sensing reconstruction". 30th Annual Meeting of ISMRM 1640, 2021.

de Buck MHS, Hess AT, Jezzard P. "Optimized DANTE preparation for intracranial DANTE-SPACE vessel wall imaging at 7T". 30th Annual Meeting of ISMRM 4201, 2021.

de Buck MHS, Kent JL, Hess AT, Jezzard P. "Improved vessel wall imaging at 7T using DANTE-SPACE with neck-specific pTx shims". ISMRM High Field Workshop, 2022.

de Buck MHS, Kent JL, Hess AT, Jezzard P. "Parallel transmit DANTE-SPACE for improved black-blood signal suppression at 7 Tesla". 31st Annual Meeting of ISMRM 2092, 2022.

de Buck MHS, Hess AT, Jezzard P. "Head-and-neck multi-channel $B1^+$ mapping using pTx head coils at 7T by combining different RF shims and transmit voltages". Annual Meeting of BIC-ISMRM, 2022.

de Buck MHS, Hess AT, Jezzard P. "RF shimming for improved $B1^+$ in the carotid arteries using parallel transmission (pTx) head coils at 7T". 32nd Annual Meeting of ISMRM 0205, 2023.

de Buck MHS, Jezzard P, Hess AT. "Improved multi-channel pTx $B1^+$ mapping in the head and neck at 7T by combining RF shims and transmit voltages". 32nd Annual Meeting of ISMRM 4587, 2023.

Kent JL, **de Buck MHS**, Dragonu I, Chiew M, Valkovič L, Hess AT. "Accelerated Volumetric Multi-Channel pTx $B1^+$ Mapping at 7T for the Brain and Heart". 32nd Annual Meeting of ISMRM 4408, 2023.

Ji Y, Wu W, **de Buck MHS**, Okell T, Jezzard P. "Accelerated intracranial time-of-flight magnetic resonance angiography using wave-encoding". 32nd Annual Meeting of ISMRM 0776, 2023.

List of Abbreviations

2D/3D = two-dimensional / three-dimensional

3T/7T = 3 tesla / 7 tesla

ASL = arterial spin labelling

B1TIAMO = $B1^+$ time-interleaved acquisition of modes

BA = basilar artery

BART = Berkeley Advanced Reconstruction Toolbox

CNR = contrast-to-noise ratio

CE-MRA = contrast-enhanced MRA

CP = circular polarization / circularly polarized

CS = compressed sensing

CSF = cerebrospinal fluid

CoV = coefficient of variation

CoW = Circle of Willis

CTA = computed tomography angiography

DANTE = delay alternating with nutation for tailored excitation

DICOM = digital imaging and communications in medicine (data format)

DSA = digital subtraction angiography

EPG = extended phase graphs

ESPIRiT = eigenvalue iterative self-consistent parallel imaging reconstruction

ETL = echo train length

FA = flip angle

FID = free induction decay

FISTA = fast iterative shrinkage-thresholding algorithm

FLASH = fast low angle shot

FOV = field-of-view

FSL = FMRIB Software Library

FWHM = full width at half maximum

g-factor = geometry factor

GRAPPA = generalized autocalibrating partially parallel acquisition

GRE = gradient-recalled echo

ICA = internal carotid artery

IPH = intra-plaque haemorrhage

IR = inversion recovery

k-space = spatial frequency (Fourier) space

LSA = lenticulostriate arteries

MCA = middle cerebral artery

MIP = maximum intensity projection

MOTSA = multiple overlapping thin-slab acquisitions

MPRAGE = magnetization-prepared rapid gradient-echo

MRA = magnetic resonance angiography

MRI = magnetic resonance imaging

MSDE = motion-sensitized driven equilibrium

NCE = non-contrast enhanced

PC-MRA = phase-contrast MRA

POCS = projection onto convex sets

PRELUDE = phase region expanding labeller for unwrapping discrete estimates

pTx = parallel transmission

RF = radiofrequency

RMS = root-mean-square

RMSE = root-mean-square error

ROI = region of interest

ROVir = region-optimized virtual coils

SAKE = simultaneous autocalibrating and k-space estimation

SAR = specific absorption rate

SatTFL = presaturated TurboFLASH

SD = standard deviation

SENSE = sensitivity encoding

SNR = signal-to-noise ratio

SPACE = sampling perfection with application optimized contrast using different flip angle evolutions

SPGR = spoiled gradient echo

SSIM = structural similarity

SVD = small vessel disease

TE = echo time

TIAMO = time-interleaved acquisition of modes

TOF = time-of-flight

TR = repetition time

TSE = turbo-spin echo

TWIX = raw k-space data format (Siemens)

UHF = ultra-high field

VERSE = variable-rate selective excitation

VW = vessel wall

VWI = vessel wall imaging

1

Cerebrovascular Imaging

1.1 Motivation

Although the human brain typically accounts for less than 2% of the weight of the human body, it is responsible for around 20% of the glucose-derived energy consumption in the body [1]. This energy allows the over one hundred billion nerve cells in the brain to continuously control various vital autonomic processes in the body, as well as provide us with the ability to think, sense, learn, and move.

The glucose and oxygen required for this high energy demand are provided to all parts of the brain by the blood that continuously flows into the intracranial vasculature. If the blood flow to parts of the brain is disrupted, for example due to a vessel being blocked (ischemic stroke) or ruptured (haemorrhagic stroke), cells in the affected brain region can get damaged or die within a few minutes. Since brain cells cannot regenerate, this can quickly result in severe physical or cognitive disabilities and is one of the leading global causes of death [2]. Therefore, the prevention, early detection, and treatment of cerebrovascular diseases are of high clinical importance.

Clinical assessment of the cerebrovasculature and the detection of stroke risk factors, such as pathological plaque accumulation, combine different imaging contrasts that can provide different types of information. Angiography visualizes the blood inside the vessels (the lumen). This provides information about which areas of the brain can or cannot be supplied with blood by the cerebrovasculature, and can indicate the presence of vascular malformations, aneurysms, or stenosis or occlusion. Vessel wall imaging (VWI) methods are used to evaluate abnormalities in the arterial vessel walls. In particular, VWI aims to characterize the presence and composition of pathological plaques, which are major risk factors for ischemic stroke. Finally, imaging of the perfusion of blood into the brain can be used to assess the presence of areas with compromised blood delivery, for example due to vascular stenosis or other causes of lowered blood flow.

Imaging at high spatial resolutions is especially clinically desirable for angiography and vessel wall imaging. For angiography, higher resolutions can provide improved visibility

and delineation of small and highly tortuous vessels, such as the lenticulostriate arteries (LSAs) which supply the basal ganglia and are believed to be involved in subcortical vascular dementia [3,4] and lacunar stroke. For vessel wall imaging, higher resolutions facilitate the assessment of plaque accumulation in thin arterial walls and improve the ability to delineate individual plaque components.

In this thesis, the increased signal-to-noise ratio (SNR) of ultra-high field (UHF) 7 tesla MRI is used for high-resolution magnetic resonance (MR) angiography and vessel wall imaging. In this chapter, different MR- and non-MR methods for both angiography and vessel wall imaging are first discussed. Subsequently, in Chapter 2, the most important acquisition, reconstruction, and simulation methods that are used in this thesis are introduced.

1.2 Angiography

1.2.1 Non-MR Angiography

Historically, the most common angiography method used to image vessels in the brain is a fluoroscopy technique known as digital subtraction angiography (DSA) [5–8]. DSA combines 2-dimensional (2D) X-ray images obtained before and after the administration of a radio-opaque contrast agent. Since the contrast agent changes the signal levels in the blood vessels, the difference between the pre-contrast and the post-contrast images shows the vascular anatomy. Although DSA provides high resolution images, it relies on ionizing radiation in the form of X-rays and invasive, possibly nephrotoxic, methods for arterial contrast agent administration.

An example of an alternative and less invasive [7] angiography method is computed tomography angiography (CTA) [5–7], where images are taken a certain time after the intravenous injection of a radiocontrast material. Although CTA is more rapid, cost-effective, and less invasive than DSA [6], it still relies on ionizing radiation and the invasive injection of contrast agents.

Finally, transcranial Doppler ultrasound can also be used for the visualization of (some) intracranial arteries [9,10]. It provides real-time information about the location and the velocity of arterial blood flow. However, it achieves lower sensitivity, specificity, and penetration depth (especially through the skull) compared to the other angiographic methods discussed here [10] and is therefore less commonly used for clinical diagnosis.

1.2.2 MR Angiography

Magnetic resonance angiography (MRA) methods make use of very strong magnetic fields in combination with radiofrequency (RF) pulses and spatially varying gradient magnetic fields to generate structural images. Therefore, compared to other angiography techniques, such as DSA and CTA, they have the intrinsic benefit of not requiring ionizing radiation for signal generation. In addition, MRA techniques generate contrast by utilizing the flow properties of spins (the water protons that generate the MRI signal) in the blood, and therefore do not necessarily require the use of contrast agent injections, facilitating non-invasive imaging. Depending on the combination of RF pulses and gradient fields that is used during a scan, different types of angiographic images can be generated using MRI. Those different MRA methods provide images with different contrasts, resolutions, and acquisition times, each with their own advantages and disadvantages. This section will provide a brief overview of various intracranial MRA techniques, followed by an introduction to the main MRA contrast used in this thesis, which is time-of-flight MRA.

Phase-contrast MRA (PC-MRA) [11] acquires images after the application of a bipolar gradient module, as shown in Figure 1.1a. For stationary spins, the zeroth order moment of the bipolar gradients will cancel out, without generating a phase shift. For spins that move along the gradient direction, the experienced magnitude of the field produced by the first gradient pulse is different from that of the second gradient due to the displacement of the spin. By subtracting two phase-contrast acquisitions with opposite sensitization (see Figure 1.1), the sensitization-independent signal from stationary spins can be removed while retaining contrast from the moving spins. Importantly, since the phase offsets are linearly dependent on the flow velocity of the spins, PC-MRA can also provide quantitative flow velocity information. By selecting appropriate PC-MRA gradient strengths and intervals, acquisitions can be made sensitive to different velocity ranges. Compared to other MRA techniques, PC-MRA typically suffers from long acquisition times as it requires multiple separate acquisitions with different velocity-encoding gradients. In addition, its sensitivity to partial volume effects generally requires acquiring data at high spatial resolutions, further increasing the required acquisition times.

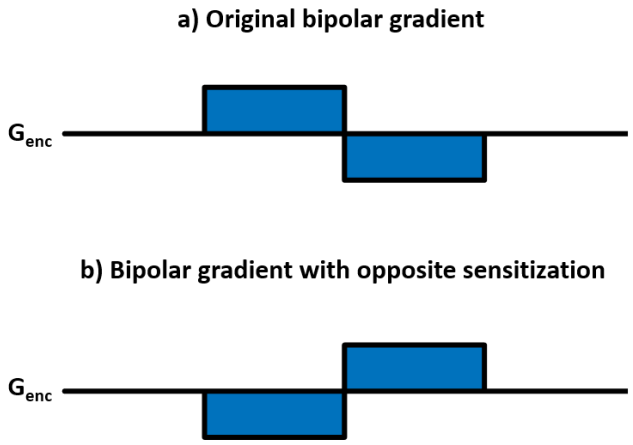

Figure 1.1: The bipolar encoding gradients (G_{enc}) with opposite sensitization as used for phase-contrast MRA.

An extension of PC-MRA is 4D flow MRI [12], in which 3D PC-MRA data with velocity encoding along 3 orthogonal directions is acquired at different timepoints in the cardiac cycle. As a result, 4D flow MRI provides quantitative time-resolved information about the blood flow along all three spatial dimensions, hence providing 4-dimensional information (x, y, z, and time). Thereby, it can provide detailed insights into complex flow patterns.

Another MRI method that can be used for both angiography and perfusion imaging is arterial spin labelling (ASL) [13,14]. Like PC-MRA, ASL uses the difference in signal between two images to separate the inflowing blood signal from the static tissue. In the case of ASL, those two images are a so-called tag image, which is an image of the brain after inverting arterial blood water spins in a region outside of the imaging volume (generally upstream in the vasculature, such as in the carotid arteries), and a control image acquired without the additional inversion outside of the imaging volume. Since the only difference between the control and tag images is the effect of the inversion pulse on spins that moved downstream into the imaging volume, subtracting the tag and the control images yields a blood-water-only image. Furthermore, the delay time between the inversion pulse and the excitation of the imaging volume can be altered to change the contrasts from angiographic weighting (shorter delay) to perfusion weighting (longer delay) [14].

As previously mentioned, most MRA techniques do not fundamentally depend on the invasive injection of contrast agents. However, contrast-enhanced MRA (CE-MRA) [15] is still regularly used in a clinical setting. In the case of CE-MRA, paramagnetic gadolinium-based contrast agents are used to shorten the MR relaxation times of blood, resulting in a brightening of the blood in T1-weighted images. It is also possible, like DSA and CTA, to further enhance the contrast of CE-MRA angiograms by taking the difference in signal between images acquired before and after the injection of the contrast agent. Although this

can produce high-contrast images of both angiography and perfusion, acquisition times are restricted by the rapid passage of the contrast bolus through the vasculature. Additionally, there is evidence that injected gadolinium is not entirely cleared from the body after the MR examination has finished, raising concerns over its long-term health effects [16].

The final MRA method discussed here is conventional (non-contrast-enhanced) time-of-flight (TOF) MRA [11], which is the main MRA method used in this thesis. In TOF MRA, a gradient-recalled echo (GRE) sequence consisting of a series of moderate flip angle RF excitation pulses with short repetition times (TRs) is used to suppress the signal from stationary tissue in a 2D slice or 3D excitation volume (slab). The suppression of stationary tissue in GRE acquisitions using short TRs can be derived from the GRE signal equation [17], from which the signal S of a tissue with proton density S_0 can be calculated as

$$S = S_0 \frac{\sin(\alpha)\left(1 - \exp\left(-\frac{TR}{T1}\right)\right)}{1 - \cos(\alpha)\exp\left(-\frac{TR}{T1}\right)} \exp\left(-\frac{TE}{T2}\right) \qquad 1.1$$

where α denotes the excitation flip angle. This indicates that $S \to 0$ as $TR/T1 \to 0$ in the low flip angle regime. This means that, over time, the series of RF pulses results in a low-magnetization steady state for stationary nuclei within the excited slab. However, fresh spins in the blood that move into the excitation slab have not yet obtained this steady state and will have a higher MR signal intensity and, therefore, a bright-blood contrast relative to the stationary nuclei (Figure 1.2a). Since the bright-blood contrast in TOF MRA is generated by the blood flowing into the imaging plane, TOF MRA does not require the invasive injection of external contrast agents.

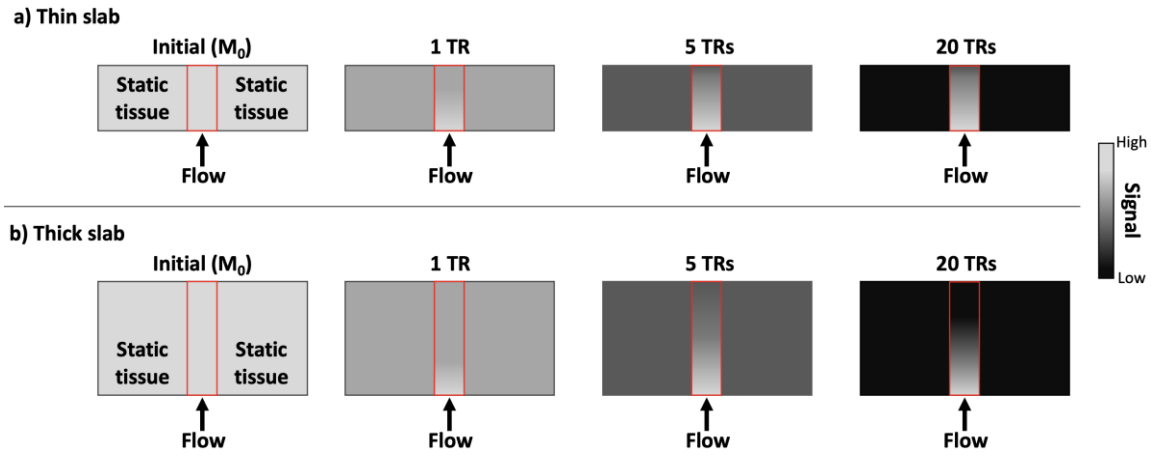

Figure 1.2: Schematic representation of the bright-blood contrast in 3D TOF MRA. **(a)** As the number of repetitions increases, the signal in static tissue gets saturated, while spins flowing into the slab in a vessel (red) perpendicular to the

imaging slab produce a bright-blood signal throughout a thin slab. **(b)** For thick slabs, some blood spins remain within the excitation volume for too long, resulting in partial saturation of the blood signal.

Since the short TR results in a progressive saturation of any spins within the imaging slab, blood spins that remain within the slab for too long will also experience signal saturation (Figure 1.2b). Therefore, when imaging a larger volume, multiple overlapping thin-slab acquisitions (MOTSA [18]) are often used. By sequentially acquiring multiple thin slabs, blood saturation effects within any given slab are limited, while a large volume can still be visualized by combining the slabs. By including a slight overlap between the individual slabs, boundary artefacts in the combined data can be reduced.

Other than the slab thickness and orientation, there are three main parameters that determine the achieved contrasts in a standard TOF MRA acquisition: the repetition time (TR), echo time (TE) and excitation flip angle (α): see Figure 1.3. The TR and excitation flip angle are typically relatively small (albeit with flip angles that are larger for 2D-TOF acquisitions) but balanced to achieve sufficient suppression of stationary spins while generating as much signal as possible from the moving spins. The TE is generally selected to be as short as possible to minimize flow-induced dephasing while maximizing the amount of retained blood signal. Asymmetric echoes can be used to facilitate shorter echo times between the RF pulse and the centre of the echo.

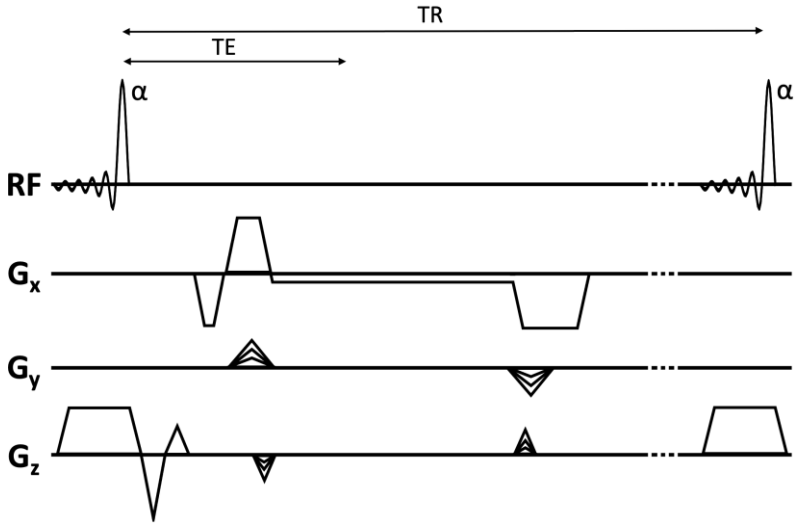

Figure 1.3: Sequence diagram for a 3D GRE TOF MRA sequence, showing the repetition time (TR), echo time (TE) and excitation flip angle (α). The sequence shown here uses slab-selective excitation along the z-direction and asymmetric echo readouts along the x-direction, which was used for the acquisitions in Chapter 4.

In this thesis, the MRA sampling strategy used for a highly accelerated compressed sensing (Section 2.2.4) is optimized to achieve improved visibility of small vessels within clinically

feasible scan times. This facilitates improved visualization of the LSAs, which are believed to be involved in subcortical vascular dementia [3,4] and lacunar stroke.

1.3 Vessel Wall Imaging

1.3.1 Principles of VWI

Intracranial vessel wall imaging methods are diagnostic techniques that aim to characterize the location, size, and composition of pathology, such as plaque burden, in (typically) arterial vessel walls. Some non-MR angiography methods, such as the previously described DSA and CTA, can be used in the context of VWI to indicate locations of vessel narrowing through the indirect observation of reduced lumen width [5]. Although those methods can provide high-resolution images, they do not provide information about the source of the luminal narrowing or the composition of any possible plaque accumulation and are less favourable due to their invasive nature and the presence of ionizing radiation. Furthermore, an *ex vivo* study of patients who died of ischemic stroke indicated that the presence of intracranial atherosclerotic disease was not visible or hardly visible based on luminal narrowing alone in 40% of the cases [19]. Ultrasound can also be used for vessel wall imaging in some parts of the vasculature but does not provide the penetration depth (in particular through the skull) or resolution required for intracranial vessel wall imaging [9,10].

MRI-based vessel wall imaging methods can provide more specific information about the size and composition of intracranial plaques. In general, they aim to delineate both the inner surface and the boundaries of the vessel wall through suppression of blood signal within and external signal surrounding the vessel walls. In the ideal case, this would facilitate the calculation of vessel wall thickness and the quantification of plaque sizes. Additionally, MRI-based VWI provides the potential to distinguish different plaque components. Variable signal contrast relative to healthy vessel wall tissue can, for example, be used to distinguish lipid cores and intraplaque haemorrhages through signal hypo- and hyperintensities, respectively, for T2-weighted VWI [20]. Alternatively, acquisitions at multiple echo times can be used to generate quantitative T2 maps [21,22], which can also determine lipid content.

Suppression of the luminal MR signal within vessels, also known as black-blood imaging, can be achieved by methods that make use of either the relaxation properties (inversion

recovery) or the flow properties of arterial blood. Suppression of the MR signal outside of the vessel wall is fundamentally more challenging. The external vessel wall boundaries can connect to different tissue types, such as CSF or brain parenchyma. This means that no single set of relaxation properties can be targeted for the simultaneous suppression of all tissue types around the vessel walls. Secondly, most of the spins surrounding the vessels are either stationary or move much more slowly than the blood, limiting the use of flow-sensitive signal suppression. In CSF, however, there is some low-velocity motion due to cardiac pulsatility and respiratory effects [23]. Although the velocity of the CSF flow is much lower than that of the blood flow, some flow-sensitive signal suppression approaches can still be used to reduce the CSF signal and improve the outer vessel wall delineation. This is especially beneficial for elderly populations, where atrophy increases the fraction of the intracranial vessels surrounded by CSF [24]. Furthermore, CSF-suppression is particularly important for T2-weighted VWI, which natively produces bright CSF signal.

In addition to simultaneously suppressing both the intravascular blood and the extravascular CSF, intracranial vessel wall imaging requires high spatial resolution data to accurately visualize the thin (often <0.4 mm [25]) vessel walls around the Circle of Willis (CoW) as well as the detail of the plaque composition [26].

In summary, MR-based VWI methods aim to achieve (1) clear delineation of the vessel wall through simultaneous suppression of blood and CSF, (2) the ability to distinguish different plaque components, and (3) high spatial resolution. Furthermore, the data need to be acquired within clinically feasible scan durations and preferably without the need for invasive contrast agents. Various MRI acquisition methods for intracranial vessel wall imaging are available in the literature. Below, different methods are briefly discussed, as well as the main vessel wall imaging method used in this thesis (DANTE-SPACE).

1.3.2 MR VWI Preparation Methods

Most MR VWI methods consist of a signal preparation module to achieve suppression of the (arterial) blood and/or the CSF, followed by a turbo spin echo (TSE) readout [27,28]. The signal preparation modules can be separated into two categories: inversion recovery modules, which aim to suppress specific tissue types based on their longitudinal relaxation times, and phase spoiling strategies, which aim to dephase moving spins.

Basic inversion recovery (IR) preparation modules use a 180° pulse to invert all spins from equilibrium magnetization into the negative M_z-direction, followed by a fixed delay time

(the inversion time) before an excitation pulse is played out [29]. By selecting an inversion time that corresponds to the time when the magnetization from a specific tissue type (such as arterial blood or CSF) crosses the zero-magnetization point, the excitation pulse does not excite the selected tissue, and its signal will be suppressed. For 2D black-blood imaging, the initial non-selective inversion pulse can be followed quickly by an additional slice-selective inversion pulse (double IR) in the plane of the imaging slice. This helps maintain the signal of the tissues and vessel walls within the slice of interest, while the non-selective inversion pulse can still null the signal from the blood that flows into the slice. However, especially when operating at higher magnetic field strengths (> 3T), this approach presents different limitations. Firstly, the one (single IR) or two (double IR) 180° inversion pulses introduce a substantial specific absorption rate (SAR) burden, where the SAR of a pulse is roughly proportional to the square of the field strength. Secondly, increased transmit field inhomogeneity at higher fields limits the accuracy and extent of the non-selective inversion pulse, thereby introducing artefacts and reducing the suppression of blood flowing upstream through the neck. Finally, the longer T1-relaxation times at higher fields increase the required inversion times, resulting in restrictively long scan times.

Phase spoiling-based preparation modules make use of the spatial dependence of the magnetic field strength when a gradient magnetic field is applied. Since the Larmor frequency scales linearly with the magnetic field strength, this results in spatially dependent precession frequencies, and in the case of moving spins, it consequently results in precession frequencies that change over time as the spins move through the gradient field. Analogously to how diffusion-weighted MRI sequences use this property for signal attenuation along the direction of applied gradients, phase spoiling-based preparation modules can use it for the suppression of moving spins in the blood and/or CSF. Two examples of such preparation modules are motion-sensitized driven equilibrium (MSDE) and delay alternating with nutation for tailored excitation (DANTE) [30,31].

MSDE modules consist of three pulses: a 90° excitation pulse, a 180° refocusing pulse, and a 90° pulse with opposite phase to the excitation pulse for return of the magnetization to the longitudinal direction. Between the pulses, two strong gradients with the same duration and amplitude are applied. For stationary spins, the dephasing during the first gradient is the same as the rephasing during the second gradient, resulting in refocusing when the third pulse is applied. Consequently, stationary spins can retain their equilibrium magnetization. For moving spins that have changed their location along the gradient direction, however, the amount of dephasing and rephasing will be different, and their

magnetization at the end of the MSDE module will be attenuated (assuming a range of velocities, such as is usually the case for laminar flow). Although MSDE can provide suppression of fast-flowing spins in the blood, the low velocity of spins in the CSF does not result in a significant change in the CSF signal [30]. As is the case for (double) inversion recovery modules, at high magnetic field strengths, MSDE also suffers from high SAR levels due to the three high-flip angle pulses [32].

DANTE is a phase-spoiling-based preparation strategy that does not require high flip angle pulses and is therefore better suited for use at ultra-high field strengths. Additionally, contrary to MSDE, DANTE can suppress the signal of slowly moving CSF as well as blood signal, facilitating the delineation of both the inner and outer vessel wall boundaries. DANTE uses a series of nonselective low-flip angle pulses (with alternating phase) with strong gradients (Figure 1.4). As the word 'excitation' in DANTE suggests, it was originally developed as a (frequency-dependent) readout module, and it has also been used for spatial tagging in cardiac MRI [33]. Li et al. [31], however, proposed that DANTE's inherent phase-spoiling properties for flow along the applied gradient direction can also be used to suppress the MR signal of moving spins. Due to the alternating phase of the DANTE excitation pulses and the fixed gradient area after each DANTE pulse, the magnetization from stationary spins remains coherent during a DANTE pulse train. Therefore, stationary spins only experience a small amount of signal attenuation (caused by relaxation effects following the RF pulses) and obtain a steady state. Spins that move along the DANTE gradient direction, however, experience quadratic phase accumulation, which rapidly attenuates their longitudinal magnetisation. This results in a contrast consisting of bright static tissues and attenuated moving tissues, where the attenuation can already be substantial for spins moving at the order of millimetres per second [31]. Due to the quadratic dependence of SAR on flip angles, the SAR of a complete DANTE-preparation module is typically smaller than that of even a single 180° refocusing pulse, as is required for MSDE- and DIR-preparation modules, despite the large number of pulses (typically 100-300) used in DANTE. Additionally, since the performance of DANTE does not require excitation with exact predefined flip angles, such as is the case for the inversion- and excitation pulses in MSDE and DIR, DANTE also benefits from reduced sensitivity to transmit field inhomogeneity.

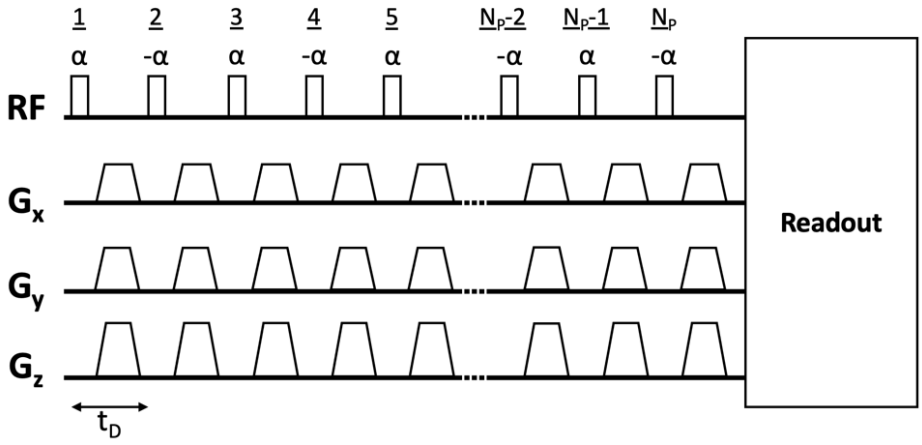

Figure 1.4: Sequence diagram of a DANTE-preparation module consisting of N_P pulses of flip angle α with DANTE interpulse repetition time t_D.

1.3.3 DANTE-SPACE

Most of the VWI preparation modules described above can be used in combination with various readout sequences. The most common type of readout modules in the context of VWI [27] are turbo spin echo (TSE) readouts [28], which benefit from intrinsic black-blood contrast due to inefficient refocusing of moving spins throughout the echo train.

TSE acquisitions facilitate rapid acquisition of high-resolution 3D data by using a single excitation pulse followed by a train of refocusing pulses. Each refocusing pulse produces an additional echo, making it possible to acquire multiple k-space lines per TR. By using short, non-selective refocusing pulses, an echo can be generated every few milliseconds. This can increase the possible length of the echo train to tens or even hundreds of readouts.

Originally, 180° pulses were used for each of the refocusing pulses in TSE acquisitions. However, variable flip angle refocusing pulses are now commonly used to increase the image sharpness and to increase number of refocusing pulses by more efficiently using the available magnetization [34], while also providing a substantial reduction in SAR. Such variable flip angle pulse trains can be optimized to provide optimal sharpness and signal for the T1 and T2 of a specific tissue [28,34], such as the vessel wall in VWI [35]. Based on those relaxation times, a specified number of refocusing flip angles (referred to as the echo train length) can be calculated to provide a prescribed signal evolution during each readout. For example, a rapid signal reduction can be prescribed at the start of the readout to facilitate a more constant signal level during the central portion of the readout [28,35], thereby reducing blurring in the resulting images.

Different MRI vendors refer to variable flip angle TSE acquisitions using different terms. In this thesis, the term SPACE (sampling perfection with application optimized contrasts by using different flip angle evolutions) is predominantly used as it is regularly used for variable flip angle TSE VWI implementations in the literature [30,35–41] (including at 7T [35]) and corresponds to the name used by the vendor used for all acquisitions shown in this thesis.

In the context of vessel wall imaging, the SPACE sequence can be combined with DANTE preparation to achieve simultaneous suppression of blood and CSF, as discussed in Section 1.3.1. The sequence diagram of this DANTE-SPACE sequence is shown in Figure 1.5. Each DANTE-SPACE pulse train consists of a series of low flip angle pulses with strong gradients followed by a variable flip angle SPACE readout.

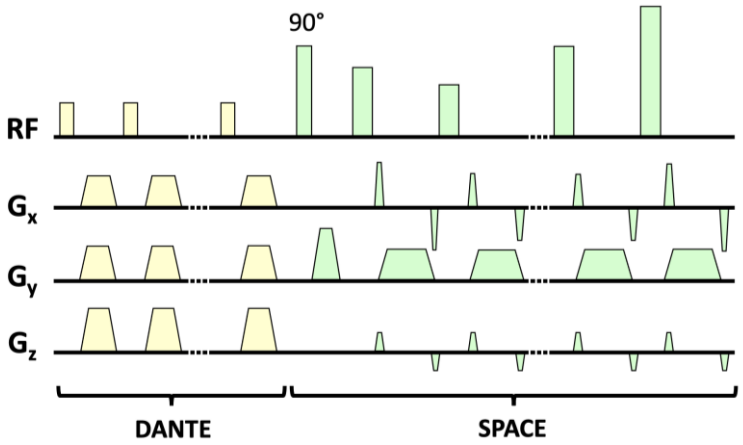

Figure 1.5: Sequence diagram of the DANTE-SPACE vessel wall imaging sequence. Yellow pulses and gradients indicate the DANTE preparation and green pulses and gradients are the variable flip angle SPACE readout. The sequence shown here uses non-selective pulses for both DANTE and SPACE, with k_y as the SPACE readout direction.

Although SPACE implementations with different weightings rely on the same variable flip angle TSE concepts for rapid image generation, they use different repetition and echo times to generate the desired contrasts. T2-weighted protocols use a long TE and a long TR, T1-weighted protocols use a short TE and a short TR, and proton density (PD)-weighted versions use a long TR but a short TE. As a result, different prescribed SPACE signal evolutions are used depending on the echo time of the selected weighting. Since constant signal is desired near the centre of k-space, short-TE implementations require a SPACE flip angle train with a constant prescribed signal level at the start of the readout. For long-TE implementations, which cross the centre of k-space near the centre of the readout train, constant signal throughout the central portion of the SPACE readout is generally required.

The sequence diagram shown in Figure 1.5 is based on the T2-weighted DANTE-SPACE implementation at 7T previously introduced by Viessmann et al. [35]. This uses non-selective pulses for both DANTE and SPACE without spatial or spectral saturation and combines 300 DANTE pulses of 10° with a T2-weighted SPACE readout using 73 variable flip angle pulses, a TR of 2.62 s, and a TE of 165 ms. Other studies in the literature have predominantly used DANTE-SPACE as a T1-weighted intracranial VWI sequence at 3T [30,36–38,40–43], with different implementations using various protocol settings (such as 94 to 300 DANTE pulses with flip angles ranging from 8° to 13°) or other additions such as spatial or fat saturation pulses.

T1-weighted DANTE-SPACE acquisitions benefit from low native CSF signal, therefore requiring less CSF suppression to achieve outer vessel wall delineation than T2-weighted acquisitions. As a result, T1-weighted intracranial VWI is regularly included in clinical practice at 3T [26], often in addition to post-contrast T1-weighted and PD-weighted contrasts but excluding T2-weighted contrasts [26]. VWI can benefit from multi-contrast acquisitions to distinguish different plaque components through variable signal contrasts [20]. For extracranial cervical VWI, T1-weighted, T2-weighted, and proton density-weighted acquisitions are routinely combined to differentiate between stable and unstable atherosclerotic plaques by identifying the major plaque components [20,26,44]. However, intracranial multi-contrast VWI is more challenging due to long acquisition times to achieve the desired contrasts and resolutions (often <0.4 mm for vessel walls around the Circle of Willis) [25,26]. The combination of their longer scan times and higher native CSF signal means that T2-weighted acquisitions are currently generally not included in clinical intracranial VWI [20,36,41,45]. In this thesis, the potential of T2-weighted DANTE-SPACE for visualizing the intracranial arteries is further investigated. Simulations are first used to optimize the protocol parameters at 7T. Finally, the results of T2-weighted DANTE-SPACE at 3T and at 7T are compared to assess the benefits of the additional SNR at ultra-high field for facilitating a more comprehensive cerebrovascular assessment.

2

High Field Acquisition and Reconstruction Methods

2.1 7 Tesla MRI

2.1.1 General

Since the first human scans in the 1980s, MRI has seen a rapid increase in both the number of MRI publications and the field strength of the MRI scanners [46]. The first scanners used sub-tesla resistive electromagnets or permanent magnets, followed by the first 0.15T superconducting magnet used for MRI in 1982 [46,47]. Nowadays, most clinical MRI systems operate at 1.5T or 3T, while nearly 100 ultra-high field 7T scanners are already available in a research setting [48].

Those higher magnetic field strengths ($B0$) are desirable in MRI because of the resulting supralinear increase in signal and SNR. For example, direct comparisons of measurements at different field strengths have found the average SNR in the brain to be proportional to $B0^{1.65}$ [49], with the SNR in the centre of a phantom scaling by as much as $B0^{1.94}$ [50]. As a result of this increased SNR, UHF MRI also allows for acquisitions at higher (spatial or temporal) resolutions. This makes it possible to detect finer structures, such as smaller vessels in MR angiography or to achieve improved plaque component characterization in VWI. Furthermore, over the range of field strengths used for MRI, increasing magnetic field strengths typically result in an increase in the T1 relaxation time and a decrease in the T2 relaxation time. This can provide both advantages and disadvantages to the resulting contrasts, depending on the sequence. For example, the background suppression in MR angiography is improved by the longer T1 of static tissue at 7T, resulting in the clear visualization of narrow vessels which are not visible at 3T [51].

Increased magnetic field strengths also introduce technical challenges and limitations. These challenges include additional concerns about implant safety and increased magnetic susceptibility artefacts, but the biggest challenges in terms of sequence design are introduced by changes in the specific absorption rate (SAR) and static and radiofrequency

field inhomogeneity. This chapter surveys the advanced MRI concepts and methodologies that are used in the subsequent experimental chapters of the thesis.

2.1.2 SAR

The SAR (in Watts/kg) is used to describe the RF power deposition in tissue due to RF pulses. To ensure subject safety, there are limits on both the global SAR and the local SAR (defined as the SAR within any 10g averaging volume). Although the global SAR limits are the same at all field strengths (with special additional local SAR limits when using local transmit coils, which is more common at 7T) [52], the SAR depends on the electric field strength E. Since the component of the electric field which is generated by the time-varying magnetic fields is proportional to the Larmor frequency ω_0 of an RF pulse, this component of E also scales with $B0$:

$$\mathrm{SAR} \propto |\mathrm{E}|^2 \propto \left(A_p \omega_0\right)^2 = \left(A_p \gamma B0\right)^2, \qquad 2.1$$

where A_p denotes the amplitude of the RF pulse and γ is the gyromagnetic ratio [53]. This shows that the B-dependent SAR component is proportional to the square of the main magnetic field strength, so with all other things (including the local E-fields around capacitors) being equal, the SAR at 7T is 5.4× higher than at 3T and 21.8× higher than at 1.5T. This means that although the SAR limits are the same at all field strengths, they impose much more stringent limitations on sequence design at 7T.

The SAR is also proportional to the square of the RF pulse amplitude A_p, even though the applied flip angle of an RF pulse is linearly proportional to A_p. This means that when reducing A_p by a factor n while increasing the pulse duration t by the same factor, the resulting flip angle FA remains the same:

$$FA = \frac{A_p}{n} * nt = A_p * t, \qquad 2.2$$

while the resulting SAR energy is reduced by a factor n:

$$E_{SAR} \propto \left(\frac{A_p}{n}\right)^2 * nt = \frac{1}{n} A_p^2 * t. \qquad 2.3$$

This property is used in this thesis to reduce the SAR of MRA acquisitions at 7T by increasing the pulse duration. In addition, calculations using the quadratic dependence of

the SAR on A_p are used to ensure that the DANTE-preparation modules using different flip angles and/or numbers of pulses remain within the SAR limits.

2.1.3 $B1^+$ Inhomogeneity

In addition to increased SAR, MRI at higher B_0 also introduces limitations to the homogeneity of the transmit ($B1^+$) and receive ($B1^-$) fields. This is a result of the high Larmor frequency of nearly 300 MHz at 7T. This means that electromagnetic waves at 300 MHz travelling at the speed of light in vacuum ($c_0 = 3 \times 10^8$ m/s) have a wavelength (λ_0) of approximately 1 metre. However, the speed of light in the human body is substantially reduced due to (in particular) the relative permittivity (ε_t) of the tissue, resulting in a reduction in the RF wavelength (λ_t) in tissue:

$$\lambda_t = \frac{2\pi c_t}{\omega_0} = \frac{2\pi c_0}{\omega_0 \sqrt{\varepsilon_t}} = \frac{\lambda_0}{\sqrt{\varepsilon_t}}. \qquad 2.4$$

Using the relative permittivity values used in the IT'IS Virtual Family [54,55], this gives an RF wavelength at 300 MHz of about 14 cm in grey matter ($\varepsilon_t = 52$) and 16 cm in white matter ($\varepsilon_t = 39$). In addition to the high relative permittivity in tissue, these wavelengths are further attenuated by the increased conductivity (σ) in tissue, which introduces a small additional reduction to the RF wavelength [56] through:

$$\begin{aligned} \lambda_t &= \frac{2\pi}{\omega_0}\left[\frac{\mu\varepsilon_0\varepsilon_t}{2}\left(1+\sqrt{1+\left(\frac{\sigma}{\varepsilon_0\varepsilon_t\omega_0}\right)^2}\right)\right]^{-1/2} \\ &= \frac{\lambda_0}{\sqrt{\varepsilon_t}}\left[\frac{1}{2}\left(1+\sqrt{1+\left(\frac{\sigma}{\varepsilon_0\varepsilon_t\omega_0}\right)^2}\right)\right]^{-1/2} = \frac{\lambda_0}{\sqrt{\varepsilon_t}}\,F(\sigma,\varepsilon_t,\omega_0), \end{aligned} \qquad 2.5$$

where the final expression is the result of Equation 2.4 multiplied by an additional attenuation factor $F(\sigma, \varepsilon_t, \omega_0) \leq 1$. For grey and white matter, $F(\sigma, \varepsilon_t, \omega_0)$ is around 0.89 and 0.91, respectively (again using the tissue properties used in the IT'IS Virtual Family [54,55]). Using Equation 2.5, this results in wavelengths at 300 MHz of about 12.3 cm in grey matter and 14.7 cm in white matter.

These values are smaller than the typical dimensions of the human head, resulting in a 'standing wave' pattern in the transmit field with areas of higher and lower $B1^+$ sensitivity. This leads to spatially varying flip angles and therefore spatially varying image contrasts at 7T. This is also shown in Figure 2.1, which indicates that the low wavelengths in tissue at

7T result in contrast variations which are less challenging at magnetic field strengths of 3T or below.

Various techniques which aim to improve the homogeneity of UHF acquisitions have been introduced. These include high-permittivity dielectric pads which manipulate the transmit field distribution [57,58], adiabatic RF pulses with reduced RF field sensitivity [59], and the use of multiple independently controlled transmission channels [60]. The latter, which is known as parallel transmission (pTx), will be further discussed in Section 2.3.

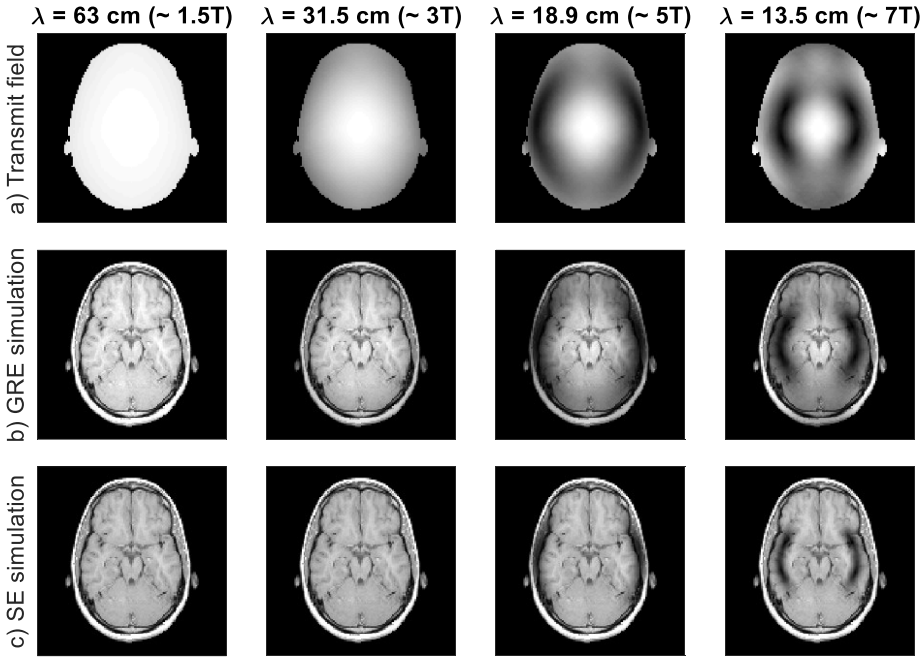

Figure 2.1: Simplified $B1^+$ inhomogeneity effects at different RF wavelengths (corresponding to different B0 field strengths). For each wavelength, the rows show **(a)** the estimated transmit field (assuming a FOV of 24×24 cm with a 30 cm diameter birdcage coil; the head is simulated as a single homogeneous volume), followed by resulting **(b)** GRE simulations (FA 20°; TE/TR = 0.01/0.05 s) and **(c)** spin-echo (SE) simulations (90° excitation pulse followed by 180° refocusing pulse, TE = 0.01 s). Simulations in (b) and (c) are generated by scaling the default MATLAB "mri" image based on the signal loss due to the transmit fields in (a), assuming T1/T2 = 1.3/0.11 s and nominal flip angles in the centre of the head.

2.2 Parallel Imaging

2.2.1 Principles

Section 2.1.3 discussed the effects of the short RF wavelengths at 7T on the resulting transmit fields. These shorter wavelengths also affect the receive sensitivity field ($B1^-$), which at UHF suffers from reduced penetration depth but also provides increased spatial separation of the sensitivity profiles of multi-channel receive coil arrays. This increased

spatial separation benefits the performance of parallel imaging techniques at UHF. Parallel imaging [61] is a robust method to accelerate MRI acquisitions by only acquiring partial k-space data, after which the information acquired from different receive channels is combined to remove aliasing artifacts. This can be used to achieve shorter acquisition times, thereby improving patient comfort, and reducing the risk of subject motion during a scan.

The individual channels in a receive coil array are positioned at different locations around the head of the subject (for intracranial imaging). As a result, each channel has a different spatial sensitivity profile, generally with the highest sensitivity close to the centre of the channel, as shown in Figure 2.2.

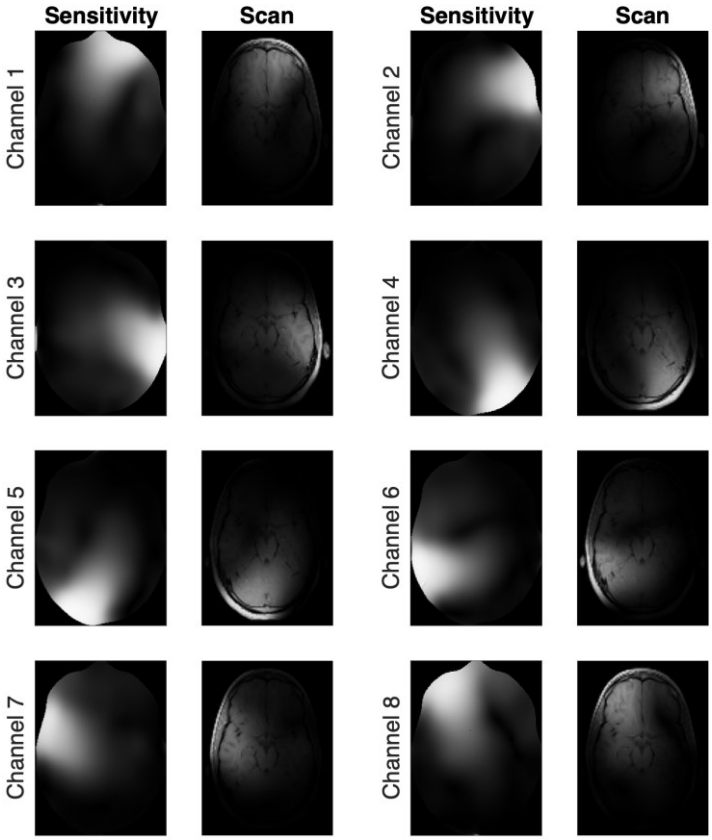

Figure 2.2: Sensitivity maps ("Sensitivity") and the resulting single-channel images ("Scan") of a synthetic 8-channel head receive coil array at 7T. The sensitivity maps shown here are a subset of the measured sensitivity maps of a 32-channel head coil, of which only 8 channels (within the same axial plane) are shown here for clarity. Brighter areas indicate increased sensitivity. The "Scan" images are generated by modulating the default MATLAB "mri" image by the respective sensitivity profiles. Uncorrelated Gaussian k-space noise was added to visualize noise propagation in later figures.

Acquisitions from the different receive channels only contain information about areas in the imaged volume where a channel has sufficient sensitivity. Different approaches can be used to combine the multi-channel data. The most straightforward approaches are to either

sum the magnitudes of the different channels at each location (Figure 2.3b), or to use the root sum-of-squares of the individual channels (Figure 2.3c). Although those approaches are straightforward, the bottom row in Figure 2.3 shows that the sum of magnitudes amplifies the noise, while the root sum-of-squares generates coil-combined images with intensity profiles which are different from the underlying MR signal. This can result in sensitivity bias and reduced SNR. However, if information about the spatial sensitivity (S_i) of each channel is available, this can be used to derive a coil-combined image (I_{cc}) which represents the underlying MR signal as [62]:

$$I_{cc} = \frac{\sum_i I_i S_i^*}{\sum_i S_i S_i^*}, \qquad 2.6$$

where I_i is the acquired image from channel i and asterisks denote the complex conjugate. As is visible in Figure 2.3d, this can provide an unbiased image estimate.

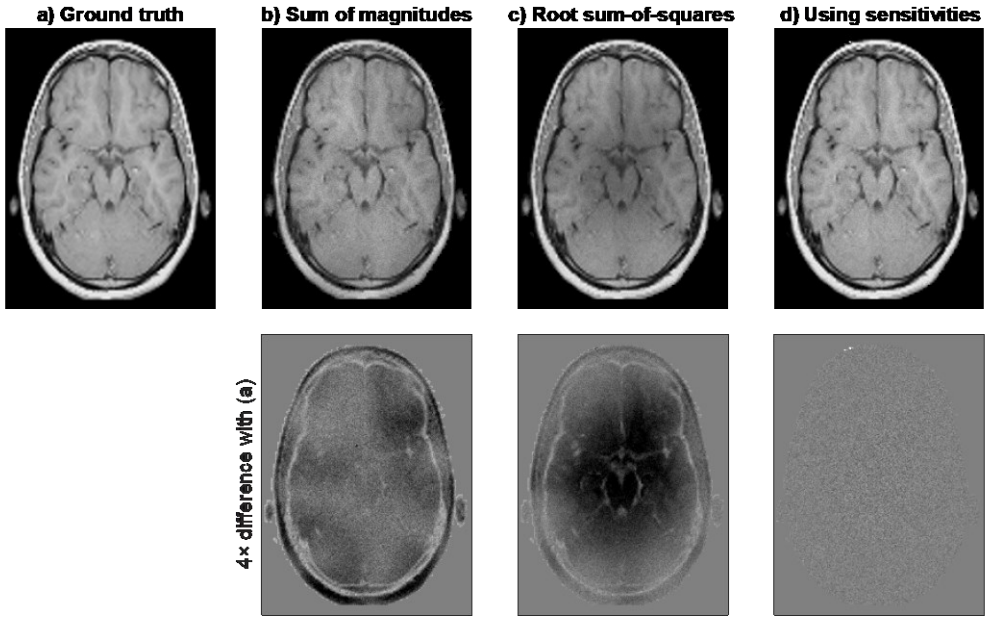

Figure 2.3: Different methods for receive coil combination, reconstructed from the 8-channel data in Figure 2.2. The first row shows **(a)** the ground truth MATLAB "mri" image, **(b)** the normalized sum of the magnitudes of the multi-channel images, **(c)** the root sum-of-squares of the multi-channel images, and **(d)** the sensitivity-weighted reconstruction (Equation 2.6). The second row shows the (4× boosted) differences between the reconstructions in (b-d) and the ground truth in (a), where brighter and darker areas correspond to signal over- and under-estimation, respectively.

The results in Figure 2.3 were generated using the synthetic multi-channel images shown in Figure 2.2 to facilitate direct comparison of the resulting coil-combined images to the underlying ground truth. This indicates bias-free coil-combined images when using Equation 2.6. In actual acquisitions, the accuracy of reconstructed images is limited by

acquisition noise (as is visible in Figure 2.3d), as well as inaccuracies in the assumed coil sensitivity profiles. Those coil sensitivity profiles depend on the loading of the coil and the positioning of the subject. Therefore, estimates of the sensitivity profiles in each individual scan session are required to provide the best sensitivity-weighted reconstructions (Equation 2.6). This is possible using ESPIRiT [63], which estimates receive coil sensitivity maps from the central portion of the acquired k-space of the different receive channels.

2.2.2 ESPIRiT Coil Sensitivity Estimation

ESPIRiT (Eigenvalue iTerative Self-consistent Parallel Imaging Reconstruction) [63] is used in this thesis for coil sensitivity estimation. This is required for sensitivity-weighted receive coil combination (Equation 2.6) and for compressed sensing image reconstruction, which will be described in Section 2.2.4. ESPIRiT achieves accurate sensitivity profile estimation through eigenvalue decomposition of a reconstruction operator $\boldsymbol{\mathcal{W}}$ in patches of the so-called calibration region, which is a fully-sampled central portion of k-space. $\boldsymbol{\mathcal{W}}$ is a function of two underlying matrix operators: the operator R_r, which extracts a calibration region patch of N samples around a location r, and the matrix $V_{\|}$, which spans the row space of the calibration matrix A. The matrix A is a Block-Hankel representation of the calibration region, in which each row corresponds to a different k-space patch (extracted by R_r): see Figure 2.4.

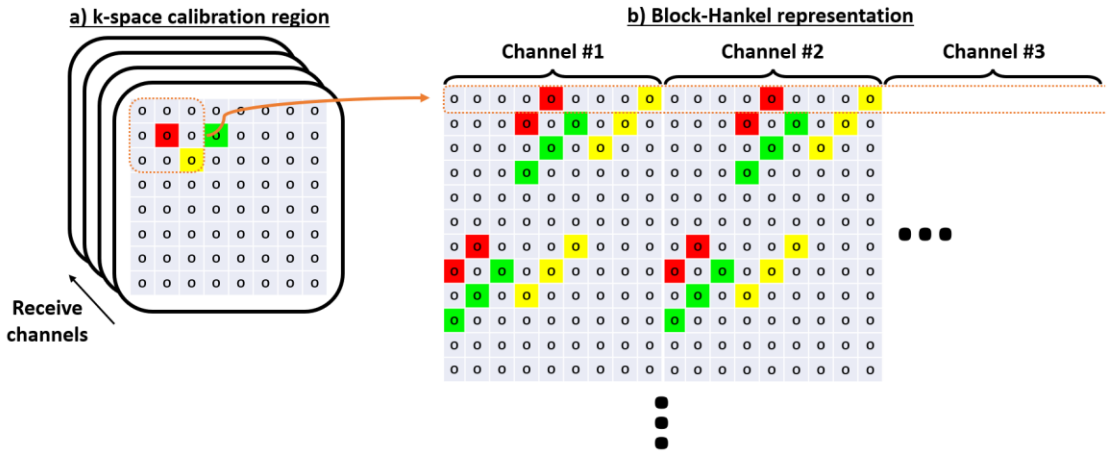

Figure 2.4: Schematic of the Block-Hankel matrix representation of the k-space calibration region as used for ESPIRiT coil sensitivity estimation [63]. The role of the operator R_r is shown using the orange arrow for a 3-by-3 kernel.

Using the patch extraction operator R_r, the calibration region row space matrix $V_{\|}$, and the number of samples per patch N, the reconstruction operator $\boldsymbol{\mathcal{W}}$ is defined as

$$\boldsymbol{W} = \frac{1}{N}\sum_r R_r^H V_\| V_\|^H R_r, \quad 2.7$$

where superscript H denotes the Hermitian (complex conjugate transpose) operation. The underlying k-space is invariant to the operator $\boldsymbol{W}$ [63]. By rewriting k-space as the Fourier transform ($\mathcal{F}$) of the underlying magnetization m weighted by the coil sensitivities S, this means that:

$$\boldsymbol{W}\mathcal{F}Sm = \mathcal{F}Sm, \quad 2.8$$

such that:

$$\mathcal{F}^{-1}\boldsymbol{W}\mathcal{F}Sm = Sm. \quad 2.9$$

This implies that the coil sensitivities form an eigenvector of $\mathcal{F}^{-1}\boldsymbol{W}\mathcal{F}$ with eigenvalue 1 at locations where $m \neq 0$. Therefore, explicit complex sensitivity maps can be found at each location with non-zero signal through eigenvalue decomposition of the matrix $\mathcal{F}^{-1}\boldsymbol{W}\mathcal{F}$ at those locations and choosing only the eigenvectors with eigenvalue 1.

Since ESPIRiT uses only the central portion of the acquired k-space data, it requires no (to very little) additional scan time while still providing high precision sensitivity estimates [63].

2.2.3 SENSE and GRAPPA

As mentioned in Section 2.2.1, parallel imaging [61] facilitates accelerated acquisition of MRI data by only acquiring specific parts of multicoil k-space data, after which the missing k-space samples are approximated using the sensitivity encoding of the different receive channels. The two main methods for reconstructing regularly undersampled k-space data are SENSE (Sensitivity Encoding [64]) and GRAPPA (Generalized Autocalibrating Partially Parallel Acquisitions [65]). Although both can be shown to obtain missing values using the same restrictions based on the subspace of the coil sensitivities [63], they are different in their implementation. Most notably, SENSE operates in image space, where it disentangles aliased reconstructions using coil sensitivity maps, while GRAPPA interpolates missing values directly in k-space, as shown in Figure 2.5.

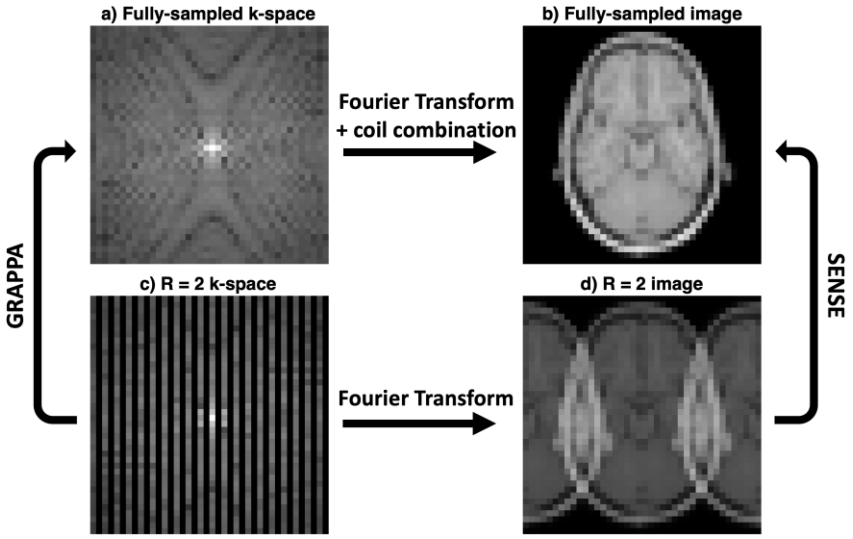

Figure 2.5: The basic ideas of GRAPPA and SENSE in unaliasing undersampled images. GRAPPA aims to directly estimate missing k-space values, while SENSE disentangles aliased images using multi-coil sensitivity information in image space. Low-resolution data are shown to more clearly visualize the undersampled k-space.

Figure 2.6 schematically shows the basic principle behind SENSE reconstruction, including a simplified example of how SENSE uses sensitivity maps to unalias multicoil acquisitions. This example is shown for an acceleration factor of $R = 2$ and using only two receive channels. The equations to the right of Figure 2.6 show how the underlying signal can be calculated as a weighted average of the measured signals. To generalize this process to higher numbers of receive channels (N_{ch}) and higher acceleration factors ($R \leq N_{ch}$), and to also account for noise correlation, the general SENSE formulation uses a more efficient matrix representation [64]. This matrix representation calculates the underlying magnetization m from the multi-channel sensitivity information S, the noise correlation matrix Ψ, and the multi-channel measured images I as:

$$m = (S^H \Psi^{-1} S)^{-1} S^H \Psi^{-1} I. \qquad 2.10$$

Although SENSE benefits from being more intuitive by operating in image space, GRAPPA is used in this thesis for the reconstruction of regularly undersampled DANTE-SPACE data.

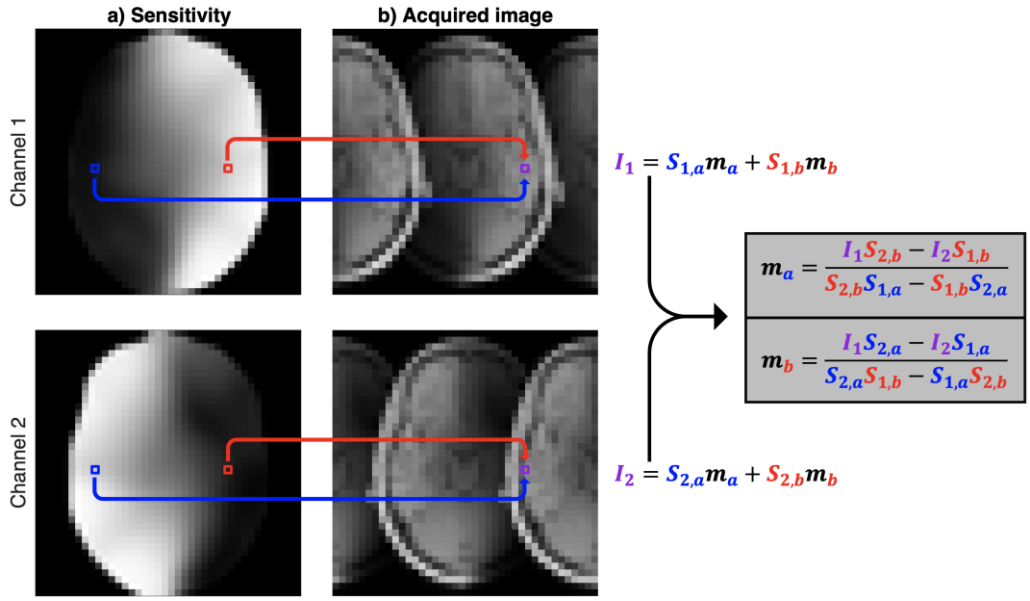

Figure 2.6: Image unaliasing of an R = 2 undersampled acquisition based on the combination of **(a)** the sensitivity profiles of two different coil channels and **(b)** the resulting acquired images. For each channel (denoted i), the measured value at a given voxel location (I_i, shown in purple) is the sum of the sensitivity-weighted signal at that location (red) and the sensitivity-weighted signal aliased from a distance $FOV/2$ away (blue). Using the sensitivity maps, the aliased images can be disentangled to calculate the underlying MR signal at both locations (m_a and m_b), as shown to the right.

Since GRAPPA operates directly in k-space, it performs the anti-aliasing correction before applying a Fourier transform (to image space) and therefore does not require explicit sensitivity maps. GRAPPA utilizes the redundancy in multi-channel k-space to interpolate missing k-space lines as a weighted average of acquired k-space lines. This redundancy, which can be proven based on the existence of a null-space of the calibration matrix A used in Section 2.2.2 [63], exists because coil sensitivity profiles result in the acquired k-space values being smeared out over a neighbouring portion of k-space [61]. As this smearing effect is the same throughout k-space, detecting its effects in one area makes it possible to extract information about missing k-space values based on the surrounding values.

The interpolation of missing values is implemented as the weighted average of acquired k-space values within a small area surrounding the missing value, known as a kernel. Interpolation using a small kernel is generally sufficient since the nearby values contribute most to a missing value, while resulting in improved computational efficiency. Although a kernel only considers a small subset of k-space, information from all receive channels is used to interpolate the missing values in each individual channel. Therefore, when using an $N_x \times N_y$ kernel, the value of each missing k-space value (for each channel) is interpolated as the weighted average of $N_x * N_y * N_{ch}$ acquired k-space values. In GRAPPA, those

weights are calculated by fitting the additional acquired data in the calibration region to the surrounding data using the same $N_x \times N_y$ kernel.

Although both SENSE and GRAPPA provide aliasing-free reconstructions within reduced scan times, they do introduce an SNR penalty. This SNR penalty consists of two components: a $\sqrt{R}$ noise amplification because of the reduced number of acquired samples, and an additional spatially variant geometry-dependent noise amplification factor $g \geq 1$ (known as the g-factor). As a result, the SNR at a location r in a parallel imaging-accelerated acquisition (SNR_{PI}) is reduced from the fully sampled SNR (SNR_{full}) as:

$$SNR_{PI}(r) = \frac{SNR_{full}(r)}{g(r)\sqrt{R}}. \qquad 2.11$$

The g-factor noise amplification profile depends on a combination of different factors, such as the number of receive coils and the separation of their sensitivity profiles, the imaging orientation, and the direction and acceleration factor of the undersampling [66]. In general, it increases as the required amount of unaliasing increases (such as at higher acceleration factors and using smaller field-of-views). This is also visible in Figure 2.7, which shows the reduced SNR and increased g-factors at higher GRAPPA acceleration factors.

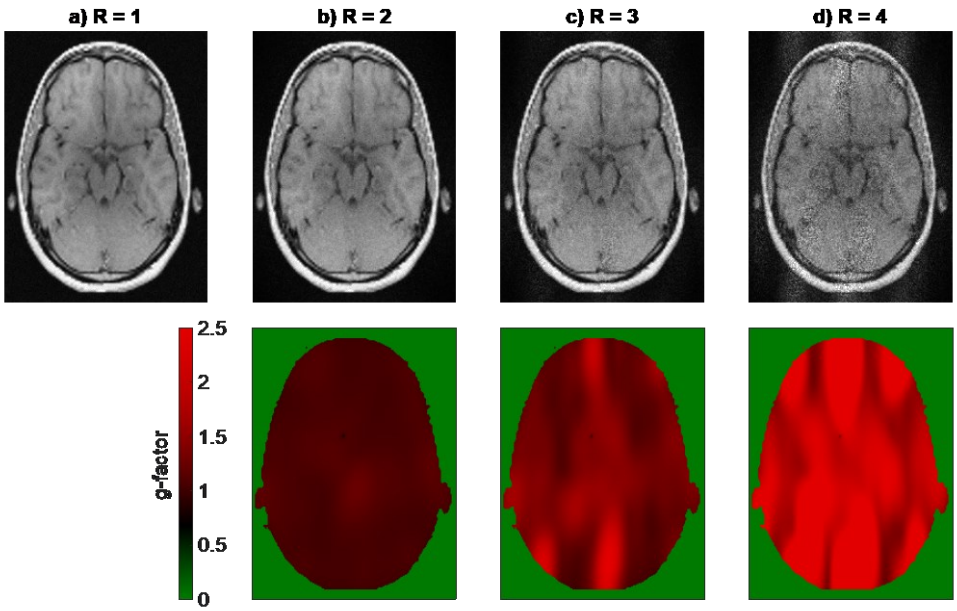

Figure 2.7: GRAPPA reconstructions and g-factor noise amplification maps at different acceleration factors R. Data were reconstructed using the simulated 8-channel coil data shown in Figure 2.2. Figures (b-d) were undersampled along the left-right direction. The g-factor maps were estimated using the method described by Breuer et al. [66] and masked for clarity.

2.2.4 Compressed Sensing

Although parallel imaging methods such as SENSE and GRAPPA can provide substantially accelerated acquisitions, they are generally limited to acceleration factors of about 3-4 due to the reduction in image quality. An alternative technique which can reconstruct data with even higher acceleration factors is called compressed sensing (CS) [67]. CS reconstruction requires (pseudo-)randomly undersampled k-space data to prevent structured artefacts.

Figure 2.8b shows that the regular undersampling used in SENSE and GRAPPA results in structured aliasing artifacts. At low acceleration factors the aliased copies can still be separated, but at $R = 10$ it becomes harder to distinguish features of the underlying image. However, using randomized sampling, Figure 2.8d shows that the image appears noisy but without structured artefacts. As a result, some basic features of the sample are still visible at very high acceleration factors.

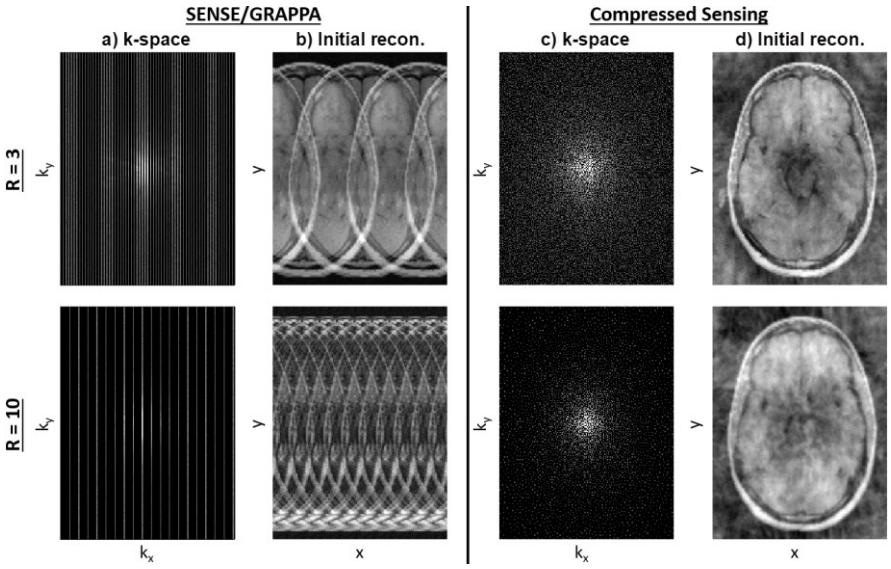

Figure 2.8: The undersampling strategies and resulting initial reconstructions as used for **(a-b)** SENSE or GRAPPA and **(c-d)** compressed sensing. Results are shown for acceleration factors of 3 (first row) and 10 (second row). An acquisition with readouts along the k_z-direction (head-foot) is shown for visualization purposes.

CS relies on the visibility of those underlying image features. In principle, the CS reconstruction algorithm iteratively (1) identifies some probable 'true' image features, (2) calculates the k-space signal corresponding to those features, (3) uses this information to improve the estimates of the missing k-space samples, and (4) reconstructs the k-space again.

If the identified features (in Step 1) are accurate, the changes to the missing k-space samples (in Step 3) reduce the amount of noise in the next reconstruction (in Step 4) and make it possible to identify further features of the underlying image. Two requirements for this approach to provide accurate reconstructions are firstly a reliable method for identifying underlying image features (in Step 1) and secondly an appropriate cost function to decide by how much k-space can be changed (in Step 3).

For the first condition, MRI CS methods usually rely on sparsity, in which an image is assumed to consist of (near-)zero values in most locations, but high values in some locations. This is inherently true for reconstructed MRA data. In MRA, (near-)zero values are found in the suppressed background tissue, with high values in the vessels which only make up a small percentage of the voxels. Therefore, the voxels with the highest signal in the initial reconstruction of a CS undersampled MRA image are probable 'true' image features in the first step of the algorithm. However, in many cases (such as the example shown in Figure 2.8), there is no such inherent image sparsity. In such cases (or to achieve even more sparse versions of inherently sparse images), sparsifying transforms can be used to introduce sparsity. Various such transforms have been proposed, including different wavelet transforms [67–69], the discrete cosine transform [67], or a total variation measure [68]. Figure 2.9 shows an example of how the wavelet transform can be used to achieve a sparse representation of an image which is not inherently sparse.

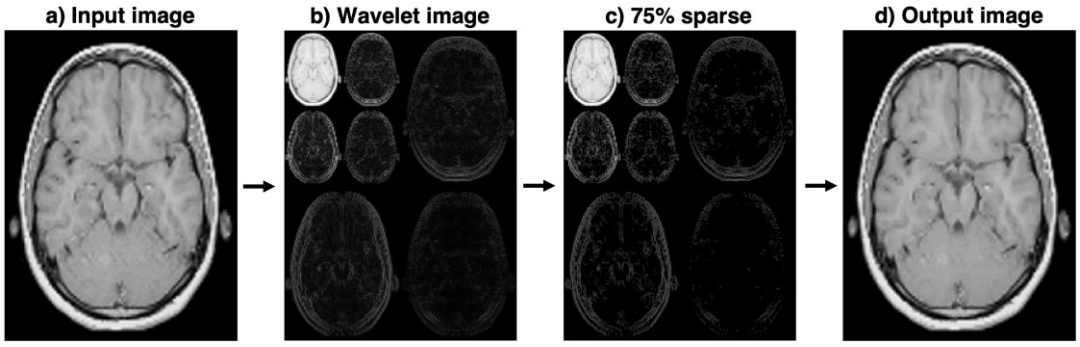

Figure 2.9: The wavelet transform as a sparsifying transform. A non-sparse image **(a)** becomes sparse when using its wavelet representation **(b)**. As an example, the corresponding wavelet representation with 75% of the values replaced by zeros **(c)** can still provide an accurate version of the original image in image space **(d)**. Results are shown for the Haar wavelet transform. In the wavelet images, horizontal, vertical, and diagonal coefficients are shown in the top-right, bottom-left, bottom-right corners, respectively. The contrast of the wavelet images is boosted to increase coefficient visibility.

CS algorithms generally use cost functions which consist of a weighted sum of two terms: a term which enforces sparsity and a data-consistency term. This results in generalized cost functions of the form:

$$\min_{x}\{|A(m) - b| + \lambda|\phi(m)|_1\}. \quad 2.12$$

$|A(m) - b|$ is the data-consistency term, in which b denotes the acquired (undersampled) k-space data and $A(m)$ is the undersampled Fourier transform operator over the reconstructed image m. The second term, $|\phi(m)|_1$, enforces sparsity on the reconstructed image m using the sparsifying transform ϕ (in this case using L1-regularization). Finally, λ is a predefined regularization parameter which controls the trade-off between the data consistency and sparsity terms.

2.3 Parallel Transmission

2.3.1 Principles

Section 2.1.3 described the limitations of UHF MRI due to $B1^+$ inhomogeneity. When using a regular (single channel) transmit coil, field inhomogeneity intrinsically limits the homogeneity of the achieved signal levels and contrasts. However, it is also possible to use coils which consist of multiple transmit channels located at different locations around the imaged object, such as the coil model shown in Figure 2.10a. Although each of the parallel transmit channels has its own (inhomogeneous) transmit field, by manipulating the power and phase of the transmitted RF signal to each of the channels it is possible to modify the resulting combined transmit field. This process, known as parallel transmission (pTx) [60], allows for modification of the $B1^+$ field. For a pTx coil consisting of N_T transmit channels, the total combined $B1^+$ field simply corresponds to the sum of the $B1^+$ fields of the individual channels:

$$B1^+_{full} = \sum_{i=1}^{N_T} B1^+_i = \sum_{i=1}^{N_T} w_i S_i. \quad 2.13$$

Here, $B1^+_i$ denotes the transmit field of the ith channel, which is the product of the inherent transmit sensitivity S_i and the complex pTx weight w_i applied to the channel. The transmit sensitivity of any given channel depends on the coil geometry and loading of the coil and is therefore fixed during a scan session. However, the phase ϕ_i and amplitude A_i of w_i can be dynamically changed over time.

When using a specific set of complex weights such that $A_i = 1$ and $\phi_i = 360° * i/N_T$ (i.e., 45° phase increments per channel for an 8-channel pTx coil), the combined transmit field of a pTx coil array corresponds to the transmit field of a single-channel birdcage coil of

similar geometry. An example of this specific combination of pTx weights, which is known as circular polarization (CP) or quadrature mode, is shown in Figure 2.10b.

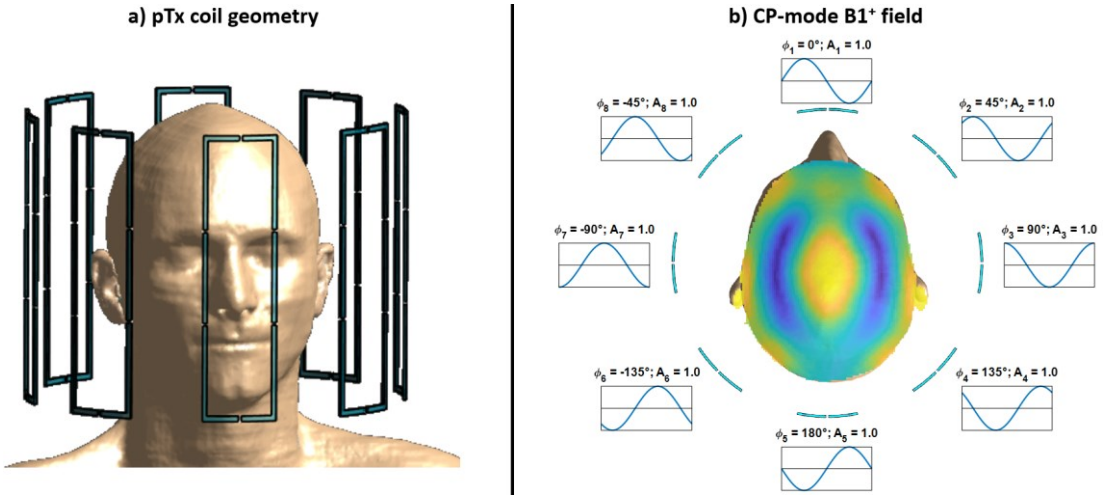

Figure 2.10: (a) Schematic 8-channel pTx coil [55] surrounding the Duke body model [54], and **(b)** an example simulation of the pTx B1⁺ field using CP-mode (shown by the 45° phase increments in the waveforms next to the different channels). A modified version of the simplified B1⁺ simulations described in Figure 2.1 was used to generate the fields in (b).

2.3.2 RF Shimming

Modification of the complex weights w_i used to drive a pTx coil with a 'conventional' RF pulse (e.g., a sinc or Gaussian pulse) applied to each channel is known as RF shimming (or static pTx) [70]. It aims to modify the combined transmit field by modulating the phase and/or magnitude of the pTx channels. When using an 8-channel pTx coil, RF shims can be calculated with 7 different phase offsets (relative to a certain channel) and 7 different amplitudes (relative to a certain nominal value), providing up to 14 degrees of freedom. Those degrees of freedom can, for example, be utilized to design RF shim combinations which (within a region of interest) maximize the B1⁺ magnitude, optimize B1⁺ homogeneity [70,71], reduce the resulting SAR [72], or any weighted combination of different targets [60,72]. Figure 2.11 shows simulated examples of a B1⁺ field resulting from (a) a phase-only RF shim [71], in which only the phase offsets of the pTx channels are changed (and $A_i = 1$ is used for all channels), and (b) a phase-and-magnitude RF shim. Note that the data shown in Figure 2.11 are equivalent to the CP-mode data shown in Figure 2.10b, but using different shim coefficients. For phase-only RF shims, the transmit field is modified by changing the interference patterns of the individual channels, resulting in different areas of constructive and destructive interference as desired. However, phase-and-magnitude RF shims can achieve improved shim performance using the N_T additional degrees of freedom.

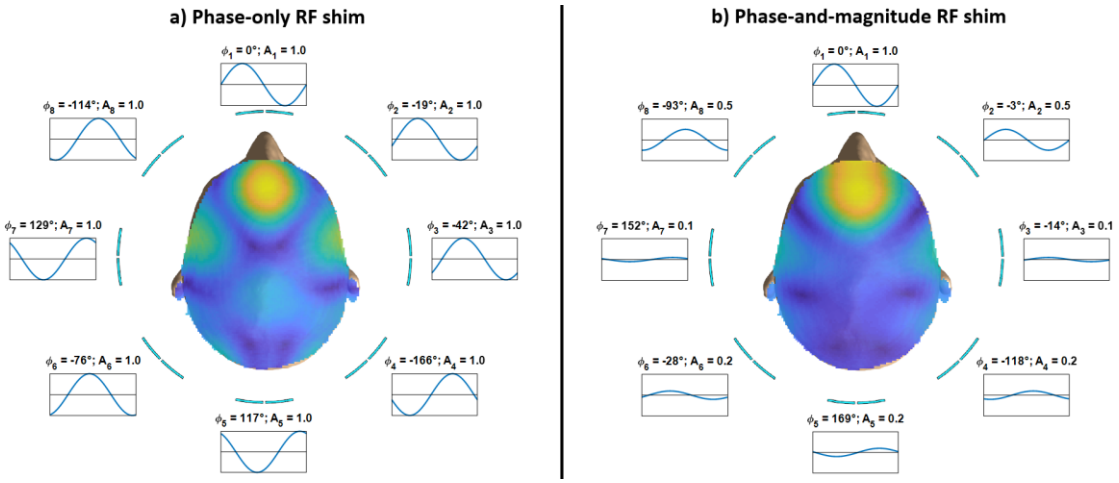

Figure 2.11: Examples of **(a)** phase-only RF shimming and **(b)** phase-and-magnitude RF shimming. For each channel i, ϕ_i denotes the phase offset (relative to Channel 1) and A_i denotes the relative amplitude of the RF waveforms shown in the surrounding subplots. Both shims aim to increase the $B1^+$ in the middle of the prefrontal cortex.

RF shimming, in which a single set of pTx weights is used during a given RF pulse, is the only pTx application used in this thesis. However, since the pTx weights can be modified on microsecond timescales, it is possible to introduce many additional degrees of freedom by continuously changing the pTx weights and waveforms during a pulse. This process, known as dynamic pTx, makes it possible to directly control the resulting magnetization at the end of a pulse (instead of only controlling the $B1^+$ field during a pulse). Therefore, it can provide substantial improvements to the resulting signal homogeneity, or it can be used to achieve highly localized excitation (without excitation outside the target region). A comprehensive overview of dynamic pTx methods and applications can be found in Ref. [60].

As mentioned in Section 2.3.1, the transmit sensitivity S_i (as used in Equation 2.13) of each individual transmit channel depends on the loading of the coil and is therefore dependent on both the anatomy and positioning of the subject within the coil. This means that the pTx methods described above require subject-specific $B1^+$ calibration measurements for the optimization of pTx weights. The acquisition (which will be discussed in Section 2.3.3) and processing of such subject-specific $B1^+$ maps at the start of each scan session takes up multiple minutes and requires manual steps to identify the target regions in the subject, limiting the practical use of pTx. However, the transmit field of a given pTx channel across different subjects is highly correlated when the same body part (such as the head) is imaged in a similar position within the coil [73]. As a result, the combined $B1^+$ field of a pTx coil using a given set of weights is also correlated across subjects. Therefore, it is often possible to design a single set of pTx weights which generates a transmit field with specific desired

properties in different subjects. Such a set of weights, which is known as a universal RF shim (or universal pulse for dynamic pTx) [73], can be calculated by simultaneously optimizing the weights based on the desired cost function in a representative population of subjects. If the resulting weights perform as desired for this population of subjects, the correlation between channels means that they generally also provide a $B1^+$ field with the desired properties in future (unseen) subjects. This means that the use of universal RF shims facilitates the calibration-free use of pTx, which substantially reduces the overall scan time and improves the (clinical) workflow.

2.3.3 $B1^+$ and B0 Mapping

The calculation of either subject-specific B0 or universal RF shims using Equation 2.13 requires accurate multi-channel $B1^+$ maps, either acquired from the imaged subject or from a database of subjects (for universal shims). Multi-channel absolute $B1^+$ maps can be obtained through direct measurement of (linear combinations of) the absolute $B1^+$ fields of the individual transmit elements. However, this is time-consuming and requires high sensitivity for the individual acquisitions. Alternatively, a single absolute $B1^+$ map ($\mathbf{B1}^+_{abs}$) can be acquired that is combined across all N_T transmit elements, together with a full set of relative $B1^+$ maps ($\mathbf{B1}^+_{rel,i}$) which are quicker and easier to obtain. Using this information, the absolute $B1^+$ field of the ith transmit element can be calculated based on its relative contribution to the combined absolute $B1^+$ field as follows:

$$\mathrm{B1}^+_i = \frac{\mathrm{B1}^+_{rel,i}}{\sum_{j=1}^{N_T} \mathrm{B1}^+_{rel,j}} \mathrm{B1}^+_{abs}. \qquad 2.14$$

Relative $B1^+$ maps can be acquired based on the signal ratios of low-flip-angle spoiled gradient echo (SPGR) images acquired from the individual transmit channels. For some pTx applications, it can be sufficient to calculate RF shims or pulses based on relative $B1^+$ maps alone. This is particularly the case when the maximum $B1^+$ in all voxels within the target region can be assumed to be similar. However, when calculating an RF shim for a region which contains voxels with a large amount of variation in the maximum $B1^+$, it is important to also take absolute $B1^+$ measurements into account to ensure homogeneous $B1^+$ for a calculated shim.

Many different absolute $B1^+$ mapping sequences are available in the literature. Those sequences differ in terms of, amongst other factors, their dynamic range, sensitivity, scan time, SAR, dimensionality (2D or 3D), and B0-dependence. A comprehensive overview

and comparison of various traditional absolute $B1^+$ mapping sequences has been presented by Pohmann et al. [74], who recommend the use of satTFL (pre-saturation TurboFLASH [75]) at ultra-high field because of its low SAR. SatTFL acquires two TurboFLASH acquisitions: an image S_{Sat} with a preceding pre-saturation pulse with nominal flip angle α_{nom}, and a reference image S_0 without an additional pulse. The effective flip angle $\alpha(r)$ at a location r can be calculated from those two acquisitions as

$$\alpha(r) = \arccos\left(\frac{S_{Sat}(r)}{S_0(r)}\right). \quad 2.15$$

Since $\alpha(r)$ only depends on the nominal flip angle, α_{nom}, and the $B1^+$ at the location r, this provides absolute information about the $B1^+$.

Traditional satTFL necessitates the use of a long delay for full signal recovery between the acquisition of the reference and prepared images, resulting in long acquisition times. A recently proposed modification of the satTFL sequence, called Sandwiched satTFL [76], removes this long delay and instead acquires S_0 and S_{Sat} images interleaved in rapid succession using modified readouts which introduce minimal magnetization history. As a result, Sandwiched satTFL facilitates the acquisition of 3D whole-head absolute $B1^+$ maps in under a minute [76].

In many cases, the calculation of pTx shims or pulses requires additional information about the static field offset ($\Delta B0$) to account for the frequency-dependent response of pulses. Such B0 maps can be acquired using 3D gradient-recalled echo acquisitions at two short but different echo times (TE_1 and TE_2). Differences in the resonance frequency (Δf) can then be derived from the phase difference between the two images (I_1 and I_2) as

$$\Delta f = \frac{\phi(I_1 I_2^*)}{2\pi(TE_2 - TE_1)}, \quad 2.16$$

where the operator ϕ extracts the phase value in radians, and the asterisk denotes the complex conjugate.

2.4 Extended Phase Graphs

In an MRI experiment, each spin experiences a series of RF pulses and gradients. For an isolated spin isochromat (a single spin or group of spins precessing at the exact same frequency), the evolution of its magnetization over time can be estimated using Bloch

simulations, which solve for the Bloch equations [77] at different points in time during a pulse sequence. However, a typical voxel in reality consists of spins precessing at a range of frequencies. As a result, Bloch simulations must be carried out for a whole ensemble of isochromats and then averaged for the results to accurately represent the measured signal in an MRI acquisition. This can require hundreds of simulations for the results to converge, resulting in very long simulation times.

Therefore, it can be more computationally effective and more accurate to express entire ensembles of isochromats based on their dephasing states. This approach is known as the extended phase graphs (EPG) formalism [78,79], in which an ensemble of isochromats is defined as a set of spins over a distance λ along the gradient direction such that a unit gradient (G) of unit duration (Δt) results in a 2π difference in phase accrual for spins a distance λ apart:

$$\lambda = \frac{1}{\gamma G \Delta t}. \tag{2.17}$$

In the EPG formalism, the ensemble magnetization is described as a combination of different configuration states, where the configuration states are defined as states which correspond to discrete multiples of the amount of dephasing from a single gradient G. This can then be used to simulate echo generation and to calculate the evolution of the transverse and longitudinal magnetization signal over time. Note that for this, the standard EPG formalism implicitly assumes that the entire ensemble of isochromats experiences the same uniform transmit and receive profiles, that RF pulses happen instantaneously, and that B0 off-resonance can be neglected. Furthermore, although multi-dimensional implementations of the EPG formalism have previously been introduced, the description and implementation used here are limited to one-dimensional simulations.

For EPG calculations, the configuration states are generally stored in a state matrix Ω which consists of three rows:

$$\Omega = \begin{bmatrix} F_0 & F_1 & F_2 & \cdots \\ F_0^* & F_{-1} & F_{-2} & \cdots \\ Z_0 & Z_1 & Z_2 & \cdots \end{bmatrix}. \tag{2.18}$$

In Ω, the elements F_k, F_{-k}, and Z_k (corresponding to the first, second, and third rows) denote different configuration states of dephasing order k. The elements in the first row (F_k) denote dephasing transverse magnetization, while the elements in the second row

(F_{-k}) denote rephasing transverse magnetization. For both F_k and F_{-k}, the dephasing order k corresponds to the number of phase cycles (corresponding to unit gradients of unit duration) by which the configuration states are dephased. When imagining an ensemble of isochromats as a stack of spins which all point in the same direction when in-phase, a dephased state of order k corresponds to a helix consisting of k twists (along a distance λ), as shown in Figure 2.12.

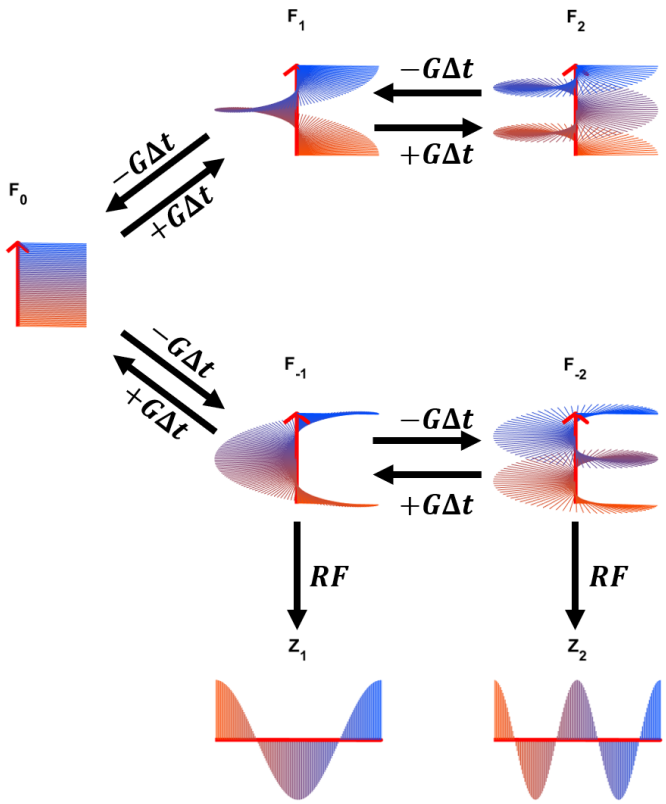

Figure 2.12: Graphical representation of the F_k, F_{-k}, and F_z EPG states. Red arrows denote locations along the gradient direction. In the F_0 state (to the far left), the phase of all transverse spins, represented by color-coded (for visibility) horizontal lines, is coherent. Application of positive or negative gradients of unit duration (as indicated by black arrows) dephases or rephases the ensemble by one period, corresponding to changing states from F_k to $F_{k\pm1}$ (for $\pm G\Delta t$). RF storage can shift dephased F_k states into the longitudinal Z_k direction, as shown on the bottom row.

The final row in Ω contains Z_k ($= Z_{-k}$) states, which denote longitudinal magnetization with periodic variation (along λ) in the amount of dephasing. Z_0 corresponds to equilibrium magnetization, and Z_k states with $k \geq 1$ are generated when the transverse magnetization in F_k or F_{-k} states is (partially) flipped back along the longitudinal axis.

In terms of the underlying longitudinal (M_z) and transverse (M_{xy}) magnetization along a distance λ, F_k, F_{-k}, and Z_k can be defined using the set of equations:

$$F_k = \frac{1}{2\pi}\int_0^{\lambda} M_{xy}(z)\, e^{-ikz} dz, \tag{2.19a}$$

$$F_{-k} = \frac{1}{2\pi}\int_0^{\lambda} M_{xy}^{*}(z)\, e^{-ikz} dz, \tag{2.19b}$$

$$Z_k = \frac{1}{2\pi}\int_0^{\lambda} M_z(z)\, e^{-ikz} dz. \tag{2.19c}$$

This shows that at equilibrium, all $F_{\pm k}$ states are zero while $Z_0 = 1$ (using $M_0 = 1$), such that the equilibrium state matrix $\Omega_0 = [0, 0, 1]^T$ describes the initial magnetization in an EPG simulation. By applying different transformations to Ω in accordance with the simulated sequence, the evolution of the state matrix can be calculated. For the EPG simulations in this thesis, five such transformations are used. These are the transformations corresponding to RF pulses (denoted T), relaxation (E), dephasing due to gradients (S), flow (J), and diffusion (D'), each of which is briefly discussed below. Using those transformations, the final state matrix can be calculated by applying the relevant transformations in chronological order. For example, for a basic spin echo sequence consisting of a 90° RF pulse followed by a 180° pulse, the resulting EPG state matrix (ignoring gradient, flow, and diffusion effects) can be calculated as $\Omega = E * T(180°) * E * T(90°) * \Omega_0$.

The RF pulse transformation is applied using a matrix multiplication which can invert states from $F_{\pm k}$ to $F_{\mp k}$, transfer between F_k and $Z_{|k|}$, or attenuate the magnitude of existing states as (for flip angle α with phase ϕ):

$$T(\alpha) = \begin{bmatrix} \cos^2\frac{\alpha}{2} & e^{2i\phi}\sin^2\frac{\alpha}{2} & -ie^{i\phi}\sin\alpha \\ e^{-2i\phi}\sin^2\frac{\alpha}{2} & \cos^2\frac{\alpha}{2} & ie^{-i\phi}\sin\alpha \\ -\frac{i}{2}e^{-i\phi}\sin\alpha & \frac{i}{2}e^{i\phi}\sin\alpha & \cos\alpha \end{bmatrix}. \tag{2.20}$$

Although $T(\alpha)$ can transfer signal between different states with the same amount of dephasing (same $|k|$), it does not change the level of dephasing. That instead happens while gradients are played out using the transformation S. Gradients introduce a change in the dephasing of transverse magnetization components, resulting in $F_k \rightarrow F_{k+\Delta k}$ for each F_k.

The relaxation in a tissue with relaxation times $T1$ and $T2$ during a time dt is calculated using the relaxation transformation E, which changes the state matrix as:

$$\Omega(t+dt) = E(dt)\Omega(t) = \begin{bmatrix} E_2 & 0 & 0 \\ 0 & E_2 & 0 \\ 0 & 0 & E_1 \end{bmatrix} \Omega(t) + \begin{bmatrix} 0 \\ 0 \\ 1-E_1 \end{bmatrix} \Omega_0, \qquad 2.21$$

where $E_1 = \exp(-dt/T_1)$ and $E_2 = \exp(-dt/T_2)$. In the final expression, the first term introduces attenuation of all existing states, while the second term introduces T1-recovery of the longitudinal signal (such that $\Omega(t+dt) \to \Omega_0$ as $dt \to \infty$).

The final two transformations, flow and diffusion, both correspond to row-wise multiplication with a diagonal matrix. Flow is defined as coherent motion of an ensemble with a velocity v and an angle β between the directions of the flow and the gradients. It introduces a phase shift to dephased components, which can be calculated using a diagonal matrix, J, with diagonal components defined as:

$$\mathrm{diag}(J) = \exp\left(-i\left[k_1 + \frac{\Delta k}{2},\ k_1 + \frac{\Delta k}{2},\ k_1\right] v dt \cos\beta\right), \qquad 2.22$$

where dt denotes the time interval, k_1 the initial dephasing state, and Δk the additional gradient dephasing during dt. Note that that since flow along the gradient direction result in the displacement of a dephased state along the dephasing direction, J only introduces a phase shift without changing the amplitudes of the underlying configuration states.

The incoherent motion of diffusing spins is simulated in a similar way using the diagonal matrix D', which increasingly reduces the contributions of higher-order terms (i.e., higher $|k|$) as described by Weigel et al. [80]. For each column in Ω, the diagonal components of the diffusion transformation are calculated as

$$\mathrm{diag}(D') = \exp\left(-\left[\left(k_1 + \tfrac{\Delta k}{2}\right)^2 + \tfrac{\Delta k^2}{12},\ \left(k_1 + \tfrac{\Delta k}{2}\right)^2 + \tfrac{\Delta k^2}{12},\ (k_1)^2\right] D dt\right), \qquad 2.23$$

where D denotes the diffusion coefficient, dt the diffusion time, k_1 the initial dephasing state, and Δk the additional gradient dephasing during dt. Note that since the coefficients in Equations 2.22 and 2.23 depend on the initial dephasing state k_1, the resulting values are different for each column in Ω.

In Chapter 5 of this thesis, the EPG framework is used to develop a simulation model for the DANTE-SPACE sequence.

3

Head-and-Neck Multi-Channel $B1^+$ Mapping and RF Shimming of the Carotid Arteries using a 7T Parallel Transmit Head Coil

Key Conclusions

- **Accurate 3D $B1^+$ maps in both the head and the neck can be reconstructed by combining data acquired with different RF shims and transmit voltages**
- **Universal phase-only RF neck shims can provide substantial $B1^+$ improvements**

This work is currently under review (first revision) as a full paper in Magnetic Resonance in Medicine and is an extension of two abstracts presented at the Annual Meeting of ISMRM [81,82].

3.1 Introduction

The increased SNR and longer T1-relaxation time for both tissue and blood at 7T have the potential to improve the contrast, resolution, and imaging time of intracranial neurovascular modalities such as cerebral angiography, vessel wall imaging, and perfusion. However, increasing B0 also introduces limitations due to increased specific absorption rate (SAR) and reduced homogeneity and spatial extent of the transmit magnetic field ($B1^+$), as described in Section 2.1.

When using typical transmit head coils at 7T, intracranial neurovascular imaging methods such as arterial spin labelling (ASL) [83–86] and intracranial vessel wall imaging [87] suffer from the rapid drop in $B1^+$ into the neck. For ASL, this drop in $B1^+$ limits the ability to effectively invert the inflowing blood in upstream labelling planes, such as in the carotid arteries in the neck [84]. For vessel wall imaging, it reduces the ability to suppress the signal in upstream arterial blood, which is required to provide sufficient black-blood contrast between the vessel wall and the inflowing arterial blood. Although higher nominal flip

angles can be applied to increase the inversion or saturation efficiency of arterial blood in low-$B1^+$ areas, this is in practice constrained by a quadratic increase in SAR and by adverse effects on the magnetization of stationary spins within higher $B1^+$ imaging regions. Dielectric pads [57,88] can be positioned near the neck to increase both the transmit and receive sensitivity [84,89], which has been found to increase the $B1^+$ efficiency in a slice just below the carotid siphon by 57% [84]. However, the use of dielectric pads increases experimental complexity and does not provide the ability to change the $B1^+$ field over time, for example between different acquisitions or between signal preparation and readout modules within a single acquisition.

Improved control over $B1^+$ in the neck can also be achieved using parallel transmission (pTx) [60] coils, which consist of multiple separate transmit channels. pTx provides improved control over the $B1^+$ field by manipulating the amplitude and/or phase of each of the individual transmit channels, known as RF shimming. This can be used to achieve improved spatial homogeneity of the $B1^+$ field [70], to reduce the SAR, to achieve spatial [90,91] and spectral [92] selectivity, or to increase the $B1^+$ magnitude within a particular region of interest. Therefore, the use of pTx coils for neurovascular imaging could be used to improve the $B1^+$ in the feeding arteries in the neck, thereby allowing improved inversion or saturation of inflowing arterial blood.

Most conventional head pTx coils are designed for imaging the brain and lack transmit penetration into the neck. To improve the $B1^+$ coverage in the brainstem, the cerebellum, and the carotid arteries, previous work proposed custom pTx coil designs that consist of transmit elements surrounding both the brain and the neck (using fixed [93,94] or geometrically adjustable [95] transmit arrays). However, the use of such coil designs adds experimental complexity and expense relative to the use of conventional pTx coil designs. Therefore, this work focuses on the potential of improving $B1^+$ in the neck using conventional head pTx coils.

Before it is possible to calculate and optimize the achieved $B1^+$ field using pTx methods, the transmit field of all individual pTx channels must be characterized. Such multi-channel $B1^+$ mapping [74] aims to measure the transmitted magnitude and relative phase of each transmit channel. Acquiring these data in both the head and the neck using pTx head coils can be challenging due to a combination of low RF penetration into the neck and the inherently limited dynamic range, defined as the range of $B1^+$ values for which a mapping method provides accurate values [74], of $B1^+$ mapping techniques. Utilizing $B1^+$ mapping

techniques with typical transmit voltages provides accurate data in the brain but does not provide useful information in the low-$B1^+$ areas in the neck. Conversely, using high transmit voltages can achieve improved $B1^+$ coverage in the neck, but is inaccurate for high-$B1^+$ regions in the head.

This chapter proposes and validates an approach which combines $B1^+$ mapping data acquired at 7T using two complementary RF shims (to ensure adequate overall coverage) and at multiple transmit voltages to allow robust reconstruction of multi-channel $B1^+$ maps for both the head and the neck. Subsequently, data acquired using the proposed method are used to investigate how RF shimming can be used to improve the $B1^+$ magnitude in the major feeding arteries in the neck.

3.2 Theory

As described in Section 2.3.3, multi-channel absolute $B1^+$ maps can be calculated from a combined absolute $B1^+$ map ($B1^+_{abs}$) and a full set of relative $B1^+$ maps ($B1^+_{rel}$) using Equation 2.14. For this, relative $B1^+$ maps can be acquired based on the signal ratios of spoiled gradient echo (SPGR) images acquired from the individual transmit channels. In the low flip angle regime, SPGR signal levels are proportional to transmit field magnitudes. However, with large spatial variation of the transmit field strength (such as between the head and the neck at 7T), this low flip angle assumption does not apply over the full FOV. Therefore, Padormo et al. [96] proposed combining SPGR data from different RF transmission voltages. For the jth transmission voltage, the measured ratio between the steady-state SPGR signal S_j and the applied transmission voltage d_j can be expressed using the low flip angle approximations as

$$\frac{S_j}{d_j} = I_{prop} + \frac{\varepsilon}{d_j} + \frac{n_j}{d_j}, \tag{3.1}$$

where $I_{prop} \propto B1^+_{rel}$ is the desired $B1^+$-proportional image intensity, ε denotes the Gaussian noise contribution, and n_j (which is always negative) corresponds to systematic errors due to the low flip angle approximation in the presence of saturation effects. Using this equation, the $B1^+$-proportional image component of each individual voxel is calculated for each transmit channel using maximum likelihood estimation [97] across the datasets acquired at different transmission voltages.

We propose using a similar approach to increase the dynamic range of absolute $B1^+$ measurements by combining acquisitions using different transmit voltages (50V, 100V, and 175V per channel). Those voltages were chosen to cover a wide range of resulting transmit values, while maintaining overlapping dynamic ranges and remaining within SAR limits. The $B1^+$ maps are acquired using Sandwiched SatTFL [76] (as described in Section 2.3.3), which has a reported dynamic range of 40° to 120° (at a per-channel voltage of 60V). We increase this dynamic range by acquiring data at different transmit voltages with overlap in the dynamic range of the maps: see Figure 3.1. We propose a series of consistency criteria to identify which voxels in each map are within the identified dynamic range. The individual reconstructions are first expressed in voltage-independent units of Hz/V. Then, on a voxel-by-voxel basis, measured values are excluded from the final (combined) $B1^+$ map if:

1. The reference image (S_0) signal is smaller than the noise standard deviation; or
2. The measured value at a given transmit voltage is outside the dynamic range (<4.44 Hz/V at 50V, <2.22 Hz/V or >6.67 Hz/V at 100V, or >3.81 Hz/V at 175V); or
3. If more than one value remains for a given voxel, retain the most appropriate value(s):
    a. Some (< 1/1000) voxels were measured within the (non-overlapping) dynamic ranges at all 3 voltages. This generally occurred at air/tissue interfaces, and the voxel values were masked to prevent unreliable values.
    b. If measurements at either both 50V and 100V or both 100V and 175V are included for a given voxel, this is the result of the respective overlapping dynamic ranges. If the average value is in the higher half of the overlapping range, the measurement at the higher transmit voltage is used to maintain higher SNR. Otherwise, include both values.

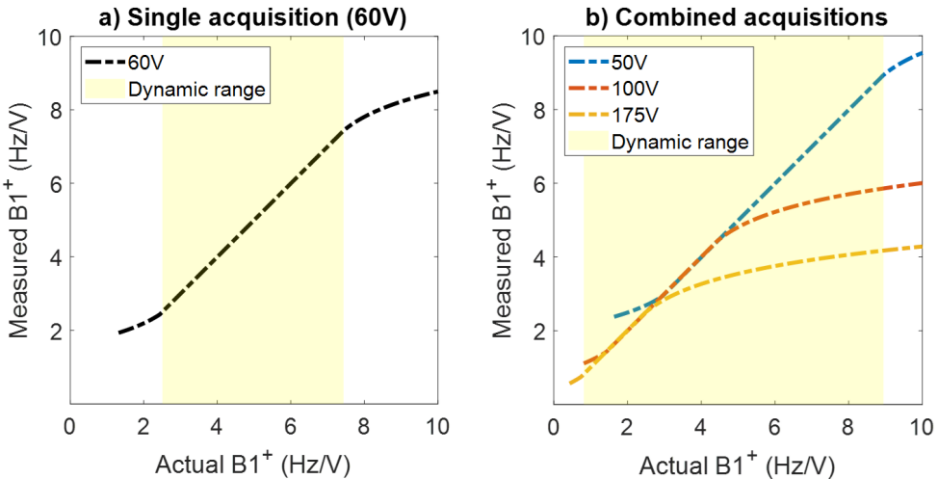

Figure 3.1: Schematic representation of the measured absolute B1+ values for acquisitions with different transmit voltages. Each single acquisition has a linear response within its dynamic range. Higher B1+ magnitudes result in underestimation of the B1+; lower values result in either overestimated or noise-dominated B1+ values. Subplots show **(a)** a single acquisition using a transmit voltage of 60V and **(b)** the larger combined dynamic range when using three separate acquisitions at 50V, 100V, and 175V.

If only one transmit voltage value remained for a given voxel after applying all three exclusion criteria, that value was used for the combined $B1^+$ map. If multiple transmit voltages remained (due to being within the lower half of the overlapping dynamic range), the average value of the $B1^+$ measurements was used.

Inaccuracies in absolute $B1^+$ data reconstructed from different transmit voltages can remain in locations with low $B1^+$ magnitudes due to destructive interference of the individual transmit channels. To provide increased coverage in areas with low $B1^+$ for any given shim, methods such as $B1^+$ time-interleaved acquisition of modes (B1TIAMO [98]) can be used to combine $B1^+$ maps acquired using different RF shims. B1TIAMO combines acquisitions using different RF shims as a weighted average of the $B1^+$ based on the signal levels of the respective reference images to provide a single combined reconstruction with more consistent accuracy.

Finally, additional B0 correction can be required when RF pulses have a frequency dependence. For example, when using a 500 µs rectangular pulse for pre-saturation (as used in this chapter), the frequency response is a sinc function with zero-crossings at ±2 kHz. However, if the frequency dependence of such an RF pulse is known, its effects can be corrected (at the cost of an SNR penalty proportional to the frequency dependence) by scaling the voxelwise $B1^+$ estimates based on a separately acquired B0 map. Note that after the start of the work presented here, the Sandwiched SatTFL implementation has been proposed to use a B0-insensitive HS8 pulse [76].

3.3 Methods

3.3.1 Wide Dynamic Range Multi-Channel B1+ Mapping

To obtain robust multi-channel $B1^+$ maps, a three-step process was used, as summarized in Figure 3.2.

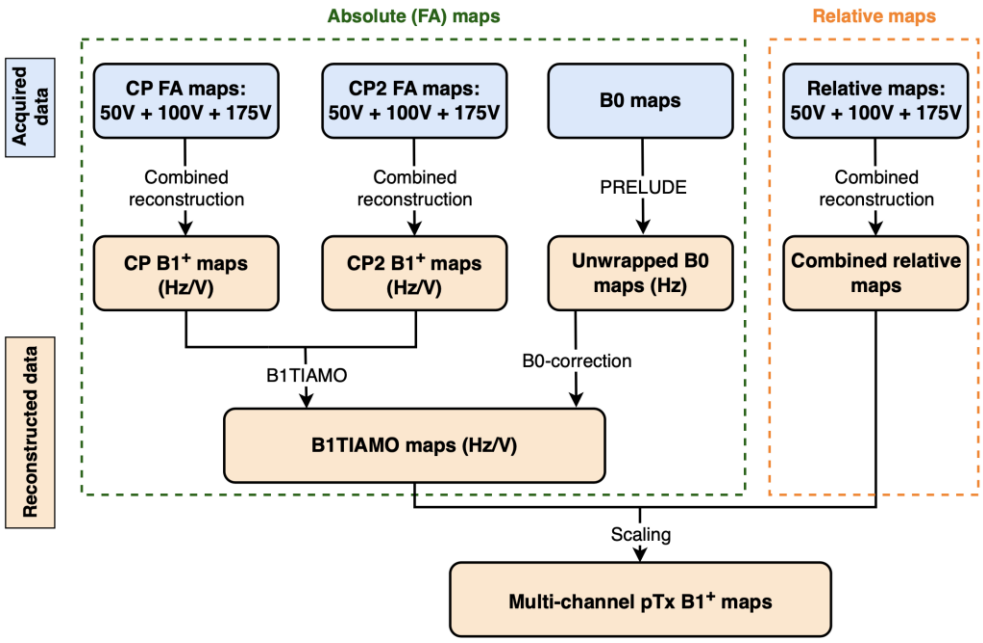

Figure 3.2: Schematic of the proposed $B1^+$ map acquisition and processing pipeline. In total, 10 different datasets are acquired (blue: 6 FA maps, 1 B0 map, and 3 sets of relative maps) to reconstruct a single set of multi-channel $B1^+$ maps.

For the first step, Sandwiched SatTFL absolute $B1^+$ maps were acquired at three different transmit voltages (50V, 100V, and 175V per channel) to achieve the required large dynamic range. Absolute $B1^+$ maps at all three voltages were acquired twice using two complementary RF shim configurations (CP-mode and CP2-mode) and combined using the B1TIAMO [98] post-processing approach. This approach calculates a weighted average of the $B1^+$ maps acquired using two RF shims. A B0 map was also acquired to correct for static field inhomogeneity effects arising from the 500 µs rectangular preparation RF pulse used for pre-saturated TurboFLASH $B1^+$ mapping, as discussed by Kent et al. [76]. All acquired absolute $B1^+$ maps and the B0 map were combined to form a single absolute $B1^+$ map in Hz/V. Secondly, relative $B1^+$ maps were acquired at multiple voltages (50V, 100V, and 175V per channel) and reconstructed using the previously described large dynamic range relative $B1^+$ mapping approach [96]. The final step combined the absolute maps with the relative maps to form complex multi-channel $B1^+$ field maps in both the head and neck (Equation 2.14; final step in Figure 3.2).

Scan parameters for each individual 3D Sandwiched SatTFL acquisition include TR = 1 s, TD = 0 s, TE = 1.78 ms, nominal flip angle = 9°, nominal preparation flip angle = 90° (using a 500 μs rectangular pulse), bandwidth = 489 Hz/px, and scan time = 36 seconds.

B0 maps were acquired using a 3D gradient-recalled echo acquisition with TR = 4.9 ms, TE_1/TE_2 = 1.02/3.06 ms, nominal flip angle = 7°, bandwidth = 538 Hz/px, scan time = 1:39 minutes. PRELUDE [99] was used to unwrap the phase maps used for B0 measurement.

Relative transmit maps were acquired using low flip angle SPGR acquisitions (TR = 2.90 ms, TE = 1.02 ms, nominal flip angle = 7°, bandwidth = 500 Hz/px, scan time = 30 seconds per single voltage acquisition). Transmit channels were excited in an interleaved fashion (with the channels ordered as 1-6-2-5-3-8-4-7) to minimise magnetisation history effects.

3.3.2 *In Vivo* Experiments

Data were acquired in 10 healthy volunteers (23-56 years old; 8 male/2 female). All acquisitions ($B1^+$, B0, and structural data) were performed in 3D using the same FOV (225×225×300 mm) in the same absolute coordinates relative to the coil. MPRAGE structural data were acquired at 1.2 mm isotropic resolution for anatomical reference. Other MPRAGE scan parameters include TR = 2200 ms, TE = 2.77 ms, inversion time = 1050 ms, flip angle = 7°, bandwidth = 238 Hz/px, and scan time = 3:57 minutes. MPRAGE data were reconstructed as the root sum-of-squares of separate datasets acquired in CP-mode and CP2-mode, to improve the coverage into the neck of the structural information. For $B1^+$ and B0 field maps a lower resolution of 7.5×5.6×6.2 mm per voxel was used.

Data were acquired on a Siemens (Erlangen, Germany) Magnetom 7T scanner using a Nova Medical (Wilmington, MA) 8Tx/32Rx head coil under an institutional ethics agreement. To ensure consistency in the acquired B0 data, the tune-up B0 shim was used for all acquisitions. Data reconstruction and shim calculation were performed using MATLAB (The MathWorks, Natick, MA) on a system using an Intel (Intel, Santa Clara, CA) Xeon CPU E5-2680 (v4) running at 2.40 GHz with 14 cores and 28 logical processors.

Using the approach outlined in Figure 3.2, large dynamic range $B1^+$ field maps were measured and reconstructed for all 10 volunteers. For four subjects (Subjects 1, 2, 9, and 10), additional absolute $B1^+$ maps were measured for validation purposes using two

arbitrary RF shims (again acquired at reference voltages of 50V, 100V, and 175V per channel to facilitate validation with full spatial coverage).

3.3.3 Carotid Artery RF Shimming

To assess the theoretical upper limit for the boost in $B1^+$ in the neck that can be achieved using pTx RF shims, the total (theoretically) available $B1^+$ was evaluated *in vivo* on a voxel-by-voxel basis by summing the $B1^+$ magnitudes across the transmit channels.

For shim calculations and evaluation, hand-drawn vessel masks, comprising the internal carotid arteries (ICAs) and the Circle of Willis, were drawn for each subject from the MPRAGE images. These ROIs were downsampled to the resolution of the $B1^+$ and B0 data and used as masks for the RF shim calculations. Where carotid-only shim targets were used, the ROIs were reduced to the areas corresponding to the carotid arteries.

Both phase-and-magnitude and phase-only RF shim combinations were calculated to assess any potential benefit of the extra degrees of freedom. Shims were calculated using cost functions that aim to maximize either $B1^+$ magnitude, $B1^+$ homogeneity, or a combination of both. The cost function $\min\{< (1/B1^+)^2 >\}$ was used to maximize the magnitude, where a quadratic term is used to ensure simultaneous minimization of the required energy (as a surrogate for SAR) to achieve a certain effective flip angle. The coefficient of variation (CoV) was used to maximize the $B1^+$ homogeneity: $\min\{CoV(B1^+)\} = \min\{std(B1^+)/< B1^+ >\}$, where std denotes the standard deviation. Finally, the combination of the magnitude and homogeneity was optimized using

$$\min\{CoV(B1^+) + \lambda < (1/B1^+)^2 >\}, \qquad 3.2$$

where λ is a regularization parameter. 0.2% of the voxels were removed from the shim calculation for having an unrealistically low amount of available $B1^+$ (under 1.5 Hz/V), which would otherwise dominate the shim calculation.

To assess the prospect of deploying a universal shim in the neck, the convergence properties of universal neck RF shims were assessed using the data from the 10 volunteers. To test the results when calculating a universal RF shim for N (≤ 10) subjects, a candidate RF shim was calculated for the first N subjects and its performance was evaluated using the multi-channel $B1^+$ data of all 10 subjects. The first N subjects were selected chronologically by acquisition date. For each comparison, tailored RF shims (where the

shim is optimized for each subject separately) were included as an indication of the theoretical upper limit of the universal shim.

3.4 Results

3.4.1 Wide Dynamic Range Multi-Channel B1⁺ Mapping

Figure 3.3 shows an example of combining absolute CP-mode B1⁺ maps acquired using different transmit voltages when using the proposed exclusion criteria. Figure 3.3b-d show the original CP-mode B1⁺ maps acquired using transmit voltages of 50V, 100V, and 175V per channel, respectively, and the resulting combined B1⁺ map is shown in Figure 3.3e. The masks of which voxel values were used to calculate the combined B1⁺ map (after application of the exclusion criteria) can be seen in Figure 3.3f-h, along with the number of values used to calculate the final combined B1⁺ map in Figure 3.3i.

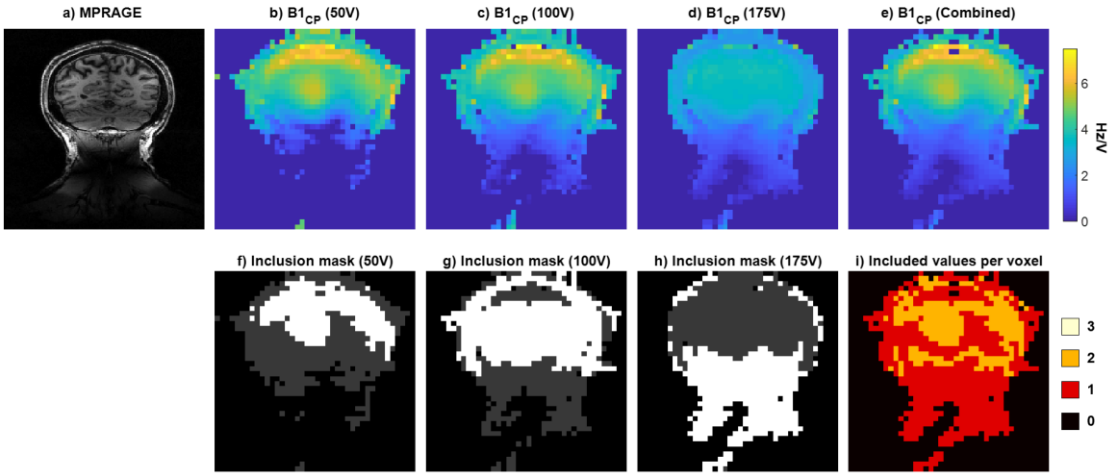

Figure 3.3: Absolute B1⁺ maps acquired at different voltages **(b-d)** are combined to obtain a single map with an increased combined dynamic range **(e)**. Voxel values from individual scans were included or excluded based on the signal levels in the reference images and exclusion criteria to impose consistency in the acquired values relative to the other acquired datasets, resulting in inclusion masks for each dataset **(f-h)**. Figure **(i)** shows the total number of included values for each voxel in the slice.

Figure 3.4 shows an example MPRAGE image along with B1⁺ maps from the first step in the B1⁺ mapping pipeline. B0 off-resonance of up to -1.2 kHz in the neck results in a B1⁺ underestimation of up to 49% if not corrected, as seen in Figure 3.4b. Figure 3.4c-e demonstrate the utility of B1TIAMO to increase the spatial coverage in areas with low CP-mode B1⁺. Figure 3.4e-f show the changes due to B0 correction of the absolute B1⁺ data based on the acquired B0 maps.

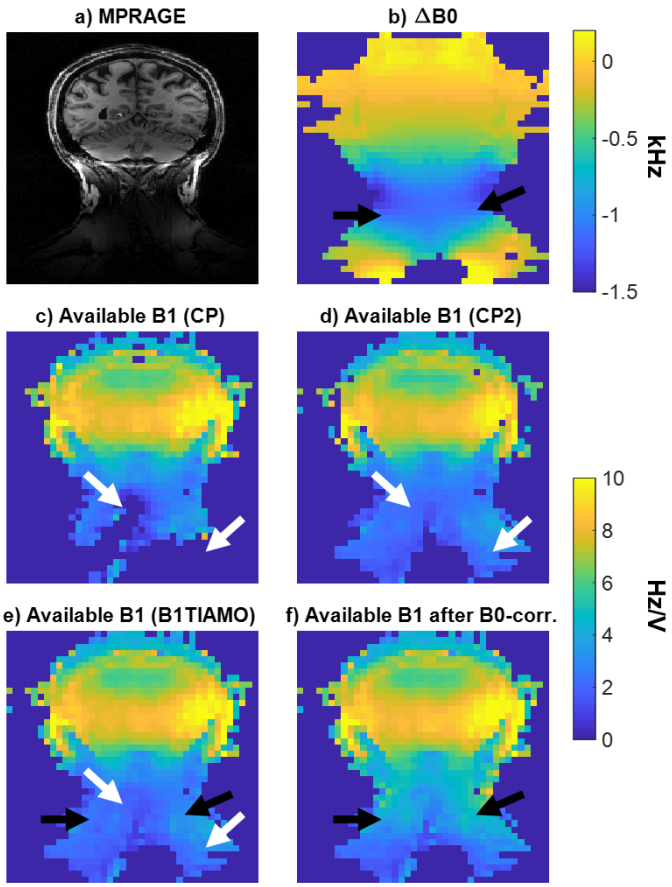

Figure 3.4: The use of B1TIAMO to mitigate signal loss in regions with low native $B1^+$ in CP-mode to obtain improved spatial coverage **(c-e)**, and the consecutive correction for $B1^+$ underestimation in the presence of high B0 inhomogeneity **(f)** based on measured B0 off-resonance fields **(b)**. White arrows indicate examples of improved spatial coverage due to B1TIAMO; black arrows indicate areas with substantial B0 offsets (up to -1.2 kHz), resulting in substantial $B1^+$ underestimation if no B0 correction is applied. All $B1^+$ data are shown in terms of the available $B1^+$.

An overview of the data acquired from the 10 healthy volunteers is shown in Figure 3.5. For each subject a coronal slice of the MPRAGE data, a coronal projection of the hand-drawn vessel masks, and the reconstructed CP-mode $B1^+$ map are shown. These data were acquired using a commonly used head pTx coil, so could also be useful for other research centres for the calculation of universal pTx shims or pulses, or for simulation purposes. Therefore, the multi-channel $B1^+$ data and the B0 data are made openly available online (DOI: 10.5287/ora-pvzkkddda).

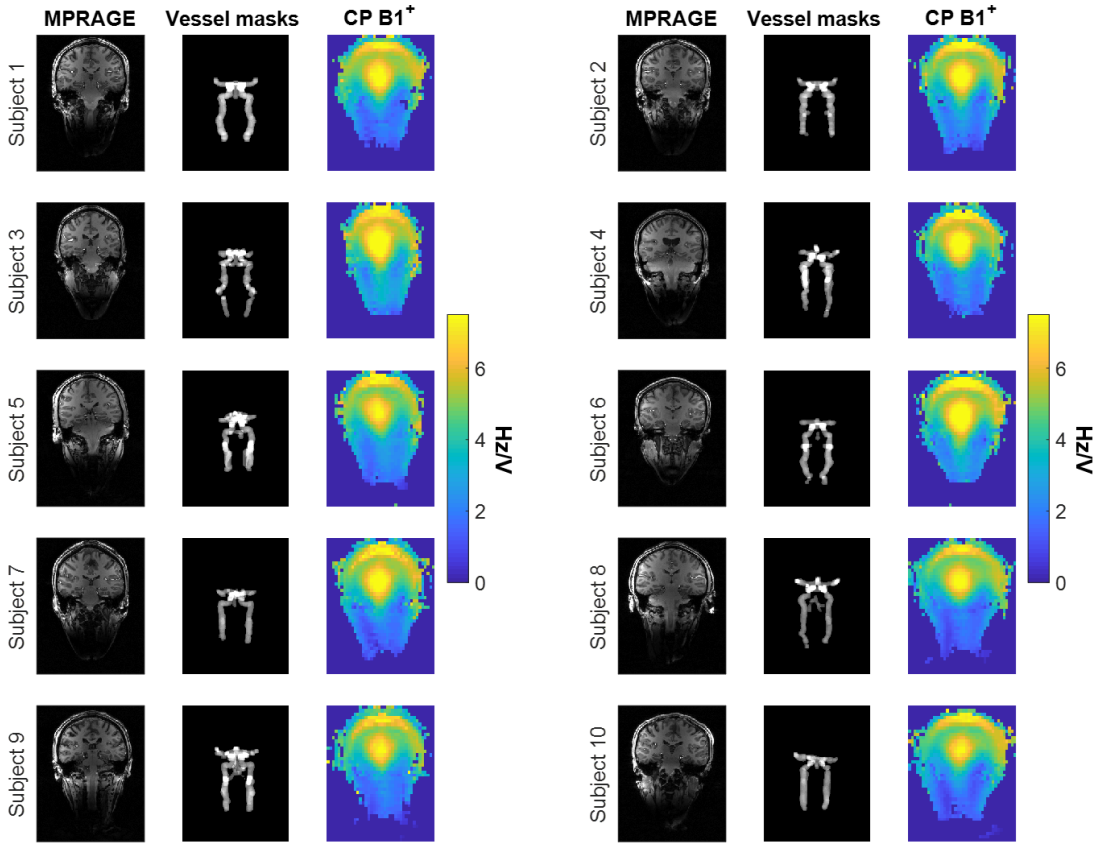

Figure 3.5: Central coronal slices of the 10-subject database (DOI: 10.5287/ora-pvzkkddda) that was acquired using the proposed method. All data were acquired using the same FOV in coil coordinates. Columns show MPRAGE data (root-sum-of-squares of CP-mode and CP2-mode to improve structural visibility in the neck), left column; coronal projections of the arterial vessel masks corresponding to the MPRAGE data, middle column; and the CP-mode $B1^+$ map for each subject, right column. The CP-mode $B1^+$ maps shown here are synthetic maps generated from the multi-channel $B1^+$ data.

For Subjects 1, 2, 9, and 10, additional absolute $B1^+$ maps were measured using two arbitrary RF shims. Figure 3.6 compares the measured (using the shim settings on the scanner) and predicted (combined multi-channel $B1^+$ maps using the corresponding shim coefficients) $B1^+$ maps for those validation shims. Visually good agreement is found for all four comparisons, with a root-mean-square error (RMSE) of 0.25 Hz/V across all comparisons and a median $B1^+$ magnitude error of 3.8%.

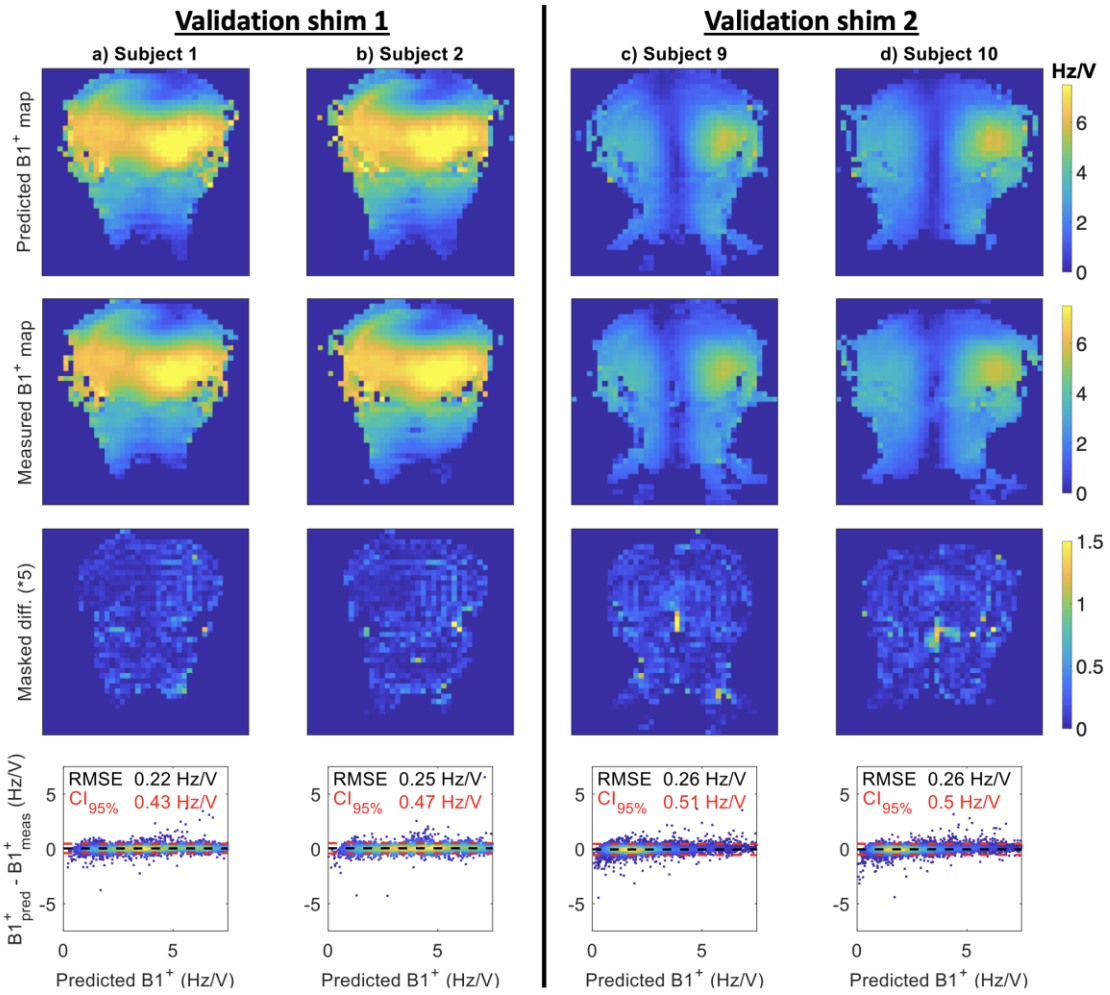

Figure 3.6: Evaluation of the agreement between predicted (1st row; calculated from reconstructed multi-channel B1⁺ maps) and measured (2nd row; acquired on the scanner using the same shim coefficients) B1⁺ magnitude maps for two arbitrary RF shims. The 3rd and 4th rows show the absolute difference (using a 5-fold boosted colour scale) between the images in the first two rows, and the difference between the predicted ($B1^+_{pred}$) and measured ($B1^+_{meas}$) voxel-wise values within the overlapping region. Dashed black lines indicate the mean errors, with dashed red lines indicating the means ± 95%. Printed values indicate the root-mean-square errors (RMSE, black) and 95% confidence intervals ($CI_{95\%}$, limits indicated in red).

3.4.2 Carotid Artery RF Shimming

The data from the 10 subjects shown in Figure 3.5 were used to study the potential B1⁺ benefits in the carotid arteries when using RF shims versus standard CP-mode.

Figure 3.7 shows the CP-mode absolute B1⁺, the total (theoretically) available B1⁺, and the resultant CP-mode B1⁺ efficiency for two slices. Figure 3.7c shows that the theoretical upper limit of B1⁺ in the neck is (as expected) low compared to the central head region. In addition, Figure 3.7d shows that CP-mode only utilizes 57 ± 5% of the theoretically available maximum B1⁺, resulting in an average B1⁺ magnitude in the neck for CP-mode

of 2.5 ± 1.0 Hz/V. This suggests that utilising pTx should be able to improve this very low $B1^+$ penetration, albeit never realising the theoretical maximum over a large region.

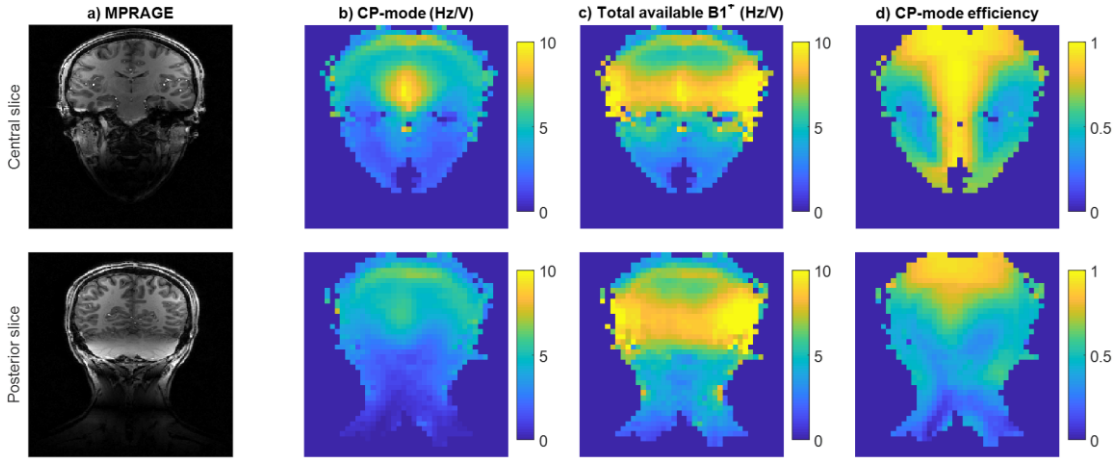

Figure 3.7: Two coronal slices from an example subject (Subject 1), showing a central slice (top row) and a more posterior slice (bottom row). Column **(b)** shows the $B1^+$ map (Hz/V) in CP-mode. Column **(c)** shows the maximum possible $B1^+$ for each voxel (calculated as the sum of magnitude $B1^+$ per channel). Column **(d)** shows the CP-mode efficiency, calculated as the CP-mode $B1^+$ divided by total available $B1^+$, indicating the loss of potential $B1^+$ arising when using CP-mode.

Based on the results in Figure 3.7, a universal RF shim can be used to increase the average $B1^+$ magnitude in the carotid arteries. An example of the resulting improvement in $B1^+$ magnitude is shown in Figure 3.8, which shows that the theoretical voxel-by-voxel upper limit indicated by the available maximum $B1^+$ is unachievable using a standard RF shimming approach.

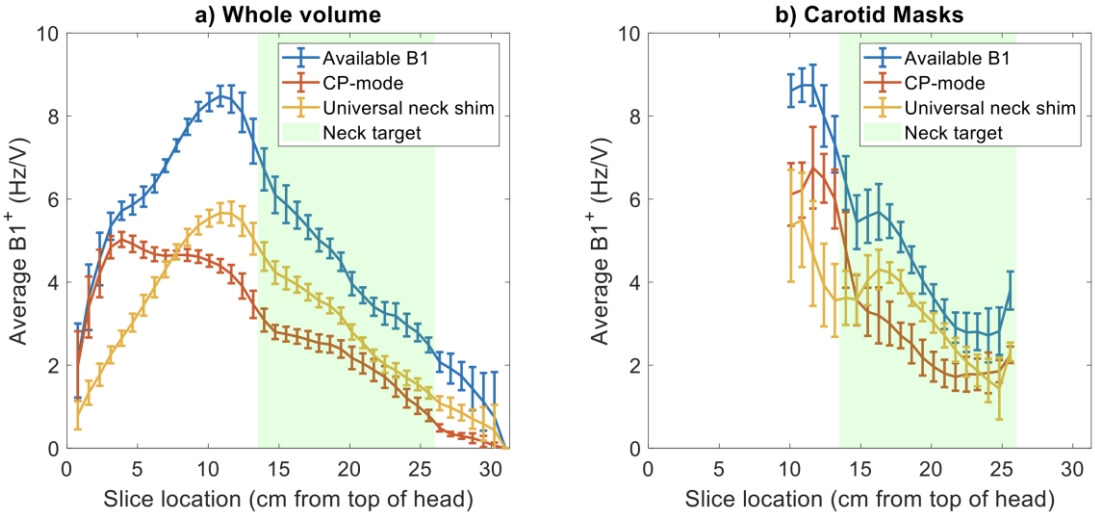

Figure 3.8: Plots showing the average $B1^+$ across all 10 subjects for CP mode (orange lines), for the total available $B1^+$ (blue lines), and the $B1^+$ achieved using a universal neck shim (yellow lines; calculated using the $B1^+$ magnitude cost function $min\{< (1/B1^+)^2 >\}$). **(a)** shows the results averaged over the whole head volume (with the neck region indicated) and **(b)** shows the data within the vessel masks only. Note that the $B1^+$ superior to the neck mask is reduced

for the universal shim relative to CP mode, whereas the $B1^+$ within the neck mask is increased for the universal shim relative to CP mode.

Figure 3.8 showed that only maximizing the $B1^+$ magnitude without including a CoV constraint can result in $B1^+$ inhomogeneity and large inferior-superior variation in the $B1^+$ profile. Therefore, Figure 3.9 shows the neck RF shim performance within the vessel mask when the CoV is included in the cost function using Equation 3.2. Both magnitude-and-phase, and phase-only $B1^+$ shimming conditions were considered. Figure 3.9b shows that phase-only shimming performs almost as well as phase-and-magnitude shimming, with nearly identical results (differences < 1%) when using a regularization parameter $\lambda > 1.5$. Based on the L-curve in Figure 3.9b, a regularization parameter λ of 1.7 is found to produce a reasonable trade-off between $B1^+$ efficiency and minimizing the CoV.

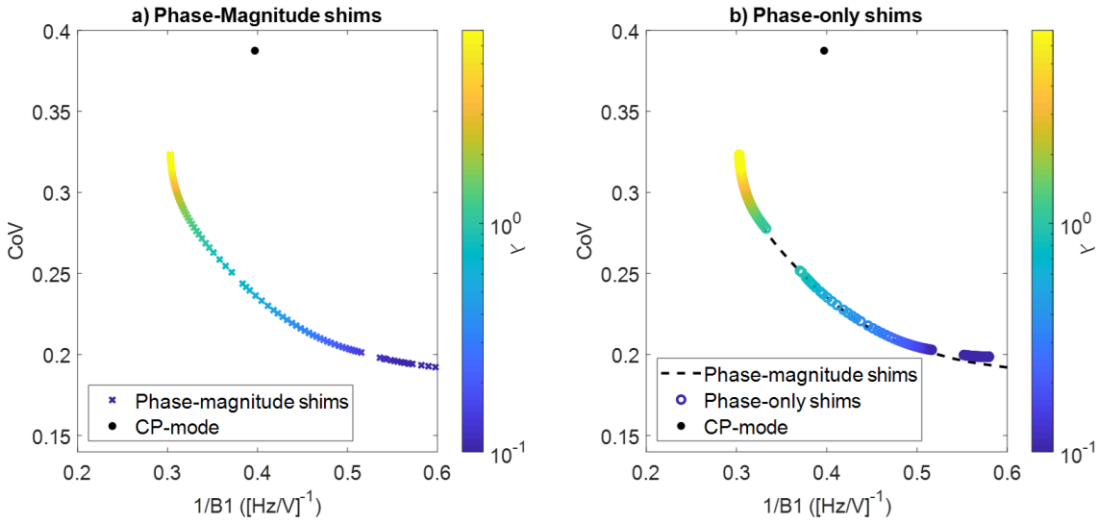

Figure 3.9: Plots investigating the trade-off between the coefficient of variation (CoV) of $B1^+$ within the vessel mask versus the achieved $B1^+$ magnitude (expressed as $1/B1^+$). The desired regularization value, λ, that reduces CoV whilst retaining a strong $B1^+$ is found at approximately $\lambda = 1.7$ (green region). **(a)** shows universal shims that allow both phase and magnitude to change per channel. **(b)** shows universal shims that allow only phase to change per channel. The dashed black line in (b) shows the data from (a) overlaid as a guide to the eye. The black dot indicates CP-mode.

Figure 3.10 evaluates the number of subjects required to generate a universal shim. Good results can already be achieved when universal shims are calculated based on a single subject, and (when using $\lambda = 1.7$) no further improvement is observed when including more than 4 subjects. For all shim targets ($B1^+$ magnitude optimized, CoV optimized, and optimized using Equation 3.2), universal shims perform only slightly worse than fully per-subject tailored shims, and substantially better than CP-mode. Additional leave-one-out comparisons, in which for each of the 10 subjects a universal phase-only neck shim is calculated based on the other 9 subjects, provide an average increase in $B1^+$ of 36 ± 14%

relative to CP-mode. The highest mean $B1^+$ increase in the leave-one-out comparisons is 62% (Subject 2) and the lowest mean increase is 8% (Subject 6, which already had the highest average $B1^+$ in CP-mode).

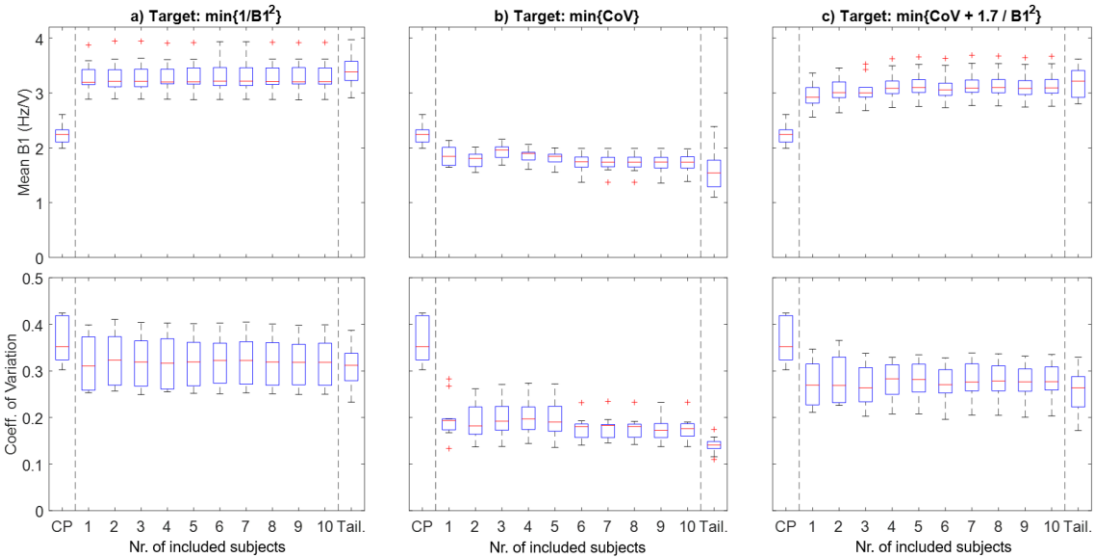

Figure 3.10: Plots showing the number of subjects needed to generate a universal neck shim (based on phase-only RF shims). For each plot the CP-mode mean $B1^+$ and CoV are shown for reference, followed by the relevant metrics for universal neck shims generated from increasing numbers of subjects. The final column for each plot shows the result when per-subject tailored shims are used (denoted Tail.). The columns show the results for three different cost functions: **(a)** minimizing $\{1/B1^2\}$; **(b)** minimizing {CoV}; and **(c)** minimizing the optimum combination of $\{1/B1^2\}$ and {CoV} with regularization value $\lambda = 1.7$.

The final RF shim, calculated as a phase-only universal shim based on all 10 subjects and using $\lambda = 1.7$, is shown in Figure 3.11. Over the full carotid artery masks, this universal RF shim achieves an average increase in $B1^+$ magnitude of 37 ± 16% relative to CP-mode, whilst reducing the CoV by 26 ± 20%. When using tailored RF shims the corresponding improvements relative to CP-mode would be a $B1^+$ magnitude increase of 43 ± 20% with a 31 ± 20% reduction in CoV.

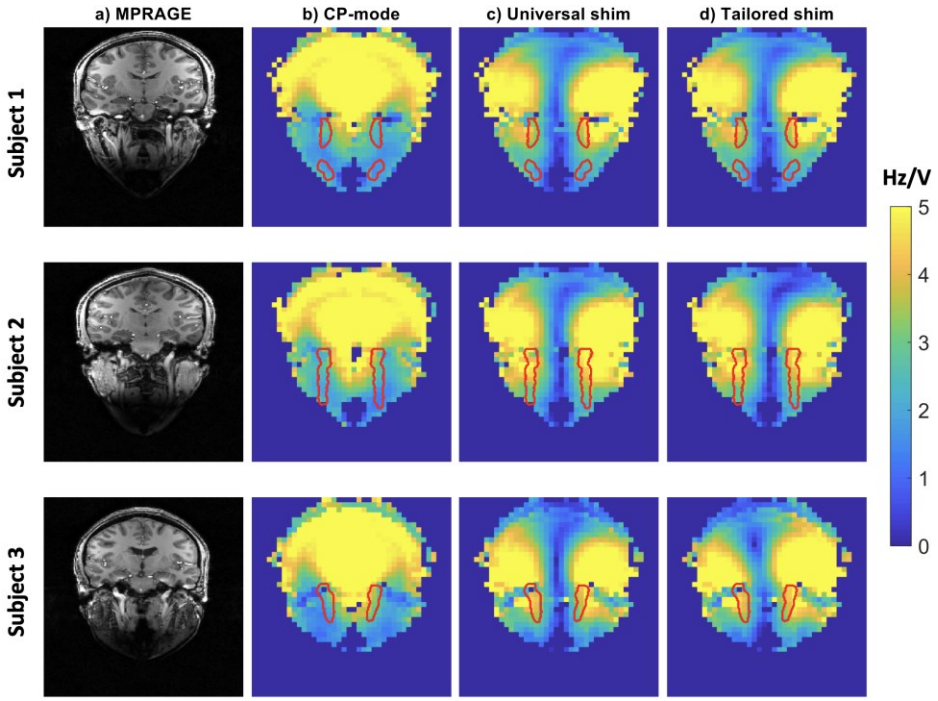

Figure 3.11: An example RF shim for the carotid arteries, shown for Subjects 1-3. Columns show **(a)** an MPRAGE slice containing a superior segment of the internal carotid arteries; **(b)** the CP-mode $B1^+$ in the same slice; **(c)** the corresponding $B1^+$ fields when using a phase-only universal shim calculated using regularization $\lambda = 1.7$; and **(d)** the $B1^+$ fields when using phase-only tailored shims which are optimized for each individual subject, again calculated using regularization $\lambda = 1.7$. The red outlines in plots (b-d) show in-slice portions of the carotid masks used for shim calculation (at their original resolution corresponding to the MPRAGE data).

3.5 Discussion

3.5.1 Wide Dynamic Range Multi-Channel $B1^+$ Mapping

When combining $B1^+$ maps acquired using CP-mode and CP2-mode and with different transmit voltages using the proposed pipeline, a robust $B1^+$ measurement can be obtained in the neck without compromising the $B1^+$ accuracy in the head. Figure 3.5 shows that this increased coverage is consistently achieved, independent of subject size and position within the coil.

Figure 3.3 and Figure 3.4 show that both the combination of multiple transmit voltages and B1TIAMO contribute to increasing the coverage of the final $B1^+$ into the neck. The inclusion masks in Figure 3.3f-h show that data reconstructed from low-voltage acquisitions are mainly used for the high-$B1^+$ areas in the centre of the brain and close to the transmit elements, while high-voltage data mainly contribute accurate information in the neck. These observations are consistent with the assumptions that motivated the use of multiple transmit voltages. Furthermore, they indicate that the exclusion criteria in

Section 2, which do not make use of the spatial location of voxels, can accurately determine which transmit values to include at different spatial locations.

A single Sandwiched SatTFL acquisition using a transmit reference voltage of 60V and using the same RF coil as this study has previously reported a dynamic range of a factor of 3 (ranging from 40° to 120°) [76]. Therefore, using transmit voltages of 50V, 100V, and 175V, the multi-voltage approach used here can provide accurate results over a dynamic range of $B1^+$ of a factor of 10.5, since the highest voltage of 175V will enable $B1^+$ regions that are as low as 13.7° at 60V to be characterized accurately ($60V/175V * 40°$ at the lower end of the linear range of the method), and the lowest voltage of 50V will enable $B1^+$ regions that are as high as 144° at 60V to be characterized accurately ($60V/50V * 120°$ at the upper end of the linear region of the method).

Despite the increased effective dynamic range when using multiple transmit voltages, even with a single shim (e.g., CP-mode) no accurate $B1^+$ information can be acquired in locations which have very low $B1^+$ values due to destructive interference of the transmit fields. In such cases, Figure 3.4 confirms that including a CP2-mode acquisition and B1TIAMO combination of CP-mode and CP2-mode data provides complementary information and therefore yields an improved spatial extent of the $B1^+$ maps. However, further improvements might be possible using different calibration RF shims than CP-mode and CP2-mode (such as designated neck shims) or additional RF shims in the B1TIAMO computation.

Although combining data acquired using different RF shims and transmit voltages provides $B1^+$ information with a larger spatial extent, B0 off-resonance effects can reduce the accuracy of the measured $B1^+$ values. In this work, we used rectangular pulses that required an additional B0 correction step (Figure 3.4) to obtain accurate values in areas with high B0 off-resonance (up to -1.2 kHz were observed). Alternatively, non-adiabatic broadband full-passage hyperbolic secant (HS8) pulses [100] can be used for the SatTFL acquisitions [76] to reduce the B0-dependence of the $B1^+$ estimates.

When comparing predicted $B1^+$ maps (reconstructed using the proposed pipeline) and measured $B1^+$ maps (acquired directly on the scanner) for arbitrary RF shims (Figure 3.6), excellent agreement can be observed throughout the imaging volume, including the neck. The mean RMSE of 0.25 Hz/V indicates that some differences remain between the predicted and acquired maps. However, some of this remaining disagreement may be caused by inaccuracies in the measured $B1^+$ maps rather than the predicted $B1^+$ maps. For

example, in the low $B1^+$ regions in the middle of the head for Validation Shim 2, discontinuities which do not typically appear in $B1^+$ maps are visible in the measured $B1^+$ maps, while the predicted $B1^+$ maps remain spatially smooth. This is also visible in the scatter plots in Figure 3.5, where some higher errors are observed for voxels with low predicted $B1^+$ values.

The proposed multi-channel $B1^+$ mapping method requires a total of 10 separate acquisitions (6 absolute $B1^+$ maps, 3 sets of relative $B1^+$ maps, and 1 B0 map) with a total scan time of 6:45 minutes for the reconstruction of a single set of multi-channel $B1^+$ maps. This additional scan time would be a limiting factor if acquiring subject-specific field maps at the start of a clinical exam. However, this is not a limitation if using the method to acquire a $B1^+$ database for the calculation of universal RF shims or pulses.

3.5.2 Carotid Artery RF Shimming

Figure 3.7 shows that the $B1^+$ efficiency of CP-mode is low in the neck ($57 \pm 5\%$ along the carotid arteries), meaning that there is substantial opportunity for improvement using (universal) RF shims. Figure 3.8 confirms that a universal shim can substantially improve the carotid $B1^+$, while showing a reduction in $B1^+$ in the Circle of Willis (which, depending on the application, may be an advantage or a disadvantage, as will be found in Chapter 6). However, there is also substantial $B1^+$ variation along the vessel, suggesting that the shim performance can be improved by adding a $B1^+$ homogeneity constraint.

The results in Figure 3.9 show that combining $B1^+$ homogeneity optimization with $B1^+$ magnitude optimization (using Equation 3.2) can improve the average homogeneity with a minimal reduction in $B1^+$ magnitude. When using a regularization parameter, λ, of 1.7, the CoV is reduced by 25% while the average $B1^+$ magnitude is reduced by only 5%. Figure 3.9b indicates that the results using phase-only shims are nearly equal to those of phase-and-magnitude shims when using $\lambda > 1.5$, indicating an inherent requirement for high $B1^+$ utilization from all channels to achieve sufficient $B1^+$ in the neck.

The universal shim convergence comparison in Figure 3.10 shows that a universal shim in the vessels in the neck can easily be found (even based on a single subject), with no further improvement in shim performance when including more than 4 subjects in the shim calculation. Furthermore, Figure 3.10 shows that universal RF shims perform almost as effectively as fully tailored per-subject RF shims, while consistently outperforming CP-mode in terms of both $B1^+$ magnitude and CoV. The results in Figure 3.11 show that both

tailored and universal shims result in similar $B1^+$ profiles, explaining why the results in Figure 3.10 indicate that a shim calculated from a single subject can already provide reasonable results when used as a universal shim for all other subjects.

Figure 3.11 also shows that, using a universal RF shim and $\lambda = 1.7$, the $B1^+$ magnitude in the vessels in the neck can be increased by 37%, whilst reducing the coefficient of variation by 26%. This can be achieved using phase-only RF shimming and does not require phase-and-magnitude RF shimming. Since a linear increase in $B1^+$ for phase-only RF shimming implies a quadratic reduction in the required SAR to achieve a given flip angle, the reported 37% increase in $B1^+$ magnitude corresponds to a 47% reduction in SAR. These results are based on optimization of the $B1^+$ over the entire region of the carotid vessels in the vessel masks in Figure 3.5. For some applications, in particular for ASL, excitation targets can consist of a smaller portion of these vessels, for example when only labelling in a single thin plane (pseudo-continuous ASL) or when using vessel-selective pulsed ASL [101]. In such cases, the optimization is less constrained, allowing for larger improvements in RF shim performance.

For example, if a given application only requires the left internal carotid artery as a shim target, a phase-only universal RF shim can simultaneously achieve a 43% increase in $B1^+$ magnitude and a 42% decrease in CoV relative to CP-mode (data not shown). When optimizing for a shim target consisting of the vessels within a single slice just below the carotid siphon, the increase in $B1^+$ magnitude using a phase-only universal RF shim improves to 62% (with a 55% reduction in CoV). This indicates a slightly larger improvement than the increase in $B1^+$ magnitude in the same area when using dielectric pads instead of RF shimming, which were previously found to result in a 57% $B1^+$ increase [84]. Using this single-slice shim, the minimum $B1^+$ in the labelling plane across the 10 subjects increases from 1.7 Hz/V to 2.9 Hz/V. When using 0.3 ms PCASL labelling pulses of 15° [86], this corresponds to a reduction in the peak transmit voltage from 165 V to 96 V, thereby reducing the need to increase the TR [85,86] or use VERSE-shimming [85] to remain within SAR limits [102].

It should be noted that the vessel masks used in this study were drawn based on the vasculature of healthy volunteers. Although the results presented here indicate consistently improved $B1^+$ in the carotid arteries for subjects with typical (vascular) anatomy, both the $B1^+$ fields and the locations of the vessels in the neck might be different for patients with non-standard anatomies. Figure 3.11e shows a consistent increase in $B1^+$ across both the

left and the right side of the neck when using the proposed shim, with a decrease in $B1^+$ in the centre of the neck. Although morphological variations in the shape of the internal carotid arteries increases with age [103], a patient study into the variability of the medial location of the ICAs [104] found that the ICAs of most (96.1%) patients are located within the lateral half on each side of the neck and would therefore be expected to achieve substantial $B1^+$ improvements even for the universal RF shim. 3.6% of the ICAs were found in the medial half of the lateral mass, where the $B1^+$ in CP-mode is similar to the $B1^+$ using the proposed shim. The $B1^+$ reduction in Figure 3.11e would only correspond to the location of the ICAs in the remaining 0.3% of patients, who had ICAs located medial to the lateral mass.

Furthermore, the results presented here are all based on simple RF shims which are constrained to the superposition patterns that can be achieved using the available transmit channels. Since the average $B1^+$ efficiency of the proposed universal RF shim is 74 ± 3%, it is expected that further improvements can be achieved when using more advanced dynamic pTx pulses, where additional degrees of freedom are introduced by continuously changing the pTx coefficients in combination with the gradient waveforms and pulse amplitudes. Dynamic pTx can be used to achieve further improved $B1^+$ homogeneity and/or localization. However, an advantage of using RF shims is that they can directly be implemented into existing sequences without requiring further pulse design or introducing sequence timing restrictions, thereby not increasing experimental complexity for existing sequences while still achieving substantially improved $B1^+$ efficiency and homogeneity. Finally, a combination of dielectric pads and pTx might provide even further improvements to the resulting $B1^+$ in the neck.

3.6 Conclusion

Combining $B1^+$ data acquired using different voltages with CP- and CP2-mode RF shims allows the reconstruction of accurate multi-channel head-and-neck $B1^+$ maps for pTx head coils at 7T. Using this, universal RF shims can be designed that increase the $B1^+$ magnitude in the arteries in the neck by 37%, while also improving the homogeneity. This is possible using phase-only universal RF shims, facilitating easy implementation in existing sequences at 7T.

4

Optimization of Undersampling Parameters for 3D Intracranial Compressed Sensing MR Angiography at 7T

Key Conclusions

- **Very small calibration areas of 12 × 12 k-space lines increase the number of visible vessels in compressed sensing TOF MRA**
- **The importance of using optimized undersampling parameters increases for higher acceleration factors**

This chapter is based on the publication "Optimization of undersampling parameters for 3D intracranial compressed sensing MR angiography at 7T" [105], which is an extension of an abstract presented at the Annual Meeting of ISMRM [106].

4.1 Introduction

Time-of-flight (TOF) magnetic resonance angiography (MRA) is a valuable technique for clinical study of the vasculature. It visualizes the blood in a certain region (slice or slab) by generating bright-blood contrast between inflowing and stationary spins. In the brain it can be used for detection of various types of vascular complications, such as atherosclerosis and stenosis [107] or aneurysms [8,108]. Compared to other angiography techniques, such as computed tomography angiography, TOF MRA has the benefit of being a non-invasive technique, without the need for intravenous contrast agents, and without exposing subjects to ionising radiation.

High spatial resolution MRA can visualize small and highly tortuous vessels such as the lenticulostriate arteries (LSAs) [4], which are implicated in up to a third of symptomatic strokes [109]. In general, the quality of clinical MRA examinations benefits from a higher static magnetic field strength. MRA can be further improved by using ultra-high field MRI, defined as those scanners with static magnetic field strengths of ≥7 tesla [110]. TOF MRA at 7T benefits from longer T1-relaxation times and increased signal-to-noise ratio (SNR),

resulting in the potential for higher resolution acquisitions and improved depiction of small vessels [4]. However, the achieved spatial resolution is limited by long acquisition times, which can lead to patient discomfort, increased patient movement, and increased clinical costs. In order to remain within clinical scan durations, sub-Nyquist sampling techniques are generally required, for example using parallel imaging techniques [61].

Compressed sensing (CS) [67] techniques have the potential to achieve still higher acceleration factors. CS combines highly undersampled non-uniform acquisitions and an assumption of sparsity in a given transform domain to restore image quality. Due to the intrinsic sparsity of TOF MRA data in both the image and wavelet domain, and the improved MRA contrast at 7T, it has already been shown that acceleration factors of 7.2 [69] or higher [111,112] can be achieved with a minimal reduction in clinical image quality [113], or even with improved diagnostic image quality compared to conventional acceleration methods [112].

Cartesian undersampled k-space trajectories for three-dimensional TOF MRA with CS reconstruction are commonly designed using two-dimensional undersampling covering the two phase-encode directions (k_y, k_z), with each sampled point in the (k_y, k_z)-plane representing a continuously sampled line in the frequency-encode direction (k_x). Such undersampling masks are often created using pseudo-random variable-density Poisson disks [114] with a fully-sampled calibration region in the centre of the (k_y, k_z)-plane [69,113–118]. Variable-density Poisson disk-undersampling distributions are characterized by three parameters: (1) the undersampling factor (R), (2) the polynomial order of the sampling density variation (pp), and (3) the size of the fully-sampled calibration region ($calib$).

Although the image quality depends on those undersampling parameters, no conclusive information is available about their optimal values for 3D TOF MRA at 7T. It also remains unclear how the optimal acquisition parameters depend on the acceleration factor and resolution being used. Earlier work on reconstruction optimization for 2D-multislice Nesterov reconstruction of 3T TOF MRA found the best reconstruction results using the smallest of three calibration region sizes (corresponding to $calib$ = 48, 60, and 72) [118], but this smallest region for 2D MRA ($calib$ = 48) was still substantially larger than the calibration regions recently used for 7T CS TOF MRA in 3D ($calib$ = 32) [69]. Other work has compared the image quality from retrospectively undersampled 3D-MRA data for various accelerations factors [111,115] or for the combination of acceleration factor and calibration region size in undersampled 2D MRI acquisitions for different contrasts

[119]. For dynamic MRI [120] and numerical T1-weighted brain models [121], studies into the optimization of undersampling parameters are available. However, it is unclear how this translates to the case of 3D TOF MRA, which requires the visibility of smaller structures in the reconstructed images, and which has the potential for higher acceleration factors due to the higher intrinsic sparsity.

In this chapter, 3D TOF MRA undersampling parameters are optimised by retrospectively evaluating different calibration region sizes and polynomial orders across six acceleration factors (5 to 15). Finally, the identified undersampling patterns were evaluated in healthy subjects using additional prospectively undersampled acquisitions that adopted the optimized parameters.

4.2 Methods

4.2.1 Data Acquisition

Data were acquired using a 3D gradient-echo non-contrast-enhanced TOF MRA sequence on a Siemens (Erlangen, Germany) Magnetom 7T scanner using a 1Tx/32Rx head-coil. All experiments were performed under an institutional agreement for technical development, in accordance with IEC and UK Health Protection Agency guidelines. In each subject, 4 sequential slabs [18] consisting of 640×506×56 voxels with a resolution of $(0.31\ \text{mm})^3$ were acquired using a slab overlap of 19.64% and a combined field-of-view of 200×157×60 mm. Further sequence parameters were: TR/TE = 14/5.61 ms (allowing for asymmetric echo), flip angle = 20°, bandwidth = 118 Hz/pixel. The excitation pulse duration was increased from 1.024 ms to 1.536 ms, which reduced its SAR by 33%. Flow compensation (gradient moment nulling) was used for the readout gradients. No motion correction was used. The acquisition time was 26:39 minutes for a fully-sampled acquisition.

Fully-sampled datasets from two subjects were used for parameter optimization through retrospective undersampling ("Cohort 1"). Additional datasets were acquired from seven healthy volunteers ("Cohort 2") using a modified version of the Siemens TOF MRA product sequence, which was modified to allow for compressed sensing undersampled acquisitions. For this, the undersampling was implemented using pre-defined Cartesian undersampling masks, which were generated for various combinations of undersampling parameters and stored on the scanner as text files indicating which k-space locations were

to be sampled. Readout lines were acquired based on a centre-out spiral reordering of the sampled locations in the phase-encode (k_y, k_z)-plane.

A fully-sampled acquisition and four different undersampled datasets, using both the optimized ($calib$ = 12, pp = 2.0, R = 7.2 and 15) and more conventional ($calib$ = 32, pp = 2.0, R = 7.2 and 15) undersampling parameters, were acquired from each volunteer in Cohort 2. The reconstructed image quality for those additional datasets was compared to assess the consistency of the findings. Finally, the reconstructed image quality from compressed sensing reconstructions using the optimized undersampling parameters was compared to the reconstructed image quality using two alternative acquisition acceleration approaches: firstly data acquired at various lower resolutions but reconstructed at a resolution of $(0.31\ \text{mm})^3$, and secondly compressed sensing undersampled data acquired without a fully-sampled calibration region, using SAKE (simultaneous autocalibrating and k-space estimation [122]) for sensitivity estimation.

For further validation, retrospective parameter optimization was also performed on artificially downsampled k-space datasets (at 0.5 mm and 0.6 mm isotropic) to confirm the consistency of the optimized undersampling parameters.

4.2.2 Undersampling

Undersampling masks were generated using the SPIRiT Toolbox v0.3[1], characterised by the three previously described parameters (R, pp, and $calib$). A polynomial order of 0 corresponds to homogeneous undersampling, with higher values corresponding to denser sampling (i.e. lower Poisson disk radii) closer to the centre of k-space: the Poisson disc radius at different distances r_k from the centre of k-space increases as $r_k^{pp/2}$. Larger calibration regions (consisting of a $calib \times calib$ portion of fully sampled frequency-encode lines) improve the estimation of coil sensitivities [63], but take up more scan time (Figure 4.1), thereby reducing the available time to acquire other regions of k-space for scan-time-matched acquisitions. Undersampling was performed retrospectively from the fully-sampled data acquired in Cohort 1 at acceleration factors ranging from 5 to 15. The calibration region size was chosen to range from the lower limit for the ESPIRiT tool ($calib$ = 10) to the highest value found in the literature for 3D MRA ($calib$ = 32) [69]. In

[1] https://people.eecs.berkeley.edu/~mlustig/Software.html. Note that in this work the acceleration factor refers to the *effective* acceleration (i.e., including the time taken to scan the calibration region), which is different from the definition of the "acc" parameter in the SPIRiT-vdPoisMex tool.

Cohort 2, prospectively undersampled data were acquired for validation at $R = 7.2$ (which was previously found to be "a reasonable trade-off between scan time and image quality" [69]) and $R = 15$ (higher acceleration to compare the resulting loss in small vessel visibility). Note that the undersampling masks in this work were generated using the SPIRiT Toolbox, which uses a polynomial variation for the sampling density distribution (given by the value of pp). Alternative ways of varying the sampling density distribution can also be used for Poisson disk undersampling, such as Gaussian density distribution (with the Poisson disc ratio scaling to $e^{C*r_k^2}$ for a given density variation parameter C), as for example used in Ref. [69].

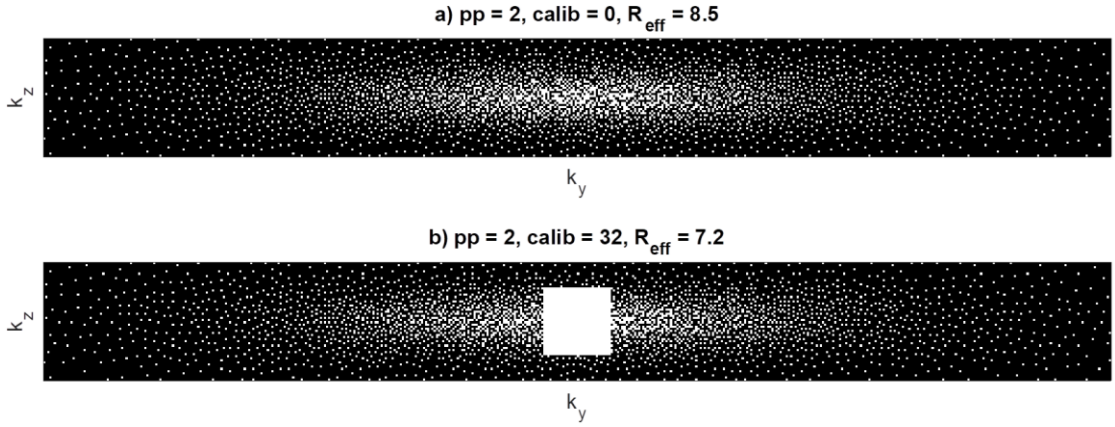

Figure 4.1: Two example undersampling masks, **(a)** without and **(b)** with a fully-sampled calibration region in the centre of k-space. The phase-encode directions k_y and k_z are shown. Each sampled location (in white) indicates a continuously sampled readout line (k_x). Note that although the sampling outside the calibration region is identical for both masks, the effective acceleration factor R_{eff} is lower in (b) due to the inclusion of the fully-sampled calibration region. Note that the masks shown are for visualization purposes and do not correspond to the masks used for data acquisition (which are shown in Figure 4.5).

4.2.3 Reconstruction

For all reconstructions with a fully-sampled calibration region in the centre of k-space, coil sensitivities were estimated using ESPIRiT [63]. For the reconstruction of undersampled data, compressed sensing was implemented using a FISTA (fast iterative shrinkage-thresholding algorithm)-based algorithm [123] with ℓ1-regularization in the wavelet domain [68,118] using the pics (parallel imaging and compressed sensing) tool in the BART-toolbox [124,125] (v0.4.02). FISTA is a computationally efficient method for iteratively solving linear inverse problems using a gradient descent method. Convergence to a solution which optimizes predefined criteria is achieved using a soft-thresholding regularization term. In the implementation used here, a soft-thresholding ℓ1-regularization term is used to impose sparsity in the wavelet domain of the reconstructed images

(Equation 4.3). Compared to other iterative soft-thresholding algorithms, FISTA achieves increased computational efficiency by using a proximal gradient method to update the image estimate in each iteration, which allows for a larger step size and faster convergence. Specifically, this proximal gradient method uses a weighted linear combination of the last two estimates (x_k and x_{k-1}) as the starting point (y_{k+1}) for the next shrinkage step:

$$\mathrm{y_{k+1}} = x_k + \left(\frac{t_k - 1}{t_{k+1}}\right)(x_k - x_{k-1}) \,, \tag{4.1}$$

where t_k is the stepsize parameter and

$$\mathrm{t_{k+1}} = \frac{1+\sqrt{1+4t_k^2}}{2} \,. \tag{4.2}$$

In this work, FISTA is used to reconstruct undersampled acquisitions by optimizing for

$$\min_{\mathrm{x}}\{|\mathrm{A(x)} - \mathrm{b}| + \lambda|\phi(\mathrm{x})|_1\} \,, \tag{4.3}$$

where b represents the acquired (undersampled) k-space data, A is the undersampled Fourier Transform operator over the reconstructed image x, λ is a regularization parameter, and ϕ denotes the Daubechies wavelet transform. The first term ($|\mathrm{A(x)} - \mathrm{b}|$) ensures data consistency, whereas the second term ($\lambda|\phi(\mathrm{x})|_1$) enforces sparsity in the wavelet domain.

Before the undersampling parameter optimization was performed, appropriate values for λ and the number of iterations (n_{iter}) were first established by reconstructing two different undersampled datasets (at $R = 9$ and $R = 13$) for each subject using various values for n_{iter} and λ, and comparing the resulting reconstructions to the fully-sampled reference data using the SSIM metric described in Section 4.2.4. Parameter values ($\lambda = 0.007$, $n_{iter} = 20$) which consistently achieved amongst the highest structural similarity compared to the fully-sampled data were used for all other reconstructions: see Figure 4.2. The initial reconstruction parameter optimization was performed using arbitrarily chosen undersampling masks. For validation, this reconstruction parameter optimization was repeated at the end of the study using the established optimized undersampling masks. This confirmed that the initial optimized reconstruction parameters were still consistent when using the final undersampling masks.

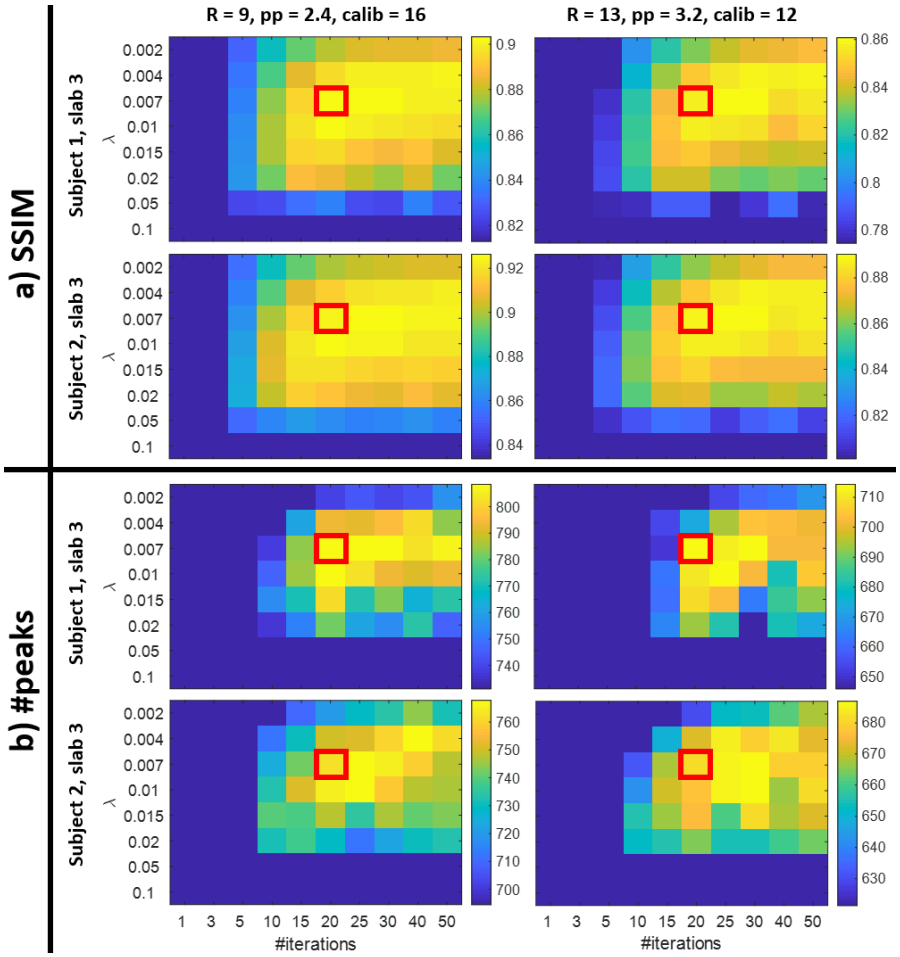

Figure 4.2: Results of the initial reconstruction parameter optimization, used to estimate appropriate values for n_{iter} and the regularization parameter λ. Reconstruction accuracy is calculated using **(a)** the mean vessel-masked SSIM and **(b)** the number of detected peaks, as described in Section 4.2.4. Results are shown for two different imaging volumes, each undersampled using two different sets of undersampling parameters (as indicated at the top of both columns). Red boxes indicate the set of reconstruction parameters (λ = 0.007, 20 iterations) used for all later reconstructions because of the consistently good results using both metrics, within reasonable reconstruction times.

SAKE reconstruction [122] was implemented for comparison of reconstruction quality when acquiring datasets without a fully-sampled central k-space region. SAKE is a calibration-free parallel imaging approach in which missing k-space values are estimated by iteratively enforcing data consistency on the data represented as a structured low-rank matrix. This matrix is first constructed using an ESPIRiT-like kernel inside the k-space region of interest. For this, the central 32×32 k-space lines were completed using a 5×5 kernel and 50 fixed iterations as an initial indication of the relative performance of SAKE. Note that although SAKE can in theory be used to complete the full undersampled k-space, results are here reported using SAKE to complete the central 32×32 k-space lines, after which ESPIRiT coil sensitivity estimation and compressed sensing reconstruction are used for further k-space completion. This was found to provide improved image quality

compared to full SAKE reconstruction of the highly-undersampled high frequency k-space.

All reconstructions were performed off-line in MATLAB using an Intel (Intel, Santa Clara, CA, USA) Xeon CPU E5-2680v4 running at 2.40GHz with 14 cores and 28 logical processors. A single-slab CS reconstruction took approximately 14 minutes.

4.2.4 Quantification of Reconstruction Quality

Previous work found that when comparing reconstructions from retrospectively undersampled MRA data to the corresponding fully-sampled data, the vessel-masked structural similarity index (SSIM) correlates very well with visual evaluation by radiologists [126]. The root-mean-square error, which is also often used in the literature, was found in Ref. [126] to result in low agreement with visual evaluation by radiologists and is therefore not used in this work.

The structural similarity index is a quantitative estimate of the perceived visual agreement between a set of images based on local intensity variations. Using a sliding window, it compares the similarity between two different versions (x and y) of the same image based on their similarity in terms of luminance (l), contrast (c) and structure (s). Each of those three components is calculated based on the signal intensity (μ_i) and variance (σ_i^2) of the respective images segments, as well as their covariance (σ_{xy}), and additional dynamic range-dependent constants (c_1 and c_2) to prevent division by (near) zero [127]:

$$\mathrm{SSIM}(x,y) = l * c * s = \frac{(2\mu_x\mu_y+c_1)(2\sigma_{xy}+c_2)}{(\mu_x^2+\mu_y^2+c_1)(\sigma_x^2+\sigma_y^2+c_2)}. \qquad 4.4$$

A higher SSIM indicates greater agreement between a set of images, with a value of 1 indicating perfect agreement. Based on the method used by Akasaka et al. [126], the SSIM is calculated from axial maximum intensity projections (MIPs) normalized to the 99th intensity percentile for each dataset that was compared. The mean SSIM, which serves as the main quality metric, is calculated over a vessel-masked region (Figure 4.3b), which reduces the sensitivity of the SSIM calculation to variations in the background signal.

The SSIM requires spatial consistency of the information in the two images being compared. This limits its use when comparing prospectively undersampled datasets, since minor subject motion between consecutive scans can significantly influence the SSIM. Therefore, a different metric ('number of detected peaks'), designed to estimate the change

in the number of visible vessels in an image [69], was used to assess the quality of prospectively undersampled data. From the MIPs, 100 cross-sectional lines in the left-right direction were taken, covering the central 50% of the field-of-view in the anterior-posterior direction. Along these lines, peaks in the intensity profiles were detected using the findpeaks function in MATLAB. A minimum peak prominence, defined as the height of the peak relative to the highest of its surrounding valleys (on the normalized MIPs) of 0.15 was used for all shown figures and significance tests. The results when using other minimum peak prominence values (between 0.10 and 0.25) were also computed to confirm the robustness of the results.

To quantify the difference in visibility of small vessels, specifically, in prospectively undersampled acquisitions, a comparable approach was used to estimate the visibility of the LSAs in coronal projections.

4.3 Results

4.3.1 Fully-Sampled Data

Figure 4.3 shows MIPs of the fully-sampled reconstructions of the central 2 (out of 4) slabs for both subjects in Cohort 1, which were used for parameter optimization. Those slabs were used as the ground-truth reference for all combinations of parameters used to assess the different retrospectively undersampled reconstructions. Only 2 slabs per subject were used to remain within a reasonable computation time. The central slabs were found to contain vessels of various sizes and degrees of tortuosity (Figure 4.3), making it possible to compare undersampling parameter optimization results for different parts of the vasculature.

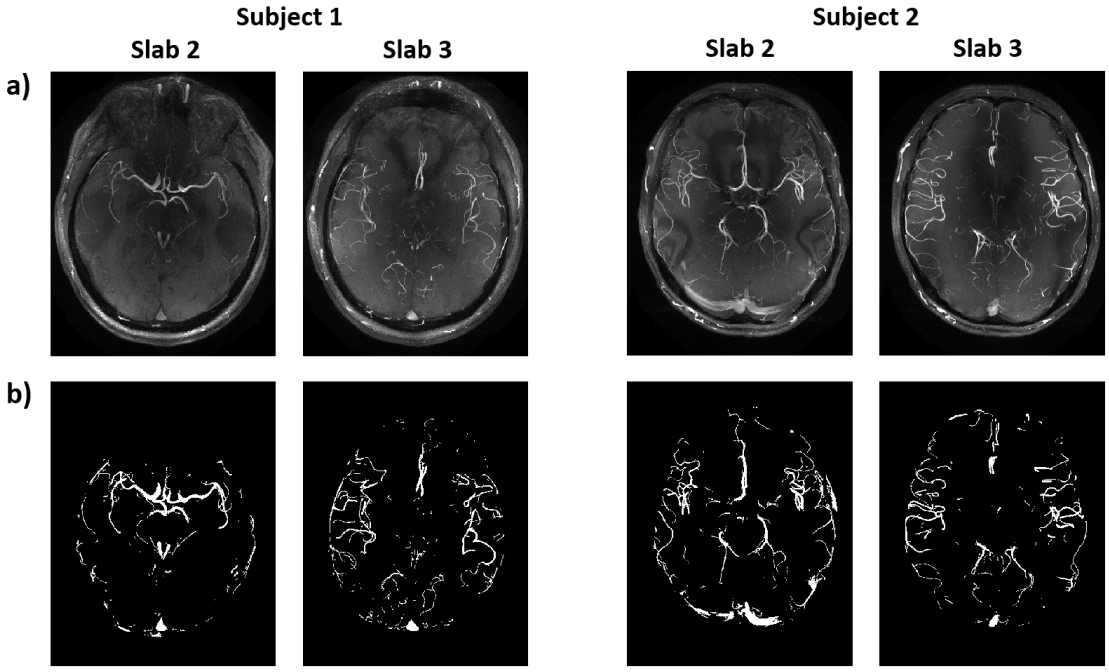

Figure 4.3: The four slabs used to test retrospective undersampling strategies (from Cohort 1). **(a)** MIPs of the fully-sampled reconstruction for each slab. **(b)** The corresponding vessel masks, used for computing the vessel-masked SSIM**.**

4.3.2 Retrospective Undersampling Optimization

The mean vessel-masked SSIM resulting from the retrospective undersampling parameter optimization for six acceleration factors R (5 to 15) for all four slabs (in Figure 4.3) are presented in Figure 4.4. Each of the values in Figure 4.4 is the mean value for two different undersampling masks (generated using the same undersampling parameters but with a different randomized initialization point for the resulting sampling pattern), such that each datapoint is the average of 8 comparisons: four different slabs, with two different undersampling masks each. Although Figure 4.4 only shows the average results across all four slabs shown in Figure 4.3, the results for each individual slab (data not shown) are generally consistent in terms of both the observed minimum calibration region size and the optimum region for the polynomial order of the sampling density distribution.

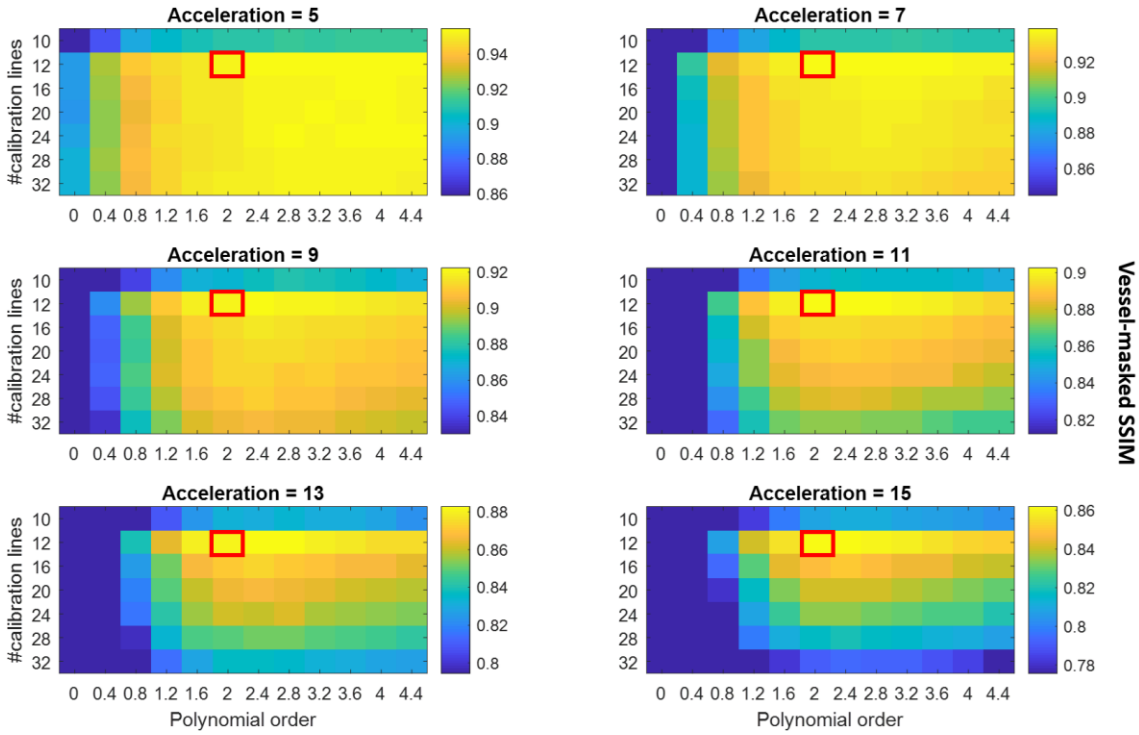

Figure 4.4: Average SSIM indices for various sets of undersampling parameters. Each datapoint represents the mean vessel-masked SSIM values of the four slabs shown in Figure 4.3. The scaling of the SSIM-values in each individual figure runs from the maximum value (for the given acceleration factor) to 90% of that maximum value, to maximize the visibility of the relative image quality for each acceleration factor. Red boxes indicate the proposed optimized undersampling parameters of $pp = 2$, $calib = 12$.

Especially for higher acceleration factors, Figure 4.4 indicates that for matched scan time an optimal set of undersampling parameters occurs for 12×12 calibration lines ('$calib = 12$') with a polynomial order of approximately 2.0 to 2.4. For datasets reconstructed from the Cohort 1 data with a downsampled spatial resolution (0.5 mm and 0.6 mm isotropic), optimal undersampling parameters consisted of 12×12 calibration lines and a polynomial order of approximately 1.6 to 2.0 (data not shown).

For validation, the initial reconstruction parameter optimization was repeated for those optimized undersampling parameter values. This confirmed the generally good performance of the previously established reconstruction parameter values ($\lambda = 0.007$, $n_{iter} = 20$).

4.3.3 Prospective Validation of Optimized Undersampling

For validation of the retrospectively optimized undersampling parameters, additional datasets were acquired (Cohort 2). These datasets consisted of data acquired and reconstructed from fully-sampled data; prospectively undersampled data with literature-

based parameters [69]; and prospectively undersampled data using the optimized parameters identified above. All undersampled acquisitions were acquired using acceleration factors of $R = 7.2$ and $R = 15$. "Optimized" undersampling masks were generated using $calib = 12$ and $pp = 2.0$, and "literature-based" masks were generated using $calib = 32$ and $pp = 2.0$ (based on Ref. [69]) with matched scan time: see Figure 4.5.

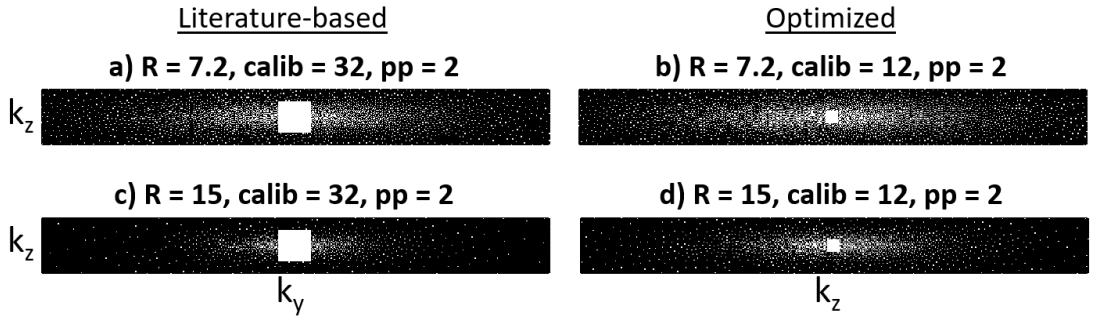

Figure 4.5: The four undersampling masks used for the acquisition of prospectively undersampled validation of the optimized undersampling parameters. Masks **(a)** and **(c)** correspond to the "Literature-based" undersampling parameters, while **(b)** and **(d)** are generated using the "Optimized" parameters, as specified in the figures. Since the total amount of acquired data is fixed for a certain acceleration factor, undersampling masks with smaller calibration region sizes contain more k-space locations outside the calibration region.

Figure 4.6 and Figure 4.7 show example reconstructions from fully-sampled data, as well as using the four undersampling schemes in Figure 4.5.

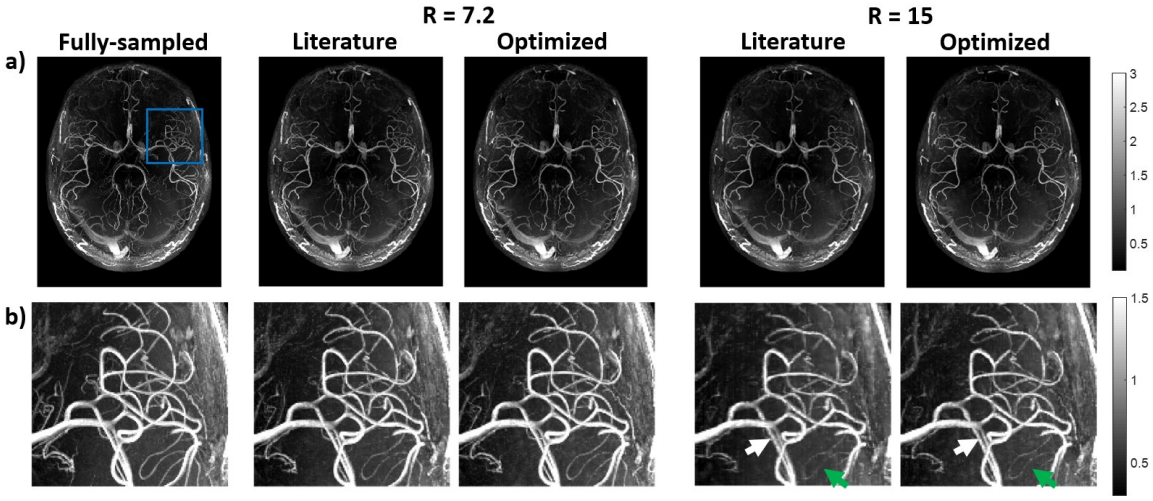

Figure 4.6: Comparison of axial MIPs from optimized ($calib = 12$) and literature-based ($calib = 32$) undersampling schemes for $R = 7.2$ and $R = 15$. **(a)** Reconstructed images from fully-sampled data and the different prospectively undersampled acquisitions. **(b)** Close-up of the region marked with a blue square in (a), for all acquisitions. Green arrows indicate examples of improved vessel visibility when using optimized undersampling parameters; white arrows indicate improved vessel sharpness. The windowing was reduced for (b) to improve the visibility of small vessels.

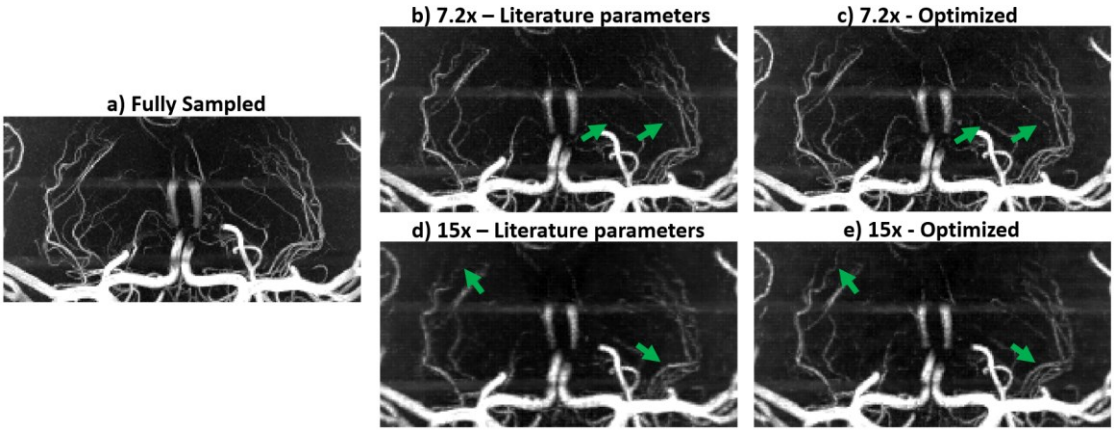

Figure 4.7: Comparison of coronal MIPs of the LSAs from optimized and literature-based undersampling schemes. Images are shown for **(a)** fully-sampled data; **(b-c)** data acquired with $R = 7.2$ using literature-based (b) and optimized (c) prospectively undersampled acquisitions; and **(d-e)** data acquired with $R = 15$ using literature-based (d) and optimized (e) prospectively undersampled acquisitions.

Figure 4.8 shows examples of the implementation of the 'number of detected peaks'-metric, as well as the resulting differences between the various undersampling schemes for the seven volunteers in Cohort 2. Results are shown for whole-brain axial MIPs and coronal MIPs of the lenticulostriate region.

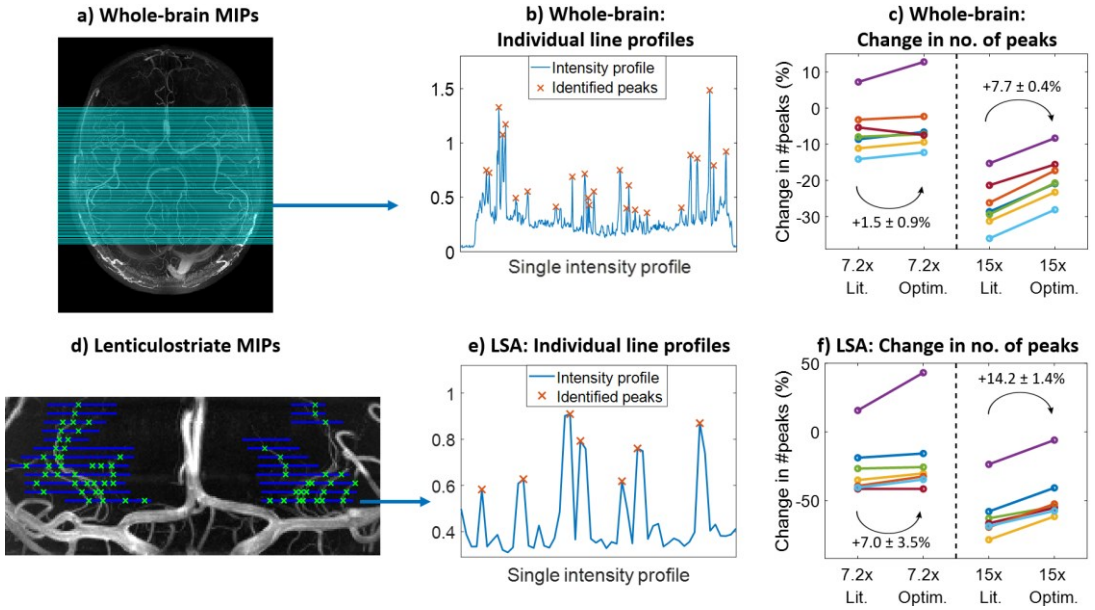

Figure 4.8: Quantification of the change in the number of detected peaks (expressed as the percentage difference in reconstructions from undersampled data relative to the corresponding fully-sampled acquisitions). **(a-c):** Whole-brain MIPs. **(a)** The 100 lines along which peaks in the intensity profiles were identified on all datasets (as shown in (b) for Line 25). **(c)** The change in the identified number of peaks for optimized ("Optim.") and literature-based ("Lit.") undersampled acquisitions, relative to fully-sampled acquisitions. Each colour indicates a subject from Cohort 2. **(d-f):** The same as (a-c) for MIPs of lenticulostriate ROIs. Line locations in (d) were drawn manually at 5-pixel intervals.

At $R = 7.2$, the mean relative number of detected peaks when using 12×12 compared to 32×32 calibration lines increases by 1.5 ± 0.9 percentage points (from -6.1% to -4.6%) for axial MIPs and by 7.0 ± 3.5 percentage points (-26.5% to -19.5%) for the LSAs. At $R = 15$, the number of detected peaks increases by 7.7 ± 0.4 percentage points (-26.9% to -19.2%) for axial MIPs and by 14.2 ± 1.4 percentage points (-60.9% to -46.7%) for the LSAs.

The change in the number of detected peaks when using optimized undersampling parameters is statistically significant at $R = 15$, based on one-sided paired-sample t-tests: $P < 0.001$ for both whole-brain and LSA MIPs and at $R = 7.2$ for LSA MIPs ($P = 0.047$). At $R = 7.2$ statistical significance was not reached for the whole-brain MIPs, but a trend value of $P = 0.063$ was obtained. All of those results (changes in the number of detected peaks as well as significance values) were calculated using a minimum peak prominence of 0.15. Highly consistent results were found when detecting peaks using minimum peak prominences ranging between 0.10 and 0.25.

4.3.4 Comparison to Alternative Acceleration Approaches

Figure 4.9 shows the reconstructed image quality from undersampled reconstructions using literature-based compressed sensing undersampling parameters (shown in yellow); using our optimized compressed sensing undersampling parameters (orange); and for acquisitions that were accelerated by acquiring data at a lower resolution (blue; reconstructed at acceleration factors matching the acquisition times for the compressed sensing reconstructions as well as lower acceleration factors). The black arrows indicate examples of equivalent image quality (same y-axis value) between reconstructions for $R = 11$ using optimized undersampling parameters versus reconstructions for $R = 15$ using literature-based reconstruction parameters. I.e., these reconstructions achieve similar image quality based on both the metrics of vessel-masked SSIM and the errors in the detected numbers of peaks.

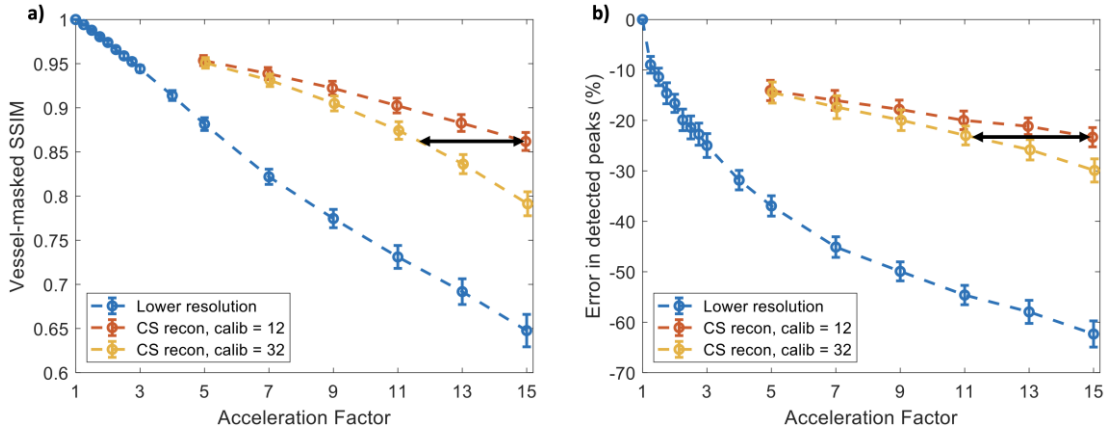

Figure 4.9: Reconstructed image quality for different undersampling approaches, from retrospectively undersampled data. Results are shown using **(a)** the vessel-masked SSIM and **(b)** the error in the number of detected peaks. Black arrows indicate an example of the increase in acceleration factor when using $calib = 12$ instead of 32, which can be achieved without loss in image quality.

Figure 4.10 compares the achieved reconstructed image quality using compressed sensing with 12×12 calibration lines to reconstructions without calibration regions (using SAKE for sensitivity estimation), but with matched acquisition times. The SAKE-reconstructions perform best for data undersampled with a polynomial sampling density order of 2, but higher vessel-masked SSIM values are achieved at both $R = 7$ and $R = 15$ when using a small calibration region instead of SAKE for sensitivity estimation.

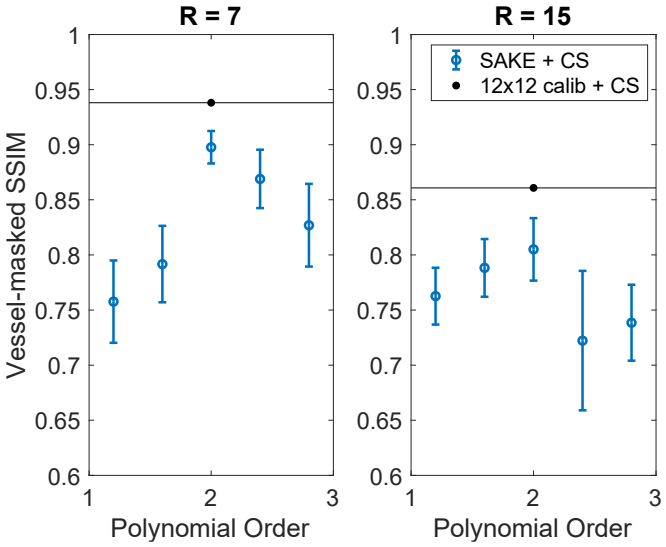

Figure 4.10: Comparison of image quality in reconstructions from retrospectively undersampled k-space data without calibration regions (using SAKE-calibration for sensitivity estimation) versus the image quality in reconstructions using 12×12 sampled lines in k-space for calibration. After sensitivity estimation, both approaches were reconstructed using the same compressed sensing pipeline. Results are shown as the mean vessel-masked SSIM ± the standard deviation across the 4 slabs shown in Figure 4.3.

4.4 Discussion

Although differences in the image quality are visible when using various auto-calibration region sizes and polynomial orders for all acceleration factors in Figure 4.4, the relative importance of using optimized parameters increases at higher acceleration factors. For all acceleration factors, 12×12 calibration lines with a polynomial order of 2—2.4 consistently yielded the best reconstruction accuracy. Simulation results at reduced spatial resolutions indicate the same optimal calibration region size, but with slightly lower polynomial orders (approximately 1.6—2.0 at $(0.6\ \mathrm{mm})^3$). For all resolutions, optimization of the calibration region size has a bigger influence on the image quality than optimization of the polynomial order. This optimal calibration region size is considerably smaller than values found in the literature. Reducing the calibration region size from 32×32 to 12×12 lines in k-space corresponds to an 86% reduction in the amount of scan time required for scanning this central k-space region. For a fixed scan time, this makes it possible to spend more scan time acquiring data at higher spatial frequencies (allowing for the acquisition of 30% more samples outside the calibration region at $R = 7.2$ and 102% more at $R = 15$), explaining the observed improvement in small vessel visibility. The use of such reduced calibration region sizes requires high quality B0 shims to ensure that the central k-space signal region is contained within this small calibration region. However, no such issues were encountered in any of the reconstructions from undersampled data presented here. Asymmetric calibration regions, with reduced coverage in the partition-direction (k_z), were not included in this work because of limitations in the used implementation of ESPIRiT.

For the prospectively undersampled data, the performance of these optimized undersampling parameter values was compared to those taken from Ref. [69]. Figure 4.6 and Figure 4.7 show a clear reduction in the number of visible vessels at high acceleration factors using both optimized and literature-based acquisition parameters, compared to a fully-sampled acquisition. However, vessel visibility and sharpness noticeably improve when using optimized undersampling parameters versus literature parameters, especially for small vessels and at high acceleration factors. Although accurate quantitative comparison of different prospectively undersampled acquisitions using SSIM is not possible due to subject motion between scans, the reduction in signal loss when using optimized parameters was quantitatively approximated using the detection of vascular signal peaks. The identified peak locations in reconstructions from prospectively undersampled data are consistent with the locations of the peaks in the corresponding

fully-sampled data (not shown), indicating that the metric gives a representative approximation of relative image quality.

Prospectively and retrospectively undersampled data can differ in image quality because of the possibility of eddy-current artifacts due to larger gradient switching in prospectively undersampled acquisitions and different amounts of total subject motion due to the different scan times. However, the observed improvement in image quality when using optimized undersampling schemes identified using the retrospectively undersampled data (Figure 4.4) is consistent with the results found in Figure 4.6-Figure 4.8 for prospectively undersampled data. This applies to both the improvement in image quality when using smaller calibration regions (in particular, 12×12 calibration lines) and to the increased importance of acquisition parameter optimization at higher acceleration factors. This improvement when using optimized undersampling parameters can be achieved without increasing scan time or reconstruction time, and without additional technical requirements. This improvement in image quality at a given acceleration can also be interpreted as an opportunity to increase acceleration factor to achieve equal image quality (Figure 4.9). For example, a scan duration of 2:36 minutes ($R = 11$) when using 32×32 calibration lines provides comparable results to a scan duration of 1:57 minutes ($R = 15$) using 12×12 calibration lines. As expected, Figure 4.9 also confirms that accelerating acquisitions by reconstructing lower resolution data (without acquiring higher frequency k-space areas) results in a more rapid loss of vessel visibility than in compressed sensing reconstructions.

Since a small calibration region size was observed to improve performance, reconstructions from k-space data without calibration regions were also evaluated, using SAKE-calibration [122] for sensitivity estimation (Figure 4.10). This did not provide improved image quality compared to the reconstructions using 12×12 sampled lines in k-space.

For one of the seven volunteers in Cohort 2, an increase in the number of detected peaks is visible in the undersampled acquisitions (purple data in Figure 4.8). This is likely caused by a reduction in image quality in the fully-sampled dataset due to subject motion during that scan, highlighting a benefit of accelerated acquisitions.

The data used in this work were acquired using a relatively simple protocol, which does not make use of techniques such as additional (e.g. fat or venous) signal saturation [69,128,129], parallel transmission for reduced $B1^+$ inhomogeneity [60,130], VERSE-shimming for further SAR reduction (in particular when using additional saturation pulses) [69,128,131], or intravenous contrast agents for enhanced contrasts [15,132]. Such techniques can

enhance contrast and increase sparsity, and thereby improve the CS reconstruction results. However, the optimal undersampling parameters were found to be consistent for volumes with high differences in vascular characteristics and visibility (Figure 4.3), and are therefore also expected to remain consistent for different contrasts. The improvement in image quality when using 12×12 calibration lines was also found to be consistent for data acquired using various acceleration factors and spatial resolutions. Although 32-channel receive coils are most commonly used in 7T MRI, it remains unclear how the results presented here would translate to different coil configurations.

Previous work on the optimization of acquisition parameters for CS T1-weighted MRI in 3D found that optimized sampling schemes require increasingly dense sampling in the centre of k-space for higher acceleration factors [121], and that the extent of the calibration region should be as high as possible for 2D-MRI [119]. This is different from the results found here, with an optimized set of acquisition parameters which appears to be consistent for all acceleration factors and which uses a small calibration region. This difference may be explained by the inherently sparser image contrast of MRA compared to T1-weighted structural MRI, and the use of three-dimensional instead of two-dimensional k-space data. Since this sparser image signal is contained in high-frequency areas of k-space, sampling at off-centre locations of k-space remains important at higher acceleration factors for MRA.

4.5 Conclusion

Optimized undersampling parameters for 3D MRA at 7T using compressed sensing reconstruction were established. For all acceleration factors, the highest image quality was achieved by using a fully-sampled calibration area of 12×12 lines and a Poisson disk polynomial order of 2. Although the optimized undersampling parameters were the same for all acceleration factors, the importance of using optimized undersampling parameters was found to increase for higher acceleration factors.

5

An Extended Phase Graph-Based Framework for DANTE-SPACE Simulations Including Physiological, Temporal, and Spatial Variations

Key Conclusions

- **A comprehensive EPG-based DANTE-SPACE simulation framework is presented**
- **The addition of vessel wall and CSF pulsation in simulations can explain previously observed DANTE-SPACE signal heterogeneity**

5.1 Introduction

The DANTE-SPACE sequence, introduced in Section 1.3.3, facilitates three-dimensional intracranial vessel wall imaging with simultaneous suppression of blood and CSF. It has been used at both 3T [30,36–43,133–135] and 7T [35,87,136], and with SPACE parameter configurations resulting in T1-weighted [30,36–38,40–43,135], T2-weighted [35,39,87,136], and proton density-weighted [42,133,135] contrasts. Across different implementations, many different protocol settings have been used, such as DANTE pulse trains ranging from 94 pulses [43] to 300 pulses [35,134,135] and DANTE flip angles ranging from 8° [37,38,40,135] to 13° [43]. This choice of parameters directly affects the resulting blood, CSF, and vessel wall (VW) signals. Various authors have used DANTE calculations [31,133], Bloch simulations [35,36,39,40,134,135], or direct comparison of acquisitions using multiple parameter combinations [135] to select parameters aiming to achieve the highest contrasts between vessel walls and both blood and CSF.

The validity and accuracy of such approaches depend on the approximations and assumptions used in the design. Li et al. [31] derived a T1-decay model to approximate signal decay in moving spins during DANTE. This approach is both intuitive and computationally efficient. However, it assumes full velocity-independent spoiling of the transverse magnetization in moving spins, which can be inaccurate for very slowly moving

or pulsating spins, especially in high-resolution acquisitions. Furthermore, this model only accounts for the effects of DANTE, without taking the effects of readout pulses and multiple repetitions into account. More accurate models can be achieved using Bloch simulations (either including [36,40] or excluding [35,134,135] readout effects) by directly including flow effects in the simulations. This requires that, in addition to the relaxation parameters of the simulated tissues, flow parameters are added as input parameters. This is particularly relevant for CSF, which is often assumed to be either static [40] or moving substantially faster (≥2 cm/s [35,134,135]) than the values found in the literature for the CSF near the Circle of Willis (e.g., 0.37 cm/s in the 3rd ventricle [23] and up to 0.85 cm/s in the cerebral aqueduct [137]). Furthermore, other processes affecting the measured signal levels, such as intravoxel dephasing and pulsatile flow velocity variation, are generally also not modelled in those simulations. Especially at 7T, another often non-negligible factor is the effect of transmit field variations on the obtained MRI signals and contrasts. Although this can be expected to have a limited effect near the Circle of Willis (located in the central region of high $B1^+$ efficiency at 7T when using a transmit head coil), it can affect the magnetization of blood spins, which during a single DANTE-SPACE module can travel from low-$B1^+$ areas in the neck into higher-$B1^+$ areas near the Circle of Willis.

To accurately account for all these effects, a comprehensive DANTE-SPACE framework is introduced in this chapter. By including physiological processes such as pulsatile flow velocity variation, varying flow directions, intravoxel dephasing, and diffusion, as well as $B1^+$ effects, this framework attempts an accurate representation of the mechanisms behind the achieved signal levels (VW, CSF, and blood). This in turn can be used for accurate optimization of sequence parameters, and to obtain a further understanding of the DANTE-SPACE contrast mechanisms.

To support the availability and reproducibility of both this framework itself and the results presented in this chapter, the simulation framework and a script that reproduces all simulation results in this chapter are openly available online (git.fmrib.ox.ac.uk/ndcn0873/dantespace_epg). Please note that instead of the *Methods* and *Results* sections used in the other chapters in this thesis, this chapter contains two sections discussing the development of the simulation framework (Section 5.2) and some initial tests of the resulting simulations (Section 5.3). Within those sections, each subsection describes all components of the simulation framework in turn, including the effects of each individual component on the resulting simulations.

5.2 Development of the Simulation Framework

5.2.1 General Simulation Settings

All code was implemented in MATLAB R2019a. Extended phase graph (EPG) simulations [78,79], which are introduced in Section 2.4, were used to efficiently simulate the magnetization evolution of ensembles of spin isochromats. This provides a more accurate representation of the signal behaviour in an acquired voxel than Bloch simulations of single isochromats, while being much more computationally efficient than averaging the results from hundreds of individual Bloch simulations to approximate spin ensemble behaviour. Code from the MRSignalSeqs toolbox by Brian Hargreaves (github.com/mribri999/MRSignalsSeqs) was used to propagate EPG states through periods of relaxation, gradient waveforms, RF pulse rotation, and diffusion. A tool to simulate flow effects (as described by Mugler [28]) was added based on the diffusion simulation code. All simulations were performed on a system using an Intel (Intel, Santa Clara, CA, USA) Xeon CPU E5-2680v4 running at 2.40 GHz with 14 cores and 28 logical processors.

All simulation results shown in this chapter were obtained assuming relaxation properties and $B1^+$ field effects corresponding to 7T. T1 and T2 relaxation times for vessel wall tissue were based on carotid artery measurements presented by Koning et al. [138]; for blood and CSF, the same relaxation times as used by Viessmann et al. [35] (based on various original sources [139–141]) were used. The resulting values are:

- VW: T1 = 1628 ms, T2 = 46 ms
- Blood: T1 = 2290 ms, T2 = 100 ms
- CSF: T1 = 4019 ms, T2 = 311 ms

The contrast between tissue types was calculated from the point spread function amplitude of the transverse magnetization during the SPACE-readout for the various tissue types after correcting for differences in proton density ($PD_{VW} = 0.72\ PD_{CSF} = 0.72\ PD_{blood}$) [35]. For $B1^+$ effects (Section 5.2.3.5), CP-mode $B1^+$ data from a representative subject (Subject 1) in the $B1^+$ database presented in Chapter 3 were used.

This section introduces the various components of the DANTE-SPACE simulation framework. First, the basic EPG simulations for DANTE and SPACE are presented and validated using previous literature in Section 5.2.2. Section 5.2.3 then discusses the various

additional physiological or transmit field-related variations that were added to the model. All DANTE-SPACE simulations in this section were performed using the T2-weighted 7T protocol adopted by Viessmann et al. [35]. This includes 300 DANTE pulses of 10°, 74 SPACE refocusing pulses per TR with an echo spacing of 4.6 ms (giving an echo train length of 345 ms), an effective TE of 165 ms, and a TR of 2620 ms.

5.2.2 Basic Simulations

5.2.2.1 DANTE Simulations

EPG DANTE simulations were validated by comparing EPG results to the results of Bloch ensemble simulations. The Bloch simulations themselves were first validated by comparing single isochromat simulation results to the Bloch simulation results presented by Li et al. [31]. Figure 5.1a demonstrates an accurate replication of the single isochromat Bloch DANTE simulations shown in Figure 3a of Ref. [31].

For Bloch ensemble simulations, the average results of 1000 Bloch simulations along a distance λ corresponding to unit phase accumulation along the gradient direction were used. The distance λ can be calculated as

$$\lambda = \frac{1}{\gamma \int Gdt} = 0.22\ cm, \tag{5.1}$$

where $\gamma = 42.6\ MHz/T$ is the gyromagnetic ratio of water protons and $\int Gdt$ denotes the area under each DANTE gradient. The results of Bloch simulations averaged across 1000 Bloch spin isochromats over a distance λ are shown in Figure 5.1b, with the corresponding EPG simulation results shown in Figure 5.1c. These results indicate good agreement between the EPG simulations and the Bloch ensemble simulations. The computation time, however, of the EPG results was two orders of magnitude shorter (0.4 s instead of 57.5 s), which confirms that EPG simulations can provide accurate isochromat ensemble simulations with high computational efficiency.

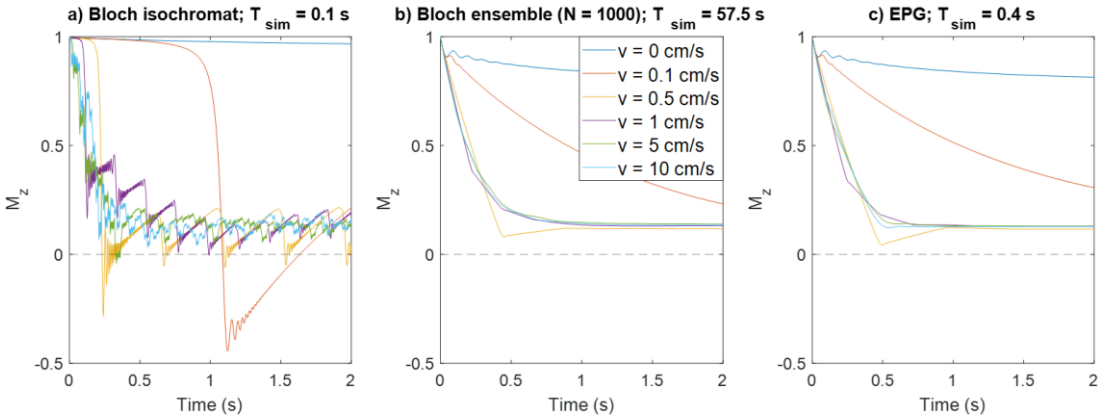

Figure 5.1: Comparison of DANTE simulations using Bloch equations and EPG. The results are shown for **(a)** Bloch isochromat simulations, **(b)** Bloch ensemble simulations, and **(c)** EPG simulations. T_{sim} indicates the computation time of the simulation results shown in each figure.

5.2.2.2 SPACE Simulations

To validate the SPACE-readout simulation using the EPG framework, the simulated transverse magnetization evolution in stationary vessel walls was cross-checked against the previously described target SPACE magnetization function [28,35]. This prescribed signal evolution consists of three parts, designed to increase the useable duration of the signal during the echo train [28]: a mono-exponential decay (time constant 17.5 ms; first 9 SPACE pulses), a constant segment (pulses 10-40), and a second mono-exponential decay (time constant 29.0 ms; pulses 41-74) [35]. This corresponds to the signal evolution shown in Figure 5.2a, which is highly similar to the simulated EPG SPACE signal evolution for the SPACE flip angle train (Figure 5.2b). However, when adding the DANTE-preparation to the simulation model (Figure 5.2c), the change in the magnetization state before the SPACE excitation pulse reduces the level of agreement with the desired magnetization evolution in Figure 5.2a. This reduces the signal intensity (by 29% for the DANTE parameters used here) while also slightly increasing the point-spread function of the vessel walls (by 6%). Those signal intensity values are calculated from the amplitude of the point spread function of the simulated transverse magnetization during the SPACE readout.

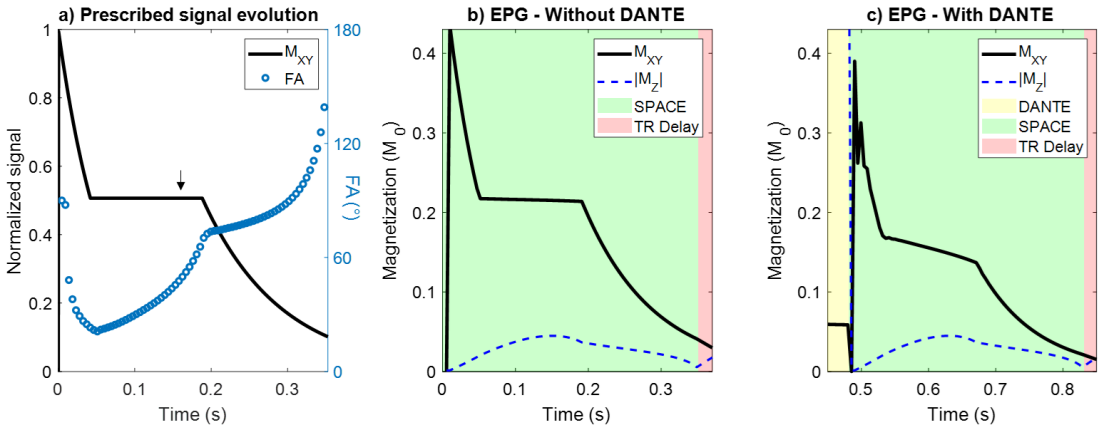

Figure 5.2: Comparison of the transverse magnetization during the SPACE readout. **(a)** shows the prescribed vessel wall signal evolution (black line) for which the SPACE flip angle train (blue circles) is calculated. The black arrow indicates the equivalent echo time of the acquisitions. **(b)** shows the resulting EPG simulation for SPACE acquisitions (without DANTE), while **(c)** shows the EPG simulation for DANTE-SPACE acquisitions. Note that the x-axis in (c) starts near the end of the DANTE preparation.

5.2.2.3 Simulations for Vessel wall, CSF, and Blood

The simulation results for the combination of the EPG DANTE- and SPACE-modules are shown in Figure 5.3 for VW, CSF, and blood. The results show only the most basic simulations of the different tissue types, so only using their respective relaxation times and (constant) average velocities. The format used here, with parts of the sequence shaded in yellow, green, and red, denoting DANTE-preparation, SPACE-readouts, and TR delay, respectively, will be used for all future simulated magnetization evolution plots.

Note that the results in Figure 5.3 are shown during the 2nd TR for the VW and CSF simulations, but for the 1st TR for the blood. This reflects the fact that while blood rapidly flows in from the upstream arteries (resulting in 'fresh' blood spins without magnetization history arriving in the CoW in each TR), the VW and CSF remain in the same scan region throughout an acquisition. For the latter two, the 2nd TR was chosen since it was found to provide good convergence of the resulting signal within a reasonable simulation time: for the VW, the signal reduces by 24% from the first to the second repetition, after which it changes by less than 0.01% over the next 5 repetitions (while the simulation time for 3 TRs is approximately twice the simulation time for 2 TRs). For CSF, the simulated signal reduces by 25% from the first to the second repetition, with about a 1.1% change over the next 5 repetitions (while requiring 3.3× more simulation time). Based on this argument, all future simulation results will also be based on 2 repetitions for VW and CSF, but only a single TR for blood.

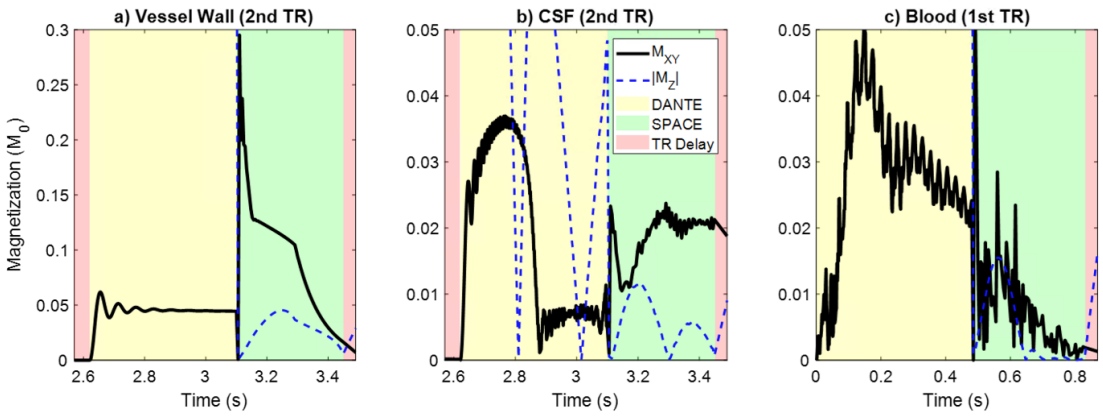

Figure 5.3: DANTE-SPACE simulations of the VW, CSF, and blood, assuming constant velocities and excluding the effects of intravoxel dephasing, diffusion, pulsatility, flow trajectories, and B1+ variations. Note that a different y-axis range is shown for VW (a) than for CSF and blood (b-c).

5.2.3 Additional Variations

This section first discusses various additions to the simulations on a per-phenomenon basis. After all individual additions have been discussed, Section 5.2.3.6 shows the effect when all variations are included simultaneously, as will be used for most simulations used in the main thesis work.

5.2.3.1 Intravoxel Velocity Variation

As was visible in Figure 5.3b-c, where moving spins were simulated with an isolated velocity, simulations using a unique velocity result in unstable transverse magnetization. In particular, isolated velocities with per-cycle phase accrual corresponding to an integer fraction of 360° result in unrealistically increased magnetization levels. Since a typical voxel in fact contains spins moving with slightly varying velocities around a certain average value, the actual measured MR signal is generated by the transverse magnetization of spins within such a range of velocities. To model this intravoxel velocity averaging effect in the simulations, each individual simulation was repeated 100 times using slightly different velocity values described by a normal distribution with $\sigma = 10\%$ around the nominal velocity. This distribution, and the resulting change in the magnetization evolution when accounting for a range of velocities, are shown in Figure 5.4 for CSF and blood. The simulations with intravoxel averaging (Figure 5.4c and f) indicate higher temporal stability of magnetization evolution for both tissue types, resulting (especially for blood) in lower transverse magnetization magnitude during the SPACE readout and therefore reduced simulated signal levels.

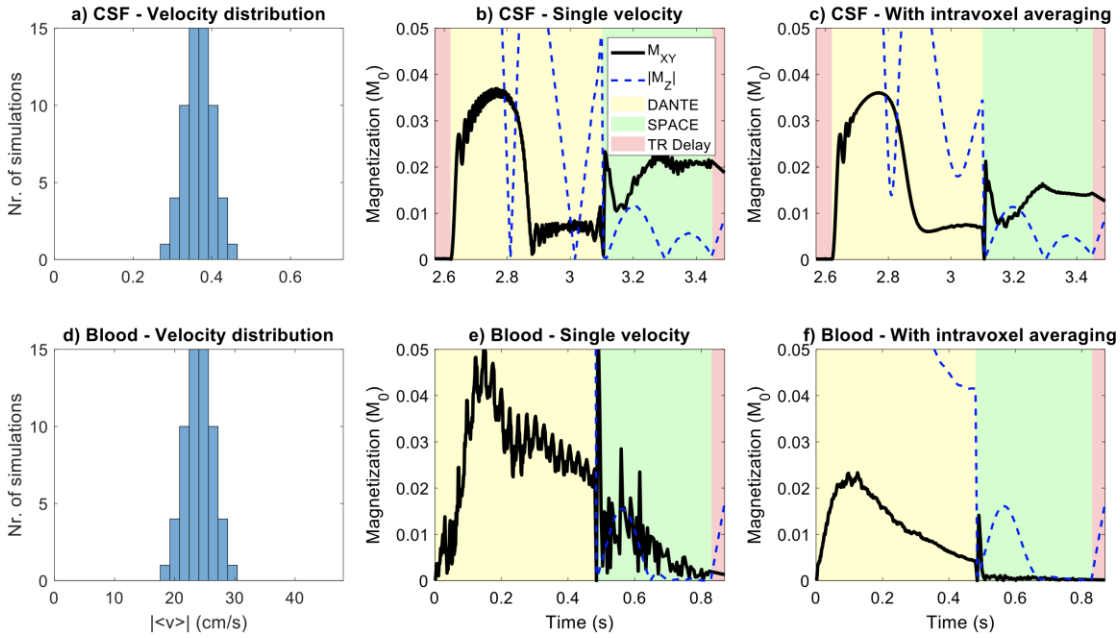

Figure 5.4: Intravoxel dephasing in simulations by using the average of 100 simulations with a distribution of flow velocities. For CSF, **(a)** shows the distribution of velocity values (corresponding to a normal distribution with $\sigma = 10\%$ around the nominal velocity), **(b)** shows the result of a simulation using a single isolated velocity, and **(c)** shows the average result of the 100 simulations using the velocities from the distribution in (a). **(d-f)** show the corresponding results for blood.

5.2.3.2 Pulsatile Motion

Pulsatile velocity variations over time were also added to the simulations to represent fluid dynamics and pulsatile oscillations. Figure 5.5 shows the flow velocity variations that were modelled and the resulting changes in simulated signal for CSF and blood. Temporal velocity variations due to pulsatile CSF (Figure 5.5a) were added based on literature-sourced time-varying CSF flow measurements at the third ventricle, which indicate an average flow velocity of 0.37 cm/s [23]. The temporal variation in blood flow velocity (Figure 5.5d) was modelled on the cardiac pulsatility of blood in the internal carotid arteries taken from Ref [142]. Both pulsation profiles assume a heart rate of 60 beats per minute. Because no cardiac gating is used for DANTE-SPACE acquisitions, a different random starting point was used for the pulsatile profiles in each of the 100 simulations.

Since the velocity of the blood remains relatively high throughout the cardiac cycle (with a minimum velocity of around 16.5 cm/s), the simulated magnetization of blood remains similar with and without the inclusion of pulsatility in the simulations (Figure 5.5e and f). Contrary to that, CSF displacement is assumed to oscillate around a certain central position. This introduces two effects that change the signal attenuation efficiency during DANTE (which were not included in earlier versions of this simulation framework [87,136]): periods

of near-zero velocity reduce the signal attenuation during DANTE, and partial rephasing can occur when the oscillations change direction. This results in the visible change in magnetization evolution between Figure 5.5b (without pulsatility included) and Figure 5.5c (with pulsatility included).

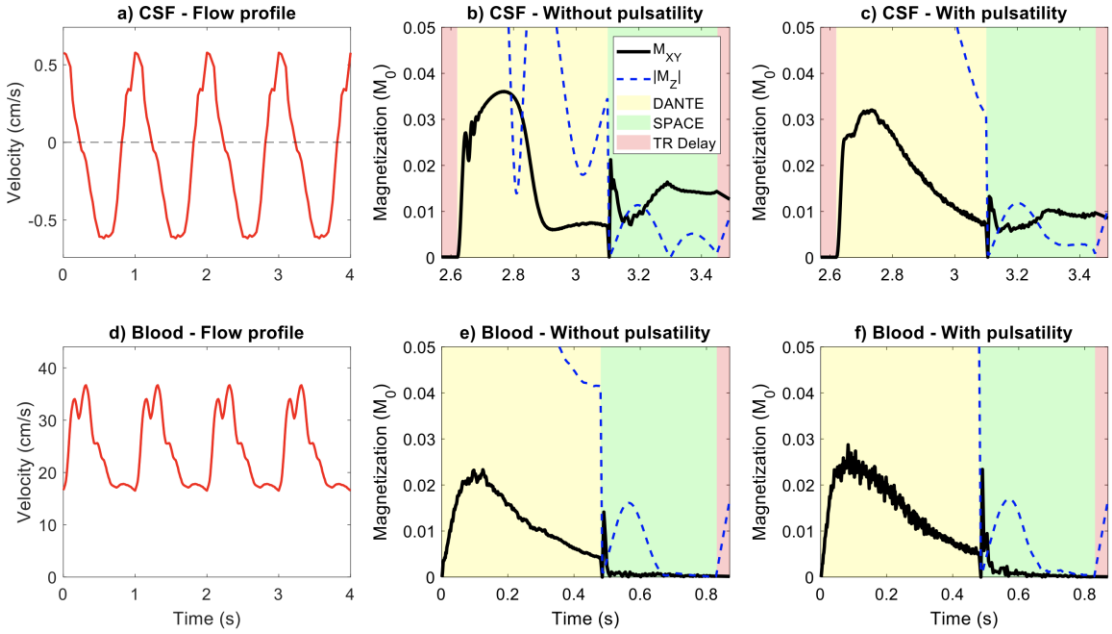

Figure 5.5: Pulsatile velocity variations of **(a-c)** CSF and **(d-f)** blood, and the resulting changes in the simulated magnetization evolution for both tissue types (averaged across 100 random starting points in the cardiac cycle).

5.2.3.3 Diffusion

In addition to spins moving due to flow and pulsation, the effects of diffusion were included (as described by Weigel [79]) for CSF and blood using a diffusion coefficient of 3×10^{-3} mm^2/s, corresponding to free water diffusion at body temperature. Diffusion effects were excluded for vessel wall simulations, although the hypothetical results of including VW diffusion in the simulations will be discussed later (in Section 5.3.1.3). For CSF, the inclusion of diffusion reduces the longitudinal magnetization at the end of the DANTE-preparation, resulting in a 54% reduction in the measured signal during SPACE.

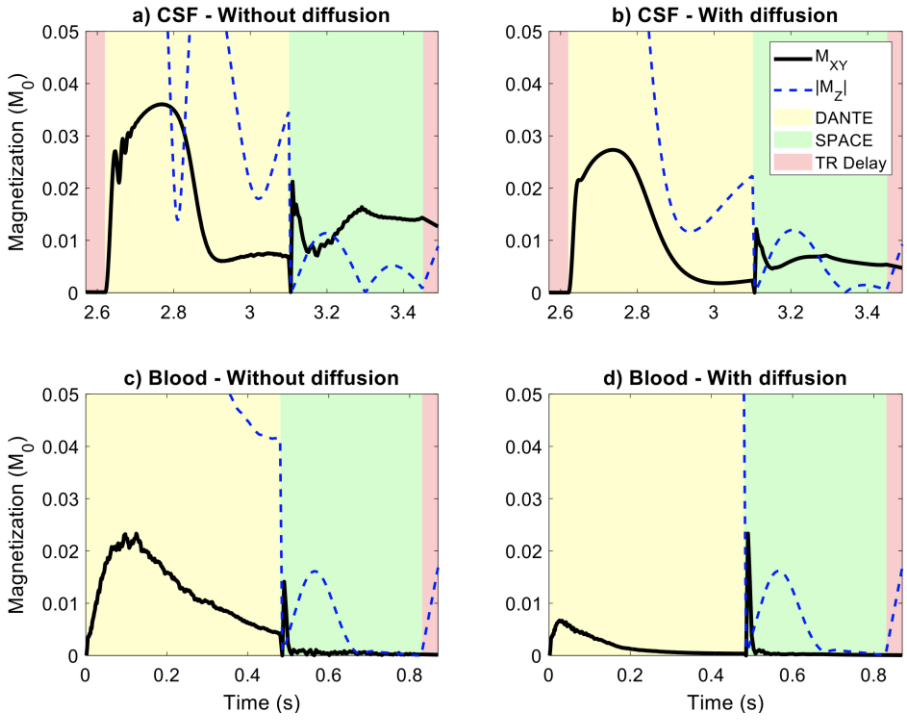

Figure 5.6: The effect of diffusion with a diffusion coefficient of 3×10^{-3} mm^2/s on **(a-b)** CSF simulations and **(c-d)** blood simulations.

5.2.3.4 Flow Trajectory

For blood flow, a typical flow trajectory (downstream from the carotid bifurcation) was included in the simulations to introduce time-varying flow directions relative to the DANTE-gradient vector direction. This flow trajectory was drawn manually on a bright-blood MPRAGE dataset from the database introduced in Chapter 3, as shown in Figure 5.7a. Blood was assumed to flow through this trajectory at the mean flow velocity used in simulations (24 cm/s), resulting in time-dependent variations in the flow direction as the blood moves through the vessel. At each timepoint in the simulations, the resulting angle β_{blood} between the flow direction and the gradient vector was used to modify the effective blood flow velocity along the gradient through multiplication by $\cos(\beta)$. For simplicity, only orientations within the coronal plane were assumed.

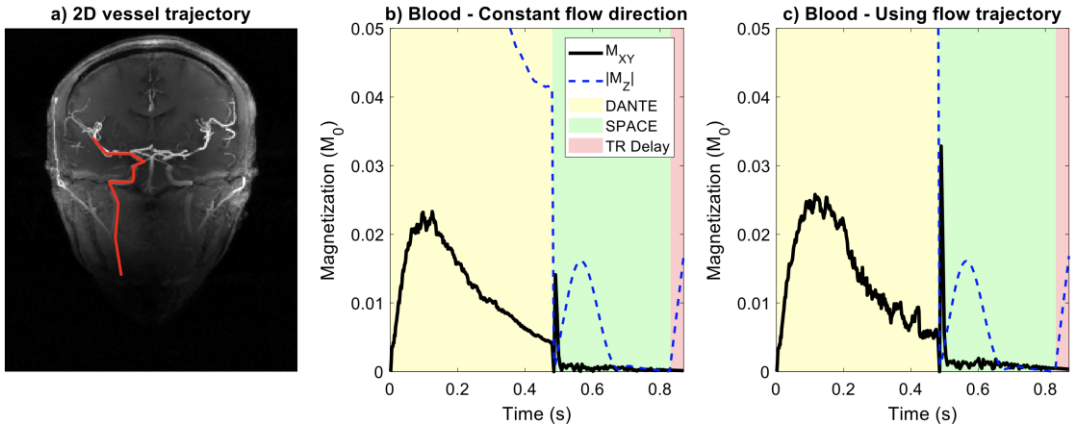

Figure 5.7: The blood flow trajectory used for simulations **(a)**, and the resulting change in the simulated magnetization **(b-c)**.

For CSF, directions of motion (on the relevant timescales) are known to vary throughout the brain [142]. To simplify the simulations while accounting for this variation, the angle β_{CSF} between the CSF flow direction and the gradient vector was fixed as the average angle between a given vector (i.e., the DANTE-gradient vector) and all other possible vector directions (i.e., the possible CSF motion vectors) on a unit semi-sphere:

$$< \beta_{CSF} > = \frac{1}{V_{SS}} \int_{SS} \beta dV = 57.3°. \qquad 5.2$$

5.2.3.5 $B1^+$ Along the Blood Flow Trajectory

$B1^+$ variations in different parts of the vasculature (for blood simulations) as well as near the Circle of Willis (for CSF and vessel wall simulations) were included in the model based on measured $B1^+$ maps. For this, data from the previously presented database of 7T multi-channel $B1^+$ flip angle maps in both the head and the neck (Chapter 3) were used. The blood flow trajectory in Figure 5.7a was used to extract the $B1^+$ values along the vessel trajectories from the $B1^+$ maps, as shown in Figure 5.8a. For CSF and VW, a constant $B1^+$ offset can be added to simulations, for example to model the effects of different pTx RF shims on the achieved CSF suppression.

The measured $B1^+$ values were used in the simulations as a scaling factor between the nominal flip angle (FA) and the effective applied flip angle. For this, the measured values were first normalized by the average $B1^+$ in a rectangular ROI in the middle of the brain to calculate a scaling factor between the nominal flip angle and the effective flip angle at each location. In the neck, with typically very low $B1^+$ at 7T as discussed in Chapter 3, this

effectively reduces the applied flip angles at the start of the DANTE trajectory. This reduces the suppression due to DANTE, which results in a slight increase in the (measured) transverse magnetization during the SPACE readout, as is visible in Figure 5.8c-d.

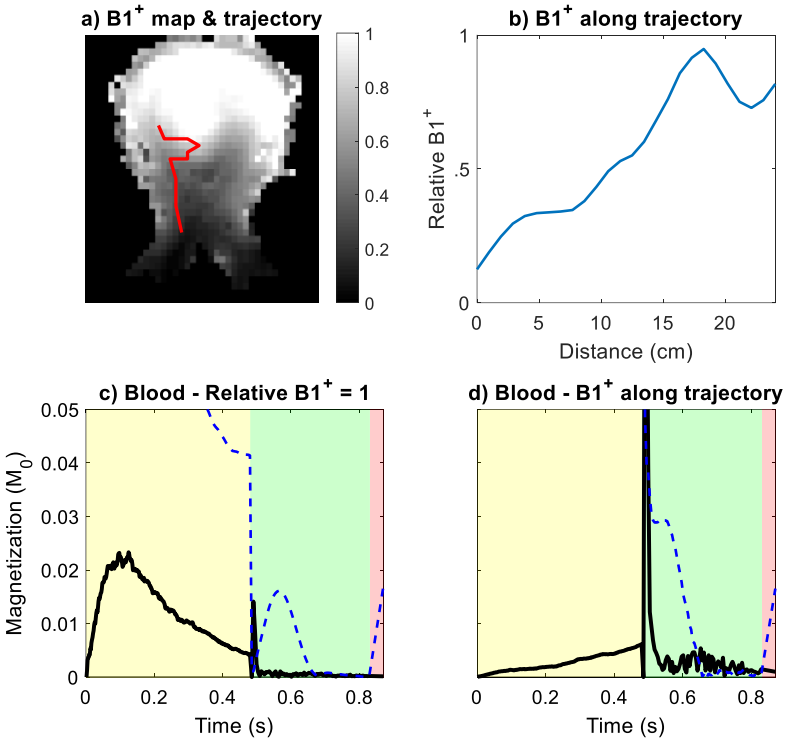

Figure 5.8: B1+ variations along the blood flow trajectory. **(a)** Measured B1+ maps (in CP-mode) were used to provide values along the previously described vessel trajectories, which are shown in **(b)**. This results in a change in the simulated blood magnetization between simulations **(c)** without B1+ effects and **(d)** with B1+ effects.

5.2.3.6 Combined Variations

Sections 5.2.3.1 to 5.2.3.5 discussed how intravoxel velocity averaging, pulsatile motion, diffusion, flow trajectories, and $B1^+$ variation were implemented in the EPG simulations, while showing the isolated effect of each individual addition. Figure 5.9 demonstrates the effect of simultaneously including all described model enhancements. For the examples shown here (using the protocol parameters as proposed by Viessmann et al. [35] and CP-mode $B1^+$ maps), the combined model enhancements result in a 57% reduction in CSF signal and a 27% reduction in blood signal versus the case in which only a basic simulation is performed.

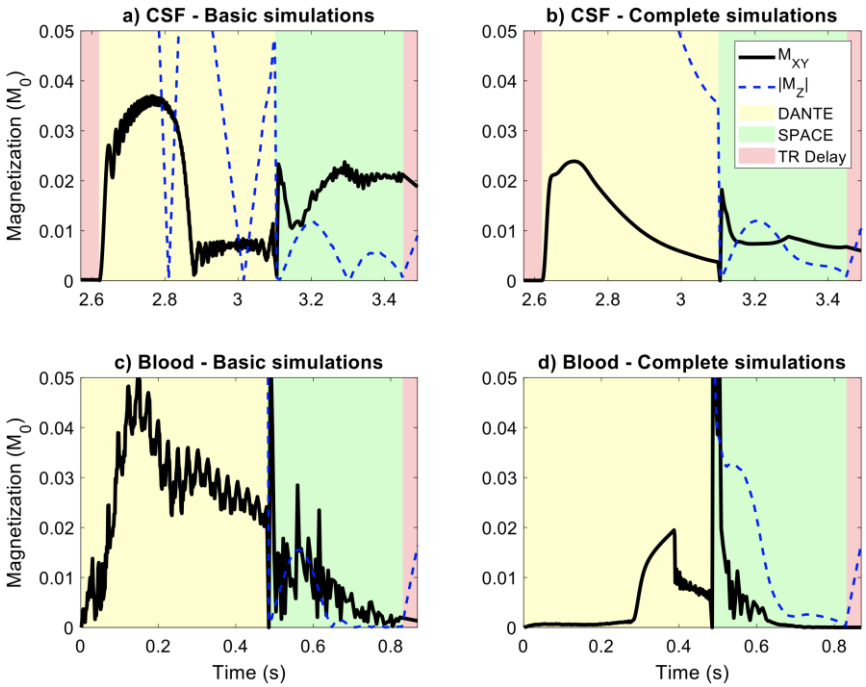

Figure 5.9: The combined effect of intravoxel velocity averaging, pulsatile motion, diffusion, flow trajectories, and $B1^+$ variation on DANTE-SPACE simulations of CSF **(a-b)** and blood **(c-d)**.

Like all CSF and blood simulation results presented in this chapter, the results in Figure 5.9 are shown using a small y-axis range to clearly visualize the changes in the transverse magnetization during the SPACE readout. Figure 5.10 shows the same results as Figure 5.9 but using the full y-axis (ranging from 0 to M_0) to also indicate the changes in the evolution of the longitudinal magnetization during the DANTE-preparation. This shows that in the complete simulation model (Figure 5.10d), the longitudinal magnetization of the blood during DANTE decreases more slowly due to the reduced efficiency of the DANTE-preparation in areas with low $B1^+$.

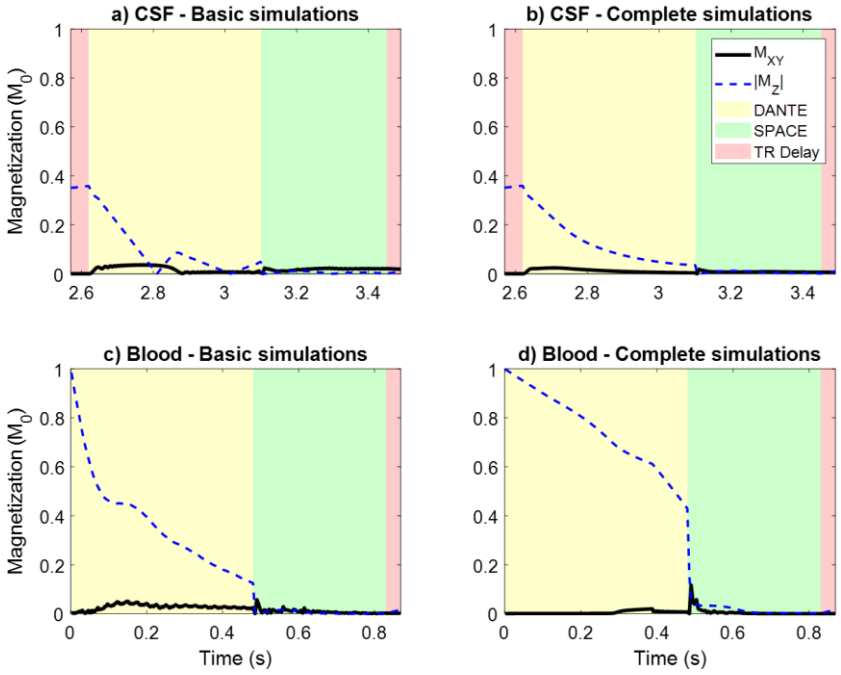

Figure 5.10: The combined effect of intravoxel velocity averaging, pulsatile motion, diffusion, flow trajectories, and B1+ variation on DANTE-SPACE simulations of CSF **(a-b)** and blood **(c-d)**, shown for the full y-axis range.

5.3 Initial Results

5.3.1 Effects of Selected Tissue Properties

The simulations use various tissue-specific properties to distinguish the different tissue types. This includes T1 and T2 relaxation times, mean velocities of flow or pulsation, flow directions, the amount of intravoxel dephasing, and the diffusion coefficients. For VW, CSF, and blood, each of these values was carefully chosen with the aim of accurately representing the resulting signal behaviour. To assess the extent to which the simulations depend on the exact choice of tissue parameters, and to ascertain that the results are robust to small changes to the selected values (e.g., due to measurement uncertainty), this section compares simulations using different tissue properties.

5.3.1.1 T1 & T2 Relaxation Times

As described in Section 5.2.1, the T1 and T2 values for VW, CSF, and blood were based on various measurement results from the literature. Each of the resulting values has a certain amount of measurement uncertainty (up to 28% [141]). Therefore, Figure 5.11 compares the results of simulations for all three tissue types where the T1 and T2 values are varied between the standard value ± 30%. This indicates that the results are largely independent of the T1 of blood and the T2 of both CSF and blood. The T2-dependence

of the vessel wall signal is consistent with the T2-weighting of the SPACE readout, which is calculated based on the vessel wall relaxation times [35]. Despite this T2-weighting, Figure 5.11 also shows some T1-dependence of the VW and CSF signals. This is a result of the DANTE-preparation, during which a higher T1 results in increased suppression of the longitudinal magnetization as well as reduced longitudinal magnetization recovery during the TR delay. Because of its higher T1, and increased DANTE sensitivity, this T1-dependence is more pronounced in CSF. However, the resulting CSF signal remains much smaller than the VW signal for all simulated values.

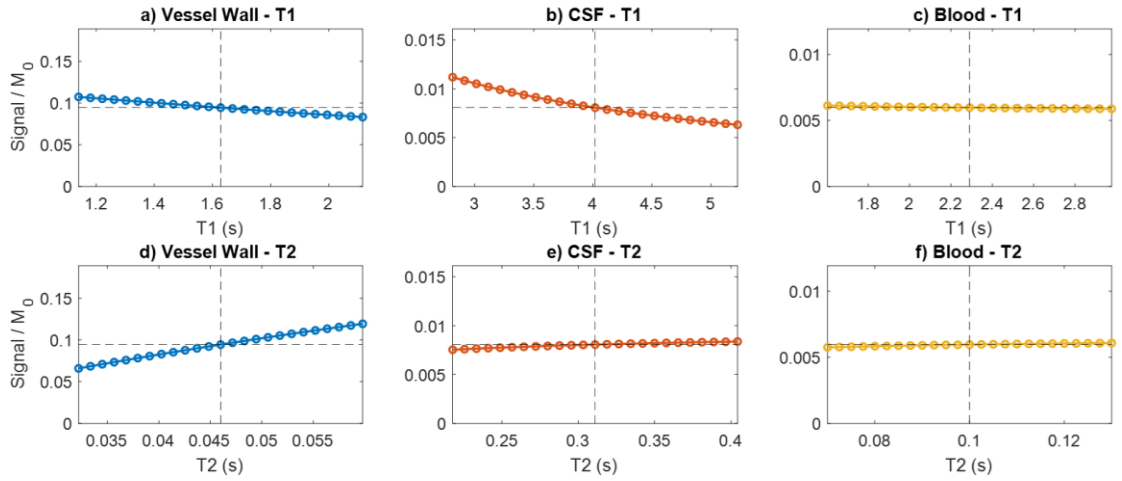

Figure 5.11: Simulation results when using different T1 and T2 relaxation times. Results are shown for each tissue type for the standard values ± 30% (x-axes). Different y-axes are used for the different tissue types, all of which are scaled from 0 to twice the simulated signal using the standard (T1/T2) values. Dashed lines indicate the standard T1/T2 values and their corresponding simulated signal.

5.3.1.2 Flow Velocity

Figure 5.12 shows the effect of different average flow velocities on the simulated VW, CSF, and blood signal. As expected when using DANTE, higher velocities result in increased signal attenuation for all tissues. However, the velocity at which the signal converges differs between tissue types due to their different relaxation properties and, in particular for blood, $B1^+$ effects and flow directions. For example, the required velocities to reach a signal of less than 0.02 M0 are around 0.1 cm/s for VW, 0.2 cm/s for CSF, and 1.6 cm/s for blood.

This required velocity is the highest for blood because of the velocity responses of both DANTE and SPACE. During DANTE, the lower $B1^+$ experienced by blood flowing in from the neck means that higher velocities are required for DANTE to be effective. During SPACE, the flow direction of blood is nearly perpendicular to the DANTE gradient direction. As a result, higher velocities are required to obtain the inherent black-blood SPACE contrast (even without DANTE). However, since the typical flow velocity of

blood is still substantially higher than the required velocity to achieve black-blood contrast, this is not a limitation in practice.

For CSF, the simulated average velocity of 0.37 cm/s [23] is closer to the critical velocity required to achieve sufficient signal suppression, so increases in CSF signal level can be expected with slight changes in the average velocity or flow direction. For the vessel wall, signal attenuation already occurs at very low velocities. This is not desirable for VWI and indicates that observed variations in vessel wall signal *in vivo* might be explained by the presence of slowly pulsating vessel wall tissue. This will be further discussed in Section 5.3.3.

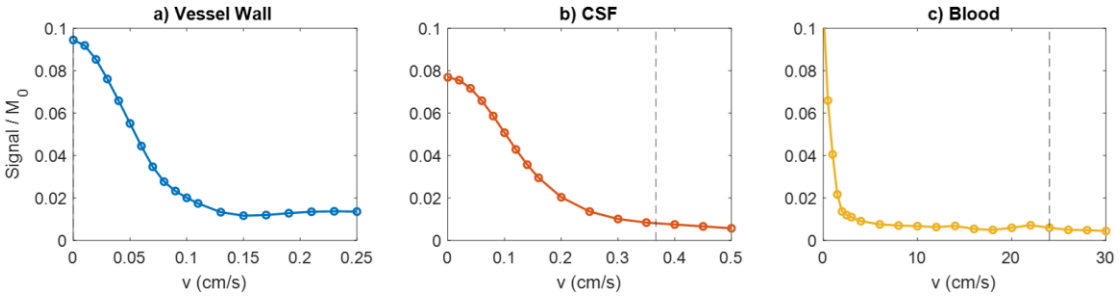

Figure 5.12: The effect of the average flow velocity magnitude on the simulated signal of **(a)** vessel wall, **(b)** CSF, and **(c)** blood. Dashed lines indicate the velocities generally used in the simulation model (0 cm/s for the vessel wall).

5.3.1.3 Other Motion Processes

The effects of assuming various values for intravoxel dephasing, the direction of CSF pulsation, and the presence of VW diffusion are shown in Figure 5.13.

Figure 5.13a indicates that although velocity averaging substantially affects the simulated signal of blood (compared to using $\sigma = 0$), the exact choice of (non-zero) value for σ does not have a large effect on the resulting averaged signal.

The direction of CSF pulsation (Figure 5.13b), defined as the angle between the pulsation direction and the DANTE gradient vector, results in substantially reduced CSF suppression for near-$90°$ angles. Since a $90°$ angle means that there is no effective velocity along the gradient direction, this corresponds to the simulation with $v_{CSF} = 0$ cm/s in Figure 5.12b.

VW diffusion, as shown in Figure 5.13c, is not included in the general simulations because it is challenging to select an appropriate diffusion coefficient for vessel wall tissue on the time-scales and gradient directions appropriate to the DANTE-SPACE sequence. However, it can be assumed to be much smaller than the value for free water ($3\ \mu m^2/ms$),

for which Figure 5.13c suggests that there is a limited effect on fully stationary VW (yellow), and a negligible effect on slowly pulsating VW (purple). Therefore, a diffusion coefficient of 0 was used for VW for all simulations.

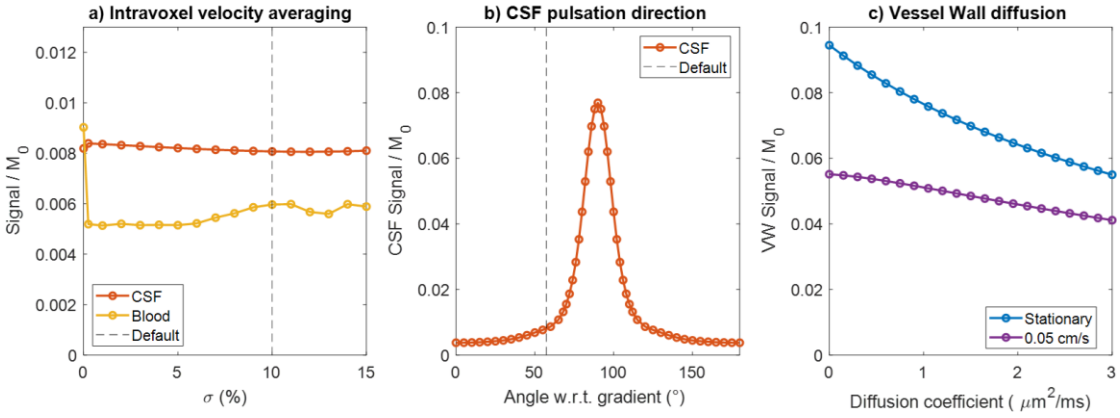

Figure 5.13: The effects on the simulations of the selected parameter value for **(a)** intravoxel velocity averaging, **(b)** the CSF pulsation direction, and **(c)** the vessel wall diffusion coefficient (for both moving and slowly pulsating VW, shown up to the diffusion coefficient corresponding to free water diffusion). Dashed lines indicate the default values (0 for (c)).

5.3.2 Effects of Sequence Parameters

This section compares the effects of several DANTE-SPACE parameters on the simulated signal levels and the resulting VW/CSF and VW/blood contrasts. Results are presented for the protocol used by Viessmann et al. [35], while changing one parameter at a time. The results provide information about ways to improve contrasts as well as insight into the different underlying contrast mechanisms. Note that the results presented here are mainly intended to provide indications of the general effects of the different parameters. Chapter 6 aims to provide a more comprehensive optimization by simultaneously considering multiple parameters while also considering the use of different pTx RF shims and slowly pulsating vessel walls.

5.3.2.1 Sequence Timing Parameters

Figure 5.14 shows the effect of changing the TR, DANTE interpulse time, or SPACE echo spacing. The TR (of 2.62 s) was used in the calculation of the SPACE flip angle train (which aims to maximize the VW signal efficiency), and Figure 5.14a confirms that it also provides optimized contrast when including DANTE-preparation. Shorter TRs reduce the VW signal recovery during the TR delay, whereas longer TRs introduce longer scan times without proportional signal benefits.

The signals of all three tissues are mostly independent of the DANTE interpulse time beyond a certain minimum duration (Figure 5.14b). For the SPACE interpulse time,

however, the results in Figure 5.14c suggest that using the (hardware-restricted) lowest possible value provides an increase in VW signal efficiency, as expected from the literature [28]. Furthermore, a shorter echo time could also allow for further improvement of the signal efficiency by allowing, within a given echo train duration, the use of more SPACE echoes.

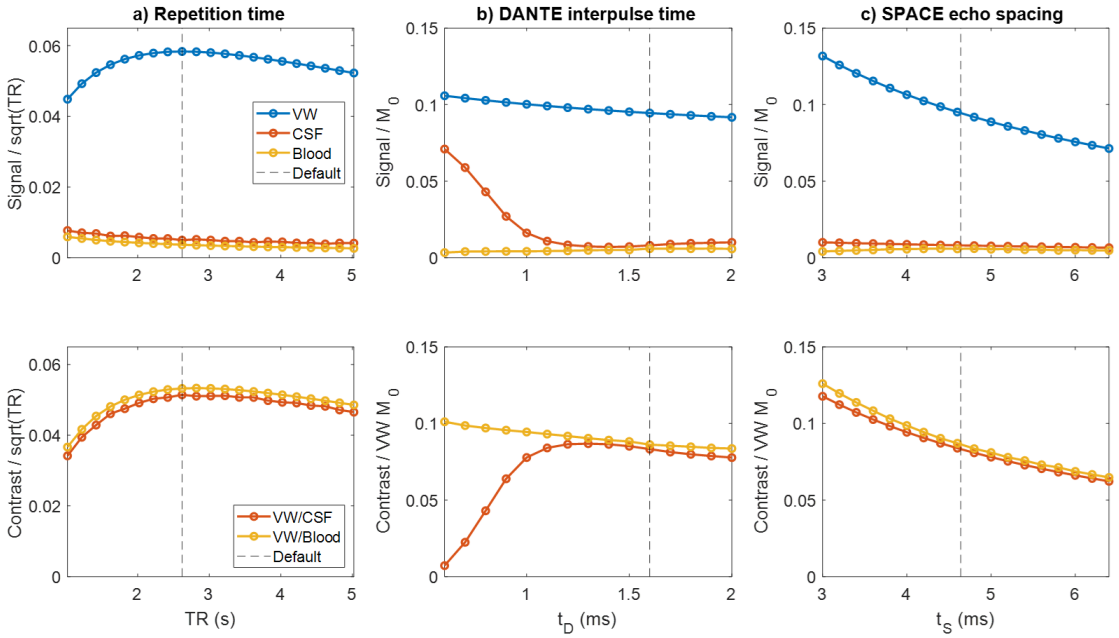

Figure 5.14: Simulated DANTE-SPACE signal levels (top row) and resulting contrasts (bottom row) when using a different **(a)** repetition time, **(b)** DANTE interpulse time, or **(c)** SPACE echo spacing. The results in (a) are presented in terms of "Signal / √(TR)" such that the highest value corresponds to the parameters that provide the highest contrast for scan time-matched acquisitions.

5.3.2.2 Other Parameters

The effects of three further DANTE parameters are compared in Figure 5.15. For all three parameters (flip angle, number of pulses, and gradient strength), adequate CSF suppression is not achieved until sufficiently high values of these parameters are used. However, still higher values for the FA and the number of pulses result in reduced VW signal, and so parameter values for these two should be chosen to be above the CSF-suppression threshold, but no more. For all three parameters used here, the default values as used by Viessmann et al. [35] are close to the optimum values based on Figure 5.15. However, Chapter 6 will show that these optima change when considering slowly pulsating vessel walls and when optimizing multiple parameters simultaneously.

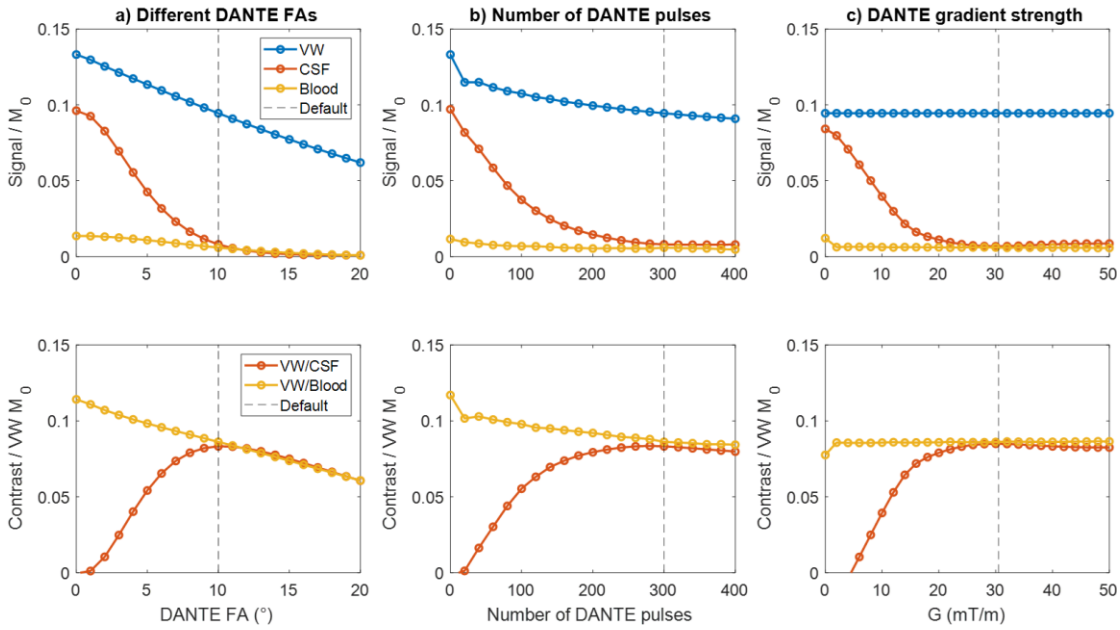

Figure 5.15: Simulated DANTE-SPACE signal levels (top row) and resulting contrasts (bottom row) when changing the DANTE **(a)** flip angle, **(b)** number of pulses, or **(c)** gradient strength.

5.3.3 Vessel Wall Motion

5.3.3.1 Methods

So far, the simulations in this chapter assumed fully stationary vessel walls. However, preliminary *in vivo* acquisitions (presented in Ref. [136]) showed signal variations in the vessel wall, which can be explained in simulations by including very slow pulsation of vessel wall tissue (as found in Section 5.3.1.2). To estimate the average velocity of this vessel wall pulsatility and to include it in subsequent simulations, this section compares results from preliminary *in vivo* acquisitions to VW simulations assuming various velocities. These preliminary data were acquired on a Siemens (Erlangen, Germany) Magnetom 7T scanner using a 1Tx/32Rx head coil. Data were acquired from 5 healthy volunteers, using up to three different T2-weighted DANTE-SPACE protocols:

1. The protocol presented by Viessmann et al. [35], which uses 300 DANTE pulses of 10° (acquired for all 5 subjects);
2. The same protocol but using 200 DANTE pulses of 9° (acquired for all 5 subjects); and
3. The same SPACE protocol but without DANTE preparation (acquired for 3 out of 5 subjects).

Using these data, the average VW velocity was estimated such that the estimated signal intensities from simulations agreed with observed (experimental) vessel wall signal changes

in hand-drawn VW masks. To quantitatively compare *in vivo* measurements to simulations, both scan data and simulations were expressed relative to the values for stationary VW signal intensity without DANTE preparation. This was used to obtain an consistent separate reference point with minimal velocity-dependence due to the absence of velocity-dependent DANTE effects (equivalent to the case with 0 DANTE pulses in Figure 5.15b). For simulations, this was calculated by expressing the simulated VW signal (S_{sim}) as a percentage of the signal from a simulation for stationary VW without DANTE ($S_{NoDante}$):

$$S_{sim}(\%) = \frac{S_{sim}(M_0)}{S_{NoDante}(M_0)} * 100\%. \quad 5.3$$

For *in vivo* acquisitions, the 80th percentile of the measured signal intensity values in VW voxels in acquisitions without DANTE ($S_{NoDante,80\%}$) was used as a benchmark for the signal level for stationary VW tissue. From that value, the relative value in each voxel (and for any protocol) was calculated as

$$S_{scan}(\%) = \frac{S_{scan}(SNR)}{S_{NoDante,80\%}(SNR)} * 100\%. \quad 5.4$$

Note that here, the SNR is calculated from the standard deviation of a noisy ROI in the corner of the 3D image. Calculation in SNR units from direct noise measurements (which will be used in Chapters 6 and 7) was not possible in this case since the raw data for those preliminary acquisitions was not stored. However, this does not affect the resulting relative signal values ($S_{scan}(\%)$) which were used for the analysis here.

The resulting signal distributions were then compared to estimate the average velocity of vessel wall pulsation, which will be used to include pulsating vessel wall as an additional tissue type in simulations shown in subsequent chapters.

5.3.3.2 Results

First, simulations were performed using the protocol with 300 DANTE pulses of 10°, and the protocol with 200 DANTE pulses of 9°. In those simulations, the VW pulsation was assumed to follow the same pattern as CSF (Figure 5.5a) since it results in a net-zero displacement during each full cardiac cycle. For both protocols, the resulting simulated VW signal at different average velocities is shown in Figure 5.16. As expected, the protocol with less DANTE-preparation (shown in orange) results in higher VW signal with less motion sensitivity.

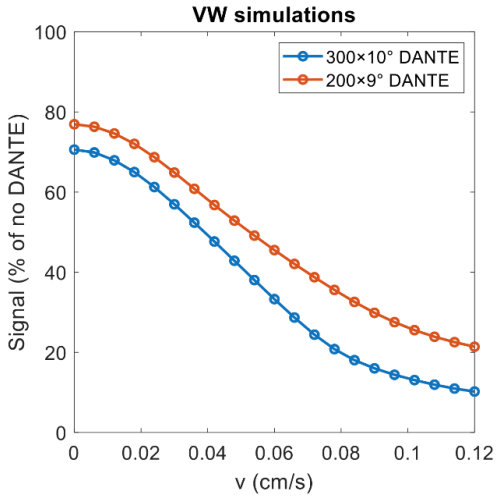

Figure 5.16: The simulated signal of VW pulsating at different average velocities in simulations with two different DANTE-preparation settings. Values are expressed relative to the simulation result for stationary VW without DANTE preparation (using Equation 5.3), which corresponds to 0.13 M0.

Importantly, Figure 5.16 indicates that for each protocol, each signal value corresponds to a single (non-degenerate) vessel wall velocity. This means that if *in vivo* vessel wall signal intensity values are also expressed relative to the signal intensity in non-DANTE acquisitions (using Equation 5.4), it should be possible to directly correlate these relative values to the corresponding average velocity in simulations.

Therefore, Figure 5.17a shows the relative vessel wall signal levels (Equation 5.4) measured from preliminary data in 5 healthy volunteers acquired using 300 DANTE pulses of 10°, and Figure 5.17b shows the corresponding distribution of velocity values that are implied by these signal levels when translating simulated signal to velocity via Figure 5.16. This indicates an average vessel wall velocity of 0.051 ± 0.021 cm/s.

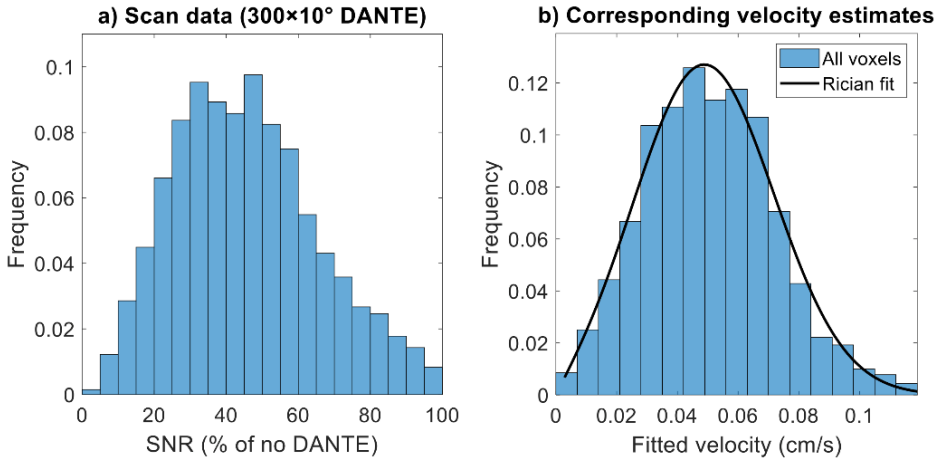

Figure 5.17: Distribution of **(a)** vessel wall signal levels in 5 healthy volunteers in acquisitions using 300 DANTE pulses of 10°, and **(b)** the corresponding velocity values in simulations. Values in (a) are expressed relative to the 80th percentile of the vessel wall signal in acquisitions without DANTE preparation (using Equation 5.4).

The corresponding results for *in vivo* data acquired from the same 5 volunteers using 200 DANTE pulses of 9° are shown in Figure 5.18. As expected based on the simulation results in Figure 5.16, Figure 5.18a shows that more VW signal is retained when using fewer DANTE pulses with lower flip angles. The resulting VW velocity estimates in Figure 5.18b suggest an average VW velocity of 0.057 ± 0.026 cm/s, which is pleasingly close to agreeing with the estimate made using 300 DANTE pulses of 10°.

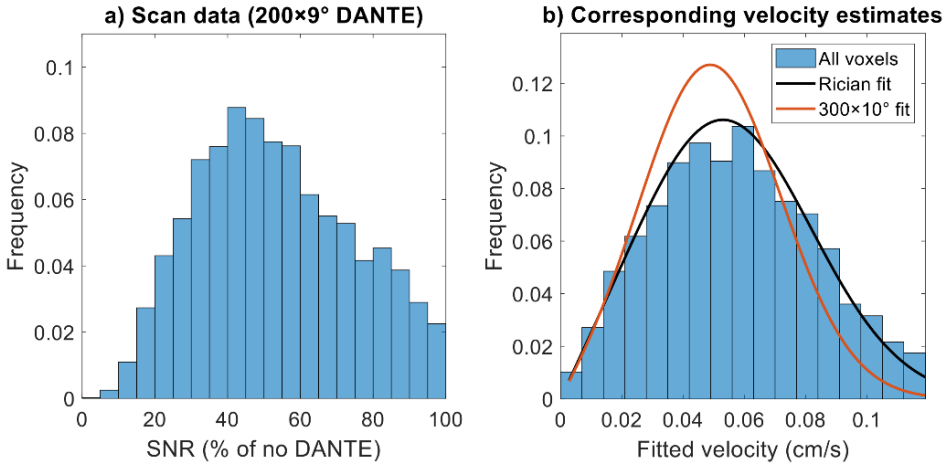

Figure 5.18: Distribution of **(a)** vessel wall signal levels in 5 healthy volunteers in acquisitions using 200 DANTE pulses of 9°, and **(b)** the corresponding velocity values in simulations. Values in (a) are expressed relative to the 80th percentile of the vessel wall signal in acquisitions without DANTE preparation (using Equation 5.4). The orange curve in (b) shows the Rician fit based on the data in Figure 5.17b for comparison.

Given the close agreement between these two estimates of the vessel wall velocity we chose to use the average (0.054 cm/s) for the final simulations. When assuming the VW pulsation to follow the same pattern as CSF (Figure 5.5a), as was used in the simulations in Figure

5.16, this average velocity of 0.054 cm/s corresponds to a maximum displacement of around 200 μm.

5.4 Discussion

This chapter presents an EPG-based DANTE-SPACE simulation framework. By including various physiological and spatial variations to enhance the model, it aims to accurately reproduce the contrast mechanisms for the case of *in vivo* acquisitions. This helps explain the mechanisms behind various observed contrasts in acquired data and provides further understanding on how the sequence can be modified to achieve improved contrasts.

Initial validation

The performance of the basic simulation framework design was validated by first separately comparing the performance of the DANTE- and the SPACE-module relative to literature results, which found good agreement for both. For VW tissue, the SPACE module provides the desired constant magnetization in the middle of the readout train when simulating without DANTE (Figure 5.2b). However, the addition of DANTE (Figure 5.2c) introduces a magnetization decrease in the middle of the readout. This reduces the VW signal level, which is expected when using DANTE [31,35], but also results in a slight reduction in the VW sharpness (broadening of the point spread function). To retain the desired sharpness, future work could account for the magnetization history effects due to DANTE in the calculation of the SPACE flip angle pulse train.

Additional variations to the simulations

The additional variations to the simulations that were introduced in Section 5.2.3 affect the simulation results in multiple ways. Simulations with intravoxel velocity averaging (Figure 5.4c and f) increase the temporal stability of the magnetization evolution of moving tissue, resulting in a reduced simulated signal and improved robustness against small changes in the selected mean velocity. Without this velocity averaging, the magnetization over time shows rapidly fluctuating transverse magnetization, similar to what Li et al. [31] showed in DANTE simulations at different isolated velocity values (as reproduced in Figure 5.1a).

The introduction of more realistic time-varying pulsatile velocity variation (Section 5.2.3.2) mainly affects the simulations of CSF, which is assumed to oscillate around a central

location. This introduces periods of near-zero absolute velocity (which reduce the signal attenuation during DANTE), as well as partial rephasing when the oscillations change direction. In addition to those changes due to pulsation, the inclusion of diffusion (Section 5.2.3.3) reduces the longitudinal magnetization of the CSF at the end of the DANTE-preparation, substantially reducing the measured signal during SPACE.

The addition of a typical blood flow trajectory in Section 5.2.3.4 only introduces minor changes to the resulting blood signal, as the effective blood flow velocity (along the gradient direction) remains sufficiently high despite the different flow directions. However, the differences in $B1^+$ along the flow trajectory substantially reduce the efficiency of DANTE in low-$B1^+$ areas. In quadrature (CP) mode at 7T, this increases the measured transverse magnetization during the SPACE readout (Figure 5.8b-c).

All combined, the additional variations to the simulations presented in Section 5.2.3 result in a 57% reduction in CSF signal and a 27% reduction in blood signal (for the T2-weighted 7T protocol used by Viessmann et al. [35]) relative to not including these enhancements.

Magnetization transfer effects were not included in the presented framework. Future work could use the EPG framework with magnetization transfer effects [143] to further improve the *in vivo* accuracy of the simulations.

Simulations with different tissue properties

The simulations using various T1 and T2 relaxation times (Figure 5.11) indicate that the results are robust to small changes in T1 or T2 due to uncertainty in their measurements. Furthermore, while Figure 5.11 confirms that the VW signal is predominantly T2-dependent, it shows that the DANTE-preparation also introduces some T1-weighting. Therefore, when using modified protocols, it is important to include simulations for relevant pathologies to ensure that the contrast between healthy and diseased vessel wall tissue remains consistent.

Figure 5.12 indicates that the simulation results are mostly independent of the exact blood flow velocity due to the high flow velocity of blood. However, the VW and CSF simulations indicate that their respective 'critical' velocities (where the resulting signal rapidly decreases) are close to their typical velocities. Therefore, small variations in the CSF velocity (Figure 5.12b) and direction (Figure 5.13b) can result in substantial reductions in CSF suppression, whereas slow pulsation of the vessel wall would reduce the VW signal.

Both of those simulation results are consistent with previous *in vivo* observations for T2-weighted DANTE-SPACE, which showed heterogeneous signal levels in both the VW and the CSF.

The final tissue parameter discussed in Section 5.3.1 is the VW diffusion coefficient, which we assumed to be zero. This was chosen since diffusion coefficients in soft tissue in general (and especially in the narrow vessel walls) are much lower than those of CSF and water [144], while no clear literature values are available for the arterial walls in the Circle of Willis. Furthermore, literature in thicker arteries suggests substantial variation in diffusion properties across different parts of the vessel walls and along different gradient directions [145], introducing additional complexity in selecting a single ideal value. Therefore, when optimizing protocols using simulations, one could consider simulating using a range of different low diffusion coefficients. However, since this adds additional complexity and computation time to the optimizations, while Figure 5.13c suggests it only has a limited effect on the simulated VW signal, a diffusion coefficient of zero for vessel wall was used in this work.

Effects of sequence parameters

The results presented in Section 5.3.2 indicate that the 7T protocol used by Viessmann et al. [35] uses reasonable sequence parameters in terms of both VW/CSF and VW/blood contrast, with different values often resulting in reduced contrasts. In particular, the DANTE flip angle, number of pulses, and gradient strength all require sufficiently high values to achieve sufficient CSF suppression, while moving to even higher values has the detrimental effect of reducing the VW signal. However, all results in Section 5.3.2 were limited to simulations for stationary vessel walls, do not consider the effects of varying multiple parameters simultaneously, and do not consider the possible benefits of modifying the $B1^+$ field using pTx RF shims. Therefore, Chapter 6 will discuss a more comprehensive optimization of the T2-weighted DANTE-SPACE sequence at 7T.

Vessel wall motion

Figure 5.12a indicated that very slow VW motion could result in variable VW signal, which could explain the observed *in vivo* VW signal heterogeneity. Section 5.3.3 further examines this hypothesis by comparing VW simulations across a range of simulated velocities to the corresponding acquired signal distributions using two different DANTE protocols. This

indicates an average VW velocity of 0.051 ± 0.021 cm/s based on data with 300 DANTE pulses of 10° (Figure 5.17) and 0.057 ± 0.026 cm/s based on data with 200 DANTE pulses of 9° (Figure 5.18). These values are slightly different, while the underlying vessel dynamics should be the same. This could be explained by the simplifying assumption that all signal difference in the VW is a result of the VW pulsation, which does not account for signal variation due to partial volume effects, sensitivity effects, and different directions of motion relative to the DANTE gradients. Despite this, the resulting values are very similar, and the overall average value of 0.054 cm/s will be used as an approximate velocity of pulsating vessel wall in future simulations in this thesis. Furthermore, the resulting maximum displacement of 200 µm is consistent with displacement simulations in non-stenotic external iliac arteries [146], which have a similar wall thickness to the MCA. This again indicates that the value of 0.054 cm/s provides an adequate approximation. However, this VW motion approximation is based on data from healthy volunteers. A lower VW velocity might be expected in clinical populations due to reduced vessel wall flexibility resulting from pathology and aging [147].

In simulations using the protocol by Viessmann et al. [35], VW moving at 0.054 cm/s is predicted to reduce the resulting VW signal by 46%, leading to a reduction in VW/CSF contrast of 51%. When using simulations to optimize a protocol for achieved contrasts, this introduces a significant new constraint that was not accounted for in previously presented DANTE-SPACE simulation models.

In the work presented here, vessel walls were assumed to pulsate using the same time-varying pattern as CSF (Figure 5.5a). This was selected since it results in a net-zero displacement during each full cardiac cycle, which is expected for both CSF and VW but not for blood. However, it might be possible to represent the VW pulsation more accurately using other profiles.

Computational considerations

Currently, a single simulation with the computational hardware used in this thesis takes about 0.16 s for static VW (2 TRs without velocity averaging), 9.6 s for pulsating VW (2 TRs with velocity averaging), 3.6 s for blood (1 TR with velocity averaging), and 7.9 s for CSF (2 TRs with velocity averaging). The computation times of simulations with velocity averaging could be substantially reduced (by at least an order of magnitude) by parallelizing the individual simulations at each velocity. However, in this thesis the simulations for

different datapoints in parameter sweeps were parallelized instead (with each parallel CPU computing a few full simulations instead of parts of all simulations), as a more straightforward way of achieving a similar net acceleration.

The MATLAB code for the simulation framework is openly available online at git.fmrib.ox.ac.uk/ndcn0873/dantespace_epg. The main simulation tool is epg_dantespace.m, which runs the actual simulations. The script example.m shows some short examples of how to run the simulations after initializing both the desired sequence parameters (set_dantespace_parameters.m) and the tissue properties (set_tissue_parameters.m). Finally, a single script that can be used to reproduce all figures in this chapter is included (simulations_chapter.m), as well as the required underlying data ($B1^+$ map and vessel trajectory) and other tools. Running simulations_chapter.m requires the MATLAB *Image Processing*, *Statistics and Machine Learning*, *Curve Fitting*, and *Parallel Computing* toolboxes.

5.5 Conclusion

An EPG-based DANTE-SPACE simulation framework is presented that includes physiological and spatial variations to accurately reproduce *in vivo* contrast mechanisms. This helps explain observed contrasts in acquired data, such as the VW signal heterogeneity which can be explained by simulations with very slowly pulsating vessel walls. Finally, this simulation framework facilitates a more comprehensive optimization of the DANTE-SPACE sequence parameters.

6

Optimized DANTE Preparation for T2-Weighted DANTE-SPACE Vessel Wall Imaging at 7T

Key Conclusions

- **Optimized DANTE parameters improve the achieved DANTE-SPACE contrast compared to a previous literature protocol**
- **The adoption of a neck-and-CoW RF shim during DANTE provides additional suppression of inflowing blood, further improving delineation of the inner vessel wall**

6.1 Introduction

Large-artery intracranial occlusive disease is a common, and possibly the most prevalent, cause of stroke globally [148]. This mainly relates to various arteries in and around the Circle of Willis (CoW), with the distal internal carotid arteries (ICAs), basilar artery (BA), and middle cerebral arteries (MCAs) being the most involved [149,150]. Intracranial vessel wall imaging (VWI) aims to characterize the location, size, and composition of intracranial pathology such as plaque burden in arterial vessel walls. As discussed in Section 1.3, MR VWI can non-invasively provide structural information about intracranial plaques, as well as information about their composition. In general, MR VWI aims to delineate both the inner and the outer boundary of the vessel wall through suppression of signals both within and around the vessel walls [133], while maintaining high vessel wall signal [26]. Additionally, MRI-based VWI can distinguish different plaque components through variable signal contrasts relative to healthy vessel wall tissue, such as signal hyper- and hypo-intensities in intraplaque haemorrhages or lipid cores, respectively, for T2-weighted VWI [20]. For extracranial cervical VWI, T1-weighted, T2-weighted, and proton density-weighted acquisitions are routinely combined to differentiate between stable and unstable atherosclerotic plaques by identifying the major plaque components [20,26,44]. However, intracranial VWI using acquisitions with multiple weightings is more challenging due to

long acquisition times required to achieve the desired contrasts and resolutions (often <0.4 mm for vessel walls around the Circle of Willis [25,26]). Because of their inherently longer scan times and higher native CSF signal, T2-weighted acquisitions are generally not included in clinical intracranial VWI, limiting the acquired contrasts to T1-weighted acquisitions [20,36,41,45].

The DANTE-SPACE sequence has previously been introduced for T2-weighted VWI at 7T [35]. It achieves intracranial vessel wall delineation using DANTE preparation for suppression of blood and CSF followed by a variable flip angle turbo-spin-echo (SPACE) readout module for vessel wall depiction. It was introduced by Viessmann et al. [35], who optimized the SPACE flip angle train for sharp vessel wall depiction and used Bloch simulations to propose an initial DANTE implementation. However, they also reported substantial inter- and intrasubject variations in the achieved contrasts, as well as a 50% reduction in the wall-to-lumen CNR compared to regular SPACE. These limitations to the contrast levels and their homogeneity could hinder the clinical implementation of this T2-weighted VWI sequence, which requires consistently high signal levels for clear delineation and visualisation of vessel wall architecture and pathology. Furthermore, the limited contrasts restrict further improvements to the resolution and scan time of the sequence.

As discussed in the previous chapter, we developed a simulation framework for the DANTE-SPACE sequence. Previous literature often also used simulations for DANTE optimization [35,36,39,40,133–135], but excluded the effects physiological processes such as CSF and vessel wall pulsation and variations in the $B1^+$ field. By including these, we hope to further understand the signal behaviour of the sequence and to optimize the sequence for improved vessel delineation.

Furthermore, including measures of $B1^+$ inhomogeneity in the simulations makes it possible to assess the effects of reduced $B1^+$ efficiency in the carotid arteries on the suppression of blood flowing into the CoW. Preliminary data showed some residual blood signal, which could be explained by this reduced $B1^+$ in upstream blood. Based on simulation results, we propose an additional optimized DANTE-SPACE protocol which uses a pTx RF shim during DANTE for improved $B1^+$ coverage in the vessels in the neck.

Protocols optimized both with and without the use of a pTx RF shim are proposed based on simulation results and are then validated *in vivo*. The performance of the different protocols is compared using inner, outer, and overall vessel acutance (i.e., perceived sharpness) which is calculated from a semi-automatic vessel delineation approach.

6.2 Methods

6.2.1 Simulations

DANTE-SPACE signal levels for blood, CSF, and the vessel wall were simulated using the EPG-based simulation framework and 7T relaxation parameters described in Chapter 5. Blood was simulated with a mean flow velocity of 24.0 cm/s (with pulsating variation for arterial blood as shown in Figure 5.5d) and a diffusion coefficient of 3×10^{-3} mm^2/s, and CSF was simulated with a mean velocity of 0.367 cm/s (with CSF-specific pulsating variation as shown in Figure 5.5a) and a diffusion coefficient of 3×10^{-3} mm^2/s. For vessel wall motion two different scenarios were considered: firstly a fully stationary vessel wall, and secondly a slowly pulsating vessel wall (based on the results described in Section 5.3.3). For the pulsating vessel wall, a mean velocity of 0.054 cm/s was used with the CSF-specific pulsating variation. Diffusion effects were ignored for vessel wall simulations based on initial simulations indicating only minimal effects of low diffusion coefficients on vessel wall signal.

Simulations were used to compare the achieved contrasts when using different protocol parameters. Using this approach, new parameters were proposed with the aim of increasing the lowest achieved contrasts without reducing the other (higher) contrasts.

Additional simulations were performed using both the proposed parameters and the original (Viessmann et al. [35]) DANTE-SPACE parameters to ensure consistent contrast behaviour between healthy vessel wall and various plaque components (fibrous cap, lipid core, and intraplaque haemorrhage). Relaxation times for plaque components at 7T are available for formalin-fixated *ex vivo* brains [151], but these have been shown to provide substantially reduced relaxation times compared to the *in vivo* case [152,153]. Therefore, *in vivo* plaque component T2 relaxation times measured at 3T [21] were scaled based on the T2 of healthy vessel wall at both 3T and 7T [138] to approximate the expected T2 times at 7T. For T1, *ex vivo* formalin-fixated values [151] were scaled using the ratio between the T1 of *in vivo* [138] and formalin-fixated [151] healthy vessel wall tissue. This resulted in the following T1/T2 estimates at 7T: fibrous cap 1796/47 ms; lipid core 3129/31 ms; and intraplaque haemorrhage 2290/89 ms. Note that those values are extrapolated from either *ex vivo* data (for T1) or 3T measurements (for T2). In particular, the relaxation properties of lipid components in atherosclerotic plaques are known to have a temperature dependence due to the differences between liquid and crystallized cholesterols [154]. Since

the relevant transition temperatures are around body temperature, this might result in overestimation of the *in vivo* lipid core T1 when calculated from *ex vivo* measurements.

6.2.2 $B1^+$ Effects and RF Shims

The effects of $B1^+$ variations in different parts of the vasculature (for blood simulations) as well as near the Circle of Willis (for CSF and vessel wall simulations) were included based on measured $B1^+$ maps. For this, the 10-subject database of 7T multi-channel $B1^+$ flip angle maps in both the head and the neck presented in Chapter 3 was used. In addition to circular polarization (CP)-mode, the use of universal phase-only RF shims during the DANTE-preparation was studied. Shims were designed using two separate target regions with different weighting (see Figure 6.1): the Circle of Willis ("$B1_{CoW}$") and the upstream feeding arteries in the neck ("$B1_{neck}$"). These regions were defined based on the vessel masks shown in Figure 3.5, each of which was split at the slice above the carotid siphon to separate the regions corresponding to $B1_{CoW}$ (above the carotid siphon) and $B1_{neck}$ (up to the carotid siphon). Using this, two different shim targets were considered: (1) neck-only RF shims, designed to maximize the $B1^+$ in the neck during DANTE, and (2) neck-and-CoW RF shims, for which the regions were together optimized as

$$\min\left\{\left(CoV(B1_{CoW}) + \lambda_1 \frac{1}{B1_{CoW}^2}\right) + \left(CoV(B1_{neck}) + \lambda_1 \frac{1}{(\lambda_2 * B1_{neck})^2}\right)\right\}, \qquad 6.1$$

where CoV denotes the coefficient of variation (across different parts of the vessels as well as across the 10 subjects), and λ_1 and λ_2 are regularization parameters. For λ_1, which determines the relative importance of increasing $B1^+$ magnitude versus increasing the $B1^+$ homogeneity, a value of 1.7 was used based on the results presented in Section 3.4.2. λ_2 allows for higher $B1^+$ magnitudes around the Circle of Willis. For the neck-and-CoW RF shims, $\lambda_2 = 2$ was selected as the optimal trade-off for increasing $B1_{neck}$ without reducing $B1_{CoW}$ based on empirical comparisons.

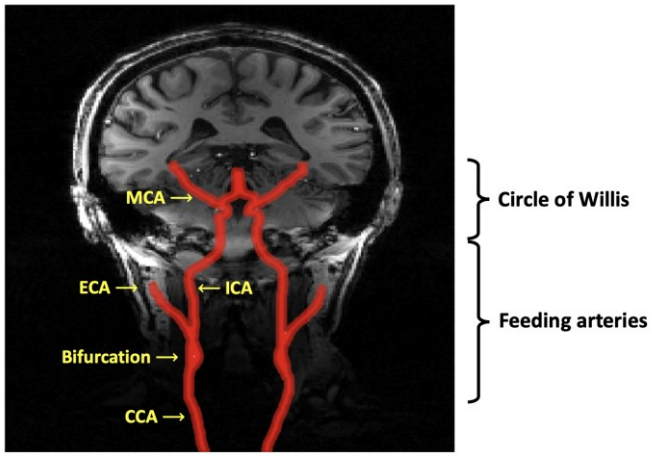

Figure 6.1: Schematic of the main arteries feeding into the MCA, indicating the two different vascular areas used for RF shim calculation. MCA, middle cerebral artery; ECA, external carotid artery; ICA, internal carotid artery; CCA, common carotid artery.

Flip angle variations due to $B1^+$ inhomogeneity were calculated by assuming the nominal flip angle to be achieved at the $B1^+$ in the centre of the brain in CP-mode (as explained in Section 5.2.3.5). For lower $B1^+$ values (in particular further down into the neck), this results in reduced effective flip angles corresponding to the reduction in $B1^+$ magnitude relative to the centre of the brain.

6.2.3 Data Acquisition

Data were acquired from 6 healthy volunteers (24-57 years old; 33 years average) under an agreed institutional ethics agreement. All volunteers were scanned on a Siemens (Erlangen, Germany) Magnetom 7T scanner using a Nova Medical (Wilmington, MA) 8Tx/32Rx head coil. The order in which different protocols were acquired was varied between subjects to ensure unbiased comparisons.

Initial scan parameters at 7T were based on the T2-weighted DANTE-SPACE protocol used by Viessmann et al. [35]. This includes data acquired at a resolution of 0.47×0.47×1.0 mm (reconstructed to 0.23×0.23×1.0 mm) with a total field-of-view of 240×180×176 mm. Other SPACE parameters include TR/TE_{eq} = 2620/165 ms, echo spacing = 4.62 ms, echo train length = 74 pulses (342 ms), GRAPPA = 4 in the left-right phase-encode direction (24×24 calibration region), turbo factor = 39, slice turbo factor = 2, echo trains per slice = 3, BW = 465 Hz/pixel, and a total scan time of 11:32. The flip angle train was calculated based on a prescribed signal evolution consisting of three parts, designed to increase the useable duration of the signal during the echo train [28]: a mono-exponential decay (time

constant 17.5 ms; first 9 SPACE pulses), a constant segment (pulses 10-40), and a second mono-exponential decay (time constant 29.0 ms; pulses 41-74) [35].

6.2.4 Reconstruction

All acquisitions were reconstructed using the same offline pipeline in MATLAB (Mathworks, Natick, MA) to facilitate reconstruction and direct comparison in SNR units [155].

First, 2D-multislice GRAPPA [65] reconstruction was applied using a 3×2 kernel. Minor spiking artefacts were encountered in the highest spatial frequencies along one side of the left-right k-space direction (due to an issue with a loose gradient cable on the x-axis that was encountered over the period of data acquisition for this study, but that was subsequently rectified by Siemens engineers). To suppress these artefacts, the outer 9% of measured k-space (containing the observed spikes) was first zero-filled and then replaced using a projection onto convex sets (POCS) [156,157] partial Fourier correction method. The reconstructed k-space was then zero-padded to obtain the desired reconstructed resolution of 0.23×0.23 mm in-plane. A 2D Fermi filter $F(k_x, k_y)$ was applied to suppress ringing artefacts which can arise from zero-padding. For an $N_x \times N_y$ k-space plane, the Fermi filter was calculated as

$$F(k_x, k_y) = \left(1 + \exp\left(\left(\left|k_x - \frac{N_x}{2}\right| - r_{f,x}\right)/w_f\right)\right)^{-1} * \left(1 + \exp\left(\left(\left|k_y - \frac{N_y}{2}\right| - r_{f,y}\right)/w_f\right)\right)^{-1}, \quad 6.2$$

where the parameters $w_f = 8$, $r_{f,x} = N_x/2.2$, and $r_{f,y} = N_y/2.2$ were chosen such that $F(N_x/2, N_y/2) = 1$ in a large central part of k-space and drops to near-zero at the edges.

Additional noise-only measurements were acquired for every acquisition and used for reconstruction in B1-weighted SNR units [155,158], calculated as

$$SNR_{B1w} = \sqrt{2/R}\,\frac{|S^H N^{-1} I_{ch}|}{\sqrt{S^H N^{-1} S}}, \quad 6.3$$

where SNR_{B1w} denotes the B1-weighted reconstructed image with pixel intensities in SNR units, calculated from the ESPIRiT coil sensitivities S [63], the bandwidth-scaled noise correlation matrix N, the multi-coil image data I_{ch}, and the undersampling factor *R*. Superscript *H* denotes the conjugate transpose operation. ESPIRiT receive coil sensitivities

were estimated using the Berkeley Advanced Reconstruction Toolbox (BART; v0.4.02) [124,125].

6.2.5 Quantification of Vessel Visibility

A semi-automated gradient detection algorithm [159] was used for the delineation of both the inner and outer vessel wall boundaries on individual image segments. This algorithm consists of four steps: firstly, a four-fold interpolated version of the image was unwrapped along 90 radial directions (at 4° angular intervals about the central point) to generate an image of the vessel in polar coordinates: see Figure 6.2. Secondly, the gradient of this image was calculated along the radial direction for the identification of vessel edges based on the locations where the radial signal either increases or decreases (grayscale images in Figure 6.3). On those unwrapped gradient images, some locations were manually selected to identify gradient minima and maxima which correspond to vessel edges (Figure 6.3). Those locations were then interpolated (in polar coordinates) and visually checked on the original Cartesian image (Figure 6.4a). Finally, quantitative metrics (described below) were derived based on the delineated vessel wall boundaries. This boundary delineation method was previously found to achieve excellent inter- and intra-observer agreement, as well as high reproducibility of results on repeated measurements of the same vessel from different scan sessions [159]. The latter makes this a particularly useful approach for the quantitative comparison of data acquired from the same volunteers in separate scan sessions (for which it will be used in Chapter 7).

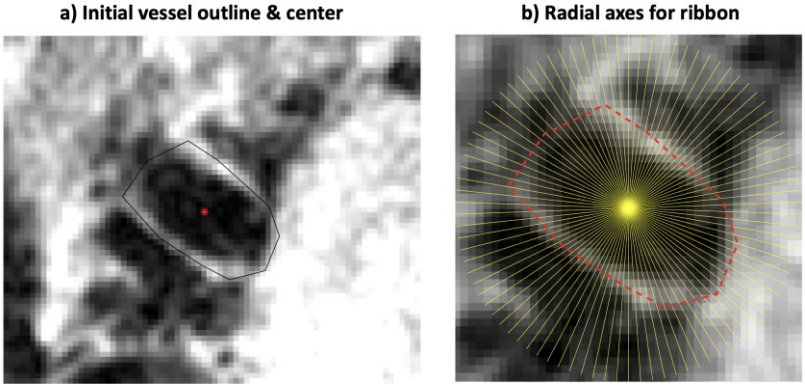

Figure 6.2: The first step of the vessel delineation algorithm: **(a)** A rough outline of the vessel is manually indicated (black line), from where the centre of the vessel area is estimated (red asterisk). **(b)** From this central location, 90 radial lines are extracted at 4° intervals (yellow lines).

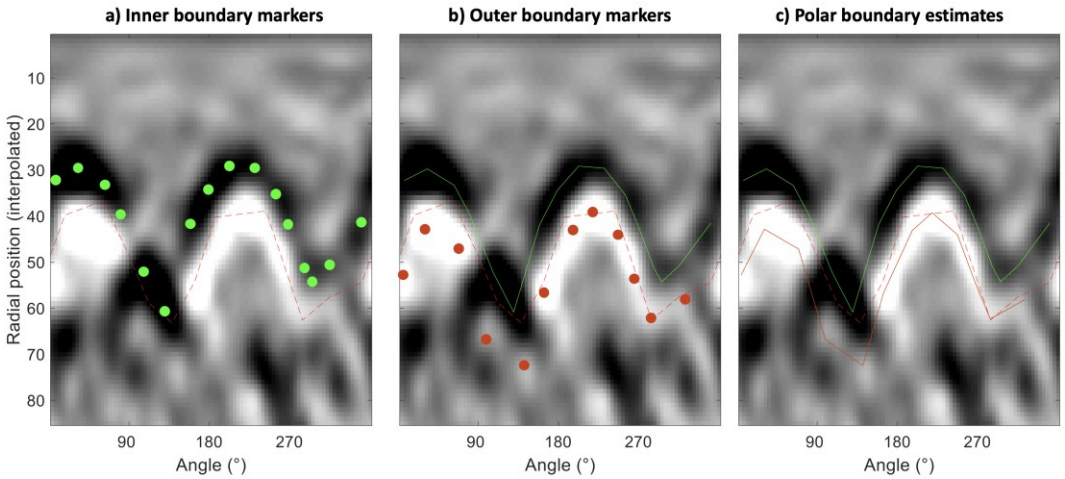

Figure 6.3: Vessel delineation on the polar gradient images. For each subplot, the y-axis indicates the distance from the centre of the vessel (central point corresponding to the top of the 2D images) and the y-axis indicates the clockwise angle, starting at 0° denoting vertical up (i.e., 12 o'clock). Greyscale images show the centre-out gradient values along each of the 90 identified vessel locations, with black corresponding to a signal increase and white to a signal decrease. The inner boundary is expected at the minimum points of the "troughs". The outer boundary is expected at the maximum points in the "peaks". The dashed red line corresponds to the initial vessel estimate drawn in the first step and serves as a guide to the eye. **(a)** Markers are manually placed at expected inner boundary locations (green circles) and **(b)** expected outer boundary locations (orange circles). The green line in (b) indicates the inner boundary estimates from (a). **(c)** The resulting manually indicated boundary estimates (inner boundary green line; outer boundary continuous orange line).

Based on the identified vessel boundaries, three quantitative parameters related to vessel sharpness and contrast were calculated along each radial direction, based on previous work by Biasiolli et al. [160]: the inner boundary acutance, outer boundary acutance, and directional root-mean-square signal gradient (G_{RMS}): see Figure 6.4. Note that contrary to previous implementations, no normalization was required when calculating the metrics described below since all analysis was performed on reconstructions calculated in SNR units.

The inner and outer boundary acutance were calculated as the maximum radial contrast across the respective vessel boundaries in polar coordinates. The maximum contrast was calculated for the identified boundary locations on the interpolated images (within a radial range of 0.3 mm) and scaled to CNR/mm units. A radial range of 0.3 mm around the identified boundary locations was found to provide consistent results for repeated measurements despite slight vessel delineation variations. Note that although the calculated inner boundary acutance corresponds to the wall-to-lumen contrast, the outer boundary acutance at each location can correspond to either wall-to-CSF or wall-to-tissue contrasts.

The third metric, the root-mean-square signal gradient G_{RMS}, calculates the signal change along the radial direction between the inner and outer vessel boundaries [160–162]. It was

previously found to correlate strongly with the subjective perception of sharpness [161]. For each of the 90 radial directions, it is calculated from the radial gradient $G_i = SNR_i - SNR_{i-1}$ at each of the n_i radial voxels across the vessel wall:

$$G_{RMS} = \sqrt{\frac{\sum_{i=1}^{n_i} G_i^2}{n_i}}. \qquad 6.4$$

The G_{RMS} is used for most quantitative comparisons in this work as it can be used as a single metric to describe vessel visibility (as opposed to separating the inner and outer boundary acutance), with the inner and outer boundary acutance reported in addition where relevant. However, all comparisons were calculated for all three metrics to confirm consistency of the results, and the resulting trends were found to be highly consistent.

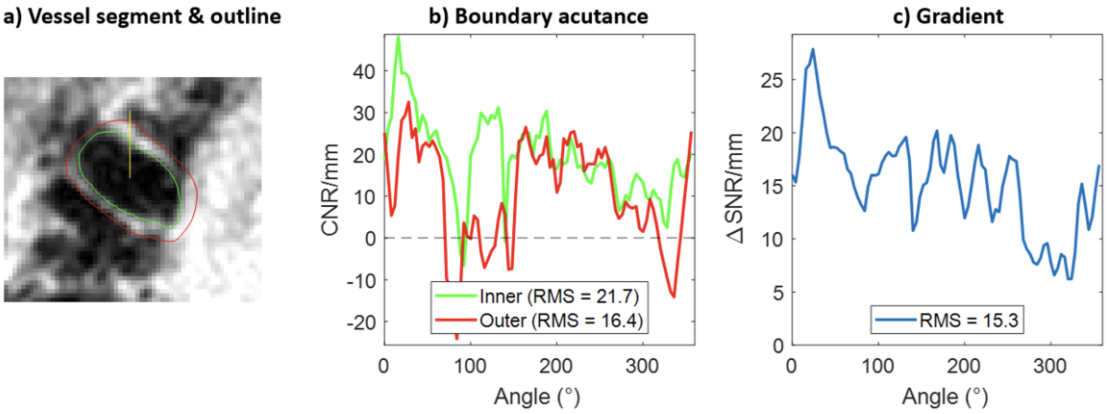

Figure 6.4: Example vessel delineation and acutance calculation. **(a)** Axial vessel segment and the estimated inner (green) and outer (red) vessel boundaries. **(b)** Calculation of the inner and outer boundary acutance at each of the 90 radial directions, sampled clockwise starting at the vertical yellow line in (a). Root-mean-square (RMS) values of the two contrasts are included in the legend. **(c)** Corresponding RMS gradient values of the vessel wall along each of the 90 radial directions.

The vessel acutance quantification using the tool and metrics described here were implemented in MATLAB based on the original code used by Biasiolli et al. [160]. The original version was modified to achieve more consistent results (including better robustness in the case of low-contrast vessels); to facilitate the delineation of more non-circular (i.e. higher aspect ratios) vessel segments; and to allow for calculation of the output metrics in SNR and CNR units (instead of normalized values). The resulting MATLAB code is available online (git.fmrib.ox.ac.uk/ndcn0873/acutance_TdB), including some example data.

The significance of differences between different protocols was assessed using paired-sample one-tailed t-tests which test the null hypothesis that the optimized version of a

protocol does not result in increased vessel visibility (G_{RMS} or inner/outer boundary acutance). The null hypothesis is rejected and results are considered significant for $p < 0.05$.

6.3 Results

6.3.1 CP-Mode Simulations

Four different DANTE parameters were considered during the simulation-based parameter optimizations using CP-mode $B1^+$ variation (as previously shown in Figure 5.8) for both the DANTE preparation and the SPACE readout. Those four parameters were the DANTE flip angle, the number of DANTE pulses, the DANTE gradient strength, and the DANTE interpulse duration. Two different contrasts (vessel wall-to-CSF and vessel wall-to-blood) were optimized, as well as two different vessel wall pulsation scenarios (stationary vessel wall and slowly pulsating vessel wall), effectively resulting in four different contrasts. Figure 6.5 only shows the optimization of the two most important DANTE parameters (flip angle and number of pulses) for all four contrasts. After that, Figure 6.6 shows the optimization for all four DANTE parameters, but only for slowly pulsating vessel wall tissue (which is considered more important for consistent vessel wall visibility because of the lower resulting contrasts than for static vessel wall).

Figure 6.5 shows substantial differences between the four achieved contrasts, with different amounts of deviation of regions of optimal parameter combinations relative to literature parameters. In particular, the pulsating vessel wall contrasts (Figure 6.5c-d) can be improved by using 170 pulses of 12° instead of 300 pulses of 10° (as used in previous literature [35]): the resulting pulsating vessel wall-to-blood contrast increases by 44%, while the pulsating vessel wall-to-CSF contrast increases by 30%. Those proposed parameters were selected such that the resulting contrasts stay mostly similar for stationary vessel wall, with a 3% contrast increase relative to blood and a 3% contrast decrease relative to CSF. The proposed parameters also result in a SAR decrease of the DANTE module of 18% relative to the literature protocol.

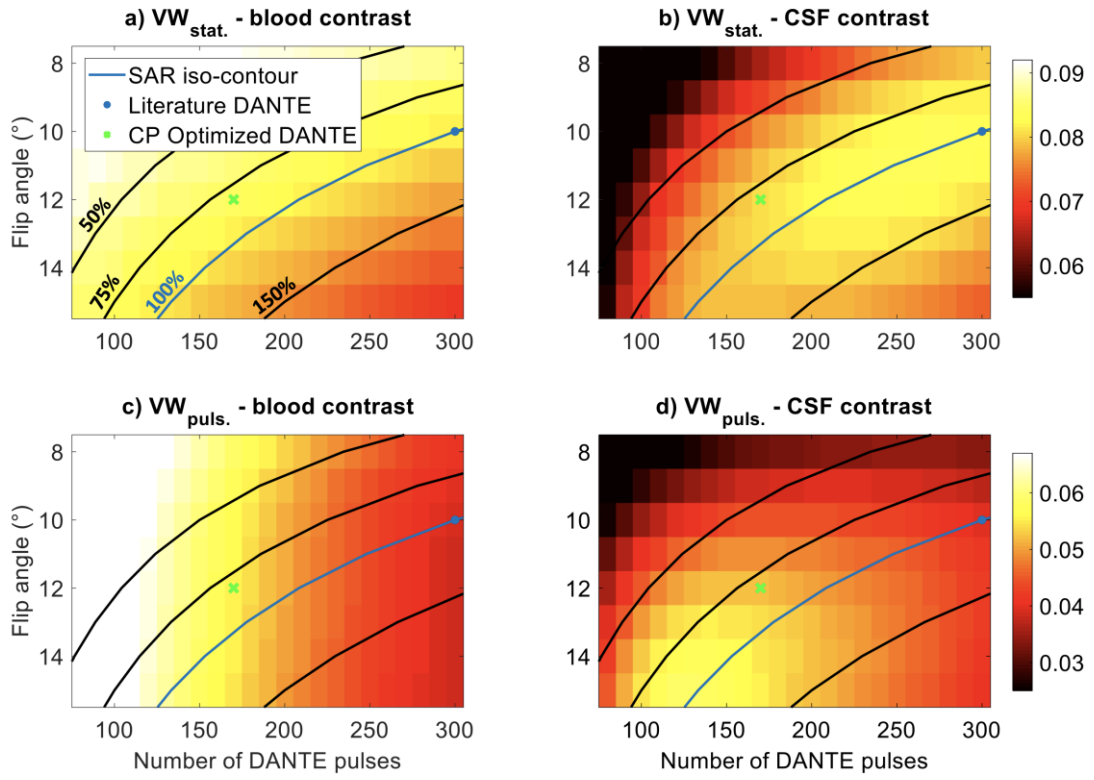

Figure 6.5: Simulated 7T CP-mode parameter sweeps for the number of DANTE pulses (x-axes) and their flip angles (y-axes). Resulting contrasts (in terms of the vessel wall M_0) are shown between **(a)** stationary vessel wall ("$VW_{stat.}$") and blood; **(b)** stationary vessel wall and CSF; **(c)** slowly pulsating vessel wall ("$VW_{puls.}$") and blood; and **(d)** slowly pulsating vessel wall and CSF. Blue circles indicate the previous literature parameters, while green crosses indicate the proposed CP-mode optimized parameters. Black and blue lines indicate SAR isocontour lines for the DANTE-preparation, with the corresponding values relative to the SAR when using the original literature parameters (blue circle) shown in Figure (a).

Figure 6.6 shows the single-parameter variation results for all four DANTE parameters, simulated for pulsating vessel walls. Results are shown as the signal levels of vessel wall, CSF, and blood as well as the resulting contrasts between the vessel wall and both CSF and blood. For the DANTE flip angles and the number of pulses, 170 pulses of 12° were chosen as discussed above. The optimized gradient strength was unchanged relative to the previous literature protocol [35], while the optimized DANTE interpulse time is reduced from 1.6 ms to 1.4 ms (with further reduction limited by the allowed protocol parameters).

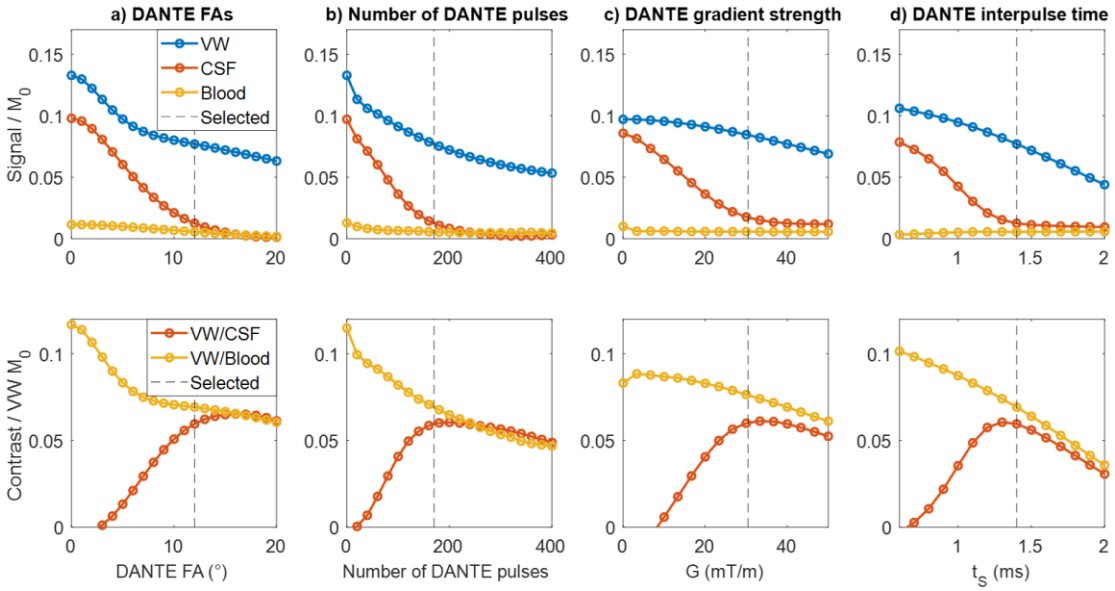

Figure 6.6: 7T CP-mode DANTE-SPACE simulation results for sweeps of the four main DANTE-parameters, simulated using slowly pulsating vessel walls. Separate subplots show the results when using various **(a)** flip angles; **(b)** numbers of pulses; **(c)** dephasing gradient strengths; and **(d)** interpulse times. Simulated signal levels for the three tissue types are shown in the top row, with the resulting VW/CSF and VW/blood contrasts in the bottom row. Dashed lines indicate the selected parameters for the *in vivo* acquisition protocol optimized for CP-mode.

When combined, using all four optimized parameters instead of the literature parameters results in the following predicted changes in the achieved contrasts: pulsating vessel wall-to-blood contrast +75%; pulsating vessel wall-to-CSF contrast +54%; stationary vessel wall-to-blood contrast +7%; stationary vessel wall-to-CSF contrast -3%.

6.3.2 Simulations using a Neck-Only RF Shim

Figure 6.7 compares the simulated (from multi-channel pTx $B1^+$ maps) $B1^+$ in the Circle of Willis and the feeding carotid arteries in the neck across 10 subjects for two RF shim configurations: CP-mode, and a universal RF shim designed to optimize the $B1^+$ in the neck. This "neck-only" RF shim is designed to increase the $B1^+$ magnitude in the neck with the goal of improving the suppression of inflowing blood. The lowest parts of the internal carotid arteries were excluded from the RF shim calculation since the arterial transit time between those locations and the Circle of Willis is longer than the time between the start of the DANTE preparation and the sampling of the centre of k-space in the SPACE-readout (approximately 0.4 seconds). The results in Figure 6.7 are the average results and standard deviations across the 10 subjects in the multi-channel $B1^+$ database described in Chapter 3. Using this shim, the average $B1^+$ magnitude in the arteries in the neck increases by 30% relative to CP-mode, while the $B1^+$ around the CoW decreases by 22%.

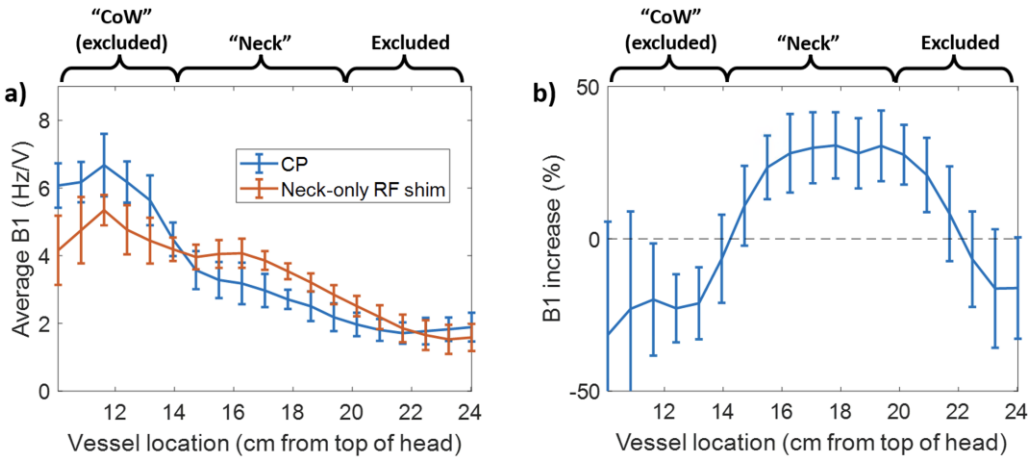

Figure 6.7: B1+ when using a "neck-only" RF shim. The B1+ magnitude in the main feeding arteries in the neck ("Neck") and in the Circle of Willis ("CoW") at 7T are shown for CP-mode (blue) and the "neck-only" RF shim (orange), calculated to optimize the B1+ in the neck. Subplot **(a)** shows the average values and standard deviations in each slice for the 10 subjects in the B1+ database; **(b)** shows the increase in B1+ magnitude when using the RF shim instead of CP-mode.

The average $B1^+$ across the 10 subjects, as shown in Figure 6.7a, was used for DANTE in DANTE-SPACE simulations using the "neck-only" RF shim (CP-mode was still used during the SPACE readout). The resulting signals and contrasts are shown in Figure 6.8, using the same optimization procedure as the one shown for CP-mode in Figure 6.6. The only difference is the use of the neck-only RF shim $B1^+$ profile along the vessel trajectory (instead of the CP-mode $B1^+$ profile), and the corresponding reduction in $B1^+$ near the Circle of Willis as shown in Figure 6.7. Figure 6.8 shows the resulting parameter sweep results for all four DANTE parameters. Although good blood suppression is achieved for most parameter options, the resulting VW/CSF contrasts are consistently lower than for CP-mode. This is a result of the reduced $B1^+$ in the Circle of Willis, leading to reduced CSF suppression. Figure 6.8a shows that when using the neck-only RF shim, sufficient VW/CSF contrast can only be achieved when using very high DANTE flip angles of up to 20 degrees. However, this would result in a 127% increase in SAR compared to the SAR of the DANTE preparation when using literature parameters [35], which would exceed the regulatory limits.

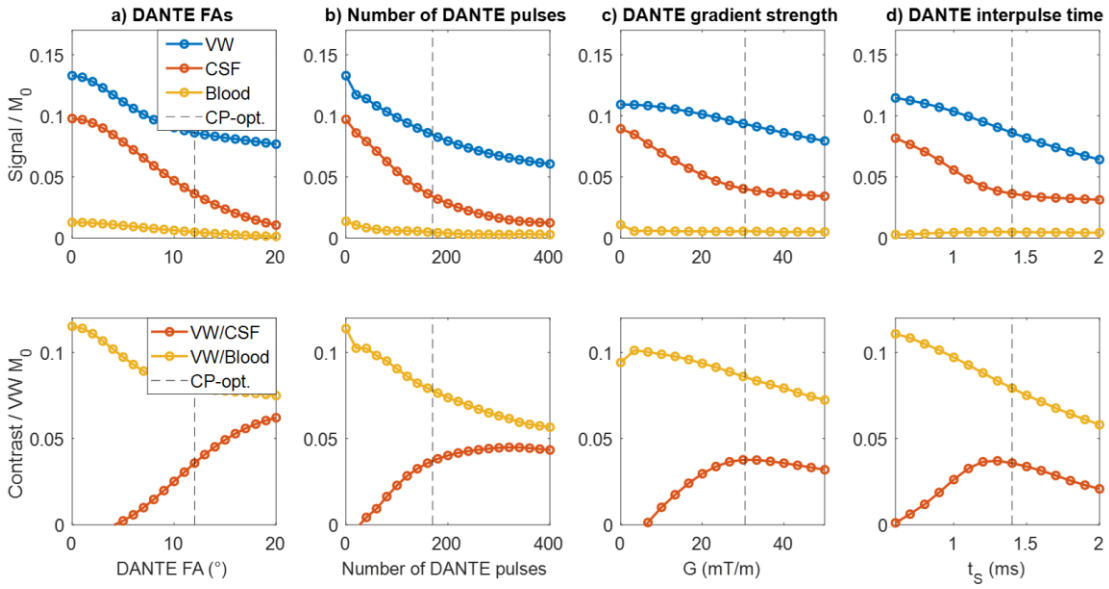

Figure 6.8: 7T DANTE-SPACE simulation results when using the "neck-only" RF shim during DANTE. Vessel wall simulations were performed assuming slow pulsation. Separate subplots show the results when using various **(a)** flip angles; **(b)** numbers of pulses; **(c)** dephasing gradient strengths; and **(d)** interpulse times. Simulated signal levels for the three tissue types are shown in the top row, with the resulting VW/CSF and VW/blood contrasts in the bottom row. Dashed lines indicate the selected DANTE parameters for CP-mode (Section 6.3.1).

6.3.3 Simulations using a Neck-and-CoW RF Shim

The result in the previous section were achieved by using an RF shim optimized for the vessels in the neck, without considering the resulting $B1^+$ around the Circle of Willis. To assess the effects of including the Circle of Willis in the RF shim calculation (calculated as described in Section 6.2.2), Figure 6.9 compares CP-mode to the simulated $B1^+$ when using a universal RF shim designed to simultaneously optimize the $B1^+$ in the neck and in the CoW. Using $\lambda_2 = 2$ in Equation 5.3, this RF shim increases the $B1^+$ magnitude in the neck without reducing the $B1^+$ in the Circle of Willis, thereby improving the suppression of inflowing blood without penalizing the CSF suppression. The lowest parts of the internal carotid arteries were again excluded from the RF shim calculation.

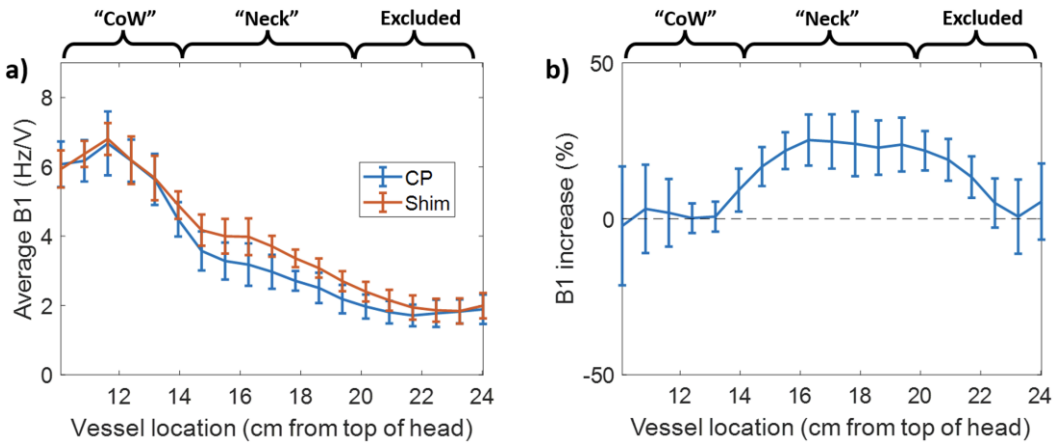

Figure 6.9: B1+ when using a "neck-and-CoW" RF shim. The B1+ magnitude in the main feeding arteries in the neck ("Neck") and in the Circle of Willis ("CoW") at 7T are shown for CP-mode (blue) and the proposed neck-and-CoW RF shim (orange). Subplot **(a)** shows the average values and standard deviations in each slice for the 10 subjects in the B1+ database; **(b)** shows the increase in B1+ magnitude when using the RF shim instead of CP-mode.

The average $B1^+$ across the 10 subjects, as shown in Figure 6.9a, was used for DANTE in DANTE-SPACE simulations using the "neck-and-CoW" RF shim (CP-mode was still used during the SPACE readout). Again, a similar optimization procedure to the one described in Section 6.3.1 was performed. The only difference was the use of the neck-and-CoW RF shim $B1^+$ profile along the vessel trajectory (instead of the CP-mode $B1^+$ profile), and the corresponding small change in $B1^+$ near the Circle of Willis as shown in Figure 6.9. Figure 6.10 shows the resulting parameter sweep results for all four DANTE parameters. Note that this is the equivalent of Figure 6.6, with the only difference being the use of the neck-and-CoW RF shim during DANTE. Due to the minimal change in $B1^+$ near the Circle of Willis during DANTE (3% increase on average), the results for VW and CSF are highly similar between Figure 6.10 and Figure 6.6. This results in a similar set of optimized DANTE parameters, with the only difference relative to the CP-mode optimization being a reduction in the number of DANTE pulses from 170 to 160.

The increased $B1^+$ in the neck for the RF shim during DANTE increases the efficiency of the blood suppression. Whereas the simulated blood signal using the CP-mode-optimized parameters is already 12% lower than when using the literature parameters, the addition of

the proposed neck-and-CoW RF shim during DANTE improves this to a 32% reduction in the remaining blood signal.

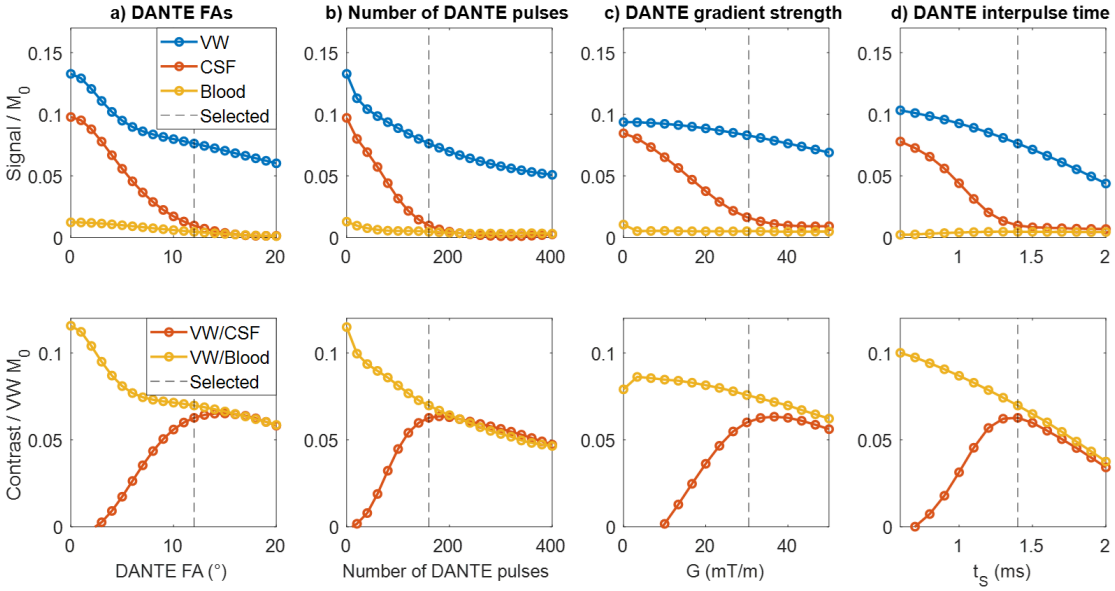

Figure 6.10: 7T DANTE-SPACE simulation results when using the "neck-and-CoW" RF shim during DANTE. Vessel wall simulations were performed assuming slow pulsation. Separate subplots show the results when using various **(a)** flip angles; **(b)** numbers of pulses; **(c)** dephasing gradient strengths; and **(d)** interpulse times. Simulated signal levels for the three tissue types are shown in the top row, with the resulting VW/CSF and VW/blood contrasts in the bottom row. Dashed lines indicate the selected parameters for the *in vivo* acquisition protocol using the neck-and-CoW RF shim.

Overall, the predicted changes in the relevant contrasts when using optimized DANTE parameters combined with the proposed universal neck-and-CoW RF shim instead of the literature parameters are: pulsating vessel wall-to-blood contrast +78%; pulsating vessel wall-to-CSF contrast +52%; stationary vessel wall-to-blood contrast +7%; stationary vessel wall-to-CSF contrast -5%. When employing this RF shim, the SAR contribution of the DANTE preparation is reduced by 23% (instead of 18%) due to the use of 10 fewer DANTE pulses.

The resulting predicted contrasts between healthy and pathological vessel wall tissue are shown in Figure 6.11. For all protocols, lipid cores consistently appear hypo-intense relative to healthy vessel walls, while intra-plaque haemorrhages appear hyperintense. Fibrous cap signal levels are consistently similar to healthy vessel wall tissue, but hyperintense relative to the internal lipid core.

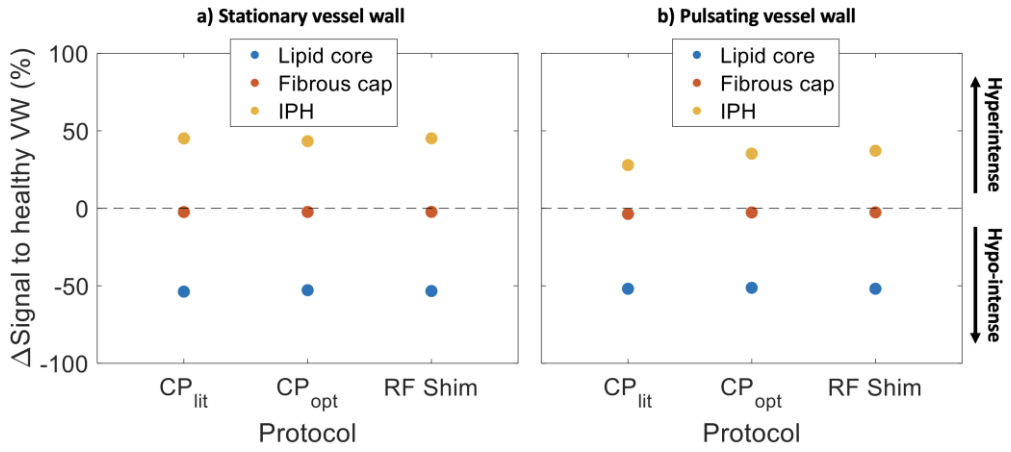

Figure 6.11: Simulated contrasts between healthy vessel wall and three plaque components: lipid core, fibrous cap, and intra-plaque haemorrhage (IPH). For each of the three plaque components, the simulated signal level relative to the signal level in healthy vessel wall is shown for the literature protocol (CP_{lit}), the CP-mode optimized protocol (CP_{opt}) and the "neck-and-CoW" RF shim optimized protocol. Results are shown for **(a)** stationary (healthy and pathological) tissues and **(b)** slowly pulsating vessel wall.

6.3.4 *In Vivo* Acquisitions

An overview of the simulation-optimized DANTE parameter combinations based on Sections 6.3.1 and 6.3.3 is shown in Table 6.1. Data were acquired using the two optimized protocols as well as the literature-based protocol in all 6 healthy volunteers.

		CP (Literature)	CP ("Optim.")	RF Shim
RF Shim		CP-mode	CP-mode	"neck-and-CoW"
#pulses		300	170	160
Flip angle	°	10	12	12
Gradient (H → F)	mT/m	40	40	40
Interpulse time (t_D)	ms	1.6	1.4	1.4

Table 6.1: Overview of the DANTE parameters used for the three acquired 7T DANTE-SPACE protocols.

Figure 6.12 shows an example slice segment from a representative subject acquired using all three acquisitions. The middle cerebral arteries and the basilar artery are visible in all three acquisitions. However, when using the optimized protocols an increase in SNR is visible in some vessel wall segments. In particular, this is visible in segments with lower signal when using the literature parameters, such as in the basilar artery. All acquisitions generally achieve good CSF and blood suppression, although some heterogeneity remains. When comparing the optimizations with and without the neck-and-CoW RF shim, a slight additional reduction in blood signal can be observed in the basilar artery and the right MCA when using the RF shim.

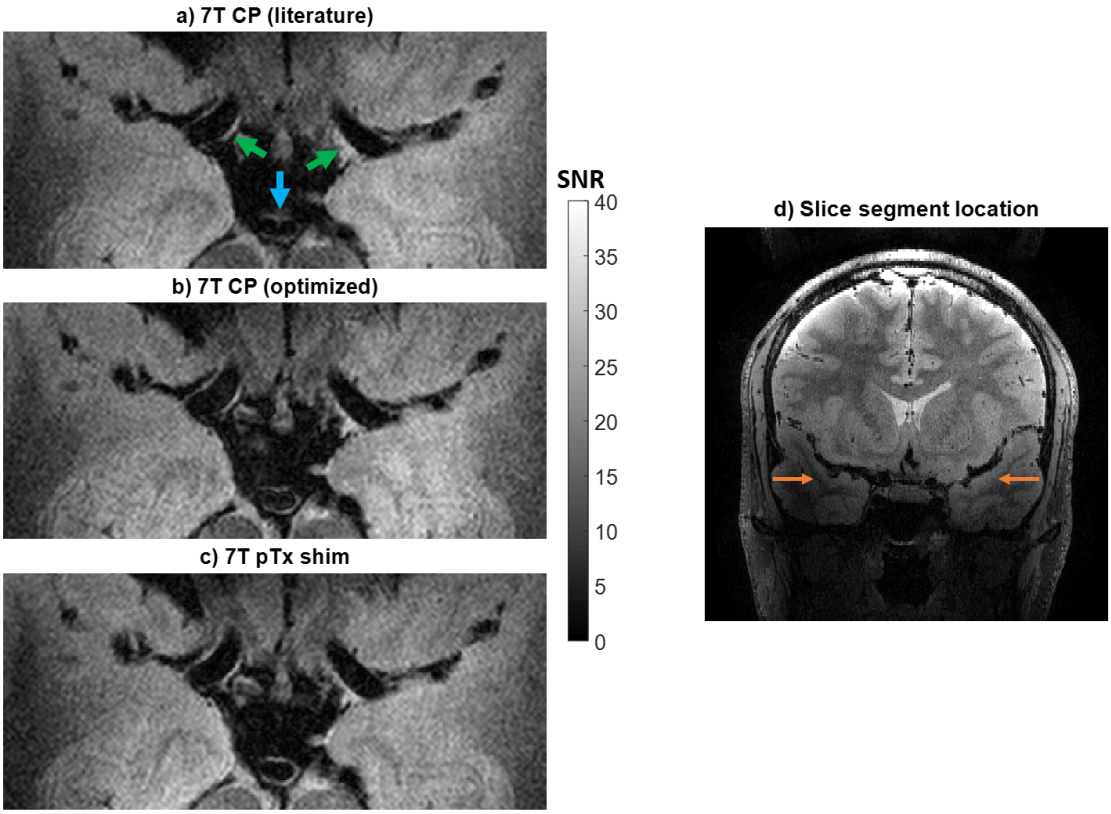

Figure 6.12: Transverse slice segment from a representative subject showing the bilateral middle cerebral artery M1 segments (green arrows in (a)), and the basilar artery (blue arrow) acquired using each of the three protocols. The location of the slice segment shown in (a-c) is indicated by the orange arrows on the coronal slice in (d).

6.3.5 Quantitative Comparison

All visible segments of the MCAs, BA, and distal ICAs in the 3 datasets from the 6 subjects were analysed using the method described in Section 6.2.5. Figure 6.13 shows the resulting average G_{RMS} values at different slice locations below the MCA M1-segment, as indicated by Figure 6.13a. When using the CP-mode optimized DANTE parameters (Figure 6.13b and d), the slice-wise average G_{RMS} increases by 19 ± 16%, with increased values at all slice locations. When employing the proposed universal neck-and-CoW RF shim during DANTE, Figure 6.13c and e show a slightly higher average G_{RMS} increase of 24 ± 23% relative to the literature parameter acquisitions. Again, an improvement is observed at all slice locations, although a larger relative increase is observed in lower slices. This difference is mainly driven by the inclusion of the BA, which (as is also visible in Figure 6.12) had a higher average G_{RMS} improvement than the other arteries: an increase of 36 ± 24% when using the neck-and-CoW RF shim and an increase of 27 ± 15% when using CP-mode optimized DANTE preparation.

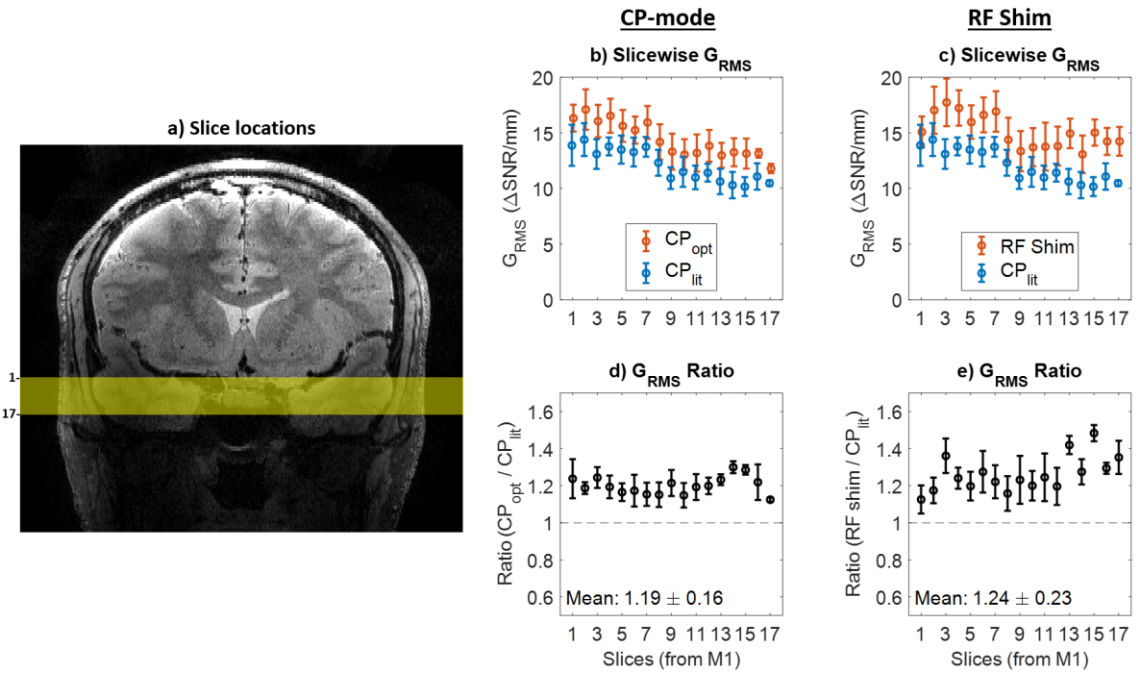

Figure 6.13: The slice-wise G_{RMS} of the optimized DANTE-SPACE protocols in CP mode ("CP_{opt}") and using the neck-and-CoW RF shim during DANTE ("RF Shim"), compared to the corresponding results using literature DANTE-parameters in CP-mode ("CP_{lit}"). Reported values are the mean values and standard errors in the MCA, BA, and distal ICA of the 6 healthy volunteers in the 17 slices in the region shaded in yellow in (a). **(b):** Optimized CP-mode 7T vs literature CP-mode 7T; **(c):** RF shim 7T vs literature CP-mode 7T. Figures **(d)** and **(e)** show the slice-wise ratio between each pair of compared protocols.

While Figure 6.13 compares the slice-wise average G_{RMS} results, Figure 6.14 shows the correlation of the achieved G_{RMS} in the different acquisitions for each individual 60° radial sub-segment. Like in Figure 6.13, an increased average G_{RMS} is observed when using the CP-mode optimized protocol (dy/dx > 1), with a slightly larger increase still when including the neck-and-CoW RF shim during DANTE.

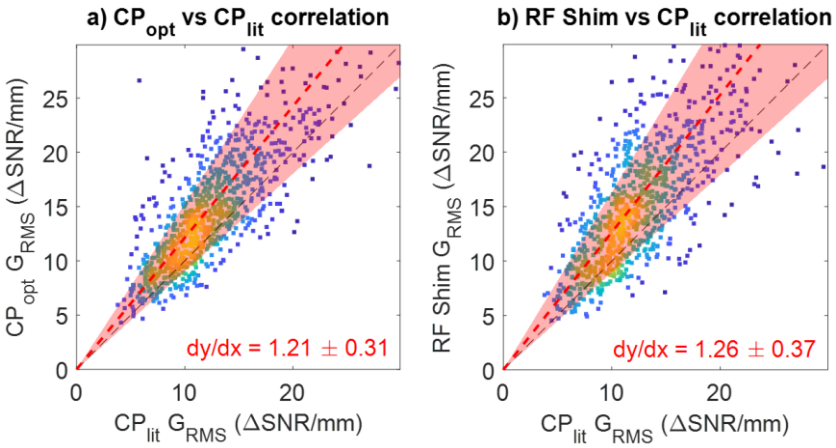

Figure 6.14: Segment-wise G_{RMS} correlation between the two optimized protocols (**(a):** CP-mode optimized ("CP_{opt}"); **(b):** using the neck-and-CoW RF shim) and the acquisitions using literature parameters ("CP_{lit}"; x-axes). The results of

each vessel wall segment are shown based on the average values of six radial sub-segments of 60°. Dashed red lines show the mean ratio (and 95% variance) between the respective acquisitions, with the corresponding values indicated in red.

The overall average G_{RMS} results are shown in Figure 6.15, which also shows the resulting inner and outer boundary acutance. Using all three metrics, both optimized protocols (for CP-mode and using the RF shim) perform significantly ($p < 0.001$) better than the CP-mode literature protocol. The optimized protocol using the universal neck-and-CoW RF shim during DANTE achieves significantly improved G_{RMS} and inner boundary acutance compared to the CP-mode-optimized protocol, but no further significant increase in the outer boundary acutance is observed.

The average percentage improvements when using the optimized protocol with the RF shim instead of literature parameters are +24 ± 23% for the G_{RMS}, +28 ± 27% for the inner acutance, and +28 ± 33% for the outer acutance.

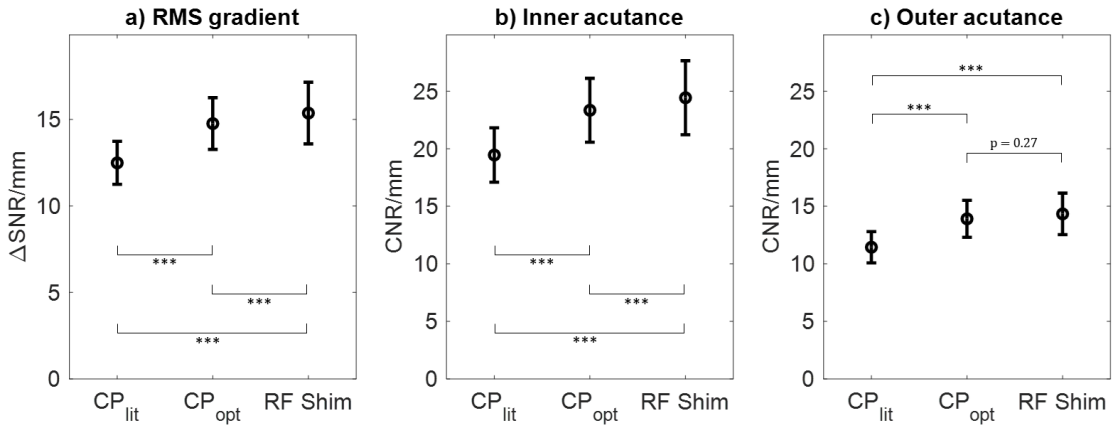

Figure 6.15: Summary results of the achieved contrasts using the three acquired protocols, compared using **(a)** G_{RMS}, **(b)** inner boundary acutance, and **(c)** outer boundary acutance. Significance levels are reported for all comparisons, where three asterisks (***) denote $p < 0.001$.

6.4 Discussion

In this work, two optimized versions of the DANTE preparation module for T2-weighted DANTE-SPACE vessel wall imaging at 7T are proposed. Both proposed protocols are based on simulations which compare the achieved contrasts when using different DANTE flip angles, numbers of pulses, gradient strengths, and interpulse durations.

For the optimizations in CP-mode, Figure 6.5 shows that the DANTE parameters used in previous literature achieve close to the maximum contrasts for static vessel wall simulations but leave substantial room for contrast improvement for pulsating vessel walls. This

simulation-based result is consistent with earlier *in vivo* results in which large inter- and intrasubject variability were observed [35], indicating that including vessel wall pulsation is indeed required for accurate simulation of the DANTE-SPACE contrast mechanisms.

Therefore, optimized CP-mode DANTE parameters (with 170 pulses of 12°) were proposed to improve the contrasts for pulsating vessel walls without substantially reducing the contrasts for stationary vessel wall tissue relative to the literature protocol. It should be noted that the CP-mode parameters proposed here differ from the parameters which we previously proposed in an abstract presented at the Annual Meeting of the International Society for Magnetic Resonance in Medicine (with 200 DANTE pulses of 9°) [136]. That result was based on an earlier version of the simulation framework which did not include the pulsatile CSF velocity variation shown in Figure 5.5. Since the addition of this CSF velocity variation introduces periods of very low absolute velocities (near the velocity zero-crossing), it requires increased DANTE flip angles to properly suppress CSF during all stages of the pulsatile cycle. Other studies using DANTE simulations generally assumed vessel wall tissue to be static [35,36,39,40,133–136] and intracranial CSF to be in varying states of motion: either static [39,40], fast-flowing ($\geq$ 2 cm/s) [35,134–136], and/or continuously flowing without pulsatile velocity variation [40,134,135]. The results presented here indicate that the addition of higher-order pulsatile motion for both vessel wall and CSF provides a more accurate representation of *in vivo* contrast mechanisms, and results in a substantial change in simulation-based optimal sequence parameters.

While Figure 6.5 shows the achieved contrasts for different parameter combinations, Figure 6.6 also shows the underlying signal levels. These show that for all four studied DANTE parameters, a strategy that alters the parameters to retain more vessel wall signal (relative to the signal levels that are achieved using the proposed parameters) would result in the unwanted corollary of an even larger increase in CSF signal. This trade-off between suppressing CSF signal while retaining vessel wall signal results in the maximized contrast at the different (updated) proposed DANTE parameters.

Section 6.3.2 shows that using a phase-only universal "neck-only" RF shim, it is possible to increase the $B1^+$ magnitude in the neck by about 30%. However, this also results in a reduction in $B1^+$ magnitude around the Circle of Willis, reducing the efficiency of the CSF suppression when using this shim during DANTE. Section 6.3.3 shows that when combining the $B1^+$ in both the neck and the Circle of Willis in the RF shim calculation, it is possible to calculate a phase-only universal "neck-and-CoW" RF shim. This shim

increases the $B1^+$ magnitude in the neck without reducing the $B1^+$ in the Circle of Willis. The simulations in Figure 6.10 suggest that, as a result, the blood suppression can be improved by 32% without penalizing the resulting CSF suppression in the region of the Circle of Willis.

Overall, the simulations suggest that using the optimized protocols that adopt the DANTE parameters as shown in Table 6.1 will lead to a substantial (up to 78%) increase the DANTE-SPACE contrasts for pulsating vessel walls, without reducing the contrasts for stationary vessel wall. This also results in an 18% (CP-mode) or 23% (neck-and-CoW RF Shim) reduction in the SAR contribution of the DANTE preparation. For the full sequence, this corresponds to a SAR reduction of 6% or 8%, respectively.

The slice segments in Figure 6.12 indicate experimental signal changes that are consistent with the simulation-based predictions: higher vessel wall signal levels are visible when using the optimized protocols (in particular in parts of the vessels with lower initial signal levels), and a further reduction in blood signal is visible when using the neck-and-CoW RF shim. Figure 6.13 and Figure 6.14 confirm that those contrast improvements when using the optimized protocols are consistently detected for vessels in all slices and in all parts of the vessels. A substantial amount of variation in both the achieved contrasts and the changes in contrasts is visible (Figure 6.14) for both optimized protocols. This could be explained by a combination of the variation in pulsatile behaviour (velocity and direction) of vessel wall and CSF in different anatomical areas, and by the outer vessel wall contrasts being dependent on anatomical locations (e.g., well-defined vessel-to-CSF interfaces or poorly defined vessel-to-tissue interfaces).

Despite this variation, Figure 6.15 confirms that both optimized protocols result in significantly improved contrasts (G_{RMS}, inner acutance, and outer acutance) relative to the literature protocol. When employing the neck-and-CoW RF shim instead of CP-mode during DANTE, a small but significant further incremental improvement is achieved for the G_{RMS} and the inner acutance, but not for the outer acutance. This is consistent with the hypothesis that the RF shim improves the blood suppression and therefore increases the inner vessel wall acutance, as well as the G_{RMS} (which is sensitive to both the inner and outer vessel wall acutance).

The average contrast changes when using the RF shim-optimized protocol instead of the literature protocol (inner acutance $+28 \pm 27\%$; outer acutance $+28 \pm 33\%$) are a combination of results from vessel wall segments with different levels of pulsation and

different outer tissue boundaries, making it hard to quantitatively compare the experimental results to the simulated results. However, the observed values are consistently between the simulated contrast changes for stationary vessel walls (as a lower bound) and pulsating vessel walls (as an upper bound).

All data used in this work were acquired from healthy volunteers without any pathology or known vessel disease. Viessmann et al. [35] scanned one patient with MCA stenosis using T2w DANTE-SPACE at 7T, demonstrating the potential of the sequence for depicting intracranial vessel wall pathology. However, further clinical validation for our recommended parameters is still required. Based on the pathological vessel wall simulations in Figure 6.11, the contrasts between clinically relevant plaque components are expected to remain consistent when using the optimized protocols proposed here. However, due to vessel wall pathology and aging [147], reduced vessel wall motion might be expected in clinical populations. That would have the benefit of reducing vessel wall attenuation, resulting in improved DANTE-SPACE contrasts in patient populations.

6.5 Conclusion

The addition of vessel wall and CSF pulsation in simulations can explain experimental DANTE-SPACE signal variations observed at 7T. Using optimized DANTE parameters based on simulation results, the achieved DANTE-SPACE contrasts can be improved over a previous literature protocol. The adoption of a neck-and-CoW RF shim during DANTE, if parallel transmit capability is available, can be used for additional suppression of inflowing blood, resulting in a further improvement in delineation of the inner vessel wall.

7

T2-Weighted DANTE-SPACE Vessel Wall Imaging at 3T

Key Conclusions

- **T2-weighted DANTE-SPACE vessel wall imaging at 3T requires more DANTE preparation than at 7T to achieve sufficient CSF suppression**
- **DANTE-SPACE at 3T provides 2× lower contrast than at 7T**

7.1 Introduction

Chapter 6 investigated the optimization of the three-dimensional T2-weighted DANTE-SPACE intracranial vessel wall imaging sequence at 7T. At such ultra-high field strengths, for which it was first introduced by Viessmann et al. [35], the sequence benefits from the increased SNR and longer T1 relaxation times associated with higher magnetic fields to achieve vessel delineation relative to both the internal blood and the surrounding CSF. However, 7T MRI is currently not a part of routine clinical practice due to the limited number of available 7T scanners, higher associated costs, additional safety considerations (increased SAR and stricter implant restrictions), and remaining limitations from regulatory bodies [48,163,164]. In contrast, 3T MRI, which is considered the minimum magnetic field strength for intracranial vessel wall imaging [26], is widely available in a clinical setting.

At 3T, DANTE-SPACE has frequently been used as a 3D T1-weighted intracranial vessel wall imaging (VWI) sequence [30,36–38,40–43], where compared to T2-weighted acquisitions it benefits from relatively short acquisition times due to a shorter TR, increased DANTE efficiency due to the shorter TR and TE, and lower native CSF signal. In 2021, Zhang et al. [39] acquired T2-weighted DANTE-SPACE images at 3T as part of a comparison of different CSF-suppression methods for 3D T2-weighted SPACE. For this, they used the same DANTE parameters as previously used in the literature for T1-weighted DANTE-SPACE at 3T [37,38,40] (consisting of 150 DANTE pulses of 8°) and observed insufficient CSF suppression for accurate vessel wall delineation [39]. Wang et al. [133]

used DANTE preparation in 2D T2-weighted and 3D proton-density-weighted turbo-spin-echo acquisitions at 3T and reported overall satisfactory CSF suppression around the major intracranial arteries, resulting in a 28% increase in CSF-to-wall contrast for proton-density-weighted DANTE-SPACE. However, no conclusive information is available about the optimization and performance of DANTE for intracranial T2-weighted DANTE-SPACE.

Secondly, no information is currently available about the achieved intracranial vessel signal, CSF suppression, and resulting contrasts of the (T2-weighted) DANTE-SPACE sequence at 3T compared to 7T. Acquisitions at 7T benefit from increased inherent SNR [50] and longer T1 relaxation times, providing more efficient DANTE suppression. However, higher field strengths also introduce limitations. Quadratically increasing SAR leads to more restrictive limits on the allowed sequence parameters, including the minimum repetition time and the allowed DANTE flip angle and number of pulses, while smaller transmit field coverage limits the suppression of inflowing blood. Finally, the simulations in Figure 5.11 indicate that while the typically longer T1 and shorter T2 times at 7T benefit CSF suppression, they also result in reduced vessel wall signal. Therefore, it is not entirely clear whether and by how much DANTE-SPACE acquisitions benefit from higher field strengths.

Here, the simulation framework presented in Chapter 5 is first used to propose an optimized T2-weighted DANTE-SPACE protocol at 3T. Subsequently, *in vivo* data from healthy volunteers at both field strengths are used to compare the performance of the simulation-optimized 3T and 7T protocols for T2-weighted VWI at both field strengths.

7.2 Methods

7.2.1 Simulations

The extended phase graph DANTE-SPACE simulation framework described in Chapter 5 was used for all simulations.

For 3T, the same physiological simulation parameters (mean velocity, diffusion coefficient, proton density) were used as at 7T. T1 and T2 relaxation times for vessel wall, CSF, and blood at 3T were estimated based on various sources. 3T vessel wall relaxation times were based on carotid artery measurements presented by Koning et al. [138]; for blood at 3T, the T1 and T2 values were based on measurements by Shimada et al. [165] and Zhao et al.

[166], respectively; for CSF at 3T, the same T1 as at 7T was used based on previous studies [140,167] that found it to be constant for different field strengths, while the CSF T2 at 3T was interpolated from measurements at various other field strengths [141,167–169]. Table 7.1 shows an overview of all relaxation time and physiological properties as used in the simulations.

Because of the improved transmit field homogeneity and extent at 3T compared to 7T [58], $B1^+$ fields were assumed to be homogeneous in all 3T simulations. As for the 7T simulations, all CSF and vessel wall signal levels were calculated based on the values during the second TR to account for magnetization history effects from previous repetitions.

The 7T optimum protocol (as proposed in Chapter 6) was used as the starting point for the simulation-based optimization at 3T. From there, simulations were first used to propose a T2-weighted SPACE protocol at 3T (still using DANTE-preparation as optimized for 7T). This consisted of optimizing the repetition time and the SPACE echo spacing, after which the echo train length was adjusted to match the total scan time at 7T. After this SPACE optimization, additional simulations were used for a separate DANTE parameter optimization (while adopting the 3T optimized SPACE protocol). As for 7T in the previous chapter (Section 6.3.1), this DANTE parameter optimization was used to determine the DANTE flip angle, the number of DANTE pulses, the DANTE gradient strength, and the DANTE interpulse time which provide the highest contrast between the vessel wall and both CSF and blood. All simulations were first performed assuming slowly pulsating vessel walls as the worst-case scenario, and then repeated to ensure that the determined protocol parameters provide consistently high contrasts for simulations assuming stationary vessel walls.

		3T	7T
T1 (vessel wall)	ms	1227	1628
T1 (CSF)	ms	4019	4019
T1 (blood)	ms	1779	2290
T2 (vessel wall)	ms	55	46
T2 (CSF)	ms	517	311
T2 (blood)	ms	122	100
Mean velocity (VW)	cm/s	0.054	
Mean velocity (CSF)	cm/s	0.367	
Mean velocity (blood)	cm/s	24.0	
Diffusion coeff. (VW)	mm^2/s	0	
Diffusion coeff. (CSF)	mm^2/s	3×10^{-3}	
Diffusion coeff. (blood)	mm^2/s	3×10^{-3}	

Table 7.1: Overview of the relaxation parameters, mean absolute velocities, and diffusion coefficients used for the simulation of vessel wall tissue, CSF, and blood.

7.2.2 Data Acquisition

DANTE-SPACE data at 3T were acquired for the same 6 healthy volunteers (24-57 years old; 33 years average) as in Chapter 6 using the simulation-based optimized protocol. Data were acquired using a Siemens (Erlangen, Germany) Prisma 3T scanner with a 32-channel receive head coil under an agreed institutional ethics agreement. Manual (non-oblique) slice positioning was used for each subject, independent from the corresponding acquisitions at 7T.

At 7T, a field-of-view (FOV) in the head-foot direction of 176 mm was used with non-selective SPACE refocusing pulses without resulting in wrap-around artefacts due to the inherently limited spatial extent of the transmit and receive fields at ultra-high field [58,170]. To suppress longitudinal wraparound artefacts due to the larger spatial extent of the B1 fields into the neck at 3T, an additional spatial saturation pulse was used between the DANTE-modules and the SPACE-readouts. Preliminary *in vivo* DANTE-SPACE data using various FOV sizes in the longitudinal direction were used to assess the required size and location of this spatial saturation region. Phantom data were then acquired to confirm the performance of the saturation band in preventing longitudinal wraparound when acquiring data using the desired FOV. For the phantom acquisitions, 60 slices of 2.93 mm were used (instead of the regular 176 slices of 1 mm) for faster acquisition of the same FOV.

To account for the lower spatial variation in the receive coil sensitivity profiles at 3T compared to 7T, a lower GRAPPA acceleration factor was used at 3T ($R = 3$) than at 7T ($R = 4$). Most other SPACE parameters, including the total scan time, field-of-view, matrix size, equivalent echo time, and receive bandwidth were matched between 3T and 7T (see Results section below for a full overview of the parameters). The SPACE echo spacing (defined as the time between consecutive pulses) and repetition time were selected based on simulation results. After all SPACE parameters were selected, the echo train length was adjusted to achieve the same total scan time at 3T as at 7T. Additional SPACE data without DANTE preparation were acquired at 3T for three volunteers.

7.2.3 Reconstruction

Data acquired at 3T and at 7T were reconstructed using the offline reconstruction method described in Section 6.2.4. However, the correction of spiking artefacts which was used for the 7T data was excluded at 3T since no spiking was encountered. All other reconstruction steps, including ESPIRiT coil sensitivity estimation [63], 2D-multislice GRAPPA [65], zero-padding with a 2D Fermi filter (Equation 6.2), and reconstruction in B1-weighted SNR units [155,158] (Equation 6.3) were performed using the same MATLAB tools.

Datasets acquired from each subject at 3T and 7T were rigidly registered using three-dimensional translation and in-plane rotation (yaw). The other two rotation orientations (pitch and roll) were excluded from the registration to prevent confounds in the calculated image properties due to interpolation-induced blurring when rotating along anisotropic voxel directions, as would be the case for pitch and roll re-registration. Although this method of image registration means that full slices may not be properly registered, it should ensure that local patches of the slice can be compared with accuracy between 3T and 7T. This is all that is necessary to compare local vessel walls across the two field strengths, despite possible differences in the original slice locations and orientations.

7.2.4 Quantification of Vessel Visibility

Data acquired using the proposed T2-weighted DANTE-SPACE protocol at 3T were compared to the proposed 7T protocol which used the neck-and-CoW RF shim (Section 6.3.3). This protocol provided the highest DANTE-SPACE contrasts and vessel acutance at 7T and was therefore selected to facilitate comparison of the best-case performance between the two field strengths.

After registration of the reconstructed datasets, the boundary delineation tool described in Section 6.3.5 (available at git.fmrib.ox.ac.uk/ndcn0873/acutance_TdB) was used for vessel acutance quantification. This boundary delineation method was previously found to achieve excellent inter- and intra-observer agreement, as well as high reproducibility of results on repeated measurements of the same vessel from different scan sessions [159]. The latter makes this a particularly useful approach for the quantitative comparison of data acquired from the same volunteers in separate scan sessions (at 3T and 7T). The resulting contrasts for data acquired at 3T and at 7T were compared slice-wise and vessel segment-wise.

The significance of differences in acutance between the various acquisitions was assessed using paired-sample one-tailed t-tests which test the null hypothesis that the optimized version of a protocol does not result in increased vessel visibility (G_{RMS} or inner/outer boundary acutance). The null hypothesis is rejected and results are considered significant for $p < 0.05$.

7.3 Results

7.3.1 Longitudinal Field-of-View and Spatial Saturation

A field-of-view in the longitudinal direction of 176 mm (176 slices) can be used with nonselective SPACE pulses at 7T without resulting in wraparound artefacts due to the limited spatial extent of both the transmit and receive fields. However, at 3T those fields reach further into the neck, as shown in Figure 7.1a. When using a smaller field-of-view (Figure 7.1c), this results in wraparound from the bottom to the top of the reconstructed image. Figure 7.1b indicates that when using 240 slices of 1 mm, a small amount of wraparound is visible on the image only when a 10-fold boosted scale is used, while artefacts of substantial size and intensity appear when using 176 slices. Based on this, a spatial saturation pulse covering a 70 mm slab below the FOV was included between the DANTE preparation module and the SPACE readout for further signal suppression inferior to the 176 mm FOV used for all acquisitions.

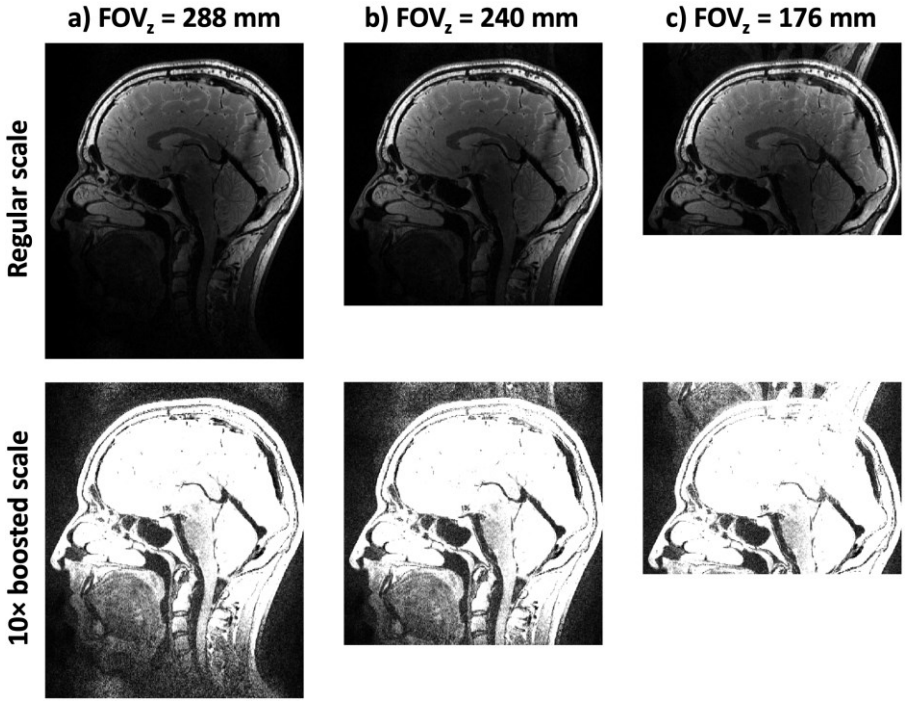

Figure 7.1: Central sagittal DANTE-SPACE slices at 3T using a longitudinal field-of-view of **(a)** 288 mm, **(b)** 240 mm, or **(c)** 176 mm. The top row shows reconstructions using a regular intensity scale (in arbitrary units), and the bottom row shows the same data on a 10× boosted scale to emphasize the increased bottom-to-top wraparound for smaller FOVs.

The performance in a phantom of this 70 mm spatial saturation band is shown in Figure 7.2, where the phantom bottle extends below the shown field-of-view. Again, longitudinal wraparound is visible in Figures (a) and (b), but this is successfully suppressed using the saturation band when it is placed at the bottom of the field-of-view in Figure (c).

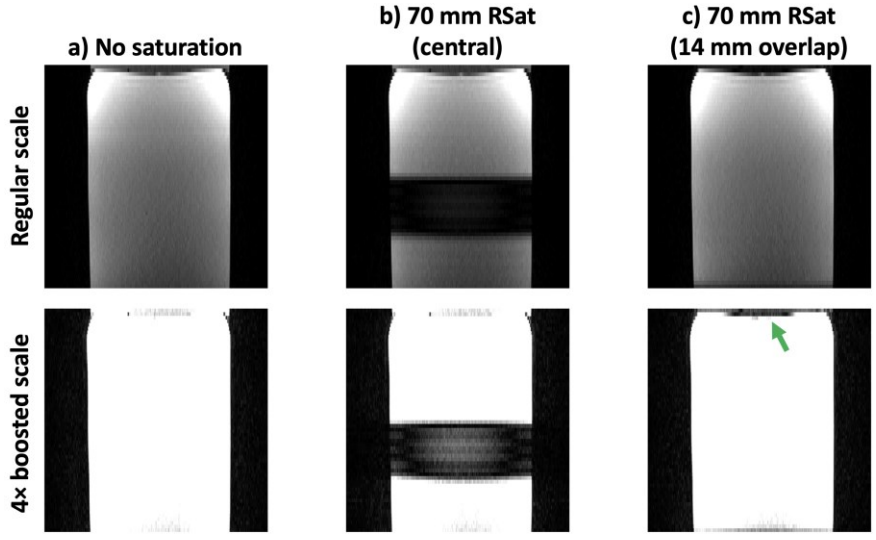

Figure 7.2: Central sagittal DANTE-SPACE slices at 3T in a phantom for acquisitions using **(a)** no spatial saturation, **(b)** a saturation region (RSat) of 70 mm in the centre of the phantom, and **(c)** a saturation region of 70 mm located inferior to the FOV with 14 mm overlap. The top row shows reconstructions using a regular intensity scale (in arbitrary

units), and the bottom row shows the same data on a 4× boosted scale. The green arrow in (c) indicates the region where longitudinal wrap-around is suppressed when using the proposed saturation band.

7.3.2 3T DANTE-SPACE Simulations

Figure 7.3 shows example initial DANTE-SPACE simulations of the vessel wall, CSF, and blood magnetization using the tissue parameters described in Table 7.1 and using the 7T-optimized DANTE-SPACE parameters for both 3T and 7T. The simulations are described in more detail in Chapter 5.

Both the longitudinal and transverse magnetization of vessel wall and CSF are highly similar between the simulations for 3T and 7T, although the resulting transverse magnetization during SPACE is higher for both tissues at 3T. The magnetization of spins in the blood changes more quickly at 3T due to the increased $B1^+$ coverage in the neck.

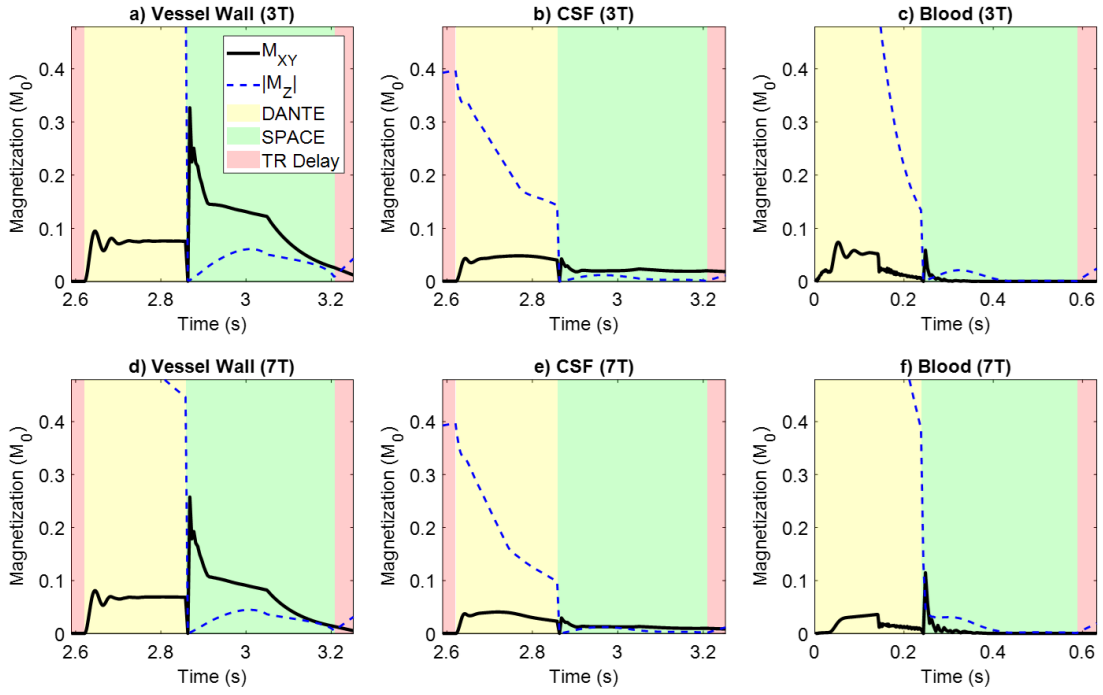

Figure 7.3: Example DANTE-SPACE simulations at 3T **(a-c)** and 7T **(d-f)** for vessel wall, CSF, and blood. The results during the second TR are shown for vessel wall and CSF to account for magnetization history effects from the previous repetition.

Expected signal levels for all tissue types were calculated from the transverse magnetization during the SPACE readout. Based on the resulting contrasts, the effects of changing the repetition time and echo spacing of the SPACE readout were first compared as shown in Figure 7.4. Results are shown as the signal levels of vessel wall, CSF, and blood as well as the resulting contrast between the vessel wall and both CSF and blood. Note that these simulations still make use of the 7T-optimized DANTE preparation (i.e., including 170

pulses of 12 degrees), which will be separately optimized later. The optimized vessel wall-CSF and vessel wall-blood contrasts are achieved using a TR of 2.10 seconds and SPACE echo spacing of 4.76 ms. Shorter echo spacing would further increase the vessel wall signal, but the minimum value is constrained by the durations of the gradients and RF pulses.

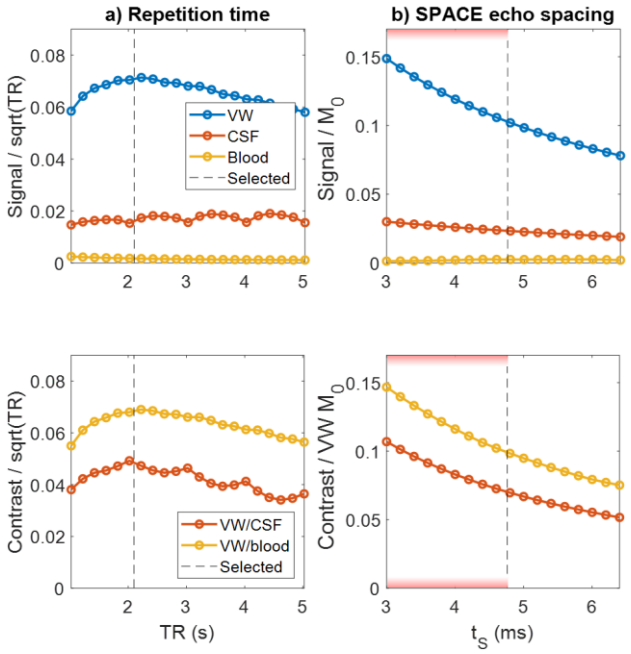

Figure 7.4: 3T simulation results when using different **(a)** repetition times and **(b)** SPACE echo spacings. Simulated signal levels for the vessel wall, CSF, and blood are shown in the top row, with the resulting VW/CSF and VW/blood contrasts in the bottom row. Dashed lines indicate the parameters selected for the 'optimized' protocol at 3T. The results in (a) are presented in terms of "Signal / √(TR)" such that the highest value corresponds to the parameters which would provide the highest contrast for scan time-matched acquisitions. The shaded red area in (b) indicates unattainable echo spacings on the scanner.

The SPACE echo train was automatically adjusted based on the selected scan parameters (echo train length, TR, TE_{eq}) and vessel wall relaxation times (T1, T2). The resulting flip angles at 3T and 7T are compared in Figure 7.5. Note that the generally higher flip angles at 3T result in a 40% increase in SAR (compared to when using the 7T flip angle train), but this was not found to be a limitation due to the inherently lower SAR at 3T.

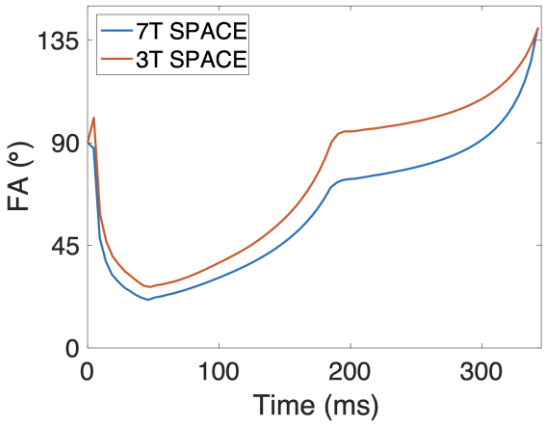

Figure 7.5: The SPACE flip angle trains for the optimized protocols at 7T and at 3T. Both start with the 90° excitation pulse, followed by 74 variable flip angle pulses with an echo spacing for of 4.62 ms at 7T or 72 variable flip angle pulses with an echo spacing of 4.76 ms at 3T. The exact values of each pulse are listed in Appendix A.3.

Using this optimized T2-weighted SPACE protocol, Figure 7.6 compares 3T SPACE (Figure 7.6a) to 3T DANTE-SPACE (Figure 7.6b-c) using two different arbitrary sets of DANTE parameters. Without DANTE preparation, very bright CSF signal is observed as expected for T2-weighted acquisitions, hindering vessel wall delineation. Both DANTE-prepared acquisitions successfully suppress most of this CSF signal, with slightly more remaining CSF signal when using less aggressive DANTE-preparation (fewer pulses, lower flip angles, and reduced gradient strengths), as indicated by the green arrows in Figure 7.6c.

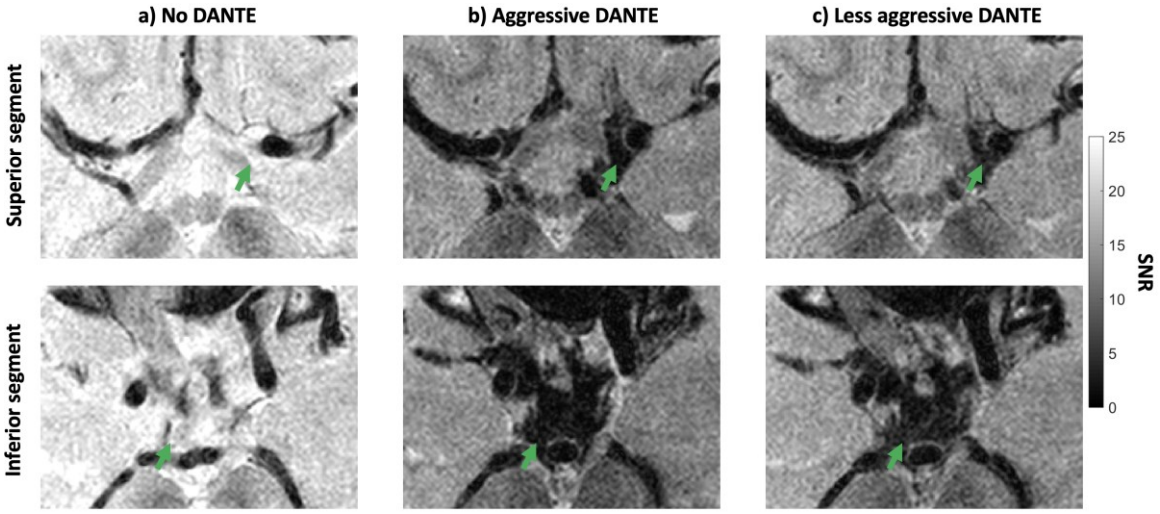

Figure 7.6: Two example transverse slice segments in the Circle of Willis showing acquisitions using the optimized SPACE protocol, **(a)** without DANTE-preparation, **(b)** with aggressive DANTE-preparation, and **(c)** with less aggressive DANTE-preparation. Green arrows indicate examples of notable CSF signal change between different acquisitions.

The preliminary results in Figure 7.6 indicate that, like at 7T, the exact choice of DANTE parameters affects the resulting vessel visibility for DANTE-SPACE acquisitions at 3T.

Therefore, the effects of varying the four main DANTE parameters were again simulated. As for the various optimizations at 7T shown in Chapter 6, those four parameters were the DANTE flip angle, the number of DANTE pulses, the DANTE gradient strength, and the DANTE interpulse duration. Figure 7.7 shows the simulation results for all four DANTE parameters, simulated for slowly pulsating vessel walls. The simulations indicate that good blood suppression is achieved using most DANTE parameter combinations at 3T, provided a sufficiently high DANTE flip angle is used. For all parameters, the highest contrasts are defined based on the trade-off between reduced CSF suppression (when using low parameter values) and reduced vessel wall signal (when using high parameter values). For the DANTE flip angles and the number of pulses, this results in the highest contrasts being achieved when using 250 pulses of 12°. The optimized DANTE gradient strength corresponds to the hardware-limited maximum of 28 mT/m, while the optimized DANTE interpulse time is 1.4 ms.

Compared to acquisitions without DANTE, the use of DANTE preparation using the proposed parameters reduces the CSF signal by 96% (-0.12 M_0) while reducing the vessel wall signal by 39% (-0.06 M_0). The blood signal is reduced by a further 94% (-0.01 M_0) but is already very low when DANTE is not used.

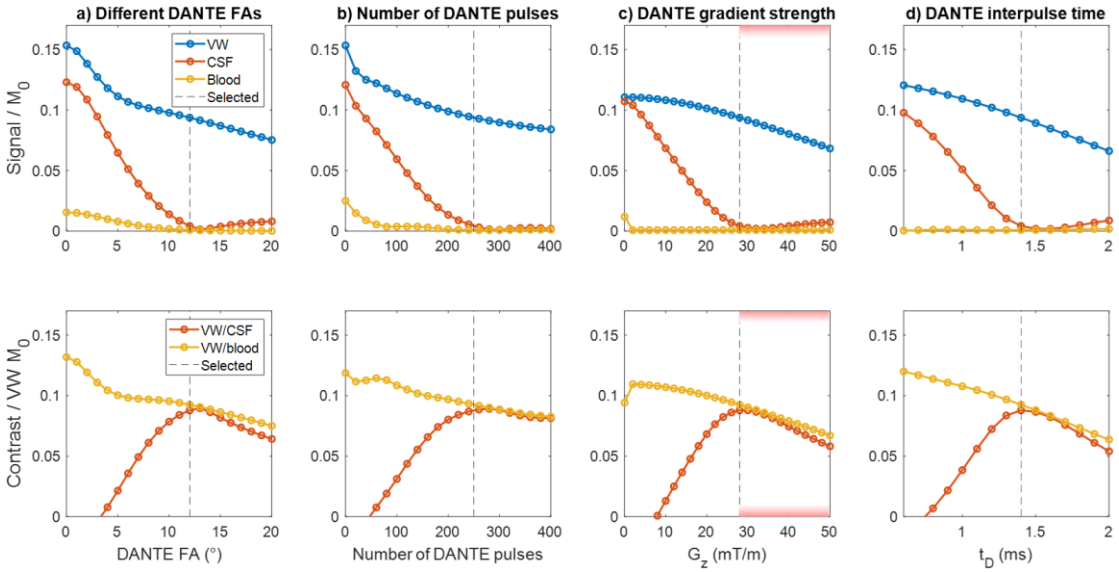

Figure 7.7: 3T simulation results for sweeps of the four main DANTE-parameters, simulated using slowly pulsating vessel walls. Separate subplots show the results when using various DANTE **(a)** flip angles; **(b)** numbers of pulses; **(c)** dephasing gradient strengths (with hardware-restricted values indicated in red); and **(d)** interpulse times. Simulated signal levels for the three tissue types are shown in the top row, with the resulting VW/CSF and VW/blood contrasts in the bottom row. Dashed lines indicate the parameters selected for the 'optimized' protocol at 3T.

7.3.3 *In Vivo* Acquisitions

An overview of the simulation-optimized T2-weighted DANTE-SPACE protocols for 3T (based on the previous sections) and for 7T (using the neck-and-CoW RF shim proposed in Section 6.3.3) is shown in Table 7.2, with the 7T literature protocol [35] also shown for reference. Data were acquired using the two optimized protocols as well as the 7T literature-based protocol in all 6 healthy volunteers. Additional SPACE-only acquisitions (without DANTE) were acquired in 3 out of 6 subjects.

			3T Optimized	7T Optimized	7T Literature
	Scan time	min	11:31	11:32	11:32
	TR	s	2.10	2.62	2.62
	Acquired resolution	mm	0.47 × 0.47 × 1	0.47 × 0.47 × 1	0.47 × 0.47 × 1
	Matrix size		512 × 384 × 176	512 × 384 × 176	512 × 384 × 176
	GRAPPA factor		3	4	4
DANTE	**DANTE – #pulses**		250	170	300
DANTE	**DANTE – flip angle**	°	12	12	10
DANTE	**DANTE – Gradient**	mT/m	28	40	40
DANTE	**DANTE – t_D**	ms	1.4	1.4	1.6
DANTE	**DANTE – RF Shim**		1Tx	Neck-and-CoW	1Tx
SPACE	**TE_{eq}**	ms	162	165	165
SPACE	**Echo spacing**	ms	4.76	4.62	4.62
SPACE	**Echo train length**		72	74	74
SPACE	**Bandwidth**	Hz/px	465	465	465

Table 7.2: Overview of the optimized T2-weighted DANTE-SPACE protocols at 3T and 7T. The first two columns show the respective optimized protocol, with the literature protocol shown in the third column for comparison.

An example slice segment in the CoW of a representative subject acquired at both 3T (with and without DANTE) and 7T (with DANTE) is shown in Figure 7.8. Slice segments are shown after rigid-body registration as described in Section 7.2.3. For the 3T acquisition without DANTE preparation (Figure 7.8a), black-blood contrast allowing for generally clear delineation of the inner vessel boundary is achieved in the MCAs. However, outer boundary delineation is impeded by bright CSF signal. The 3T DANTE-SPACE acquisition in Figure 7.8b achieves the desired CSF suppression, but at the cost of substantially decreased vessel wall signal. This limits the overall delineation of the vessel walls, which are generally more clearly defined in the registered 7T acquisition shown in Figure 7.8c.

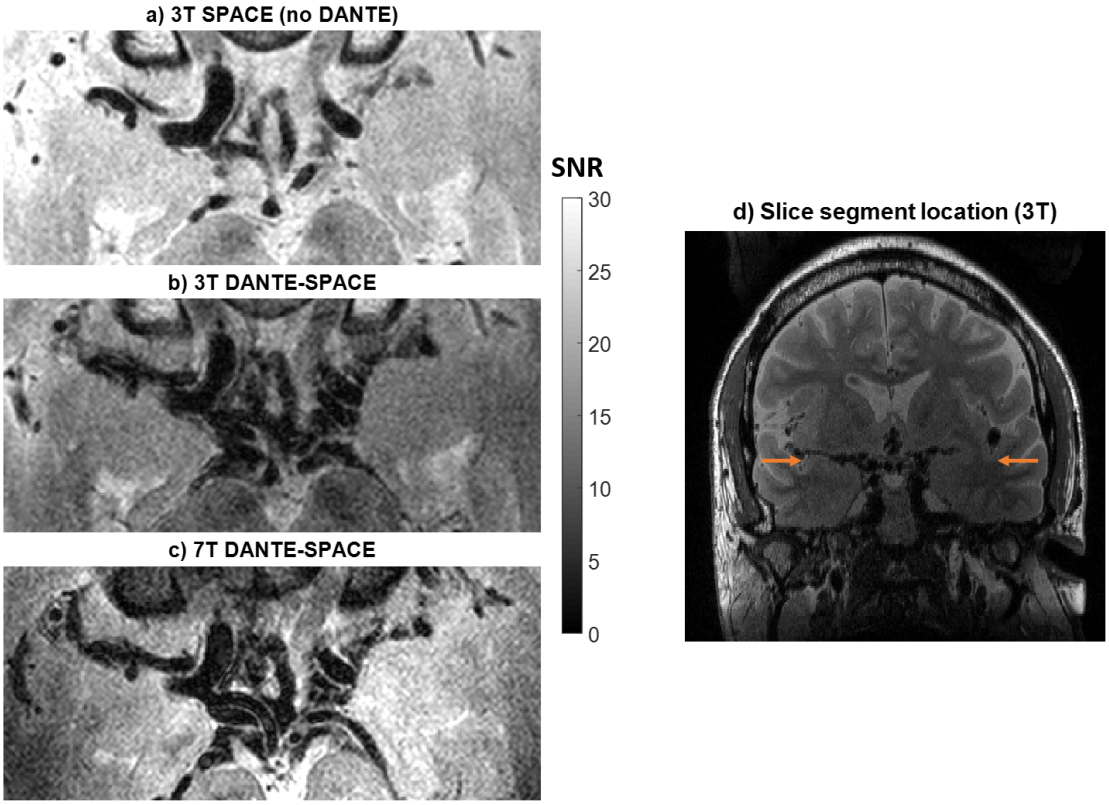

Figure 7.8: Transverse slice segment from a representative subject showing Circle of Willis as acquired using **(a)** T2-weighted SPACE without DANTE preparation at 3T; **(b)** T2-weighted DANTE-SPACE with optimized DANTE preparation at 3T; and **(c)** the registered slice segment acquired using DANTE-SPACE at 7T. The anatomical location of the slice segments in (a-c) is indicated by the orange arrows in the coronal slice shown in **(d)**.

7.3.4 Quantitative Comparison

All visible segments of the middle cerebral arteries (MCAs), basilar artery (BA), and distal internal carotid arteries (ICAs) in the 3 datasets from the 6 subjects were analysed using the method described in Section 6.3.5. Figure 7.9a shows the resulting average G_{RMS} values at different slice locations below the MCA M1-segment. As shown in Figure 7.9b, the G_{RMS} is consistently nearly two times higher at 7T than at 3T, with consistently increased values at all slice locations.

Figure 7.9c shows the correlation of the achieved G_{RMS} in both acquisitions for each individual 60° radial sub-segment. Again, substantially higher G_{RMS} is consistently observed at 7T than at 3T, with nearly two times higher contrast on average (dy/dx = 1.95).

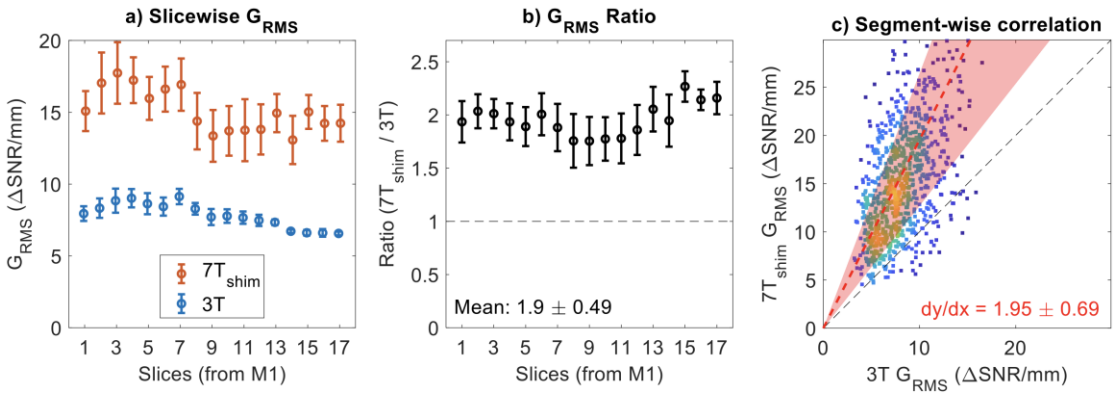

Figure 7.9: Comparison between the G_{RMS} on DANTE-SPACE data acquired at 3T and at 7T. The average results for all 6 subjects are shown using **(a)** the slice-wise G_{RMS} (corresponding to the slices shown in Figure 6.13), **(b)** the slice-wise ratio between the G_{RMS} of both protocols, and **(c)** the segment-wise G_{RMS} correlation between the two protocols, shown for radial sub-segments of 60°. The dashed red line and red shaded area indicate the mean ratio and 95% variance between the respective acquisitions, with the corresponding values indicated in red.

When comparing all vessel segments in all slices of the 6 subjects, the average G_{RMS} at 7T is again nearly two times higher, with an average difference in G_{RMS} of 8.0 ± 1.7 ΔSNR/mm ($p < 0.001$). The inner and outer boundary acutance are also significantly higher at 7T, with an average difference in inner acutance of 13.8 ± 3.2 CNR/mm ($p < 0.001$) and an average difference in outer acutance of 7.6 ± 1.8 CNR/mm ($p < 0.001$).

7.4 Discussion

In this work, the use of DANTE-SPACE as a 3D T2-weighted intracranial vessel wall imaging sequence at 3T was studied. The sequence parameters were first optimized using the previously presented simulation framework, after which the resulting achieved vessel delineation was compared between 3T and 7T.

The SPACE simulations in Figure 7.4 indicate that a shorter TR can be used at 3T than at 7T (2.12 s instead of 2.62 s). In the proposed protocol, this reduced TR makes it possible to acquire data at 3T using a lower GRAPPA acceleration factor ($R = 3$ instead of $R = 4$) without requiring a large change in the SPACE echo train length. The echo train length is the only SPACE parameter which was not either determined based on simulation results or matched to the 7T protocol. Instead, it was selected to achieve matched scan times at both field strengths. The resulting echo train length of 72 at 3T is similar to that of 74 at 7T (both shown in Figure 7.5), and only slightly shorter than the echo train length of 77 used in previous T2-weighted SPACE implementations at 3T [39].

Figure 7.7 shows the simulation results for various DANTE parameters, which directly affect the amounts of CSF signal suppression as indicated by the preliminary data shown in Figure 7.6. Compared to the result of the corresponding optimizations at 7T (Figure 6.6), the biggest difference in the resulting optimized parameters is an increased number of DANTE pulses at 3T (250 pulses at 3T versus 170 pulses at 7T). This is mainly a result of the lower maximum gradient strength available on the scanner used at 3T and the longer T2 relaxation time of CSF, both of which result in a slower suppression of the CSF signal. In addition to those differences in DANTE-SPACE parameters, data acquired at 3T also require the addition of a spatial saturation band inferior to the acquired FOV to prevent longitudinal (head-neck) wraparound, as is visible in Figure 7.1 and Figure 7.2.

The full proposed T2-weighted DANTE-SPACE protocol for 3T is shown in Table 7.2 alongside the corresponding optimized protocol at 7T. The total scan time, resolution, and matrix size of the two protocols were matched for fair comparison, while the TE and bandwidth remained similar. Most other values were optimized based on the various simulation results.

The registered CoW segment in Figure 7.8, acquired using T2w DANTE-SPACE at 3T and 7T as well as 3T SPACE without DANTE, shows that rigid-body registration limited to 3D shift and in-plane rotation achieves accurate registration. Good qualitative agreement was observed for all volunteers after registration using those 4 out of 6 possible degrees of freedom. This is consistent with the expectation of there being only small absolute displacements arising from any remaining rotations near the CoW due to its anatomical location near the centre of rotation.

The 3T (no DANTE) SPACE acquisition in Figure 7.8a shows high CSF signal levels around all vessels, obscuring vessel delineation as expected for T2-weighted acquisitions. Consistent with the simulations, the addition of the proposed DANTE preparation (Figure 7.8b) achieves good CSF suppression, while a substantial SNR reduction is visible throughout the soft tissue, and in particular in the vessel walls. When comparing the DANTE-SPACE acquisitions at 3T and 7T (Figure 7.8b-c), similar CSF suppression can be observed but with substantially higher vessel wall signal at 7T. This allows for better delineation of all visible vessels, although that still remains inherently limited by variations in vessel wall signal levels and poor contrast relative to brain parenchyma.

Quantitatively, T2-weighted DANTE-SPACE images at 7T achieve significantly higher vessel contrasts at all slice locations (Figure 7.9a-b) and for the vast majority of the vessel

segments (Figure 7.8c). Overall, a near two-fold increase in G_{RMS} is observed at 7T compared to 3T, with significant improvements in both the inner and outer vessel acutance. All data (3T and 7T) presented here were acquired using head-only 32-channel receive coils for fair comparison. However, acquisitions at 3T could benefit from the use of an integrated head/neck receive coil, which has previously been shown to facilitate simultaneous carotid and intracranial vessel wall evaluation using a T1-weighted DANTE-SPACE acquisition [36].

The proposed 3T T2-weighted DANTE-SPACE protocol uses a long DANTE preparation consisting of 250 pulses with relatively high flip angles of 12°, which was required to achieve sufficient CSF suppression. For comparison, Zhang et al. [39] previously acquired T2-weighted DANTE-SPACE data at 3T using 150 DANTE pulses of 8°. Based on the resulting acquisitions, they concluded that the CSF signal was not well suppressed and obstructed vessel wall visualization. This observation is consistent with the results of additional simulations using our simulation framework with the parameters as used by Zhang et al. [39], which suggest that their DANTE preparation results in a reduction in CSF signal of only 51%, as opposed to a 96% reduction when simulating using the parameters proposed here.

T1-weighted DANTE-SPACE protocols (as used in the literature [30,36–38,40–43]) require shorter repetition and echo times, resulting in shorter scan times to achieve a similar resolution. T1-weighted acquisitions also benefit from lower native DANTE signal, and the use of DANTE for further CSF suppression is more efficient when using shorter TRs due to the reduced time for signal recovery between consecutive DANTE-SPACE modules. This explains why good black-CSF contrast can be achieved using less aggressive DANTE preparation (e.g., 150 pulses of 8° [37,38,40], 94 pulses of 13° [43], or 100 pulses of 10° [36]) for T1-weighted DANTE-SPACE protocols. Less aggressive DANTE preparation also results in minimal vessel wall signal suppression, whereas using the greater degree of DANTE preparation that is required for T2-weighted DANTE-SPACE we observe a substantial decrease in the vessel wall signal (both in simulations and *in vivo*). This suggests that DANTE preparation might not be the ideal CSF suppression method for T2-weighted SPACE protocols at 3T, where T2-dependent inversion-recovery approaches (such as T2IR [39,171]) have previously been found to provide CSF suppression with minimal vessel wall signal reduction. However, our results indicate that, compared to 3T, DANTE-SPACE at 7T benefits from more efficient CSF-suppression (requiring fewer

DANTE pulses), while methods such as T2IR would be less feasible at ultra-high field due to high SAR requirements (2.4× higher than the proposed DANTE preparation). Therefore, DANTE preparation is a good option for CSF-suppression in T1-weighted and 7T T2-weighted vessel wall imaging, but better options might be available for T2-weighted imaging at lower field strengths.

7.5 Conclusion

Compared to 7T, T2-weighted DANTE-SPACE vessel wall imaging at 3T requires more DANTE pulses to achieve sufficient CSF suppression. This also leads to a substantial reduction in vessel wall signal, resulting in vessel contrasts which are 2× lower than at 7T. Therefore, DANTE-preparation might be more suitable for VWI at ultra-high field strengths or with different contrasts.

8

Summary and Future Directions

The aim of this thesis was to improve cerebrovascular imaging at 7T, both to image the vessels themselves, and to image the vessel wall. In general, this means utilizing the higher SNR at 7T while overcoming the intrinsic limitations of ultra-high field MRI, such as field inhomogeneity, increased energy deposition, and long scan times. This chapter briefly discusses the main results of the research presented in this thesis and presents possible future directions to further improve cerebrovascular imaging at 7T based on this thesis.

8.1 Head-and-Neck $B1^+$ Mapping and Shimming

Chapter 3 provides a method to simultaneously characterize the transmit field in both the head and the neck. This method was used to produce a 10-subject multi-channel $B1^+$ database using the widely-used Nova Medical 8-channel transmit coil, which was made publicly available. Using this multi-channel $B1^+$ data, it is shown that the fields in the feeding arteries in the neck can relatively easily be optimized using universal RF shims. As a result, it is possible to reduce the required SAR of acquisitions at 7T by locally increasing the $B1^+$ efficiency using RF shims. This is in particular useful for modalities which greatly benefit from the increased SNR at 7T but are limited by high SAR, such as pseudo-continuous ASL (PCASL). Current PCASL implementations at 7T use very long repetition times of up to 9 seconds [86,102] to remain within SAR limits. This SAR stringency is predominantly caused by the high-SAR ASL tagging pulses in the neck, which account for up to 80% of the sequence SAR [102]. The results in Chapter 3 show that universal RF shims can reduce the SAR to achieve a given flip angle in a slice in the neck by over 50%, which should facilitate a substantial reduction in the acquisition times of PCASL at 7T.

The head-and-neck multi-channel $B1^+$ data presented in Chapter 3 also make it possible to characterize and manipulate the effect of $B1^+$ variations on the suppression of inflowing arterial blood for intracranial vessel wall imaging. This is used in Chapters 5 and 6, where the black-blood contrast of DANTE-SPACE intracranial vessel wall imaging is simulated and improved based on the measured $B1^+$ in both the head and the neck.

The scope of the results presented in Chapter 3 is limited to the improvements that can be achieved using RF shims with head-only pTx coils. Further work could look into additional improvement in the $B1^+$ in the neck by combining pTx with dielectric pads. Although this might enhance the total available $B1^+$ in the neck, the potential impact of variability in pad positioning on the use of universal RF shims needs to be evaluated.

8.2 Compressed Sensing MR Angiography

In Chapter 4, retrospectively undersampled TOF MRA data were used to determine undersampling parameters which optimize the visibility of (in particular) small vessels in the brain within reasonable scan times. Using those optimized parameters (which include very small calibration regions of 12×12 k-space lines), small vessels such as the lenticulostriate arteries can be visualized at very high isotropic resolutions within a few minutes at 7T. Shorter scan times improve patient comfort and clinical workflows but can also provide improved image quality compared to longer (less undersampled) acquisitions in the presence of subject motion, as is also visible in some of the data presented in Chapter 4. Since those data were acquired from healthy volunteers with previous MRI experience, increased subject motion can be expected in patients and elderly populations. Although accelerated acquisitions benefit from reduced motion in such cases, individual motion-corrupted k-space lines can have a more detrimental effect on the reconstructed image quality due to propagation of inaccuracies into missing k-space lines. Therefore, compressed sensing reconstructions could achieve improved robustness through the correction or reacquisition of motion-corrupted k-space lines.

The optimization of TOF MRA undersampling parameters in Chapter 4 provides the largest improvement in the visibility of small arteries. This includes the lenticulostriate arteries, which are of particular clinical interest due to their expected involvement in the early stages of vascular dementia [3] and association with lacunar infarcts [172]. Therefore, 7T MRI studies into the lenticulostriate arteries could provide further understanding of the progression and possible treatment of such diseases.

8.3 DANTE-SPACE

Chapters 5, 6, and 7 introduce and use an EPG-based simulation framework for the optimization of the T2-weighted DANTE-SPACE sequence. Although various previous

DANTE-SPACE implementations in the literature used simulations to propose sets of optimized DANTE-SPACE parameters, the addition of $B1^+$ effects and various physiological processes was found to result in a more accurate representation of the resulting contrast mechanisms. As a result, the simulations provided optimized protocols for T2-weighted DANTE-SPACE at 3T and 7T, which are shown again in Table 8.1. Direct comparison of data acquired at both field strengths showed that the sequence provides nearly two times higher contrast-to-noise ratio at 7T than at 3T.

			3T	7T
			Optimized	Optimized
	Scan time	min	11:31	11:32
	TR	s	2.10	2.62
	Acquired resolution	mm	0.47 × 0.47 × 1	0.47 × 0.47 × 1
	Matrix size		512 × 384 × 176	512 × 384 × 176
	GRAPPA factor		3	4
DANTE	**DANTE – #pulses**		250	170
DANTE	**DANTE – flip angle**	°	12	12
DANTE	**DANTE – Gradient**	mT/m	28	40
DANTE	**DANTE – t_D**	ms	1.4	1.4
DANTE	**DANTE – RF Shim**		1Tx	Neck-and-CoW
SPACE	**TE_{eq}**	ms	162	165
SPACE	**Echo spacing**	ms	4.76	4.62
SPACE	**Echo train length**		72	74
SPACE	**Bandwidth**	Hz/px	465	465

Table 8.1: Optimized T2-weighted DANTE-SPACE protocols at 3T and 7T.

8.3.1 Further Sequence Optimization

The optimization at 7T included the use of neck-and-CoW pTx RF shims during the DANTE preparation, which provided slightly improved suppression of the inflowing blood. Future work could further employ the potential of pTx. In particular, direct signal control [173], in which different RF shims are used for different pulses in a sequence to generate uniform resulting signal despite nonuniform $B1^+$ fields, has previously been shown to provide excellent results for 3D fast spin-echo acquisitions at 3T. Therefore, using direct signal control for the SPACE readout element of DANTE-SPACE acquisitions could provide improved signal homogeneity throughout the brain. Another possible modification to the SPACE readout would be to account for the magnetization history from the DANTE preparation in the calculation of the SPACE flip angle train, which could provide a modest improvement to the signal level and sharpness of the vessel walls.

Currently, T2-weighted DANTE-SPACE acquisitions are limited by long scan times (> 10 minutes). Further studies could look into reducing this scan time, for example by employing compressed sensing reconstruction (which has previously successfully been used for T1-weighted DANTE-SPACE at 3T [37]). In additional to a scan time reduction, compressed sensing acceleration could potentially also reduce the noise amplification relative to our current T2-weighted DANTE-SPACE protocol at 7T (which uses GRAPPA with $R = 4$), improving the SNR and CNR in central brain regions such as the CoW.

Typical DANTE-SPACE acquisitions are also limited by the achieved resolution, and the acquisition of anisotropic voxels hinders the analysis of vessel segments along their cross-sectional plane. However, increasing the resolution along one or multiple dimensions leads to further increased scan times and reduced contrast, and disagreement in the typical wall thickness estimates from histological and MRI assessments makes it unclear to what extent increased resolutions are desirable [26].

Furthermore, turbo-spin echo acquisitions typically suffer from blurring due to the inherently different echo times at different k-space locations (which were sampled at different echo times). Based on transverse magnetization evolutions simulated using the simulation framework presented in Chapter 5, it should be possible to reduce this effect by scaling the various acquired k-space lines based on the relative simulated signal at their acquired echo time. Finally, the presented simulation framework can also be used in future work for further parameter optimizations. For that, direct experimental validation of the simulation results (e.g., comparison of simulation-based and *in vivo* acquisition results using different sets of protocol parameters) would be helpful to assess the accuracy of the simulations. However, such comparisons are difficult due to the currently required large FOV for each acquisition, resulting in long scan times (and therefore limiting the possible number of acquired datasets in a single scan session). For this, it would be helpful to either employ further acceleration methods as described above, or to reduce the acquired FOV as described in Appendix A.2 to reduce the scan time per acquisition.

8.3.2 Motion Correction

The optimized DANTE-SPACE protocols at 3T and 7T use a repetition time of 2.10 s and 2.62 s, respectively. Since the corresponding DANTE-SPACE modules only take 0.7 s and 0.6 s, this leaves a TR delay of up to 2 seconds during each repetition. Since high-resolution and long-acquisition time scans are susceptible to subject motion, this down time could be used to identify and correct for motion between different readouts.

Navigator-based motion detection methods like fat navigators [174] could be used within these long down times, as well as methods such as pilot tone [175] or pTx scattering [176] which rely on the transmission (either from an external transmitter or from a pTx coil) of signals at non-resonance frequencies.

Besides bulk subject motion, various results presented in this thesis showed that pulsatile motion in the vessel wall has a substantial but undesired attenuating effect on the achieved signal level. It might be possible to reduce this effect by implementing cardiac gating such that the motion-sensitized DANTE preparation is played out during periods of the cardiac cycle with limited vessel wall motion. The simulation framework presented in Chapter 5 could be used to estimate the resulting signal improvement, and whether the benefits of such gating would outweigh the resulting scan time increase. Furthermore, it should be considered that periods of limited vessel wall motion might correspond to times with lower CSF velocities, thereby reducing the CSF suppression.

8.3.3 T1-Weighted DANTE-SPACE

All DANTE-SPACE results presented in this thesis are specific for T2-weighted DANTE-SPACE. However, comprehensive assessment of vascular pathology also requires, in addition to other image contrasts, T1-weighted acquisitions. Although T1-weighted DANTE-SPACE has extensively been studied at 3T, it has not yet been implemented at 7T. Using the simulations framework presented in this thesis, it should also be possible to assess and optimize T1-weighted vessel wall imaging using DANTE-SPACE at 7T.

Modification of the simulation framework from T2-weighted to T1-weighted protocols requires two changes, which are shown in Figure 8.1: the use of SPACE flip angle trains corresponding to T1-weighted acquisitions, and the modified scheme for the allocation of different SPACE echoes to the corresponding k-space locations. The latter was not required for T2-weighted simulations since the centre of k-space corresponds to the central echo, such that the PSF can directly be calculated from the readout train. However, the shorter TE of T1-weighted acquisitions requires a modification of the k-space sampling scheme in which the centre of k-space is sampled near the start of the readout train.

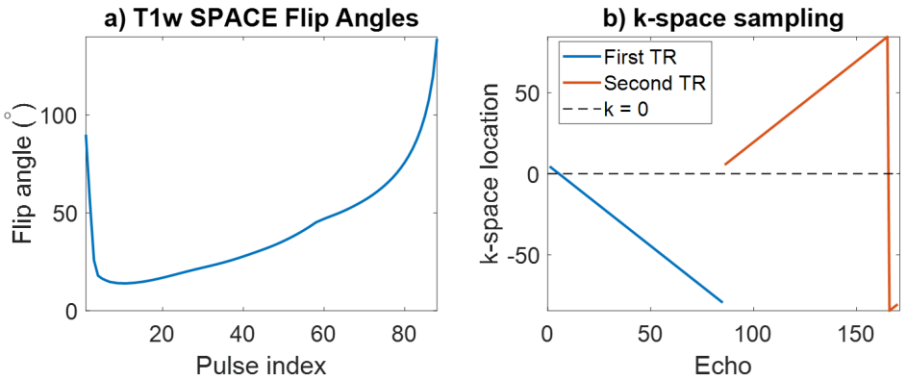

Figure 8.1: The SPACE flip angle train **(a)** and k-space sampling **(b)** used for T1-weighted DANTE-SPACE simulations at 7T. Results were based on IDEA simulations of a low-resolution T1w-protocol using literature parameters used at 3T [40], including TE = 24 ms, TR = 1.14 s, and a SPACE echo train length of 85. Note that for each partition, measured values from two SPACE readouts (shown in blue and orange) are used to fill the k-space plane.

It should be noted that the data in Figure 8.1 were generated using a simplified (i.e., low resolution with a relatively long echo train length) protocol based on the TE and TR used at 3T. Therefore, the results discussed in this section should be considered as proof-of-principle indications of T1-weighted simulations using the framework presented in Chapter 5.

Figure 8.2 shows the results of VW, CSF, and blood simulations using the SPACE flip angle train in Figure 8.1a. Without DANTE, the desired constant transverse magnetization is observed throughout the centre of k-space (note that the first two SPACE pulses are introduction pulses during which no data are acquired). As expected for T1-weighted acquisitions, low SPACE signal is observed for both the CSF and the blood. When including DANTE, signal suppression is observed for all three tissue types.

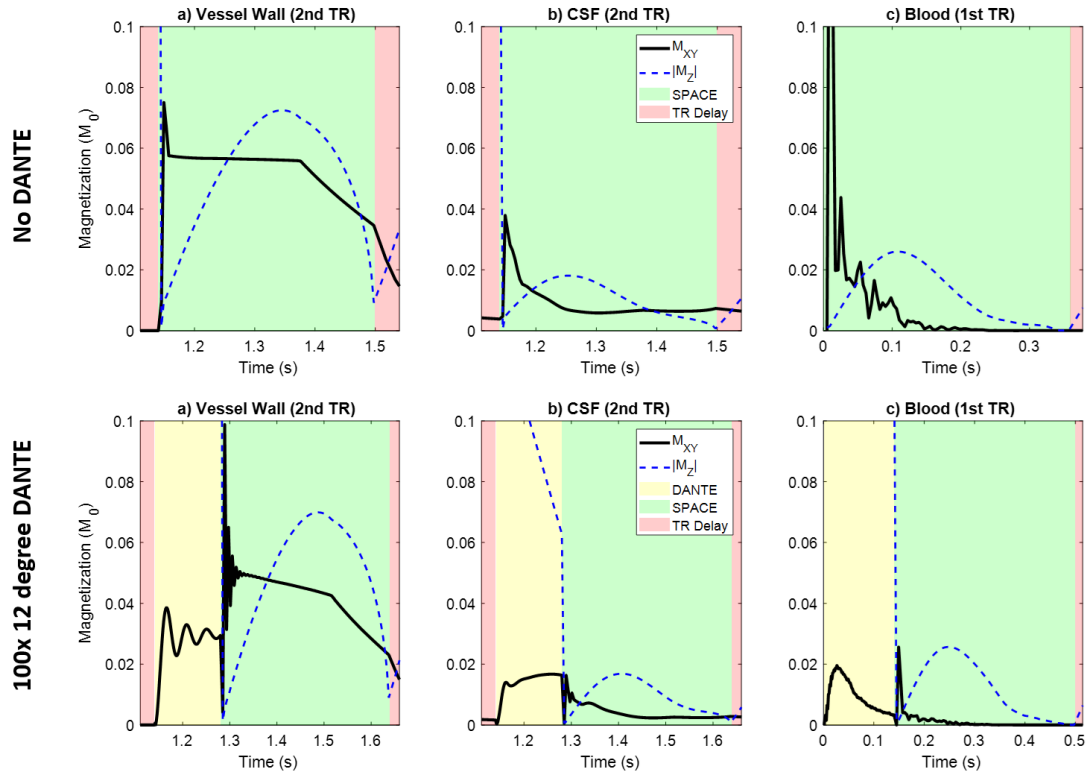

Figure 8.2: Initial T1-weighted SPACE (first row) and DANTE-SPACE (second row) simulations of **(a)** vessel wall, **(b)** CSF, and **(c)** blood.

By allocating the simulated signal intensities during SPACE (as shown in Figure 8.2) to the corresponding k-space locations (as shown in Figure 8.1b) and calculating the resulting point-spread function, the resulting signal from each simulation can be calculated. This makes it possible to assess the achieved signal levels and contrasts when using different protocol parameters. For example, the results when using different DANTE parameters are shown in Figure 8.3. Since the CSF and blood signal levels are inherently low for T1-weighted acquisitions, the addition of DANTE preparation does not make a big difference to the resulting contrasts (2nd row). Therefore, optimization of the CNR (which was generally used as the optimization target in this thesis) does not provide the most informative results. Alternatively, one could optimize parameters by requiring the CSF and blood signal levels (in the first row) to be below the noise threshold (which we, based on T2-weighted comparisons, expect to be around $0.006M_0$), or by aiming for high signal ratios (3rd row) while maintaining a certain minimum amount of contrast.

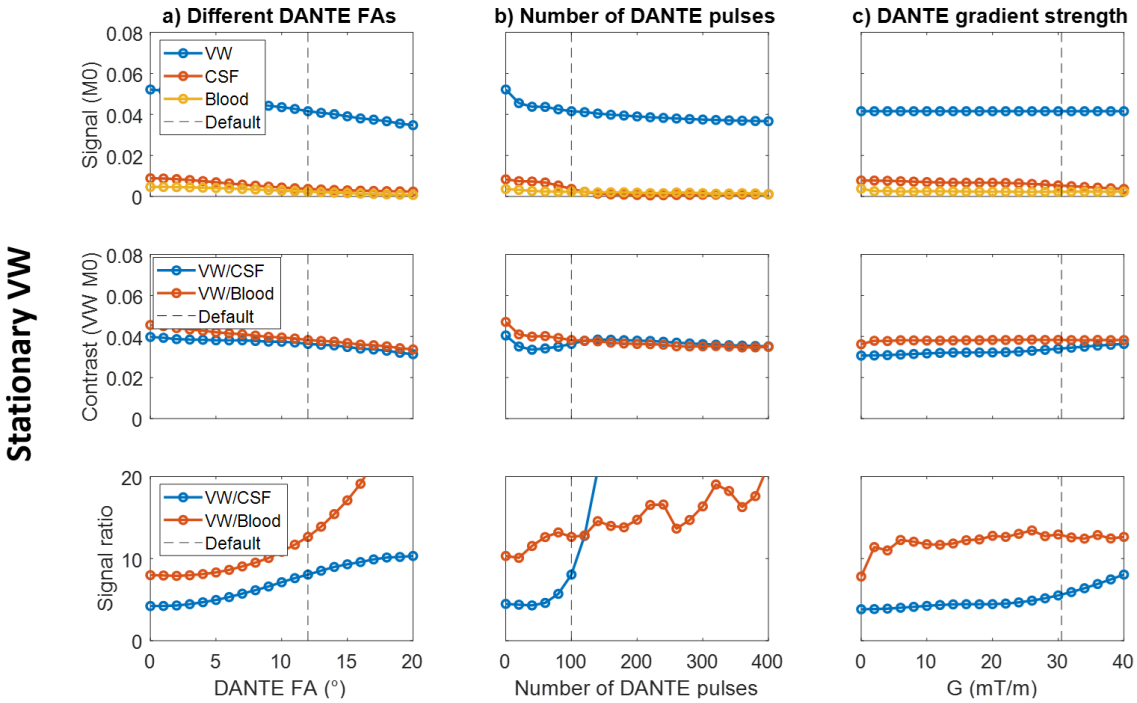

Figure 8.3: Example parameter optimization for T1-weighted DANTE-SPACE. Results are shown for **(a)** different DANTE flip angles, **(b)** different numbers of DANTE pulses, and **(c)** different DANTE gradient strengths. The three rows show the signal levels for the individual tissue types, the resulting contrasts, and the corresponding signal ratios (i.e., Sig_A / Sig_B). Results are shown assuming stationary vessel walls.

The results in Figure 8.3 show simulations for the case of stationary vessel wall. However, various results in this thesis suggested that (at least for T2-weighted optimization) it is important to include the attenuating effects of slowly pulsating vessel walls. Therefore, the simulations were repeated with vessel wall motion, and are reported in Figure 8.4. This again shows that the resulting contrasts and signal ratios are different when considering pulsating vessel walls, although the effect is less influential than for T2-weighted acquisitions (indicating that T1-weighted acquisitions might be more robust to contrast variations due to VW pulsation).

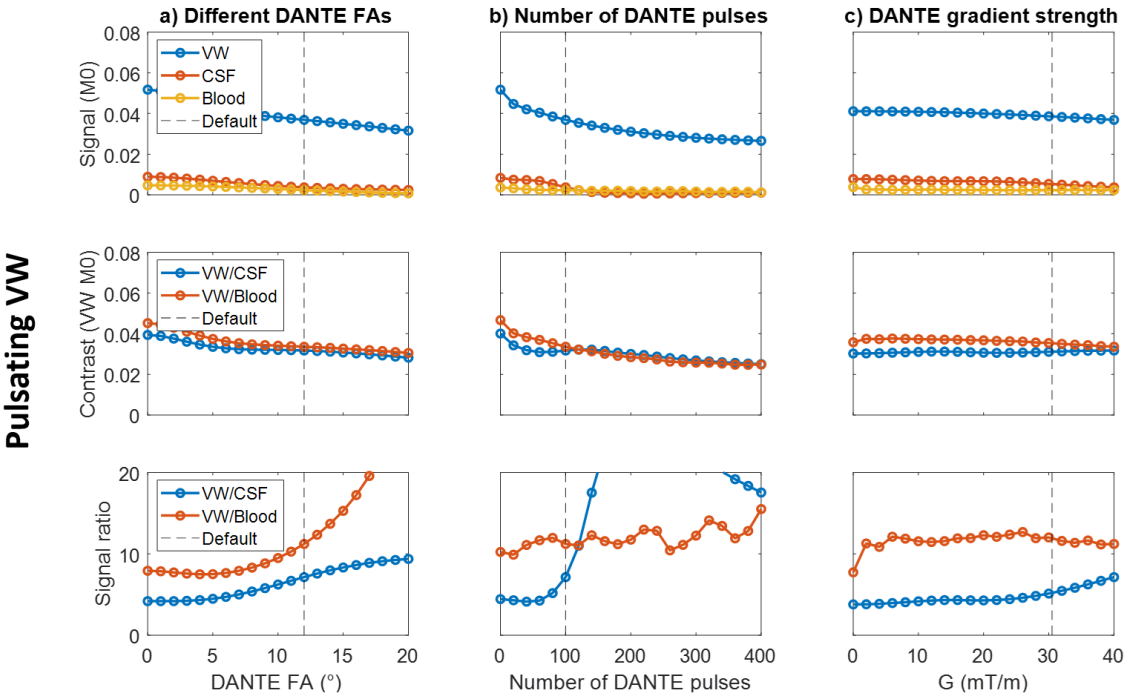

Figure 8.4: Example parameter optimization for T1-weighted DANTE-SPACE. Results are shown for **(a)** different DANTE flip angles, **(b)** different numbers of DANTE pulses, and **(c)** different DANTE gradient strengths, all simulated using slowly pulsating vessel wall as described in Chapter 5.

As a final remark it should be noted that different SAR considerations can be expected for T1-weighted acquisitions compared to T2-weighted acquisitions. For the data shown here, the T1-weighted TR (1.14 s) is 2.3× shorter than the T2-weighted TR (2.62 s). However, the T1-weighted SPACE flip angles are typically lower. As the sum-of-squares of the SPACE pulse flip angles (which is proportional to the resulting SAR) is 1.7× lower, this suggests an increase in SAR for T1-weighted acquisitions using the protocols used here of roughly 39%. The exact change in SAR directly depends on the choice of (amongst other parameters) TR, SPACE echo train length, DANTE flip angles and number of pulses. However, this indicates that SAR limitations should be carefully considered when designing a T1-weighted DANTE-SPACE protocol at 7T.

8.3.4 Further Validation

All DANTE-SPACE data presented in this thesis were acquired from healthy volunteers. However, the acquired image quality could be different in patient populations. The two main likely differences are increased patient motion, which would decrease the overall image quality, and increased vessel wall stiffness, which reduces wall signal attenuation and could therefore improve the acquired vessel wall delineation. Furthermore, validation in patients is also required to assess to what extent plaque components can be distinguished

using T2-weighted DANTE-SPACE at 7T. Therefore, patient validation of the sequence is essential to determine its clinical potential, both in general and compared to other intracranial vessel wall imaging modalities.

References

[1] Mergenthaler P, Lindauer U, Dienel GA, Meisel A. Sugar for the brain: The role of glucose in physiological and pathological brain function. Trends Neurosci 2013;36:587–97. https://doi.org/10.1016/j.tins.2013.07.001.

[2] Gorelick PB. The global burden of stroke: persistent and disabling. Lancet Neurol 2019;18:417–8. https://doi.org/10.1016/S1474-4422(19)30030-4.

[3] Seo SW, Kang CK, Kim SH, Yoon DS, Liao W, Wörz S, et al. Measurements of lenticulostriate arteries using 7T MRI: New imaging markers for subcortical vascular dementia. J Neurol Sci 2012;322:200–5. https://doi.org/10.1016/j.jns.2012.05.032.

[4] Hendrikse J, Zwanenburg JJ, Visser F, Takahara T, Luijten P. Noninvasive depiction of the lenticulostriate arteries with time-of-flight MR angiography at 7.0 T. Cerebrovascular Diseases 2008;26:624–9. https://doi.org/10.1159/000166838.

[5] Liu Q, Huang J, Degnan AJ, Chen S, Gillard JH, Teng Z, et al. Comparison of high-resolution MRI with CT angiography and digital subtraction angiography for the evaluation of middle cerebral artery atherosclerotic steno-occlusive disease. International Journal of Cardiovascular Imaging 2013;29:1491–8. https://doi.org/10.1007/s10554-013-0237-3.

[6] Philipp LR, McCracken DJ, McCracken CE, Halani SH, Lovasik BP, Salehani AA, et al. Comparison between CTA and digital subtraction angiography in the diagnosis of ruptured aneurysms. Clin Neurosurg 2017;80:769–77. https://doi.org/10.1093/neuros/nyw113.

[7] Herzig R, Buřval S, Křupka B, Vlachová I, Urbánek K, Mareš J. Comparison of ultrasonography, CT angiography, and digital subtraction angiography in severe carotid stenoses. Eur J Neurol 2004;11:774–81. https://doi.org/10.1111/j.1468-1331.2004.00878.x.

[8] Farahmand M, Farahangiz S, Yadollahi M. Diagnostic accuracy of magnetic resonance angiography for detection of intracranial aneurysms in patients with acute subarachnoid hemorrhage; a comparison to digital subtraction angiography. Bull Emerg Trauma 2013;1:147–51.

[9] Sarkar S, Ghosh S, Ghosh SK, Collier A. Role of transcranial Doppler ultrasonography in stroke. Postgrad Med J 2007;83:683–9. https://doi.org/10.1136/pgmj.2007.058602.

[10] Jaiswal SK, Fu-Ling Y, Gu L, Lico R, Changyong F, Paula A. Accuracy of Transcranial Doppler Ultrasound Compared with Magnetic Resonance Angiography in the Diagnosis of Intracranial Artery Stenosis. J Neurosci Rural Pract 2019;10:400–4. https://doi.org/10.1055/s-0039-1696586.

[11] Saloner D. An introduction to MR angiography. RadioGraphics 1995;15:453–65. https://doi.org/10.1148/radiographics.15.2.7761648.

[12] Markl M, Frydrychowicz A, Kozerke S, Hope M, Wieben O. 4D flow MRI. Journal of Magnetic Resonance Imaging 2012;36:1015–36. https://doi.org/10.1002/jmri.23632.

[13] Alsop DC, Detre JA, Golay X, Günther M, Hendrikse J, Hernandez-Garcia L, et al. Recommended Implementation of ASL Perfusion MRI for Clinical Applications. Magn Reson Med 2015;73:102–16.

[14] Okell TW. Combined angiography and perfusion using radial imaging and arterial spin labeling. Magn Reson Med 2019;81:182–94. https://doi.org/10.1002/mrm.27366.

[15] Zhang HL, Maki JH, Prince MR. 3D contrast-enhanced MR angiography. Journal of Magnetic Resonance Imaging 2007;25:13–25. https://doi.org/10.1002/jmri.20767.

[16] Kanda T, Ishii K, Kawaguchi H, Kitajima K, Takenaka D. High signal intensity in the dentate nucleus and globus pallidus on unenhanced T1-weighted MR images: Relationship with increasing cumulative dose of a gadoliniumbased contrast material. Radiology 2014;270:834–41. https://doi.org/10.1148/radiol.13131669.

[17] Buxton RB, Edelman RR, Rosen BR, Wismer GL, Brady TJ. Contrast in Rapid MR Imaging: T1- and T2-Weighted Imaging. J Comput Assist Tomogr 1987;11:7–16. https://doi.org/10.1097/00004728-198701000-00003.

[18] Parker DL, Yuan C, Blatter DD. MR angiography by multiple thin slab 3D acquisition. Magn Reson Med 1991;17:434–51. https://doi.org/10.1002/mrm.1910170215.

[19] Mazighi M, Labreuche J, Gongora-Rivera F, Duyckaerts C, Hauw JJ, Amarenco P. Autopsy prevalence of intracranial atherosclerosis in patients with fatal stroke. Stroke 2008;39:1142–7. https://doi.org/10.1161/STROKEAHA.107.496513.

[20] Mandell DM, Mossa-Basha M, Qiao Y, Hess CP, Hui F, Matouk C, et al. Intracranial vessel wall MRI: Principles and expert consensus recommendations of the American society of neuroradiology. American Journal of Neuroradiology 2017;38:218–29. https://doi.org/10.3174/ajnr.A4893.

[21] Biasiolli L, Lindsay AC, Chai JT, Choudhury RP, Robson MD. In-vivo quantitative T2 mapping of carotid arteries in atherosclerotic patients: Segmentation and T2 measurement of plaque components. Journal of Cardiovascular Magnetic Resonance 2013;15:1–9. https://doi.org/10.1186/1532-429X-15-69.

[22] Alkhalil M, Biasiolli L, Akbar N, Galassi F, Chai JT, Robson MD, et al. T2 mapping MRI technique quantifies carotid plaque lipid, and its depletion

after statin initiation, following acute myocardial infarction. Atherosclerosis 2018;279:100–6. https://doi.org/10.1016/j.atherosclerosis.2018.08.033.

[23] Linninger AA, Tsakiris C, Zhu DC, Xenos M, Roycewicz P, Danziger Z, et al. Pulsatile cerebrospinal fluid dynamics in the human brain. IEEE Trans Biomed Eng 2005;52:557–65. https://doi.org/10.1109/TBME.2005.844021.

[24] Viessmann OM. Magnetic Resonance Imaging of Cerebrovascular Anatomy and Physiology at 7 Tesla. Dissertation 2017.

[25] Yuan M, Liu ZQ, Wang ZQ, Li B, Xu LJ, Xiao XL. High-resolution MR imaging of the arterial wall in moyamoya disease. Neurosci Lett 2015;584:77–82. https://doi.org/10.1016/j.neulet.2014.10.021.

[26] Lindenholz A, van der Kolk AG, Zwanenburg JJM, Hendrikse J. The Use and Pitfalls of Intracranial Vessel Wall Imaging. Radiology 2017;286. https://doi.org/10.1148/radiol.2017162096.

[27] Song JW, Moon BF, Burke MP, Kamesh Iyer S, Elliott MA, Shou H, et al. MR Intracranial Vessel Wall Imaging: A Systematic Review. Journal of Neuroimaging 2020;30:428–42. https://doi.org/10.1111/jon.12719.

[28] Mugler JP. Optimized three-dimensional fast-spin-echo MRI. Journal of Magnetic Resonance Imaging 2014;39:745–67. https://doi.org/10.1002/jmri.24542.

[29] Edelman RR, Chien D, Kim D. Fast selective black blood MR imaging. Radiology 1991;181:655–60. https://doi.org/10.1148/radiology.181.3.1947077.

[30] Cho SJ, Jung SC, Suh CH, Lee J Bin, Kim D. High-resolution magnetic resonance imaging of intracranial vessel walls: Comparison of 3D T1-weighted turbo spin echo with or without DANTE or iMSDE. PLoS One 2019;14:1–10. https://doi.org/10.1371/journal.pone.0220603.

[31] Li L, Miller KL, Jezzard P. DANTE-prepared pulse trains: A novel approach to motion-sensitized and motion-suppressed quantitative magnetic resonance imaging. Magn Reson Med 2012;68:1423–38. https://doi.org/10.1002/mrm.24142.

[32] Wang J, Yarnykh VL, Hatsukami T, Chu B, Balu N, Yuan C. Improved suppression of plaque-mimicking artifacts in black-blood carotid atherosclerosis imaging using a multislice motion-sensitized driven-equilibrium (MSDE) turbo spin-echo (TSE) sequence. Magn Reson Med 2007;58:973–81. https://doi.org/10.1002/mrm.21385.

[33] Mosher TJ, Smith MB. A DANTE tagging sequence for the evaluation of translational sample motion. Magn Reson Med 1990;15:334–9. https://doi.org/10.1002/mrm.1910150215.

[34] Busse RF, Hariharan H, Vu A, Brittain JH. Fast spin echo sequences with very long echo trains: Design of variable refocusing flip angle schedules and

generation of clinical T2 contrast. Magn Reson Med 2006;55:1030–7. https://doi.org/10.1002/mrm.20863.

[35] Viessmann O, Li L, Benjamin P, Jezzard P. T2-Weighted intracranial vessel wall imaging at 7 Tesla using a DANTE-prepared variable flip angle turbo spin echo readout (DANTE-SPACE). Magn Reson Med 2017;77:655–63. https://doi.org/10.1002/mrm.26152.

[36] Xie Y, Yang Q, Xie G, Pang J, Fan Z, Li D. Improved black-blood imaging using DANTE-SPACE for simultaneous carotid and intracranial vessel wall evaluation. Magn Reson Med 2016;75:2286–94. https://doi.org/10.1002/mrm.25785.

[37] Jia S, Zhang L, Ren L, Qi Y, Ly J, Zhang N, et al. Joint intracranial and carotid vessel wall imaging in 5 minutes using compressed sensing accelerated DANTE-SPACE. Eur Radiol 2020;30:119–27. https://doi.org/10.1007/s00330-019-06366-7.

[38] Wan L, Zhang N, Zhang L, Long X, Jia S, Li Y, et al. Reproducibility of simultaneous imaging of intracranial and extracranial arterial vessel walls using an improved T1-weighted DANTE-SPACE sequence on a 3 T MR system. Magn Reson Imaging 2019;62:152–8. https://doi.org/10.1016/j.mri.2019.04.016.

[39] Zhang L, Zhu Y, Qi Y, Wan L, Ren L, Zhu Y, et al. T2-Weighted Whole-Brain Intracranial Vessel Wall Imaging at 3 Tesla With Cerebrospinal Fluid Suppression. Front Neurosci 2021;15:1–11. https://doi.org/10.3389/fnins.2021.665076.

[40] Zhang L, Zhang N, Wu J, Liu X, Chung YC. High resolution simultaneous imaging of intracranial and extracranial arterial wall with improved cerebrospinal fluid suppression. Magn Reson Imaging 2017;44:65–71. https://doi.org/10.1016/j.mri.2017.08.004.

[41] Sannananja B, Zhu C, Colip CG, Somasundaram A, Ibrahim M, Khrisat T, et al. Image-Quality Assessment of 3D Intracranial Vessel Wall MRI Using DANTE or DANTE-CAIPI for Blood Suppression and Imaging Acceleration. American Journal of Neuroradiology 2022;43:837–43. https://doi.org/10.3174/ajnr.A7531.

[42] Guo Y, Canton G, Chen L, Sun J, Geleri DB, Balu N, et al. Multi-Planar, Multi-Contrast and Multi-Time Point Analysis Tool (MOCHA) for Intracranial Vessel Wall Characterization. Journal of Magnetic Resonance Imaging 2022;56:944–55. https://doi.org/10.1002/jmri.28087.

[43] Kim DJ, Lee HJ, Baik J, Hwang MJ, Miyoshi M, Kang Y. Improved Blood Suppression of Motion-Sensitized Driven Equilibrium in High-Resolution Whole-Brain Vessel Wall Imaging: Comparison of Contrast-Enhanced 3D T1-Weighted FSE with Motion-Sensitized Driven Equilibrium and Delay Alternating with Nutation for Tai. American Journal of Neuroradiology 2022;43:1713–8. https://doi.org/10.3174/ajnr.A7678.

[44] Oppenheim C, Naggara O, Touzé E, Lacour J-C, Schmitt E, Bonneville F, et al. High-Resolution MR Imaging of the Cervical Arterial Wall: What the Radiologist Needs to Know. RadioGraphics 2009;29:1413–31. https://doi.org/10.1148/rg.295085183.

[45] Lindenholz A, Harteveld AA, Zwanenburg JJM, Siero JCW, Hendrikse J. Comparison of 3T intracranial vessel wall MRI sequences. American Journal of Neuroradiology 2018;39:1112–20. https://doi.org/10.3174/ajnr.A5629.

[46] Edelman RR. The history of MR imaging as seen through the pages of radiology. Radiology 2014;273:S181–200. https://doi.org/10.1148/radiol.14140706.

[47] Alfidi RJ, Haaga JR, El Yousef SJ, Bryan PJ, Fletcher BD, LiPuma JP, et al. Preliminary Experimental Results in Humans and Animals with a Superconducting, Whole-Body, Nuclear Magnetic Resonance Scanner. Radiology 1982;143:175–81. https://doi.org/doi.org/10.1148/radiology.143.1.7063723.

[48] Cosottini M, Roccatagliata L. Neuroimaging at 7T: are we ready for clinical transition? Eur Radiol Exp 2021;5. https://doi.org/10.1186/s41747-021-00234-0.

[49] Pohmann R, Speck O, Scheffler K. Signal-to-noise ratio and MR tissue parameters in human brain imaging at 3, 7, and 9.4 tesla using current receive coil arrays. Magn Reson Med 2016;75:801–9. https://doi.org/10.1002/mrm.25677.

[50] Le Ster C, Grant A, Van de Moortele PF, Monreal-Madrigal A, Adriany G, Vignaud A, et al. Magnetic field strength dependent SNR gain at the center of a spherical phantom and up to 11.7T. Magn Reson Med 2022;88:2131–8. https://doi.org/10.1002/mrm.29391.

[51] Ugurbil K. Magnetic Resonance Imaging at Ultrahigh Fields. IEEE Trans Biomed Eng 2014;61:1364–79. https://doi.org/10.1109/TBME.2014.2313619.

[52] IEC 60601-2-33. Medical Electrical Equipment - Part 2-33: Particular Requirements for the Basic Safety and Essential Performance of Magnetic Resonance Equipment for Medical Diagnosis. International Electrotechnical Commission (IEC) Committee, 2016.

[53] Panych LP, Madore B. The physics of MRI safety. Journal of Magnetic Resonance Imaging 2018;47:28–43. https://doi.org/10.1002/jmri.25761.

[54] Christ A, Kainz W, Hahn EG, Honegger K, Zefferer M, Neufeld E, et al. The Virtual Family - Development of surface-based anatomical models of two adults and two children for dosimetric simulations. Phys Med Biol 2010;55. https://doi.org/10.1088/0031-9155/55/2/N01.

[55] de Buck MHS, Jezzard P, Jeong H, Hess AT. An investigation into the minimum number of tissue groups required for 7T in-silico parallel

transmit electromagnetic safety simulations in the human head. Magn Reson Med 2020. https://doi.org/10.1002/mrm.28467.

[56] Vaidya M V., Collins CM, Sodickson DK, Brown R, Wiggins GC, Lattanzi R. Dependence of B1+ and B1- Field Patterns of Surface Coils on the Electrical Properties of the Sample and the MR Operating Frequency. Concepts Magn Reson Part B Magn Reson Eng 2016;46B:25–40. https://doi.org/10.1002/cmr.b.21319.

[57] Yang QX, Mao W, Wang J, Smith MB, Lei H, Zhang X, et al. Manipulation of image intensity distribution at 7.0 T: Passive RF shimming and focusing with dielectric materials. Journal of Magnetic Resonance Imaging 2006;24:197–202. https://doi.org/10.1002/jmri.20603.

[58] Webb AG. Dielectric materials in magnetic resonance. Concepts Magn Reson Part A Bridg Educ Res 2011;38 A:148–84. https://doi.org/10.1002/cmr.a.20219.

[59] Norris DG. Adiabatic radiofrequency pulse forms in biomedical nuclear magnetic resonance. Concepts Magn Reson Part B Magn Reson Eng 2002;14:89–101. https://doi.org/10.1002/cmr.10007.

[60] Padormo F, Beqiri A, Hajnal J V., Malik SJ. Parallel transmission for ultrahigh-field imaging. NMR Biomed 2016;29:1145–61. https://doi.org/10.1002/nbm.3313.

[61] Deshmane A, Gulani V, Griswold MA, Seiberlich N. Parallel MR imaging. Journal of Magnetic Resonance Imaging 2012;36:55–72. https://doi.org/10.1002/jmri.23639.

[62] Bydder M, Larkman DJ, Hajnal J V. Combination of signals from array coils using image-based estimation of coil sensitivity profiles. Magn Reson Med 2002;47:539–48. https://doi.org/10.1002/mrm.10092.

[63] Uecker M, Lai P, Murphy MJ, Virtue P, Elad M, Pauly JM, et al. ESPIRiT - An eigenvalue approach to autocalibrating parallel MRI: Where SENSE meets GRAPPA. Magn Reson Med 2014;71:990–1001. https://doi.org/10.1002/mrm.24751.

[64] Pruessmann KP, Weiger M, Scheidegger MB, Boesiger P. SENSE: Sensitivity encoding for fast MRI. Magn Reson Med 1999;42:952–62. https://doi.org/10.1002/(SICI)1522-2594(199911)42:5<952::AID-MRM16>3.0.CO;2-S.

[65] Griswold MA, Jakob PM, Heidemann RM, Nittka M, Jellus V, Wang J, et al. Generalized Autocalibrating Partially Parallel Acquisitions (GRAPPA). Magn Reson Med 2002;47:1202–10. https://doi.org/10.1002/mrm.10171.

[66] Breuer FA, Kannengiesser SAR, Blaimer M, Seiberlich N, Jakob PM, Griswold MA. General formulation for quantitative G-factor calculation in GRAPPA reconstructions. Magn Reson Med 2009;62:739–46. https://doi.org/10.1002/mrm.22066.

[67] Lustig M, Donoho D, Pauly JM. Sparse MRI: The application of compressed sensing for rapid MR imaging. Magn Reson Med 2007;58:1182–95. https://doi.org/10.1002/mrm.21391.

[68] Beck A, Teboulle M. A fast iterative shrinkage-thresholding algorithm with application to wavelet-based image deblurring. IEEE International Conference on Acoustics, Speech and Signal Processing 2009:693–6.

[69] Meixner CR, Liebig P, Speier P, Forman C, Hensel B, Schmidt M, et al. High resolution time-of-flight MR-angiography at 7 T exploiting VERSE saturation, compressed sensing and segmentation. Magn Reson Imaging 2019;63:193–204. https://doi.org/10.1016/j.mri.2019.08.014.

[70] Mao W, Smith MB, Collins CM. Exploring the limits of RF shimming for high-field MRI of the human head. Magn Reson Med 2006;56:918–22. https://doi.org/10.1002/mrm.21013.

[71] Ibrahim TS, Lee R, Baertlein BA, Kangarlu A, Robitaille PML. Application of finite difference time domain method for the design of birdcage RF head coils using multi-port excitations. Magn Reson Imaging 2000;18:733–42. https://doi.org/10.1016/S0730-725X(00)00143-0.

[72] Van Den Bergen B, Van Den Berg CAT, Bartels LW, Lagendijk JJW. 7 T body MRI: B1 shimming with simultaneous SAR reduction. Phys Med Biol 2007;52:5429–41. https://doi.org/10.1088/0031-9155/52/17/022.

[73] Gras V, Vignaud A, Amadon A, Le Bihan D, Boulant N. Universal pulses: A new concept for calibration-free parallel transmission. Magn Reson Med 2017;77:635–43. https://doi.org/10.1002/mrm.26148.

[74] Pohmann R, Scheffler K. A theoretical and experimental comparison of different techniques for B1 mapping at very high fields. NMR Biomed 2013;26:265–75. https://doi.org/10.1002/nbm.2844.

[75] Chung S, Kim D, Breton E, Axel L. Rapid B1+ mapping using a preconditioning RF pulse with turboFLASH readout. Magn Reson Med 2010;64:439–46. https://doi.org/10.1002/mrm.22423.

[76] Kent JL, Dragonu I, Valkovic L, Hess AT. Rapid 3D Absolute B1+ Mapping using a Sandwiched Train Pre-Saturated TurboFLASH Sequence at 7T for the Brain and Heart. Magn Reson Med 2023:964–76. https://doi.org/10.1002/mrm.29497.

[77] Bloch F. Nuclear induction. Physical Review 1946;70:460–74. https://doi.org/10.1103/PhysRev.70.460.

[78] Hennig J. Multiecho imaging sequences with low refocusing flip angles. Journal of Magnetic Resonance 1988;78:397–407. https://doi.org/10.1016/0022-2364(88)90128-X.

[79] Weigel M. Extended phase graphs: Dephasing, RF pulses, and echoes - Pure and simple. Journal of Magnetic Resonance Imaging 2015;41:266–95. https://doi.org/10.1002/jmri.24619.

[80] Weigel M, Schwenk S, Kiselev VG, Scheffler K, Hennig J. Extended phase graphs with anisotropic diffusion. Journal of Magnetic Resonance 2010;205:276–85. https://doi.org/10.1016/j.jmr.2010.05.011.

[81] de Buck MHS, Jezzard P, Hess AT. Improved multi-channel pTx B1+ mapping in the head and neck at 7T by combining RF shims and transmit voltages. Proceedings of the 32nd Annual Meeting of ISMRM, Toronto, Canada: 2023, p. 4587.

[82] de Buck MHS, Hess AT, Jezzard P. RF shimming for improved B1+ in the carotid arteries using parallel transmission (pTx) head coils at 7T. Proceedings of the 32nd Annual Meeting of ISMRM, Toronto, Canada: 2023, p. 0205.

[83] Teeuwisse WM, Webb AG, van Osch MJP. Arterial spin labeling at ultra-high field: All that glitters is not gold. Int J Imaging Syst Technol 2010;20:62–70. https://doi.org/10.1002/ima.20218.

[84] Ghariq E, Teeuwisse WM, Webb AG, Osch MJPV. Feasibility of pseudocontinuous arterial spin labeling at 7 T with whole-brain coverage. Magnetic Resonance Materials in Physics, Biology and Medicine 2012;25:83–93. https://doi.org/10.1007/s10334-011-0297-0.

[85] Tong Y, Jezzard P, Okell TW, Clarke WT. Improving PCASL at ultra-high field using a VERSE-guided parallel transmission strategy. Magn Reson Med 2020;84:777–86. https://doi.org/10.1002/mrm.28173.

[86] Wang K, Ma SJ, Shao X, Zhao C, Shou Q, Yan L, et al. Optimization of pseudo-continuous arterial spin labeling at 7T with parallel transmission B1 shimming. Magn Reson Med 2022;87:249–62. https://doi.org/10.1002/mrm.28988.

[87] de Buck MHS, Kent JL, Hess AT, Jezzard P. Parallel Transmit DANTE-SPACE for improved black-blood signal suppression at 7 Tesla. Proceedings of the 31st Annual Meeting of ISMRM, London, UK: 2022, p. 2092.

[88] Teeuwisse WM, Brink WM, Webb AG. Quantitative assessment of the effects of high-permittivity pads in 7 Tesla MRI of the brain. Magn Reson Med 2012;67:1285–93. https://doi.org/10.1002/mrm.23108.

[89] Vaidya M v., Lazar M, Deniz CM, Haemer GG, Chen G, Bruno M, et al. Improved detection of fMRI activation in the cerebellum at 7T with dielectric pads extending the imaging region of a commercial head coil. Journal of Magnetic Resonance Imaging 2018;48:431–40. https://doi.org/10.1002/jmri.25936.

[90] Zhu Y. Parallel Excitation with an Array of Transmit Coils. Magn Reson Med 2004;51:775–84. https://doi.org/10.1002/mrm.20011.

[91] Katscher U, Börnert P, Leussler C, van den Brink JS. Transmit SENSE. Magn Reson Med 2003;49:144–50. https://doi.org/10.1002/mrm.10353.

[92] Setsompop K, Alagappan V, Gagoski BA, Potthast A, Hebrank F, Fontius U, et al. Broadband slab selection with B1+ mitigation at 7T via parallel spectral-spatial excitation. Magn Reson Med 2009;61:493–500. https://doi.org/10.1002/mrm.21834.

[93] Tachrount M, Woodward B, Kopanoglu E, Italiaander M, Klomp D, Driver I. Improving RF efficiency in the brain and the neck at 7T using a novel pTx coil. Proceedings of the 27th Annual Meeting of ISMRM, Montreal, Canada: 2019, p. 1523.

[94] Güler S, Zhurbenko V, Zivkovic I, Christensen H, Rosenbaum S, Havsteen IB, et al. A head and neck array add-on to the two-channel Nova coil using six SCC elements and Nova 32 channel receive array at 7T-MRI. Proceedings of the 32nd Annual Meeting of ISMRM, 2023, p. 0217.

[95] Adriany G, van de Moortele PF, Ritter J, Moeller S, Auerbach EJ, Akgün C, et al. A geometrically adjustable 16-channel transmit/receive transmission line array for improved RF efficiency and parallel imaging performance at 7 Tesla. Magn Reson Med 2008;59:590–7. https://doi.org/10.1002/mrm.21488.

[96] Padormo F, Hess AT, Aljabar P, Malik SJ, Jezzard P, Robson MD, et al. Large dynamic range relative B1+ mapping. Magn Reson Med 2016;76:490–9. https://doi.org/10.1002/mrm.25884.

[97] Spanos A. Probability theory and statistical inference: Empirical modeling with observational data. Cambridge University Press; 1999.

[98] Brunheim S, Gratz M, Johst S, Bitz AK, Fiedler TM, Ladd ME, et al. Fast and accurate multi-channel B1+ mapping based on the TIAMO technique for 7T UHF body MRI. Magn Reson Med 2018;79:2652–64. https://doi.org/10.1002/mrm.26925.

[99] Jenkinson M. Fast, automated, N-dimensional phase-unwrapping algorithm. Magn Reson Med 2003;49:193–7. https://doi.org/10.1002/mrm.10354.

[100] Tao Y, Hess AT, Graeme KA, Rodgers CT, Robson MD. B0-Independent quantitative measurement of low B1 field for human cardiac MRI at 7T. Proceedings of the 21st Annual Meeting of ISMRM, Salt Lake City, US: 2013, p. 2596.

[101] Schauman SS, Chiew M, Okell TW. Highly accelerated vessel-selective arterial spin labeling angiography using sparsity and smoothness constraints. Magn Reson Med 2020;83:892–905. https://doi.org/10.1002/mrm.27979.

[102] Woods JG, Chiew M, Okell TW. Minimizing SAR for SNR-Efficient Pseudo-Continuouos Arterial Spin Labeling at 7T. Proceedings of the 32nd Annual Meeting of ISMRM, 2023, p. 0371.

[103] Sacco S, Totaro R, Baldassarre M, Carolei A. Morphological variations of the internal carotid artery: Prevalence, characteristics and association with

cerebrovascular disease. International Journal of Angiology 2007;16:59–61. https://doi.org/10.1055/s-0031-1278249.

[104] Hong JT, Kim TH, Kim IS, Yang SH, Sung JH, Son BC, et al. The effect of patient age on the internal carotid artery location around the atlas: Clinical article. J Neurosurg Spine 2010;12:613–8. https://doi.org/10.3171/2010.1.SPINE09409.

[105] de Buck MHS, Jezzard P, Hess AT. Optimization of undersampling parameters for 3D intracranial compressed sensing MR angiography at 7 T. Magn Reson Med 2022;88:880–9. https://doi.org/10.1002/mrm.29236.

[106] de Buck MHS, Jezzard P, Hess AT. An investigation into the optimal undersampling parameters for 3D TOF MRA at 7T using compressed sensing reconstruction. Proceedings of the 29th Annual Meeting of ISMRM, Virtual: 2021, p. 1640.

[107] Degnan AJ, Gallagher G, Teng Z, Lu J, Liu Q, Gillard JH. MR angiography and imaging for the evaluation of middle cerebral artery atherosclerotic disease. American Journal of Neuroradiology 2012;33:1427–35. https://doi.org/10.3174/ajnr.A2697.

[108] Kapsalaki EZ, Rountas CD, Fountas KN. The role of 3 Tesla MRA in the detection of intracranial aneurysms. Int J Vasc Med 2012;2012. https://doi.org/10.1155/2012/792834.

[109] Greenberg SM. Small vessels, big problems. New England Journal of Medicine 2006;354:1451–3. https://doi.org/10.1056/nejmp068043.

[110] Heverhagen JT, Bourekas E, Sammet S, Knopp M V., Schmalbrock P. Time-of-flight magnetic resonance angiography at 7 tesla. Invest Radiol 2008;43:568–73. https://doi.org/10.1097/RLI.0b013e31817e9b2c.

[111] Milles J, Versluis MJ, Webb AG, Reiber JHC. Quantitative evaluation of compressed sensing in MRI: Application to 7T time-of-flight angiography. Proceedings of the 10th IEEE International Conference on Information Technology and Applications in Biomedicine 2010:9–12.

[112] Lu SS, Qi M, Zhang X, Mu XH, Schmidt M, Sun Y, et al. Clinical evaluation of highly accelerated compressed sensing time-of-flight MR angiography for intracranial arterial stenosis. American Journal of Neuroradiology 2018;39:1833–8. https://doi.org/10.3174/ajnr.A5786.

[113] Yamamoto T, Okada T, Fushimi Y, Yamamoto A, Fujimoto K, Okuchi S, et al. Magnetic resonance angiography with compressed sensing: An evaluation of moyamoya disease. PLoS One 2018;13:1–11. https://doi.org/10.1371/journal.pone.0189493.

[114] Deka B, Datta S. A practical under-sampling pattern for compressed sensing MRI. Lecture Notes in Electrical Engineering 2015;347:115–25. https://doi.org/10.1007/978-81-322-2464-8_9.

[115] Rapacchi S, Han F, Natsuaki Y, Kroeker R, Plotnik A, Lehrman E, et al. High spatial and temporal resolution dynamic contrast-enhanced magnetic

resonance angiography using compressed sensing with magnitude image subtraction. Magn Reson Med 2014;71:1771–83. https://doi.org/10.1002/mrm.24842.

[116] Hollingsworth KG. Reducing acquisition time in clinical MRI by data undersampling and Compressed Sensing reconstruction. Phys Med Biol 2015;60:R297–322. https://doi.org/10.1088/0031-9155/60/21/R297.

[117] Moghari MH, Uecker M, Roujol S, Sabbagh M, Geva T, Powell AJ. Accelerated whole-heart MR angiography using a variable-density poisson-disc undersampling pattern and compressed sensing reconstruction. Magn Reson Med 2018;79:761–9. https://doi.org/10.1002/mrm.26730.

[118] Fushimi Y, Fujimoto K, Okada T, Yamamoto A, Tanaka T, Kikuchi T, et al. Compressed sensing 3-dimensional time-of-flight magnetic resonance angiography for cerebral aneurysms: optimization and evaluation. Invest Radiol 2016;51:228–35. https://doi.org/10.1097/RLI.0000000000000226.

[119] Kojima S, Shinohara H, Hashimoto T, Suzuki S. Undersampling patterns in k-space for compressed sensing MRI using two-dimensional Cartesian sampling. Radiol Phys Technol 2018;11:303–19. https://doi.org/10.1007/s12194-018-0469-y.

[120] Murtha N. Characterizing dynamic MRI using objective image quality metrics. Thesis 2017.

[121] Kawamura R, Hashimoto T. Statistical optimum 2D random sampling for compressed sensing MRI. 2018 IEEE Nuclear Science Symposium and Medical Imaging Conference, NSS/MIC 2018 - Proceedings 2018:2–7. https://doi.org/10.1109/NSSMIC.2018.8824318.

[122] Shin PJ, Larson PEZ, Ohliger MA, Elad M, Pauly JM, Vigneron DB, et al. Calibrationless parallel imaging reconstruction based on structured low-rank matrix completion. Magn Reson Med 2014;72:959–70. https://doi.org/10.1002/mrm.24997.

[123] Beck A, Teboulle M. A fast iterative shrinkage-thresholding algorithm. Society for Industrial and Applied Mathematics Journal on Imaging Sciences 2009;2:183–202. https://doi.org/10.1137/080716542.

[124] BART toolbox for computational magnetic resonance imaging n.d. https://doi.org/10.5281/zenodo.592960.

[125] Tamir JI, Ong F, Cheng JY, Uecker M, Lustig M. Generalized magnetic resonance image reconstruction using the Berkeley advanced reconstruction toolbox. Proceedings of the ISMRM 2016 Data Sampling and Image Reconstruction Workshop 2016;2486. https://doi.org/10.5281/zenodo.31907.

[126] Akasaka T, Fujimoto K, Yamamoto T, Okada T, Fushumi Y, Yamamoto A, et al. Optimization of regularization parameters in compressed sensing of magnetic resonance angiography: Can statistical image metrics mimic

radiologists' perception? PLoS One 2016;11:1–14. https://doi.org/10.1371/journal.pone.0146548.

[127] Wang Z, Simoncelli EP, Bovik AC. Multi-scale structural similarity for image quality assessment. Conference Record of the Asilomar Conference on Signals, Systems and Computers, vol. 2, 2003, p. 1398–402. https://doi.org/10.1109/acssc.2003.1292216.

[128] Schmitter S, Bock M, Johst S, Auerbach EJ, Uğurbil K, Van De Moortele PF. Contrast enhancement in TOF cerebral angiography at 7 T using saturation and MT pulses under SAR constraints: Impact of VERSE and sparse pulses. Magn Reson Med 2012;68:188–97. https://doi.org/10.1002/mrm.23226.

[129] Johst S, Wrede KH, Ladd ME, Maderwald S. Time-of-flight magnetic resonance angiography at 7 T using venous saturation pulses with reduced flip angles. Invest Radiol 2012;47:445–50. https://doi.org/10.1097/RLI.0b013e31824ef21f.

[130] Schmitter S, Wu X, Auerbach EJ, Adriany G, Pfeuffer J, Hamm M, et al. Seven-tesla time-of-flight angiography using a 16-channel parallel transmit system with power-constrained 3-dimensional spoke radiofrequency pulse design. Invest Radiol 2014;49:314–25. https://doi.org/10.1097/RLI.0000000000000033.

[131] Conolly S, Nishimura D, Macovski A, Glover G. Variable-rate selective excitation. Journal of Magnetic Resonance (1969) 1988;78:440–58. https://doi.org/10.1016/0022-2364(88)90131-X.

[132] Stalder AF, Schmidt M, Quick HH, Schlamann M, Maderwald S, Schmitt P, et al. Highly undersampled contrast-enhanced MRA with iterative reconstruction: Integration in a clinical setting. Magn Reson Med 2015;74:1652–60. https://doi.org/10.1002/mrm.25565.

[133] Wang J, Helle M, Zhou Z, Börnert P, Hatsukami TS, Yuan C. Joint blood and cerebrospinal fluid suppression for intracranial vessel wall MRI. Magn Reson Med 2016;75:831–8. https://doi.org/10.1002/mrm.25667.

[134] Coolen BF, Schoormans J, Gilbert G, Kooreman ES, de Winter N, Viessmann O, et al. Double delay alternating with nutation for tailored excitation facilitates banding-free isotropic high-resolution intracranial vessel wall imaging. NMR Biomed 2021;34:1–10. https://doi.org/10.1002/nbm.4567.

[135] Cogswell PM, Siero JCW, Lants SK, Waddle S, Davis LT, Gilbert G, et al. Variable impact of CSF flow suppression on quantitative 3.0T intracranial vessel wall measurements. Journal of Magnetic Resonance Imaging 2018;48:1120–8. https://doi.org/10.1002/jmri.26028.

[136] de Buck M, Hess A, Jezzard P. Optimized DANTE preparation for intracranial DANTE-SPACE vessel wall imaging at 7T. Proceedings of the 29th Annual Meeting of ISMRM, Virtual: 2021, p. 4201.

[137] Mohammad SA, Osman NM, Ahmed KA. The value of CSF flow studies in the management of CSF disorders in children: a pictorial review. Insights Imaging 2019;10. https://doi.org/10.1186/s13244-019-0686-x.

[138] Koning W, De Rotte AAJ, Bluemink JJ, Van Der Velden TA, Luijten PR, Klomp DWJ, et al. MRI of the carotid artery at 7 Tesla: Quantitative comparison with 3 Tesla. Journal of Magnetic Resonance Imaging 2015;41:773–80. https://doi.org/10.1002/jmri.24601.

[139] Rane SD, Gore JC. Measurement of T1 of human arterial and venous blood at 7T. Magn Reson Imaging 2013;31:477–9. https://doi.org/10.1016/j.mri.2012.08.008.

[140] Rooney WD, Johnson G, Li X, Cohen ER, Kim SG, Ugurbil K, et al. Magnetic field and tissue dependencies of human brain longitudinal 1H2O relaxation in vivo. Magn Reson Med 2007;57:308–18. https://doi.org/10.1002/mrm.21122.

[141] Wyss M, Kirchner T, Ringenbach A, Prüssmann K, Henning J. Relaxation Parameter Mapping Adapted for 7T and Validation against Optimized Single Voxel MRS. Proceedings of ISMRM 2013;26:47–8.

[142] Augst AD, Barratt DC, Hughes AD, McG Thom SA, Xu XY. Various issues relating to computational fluid dynamics simulations of carotid bifurcation flow based on models reconstructed from three-dimensional ultrasound images. Journal of Engineering in Medicine 2003;217:393–403. https://doi.org/10.1243/095441103770802568.

[143] Malik SJ, Teixeira RPAG, Hajnal J V. Extended phase graph formalism for systems with magnetization transfer and exchange. Magn Reson Med 2018;80:767–79. https://doi.org/10.1002/mrm.27040.

[144] Mulkern R V., Gudbjartsson H, Westin CF, Zengingonul HP, Gartner W, Guttmann CRG, et al. Multi-component apparent diffusion coefficients in human brain. NMR Biomed 1999;12:51–62. https://doi.org/10.1002/(SICI)1099-1492(199902)12:1<51::AID-NBM546>3.0.CO;2-E.

[145] Opriessnig P, Mangge H, Stollberger R, Deutschmann H, Reishofer G. In vivo cardiovascular magnetic resonance of 2D vessel wall diffusion anisotropy in carotid arteries. Journal of Cardiovascular Magnetic Resonance 2016;18:1–9. https://doi.org/10.1186/s12968-016-0304-8.

[146] Li J, Pei M, Bo B, Zhao X, Cang J, Fang F, et al. Whole-brain mapping of mouse CSF flow via HEAP-METRIC phase-contrast MRI. Magn Reson Med 2022;87:2851–61. https://doi.org/10.1002/mrm.29179.

[147] Uematsu S, Yang A, Preziosi TJ, Kouba R, Toung TJ. Measurement of carotid blood flow in man and its clinical application. Stroke 1983;14:256–66. https://doi.org/10.1161/01.STR.14.2.256.

[148] Gorelick PB, Wong KS, Bae HJ, Pandey DK. Large artery intracranial occlusive disease: A large worldwide burden but a relatively neglected

frontier. Stroke 2008;39:2396–9. https://doi.org/10.1161/STROKEAHA.107.505776.

[149] Resch JA, Loewenson RB, Baker AB. Physical factors in the pathogenesis of cerebral atherosclerosis. Stroke 1970;1:77–85. https://doi.org/10.1161/01.STR.1.2.77.

[150] Qureshi AI, Caplan LR. Intracranial atherosclerosis. The Lancet 2014;383:984–98. https://doi.org/10.1016/S0140-6736(13)61088-0.

[151] Harteveld AA, Denswil NP, Siero JCW, Zwanenburg JJM, Vink A, Pouran B, et al. Quantitative intracranial atherosclerotic plaque characterization at 7T MRI: An ex vivo study with histologic validation. American Journal of Neuroradiology 2016;37:802–10. https://doi.org/10.3174/ajnr.A4628.

[152] Lohr D, Terekhov M, Veit F, Schreiber LM. Longitudinal assessment of tissue properties and cardiac diffusion metrics of the ex vivo porcine heart at 7 T: Impact of continuous tissue fixation using formalin. NMR Biomed 2020;33:1–14. https://doi.org/10.1002/nbm.4298.

[153] Raman MR, Shu Y, Lesnick TG, Jack CR, Kantarci K. Regional T1 relaxation time constants in Ex vivo human brain: Longitudinal effects of formalin exposure. Magn Reson Med 2017;77:774–8. https://doi.org/10.1002/mrm.26140.

[154] Yuan C, Petty C, O'Brien KD, Hatsukami TS, Eary JF, Brown BG. In vitro and in situ magnetic resonance imaging signal features of atherosclerotic plaque-associated lipids. Arterioscler Thromb Vasc Biol 1997;17:1496–503. https://doi.org/10.1161/01.ATV.17.8.1496.

[155] Kellman P, McVeigh ER. Image reconstruction in SNR units: A general method for SNR measurement. Magn Reson Med 2005;54:1439–47. https://doi.org/10.1002/mrm.20713.

[156] Haacke EM, Liang ZP, Boada F. Image reconstruction using POCS, model constraints, and linear prediction theory for the removal of phase, motion, and Gibbs artifacts in magnetic resonance and ultrasound imaging. Optical Engineering 1990;29:555. https://doi.org/10.1117/12.55624.

[157] Voelker M. MRI Partial Fourier reconstruction with POCS. Matlab Central File Exchange 2012. https://www.mathworks.com/matlabcentral/fileexchange/39350-mri-partial-fourier-reconstruction-with-pocs.

[158] Kellman P, McVeigh ER. Erratum: Image reconstruction in SNR units: A general method for SNR measurement (Magnetic Resonance in Medicine (2005) 54, (1439-1447)). Magn Reson Med 2007;58:211–2. https://doi.org/10.1002/mrm.21261.

[159] Wang Q, Robson MD, Francis JM, Petersen SE, Channon KM, Neubauer S, et al. Accuracy of quantitative MR vessel wall imaging applying a semi-automated gradient detection algorithm - A validation study. Journal of

Cardiovascular Magnetic Resonance 2004;6:895–907. https://doi.org/10.1081/JCMR-200036198.

[160] Biasiolli L, Lindsay AC, Choudhury RP, Robson MD. Loss of fine structure and edge sharpness in fast-spin-echo carotid wall imaging: Measurements and comparison with multiple-spin-echo in normal and atherosclerotic subjects. Journal of Magnetic Resonance Imaging 2011;33:1136–43. https://doi.org/10.1002/jmri.22569.

[161] Higgins GC, Jones LA. The Nature and Evaluation of the Sharpness of Photographic Images. Journal of the Society of Motion Picture and Television Engineers 1952;58:277–90. https://doi.org/10.5594/j01196.

[162] Mudigonda NR, Rangayyan RM, Leo Desautels JE. Gradient and texture analysis for the classification of mammographic masses. IEEE Trans Med Imaging 2000;19:1032–43. https://doi.org/10.1109/42.887618.

[163] Barisano G, Sepehrband F, Ma S, Jann K, Cabeen R, Wang DJ, et al. Clinical 7T MRI: Are we there yet? A review about magnetic resonance imaging at ultra-high field. British Journal of Radiology 2019;92. https://doi.org/10.1259/bjr.20180492.

[164] De Cocker LJ, Lindenholz A, Zwanenburg JJ, van der Kolk AG, Zwartbol M, Luijten PR, et al. Clinical vascular imaging in the brain at 7 T. Neuroimage 2018;168:452–8. https://doi.org/10.1016/j.neuroimage.2016.11.044.

[165] Shimada K, Nagasaka T, Shidahara M, Machida Y, Tamura H. In vivo measurement of longitudinal relaxation time of human blood by inversion-recovery fast gradient-echo MR imaging at 3T. Magnetic Resonance in Medical Sciences 2012;11:265–71. https://doi.org/10.2463/mrms.11.265.

[166] Zhao JM, Clingman CS, Närväinen MJ, Kauppinen RA, van Zijl PCM. Oxygenation and hematocrit dependence of transverse relaxation rates of blood at 3T. Magn Reson Med 2007;58:592–7. https://doi.org/10.1002/mrm.21342.

[167] Hopkins AL, Yeung H N, Bratton CB. Multiple Field Strength in Vivo T1 and T2 for Cerebrospinal Fluid Protons. Magn Reson Med 1986;3:303–11.

[168] O'Reilly T, Webb AG. In vivo T1 and T2 relaxation time maps of brain tissue, skeletal muscle, and lipid measured in healthy volunteers at 50 mT. Magn Reson Med 2022;87:884–95. https://doi.org/10.1002/mrm.29009.

[169] Deoni SCL, Peters TM, Rutt BK. Determination of Optimal Angles for Variable Nutation Proton Magnetic Spin-Lattice, T1, and Spin-Spin, T2, Relaxation Times Measurement. Magn Reson Med 2004;51:194–9. https://doi.org/10.1002/mrm.10661.

[170] van de Moortele PF, Akgun C, Adriany G, Moeller S, Ritter J, Collins CM, et al. B1 destructive interferences and spatial phase patterns at 7 T with a head transceiver array coil. Magn Reson Med 2005;54:1503–18. https://doi.org/10.1002/mrm.20708.

[171] Brittain JH, Olcott EW, Szuba A, Gold GE, Wright GA, Irarrazaval P, et al. Three-Dimensional Flow-Independent Peripheral Angiography. Magn Reson Med 1997;38:343–54. https://doi.org/10.1002/mrm.1910380302.

[172] Kang CK, Wörz S, Liao W, Park CA, Kim YB, Park CW, et al. Three dimensional model-based analysis of the lenticulostriate arteries and identification of the vessels correlated to the infarct area: Preliminary results. International Journal of Stroke 2012;7:558–63. https://doi.org/10.1111/j.1747-4949.2011.00611.x.

[173] Malik SJ, Beqiri A, Padormo F, Hajnal J V. Direct Signal Control of the steady-state response of 3D-FSE sequences. Magn Reson Med 2015;73:951–63. https://doi.org/10.1002/mrm.25192.

[174] Gallichan D, Marques JP, Gruetter R. Retrospective correction of involuntary microscopic head movement using highly accelerated fat image navigators (3D FatNavs) at 7T. Magn Reson Med 2016;75:1030–9. https://doi.org/10.1002/mrm.25670.

[175] Vahle T, Bacher M, Rigie D, Fenchel M, Speier P, Bollenbeck J, et al. Respiratory Motion Detection and Correction for MR Using the Pilot Tone: Applications for MR and Simultaneous PET/MR Examinations. Invest Radiol 2020;55:153–9. https://doi.org/10.1097/RLI.0000000000000619.

[176] Hess AT, Tunnicliffe EM, Rodgers CT, Robson MD. Diaphragm position can be accurately estimated from the scattering of a parallel transmit RF coil at 7 T. Magn Reson Med 2018;79:2164–9. https://doi.org/10.1002/mrm.26866.

[177] Kim D, Cauley SF, Nayak KS, Leahy RM, Haldar JP. Region-optimized virtual (ROVir) coils: Localization and/or suppression of spatial regions using sensor-domain beamforming. Magn Reson Med 2021;86:197–212. https://doi.org/10.1002/mrm.28706.

A

Appendices

A.1 TOF MRA: Slab Boundary Artefacts

Despite the use of 19.64% slab overlap for the multi-slab TOF MRA acquisitions in Chapter 4, the presented coronal MIPs (e.g., in Figure 4.7) suffer from horizontal slab overlap artefacts (i.e., horizontal areas of increased background signal at the slab interfaces). These artefacts can appear when the excited slab is thicker than the acquired slab, resulting in signal pile up due to wrap-around at the edges of the acquired slab. The original Siemens a_fl_tof product sequence aims to suppress this by targeting an excitation slab which is thinner than the acquired slab. However, after the work presented in Chapter 4 was completed, we found that this correction was no longer performed in our modified (compressed sensing undersampled) sequence. Therefore, we further modified the sequence to facilitate a reduction of the target excitation slab thickness relative to the size of the acquired slab by a predefined factor (F_{exc}). In terms of this factor the previously presented data effectively used $F_{exc} = 100\%$.

Figure A.1 shows a phantom comparison of the signal intensity in a single slab when using this updated sequence with different values for F_{exc}. These results confirm that $F_{exc} = 100\%$ results in a signal increase at the edge of the slab. Since low values ($F_{exc} \leq 70\%$) result in a signal reduction within the non-overlapping acquired slab region, $F_{exc} = 80\%$ was used for an (N = 1) *in vivo* validation acquisition.

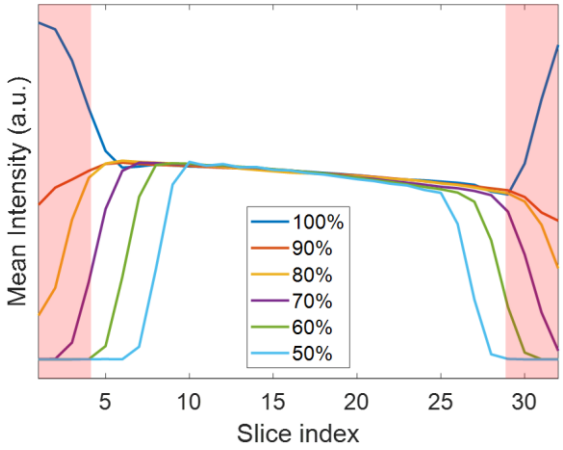

Figure A.1: Phantom data showing the mean signal intensity within the phantom per acquired slice within a single slab. Different lines indicate different values for F_{exc}, as indicated by the percentages in the legend. Red shaded areas indicate the areas of the slice-direction FOV which will be removed to correct for slab overlap.

The results of this validation acquisition are shown in Figure A.2, confirming that the use of a reduced excitation slab thickness ($F_{exc} = 80\%$) largely removes the previously observed artefacts.

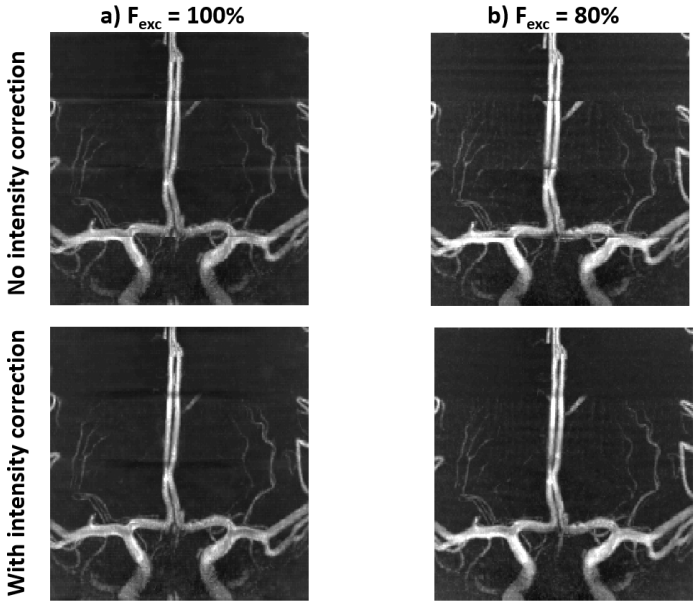

Figure A.2: Coronal MIPs surrounding the LSAs in a healthy volunteer using **(a)** $F_{exc} = 100\%$ and **(b)** $F_{exc} = 80\%$. The bottom row shows reconstructions using an additional intensity correction (with gradually overlapping slabs) at the slab interface. Data were acquired using the optimized protocol used in Chapter 4 with $R = 15$.

A.2 DANTE-SPACE at 7T: Field-of-View Reduction

The 7T DANTE-SPACE sequence used in this thesis acquires a 3D field-of-view of 17.6 cm in the head-food direction using 176 partitions. Due to the low spatial extent of the transmit and receive fields at 7T, this results in data without longitudinal wrap-around artefacts. However, the true region of interest (consisting of the arteries near the Circle of Willis) only spans a few centimetres at the centre of the acquired volume. Therefore, reducing the DANTE-SPACE field-of-view could facilitate a substantial scan time reduction while still providing all desired information. This appendix compares three possible approaches for acquiring a smaller field-of-view without longitudinal aliasing, by suppressing signal from outside the acquired slab.

A.2.1 Spatial Saturation and Selective Excitation

The first approach is the use of spatial saturation bands inferior and superior to the acquired volume. For this, we modified the sequence timing such that the saturation pulses were played out between the DANTE preparation and the SPACE readout (by default the spatial saturation module played out before the DANTE module). The resulting suppression was first tested using a phantom, as shown in Figure A.3. Figure A.3c confirms that, without saturation, the acquired signal when using a smaller FOV changes substantially due to signal wrap-around. This signal change (when using a smaller FOV) is reduced when using the saturation bands, which (as shown in Figure A.3a) substantially but not completely suppresses the signal in the saturated area.

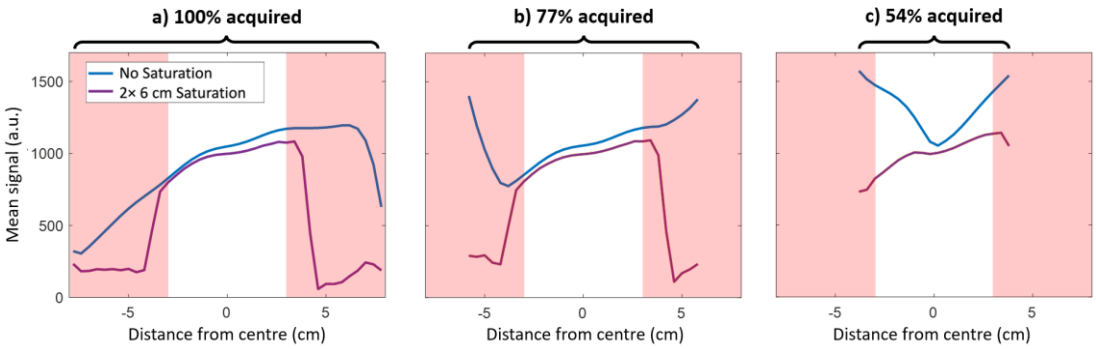

Figure A.3: Comparison of phantom data acquired with and without spatial saturation bands (at both sides of the phantom), acquired for **(a)** the full field-of-view (17.6 cm), **(b)** 77% of the field-of-view (13.6 cm), and **(c)** 54% of the field-of-view (9.5 cm), as indicated by the black curved braces. The average value within the phantom is shown for each slice. Areas shaded in pink indicate the areas covered by the saturation slabs.

Similar results are observed *in vivo*, as shown in Figure A.4b: the signal in a central slice remains similar with and without the use of a saturation band, while the signal in a

suppressed superior slice is substantially reduced (as desired). However, some remaining signal is still observed, especially in the fat around the scalp. To attempt to further reduce this remaining signal, an additional dataset was acquired using saturation pulses in combination with selective excitation in the slab of interest. The result is shown in Figure A.4c.

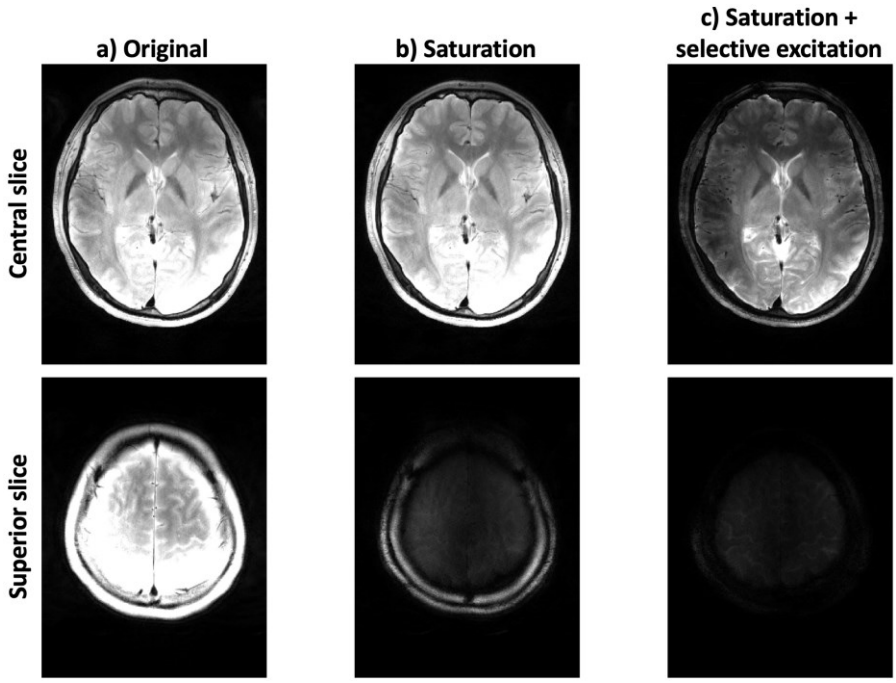

Figure A.4: DANTE-SPACE data acquired at 7T from a healthy volunteer using a 17.6 cm FOV **(a)** without any spatial saturation or selective excitation, **(b)** using spatial saturation bands as used in Figure A.4, and **(c)** using saturation bands in addition to slab-selective excitation (but full acquisition). Data are shown for a slice in the centre of the FOV (first row) and at a superior slice location within the suppressed area for (b) and (c) (second row). Data were acquired at an increased resolution of 4.5 mm in the longitudinal direction for scan time reduction. All data are shown with the same colour scaling.

This slab-selectivity can be achieved by replacing the non-selective 90° SPACE excitation pulse by a slab-selective pulse. However, this would increase the duration of this excitation pulse, which is not possible within the rapid sequence timing (in which the excitation pulse duration is typically of the order of 100s of μs) of the SPACE readout. Therefore, a slab-selective 90° excitation pulse followed by a non-selective 180° refocusing pulse is used instead, as described by Mugler [28]. The time interval between those two pulses can then be increased as needed based on the desired pulse profile, as long as the resulting spin echo is generated exactly half the SPACE echo spacing duration before the first variable flip angle SPACE pulse is played out.

Although the addition of such selective excitation provides improved suppression of the fat around the head, as is visible in Figure A.4c, a substantial reduction in the acquired signal in the central slice is also observed. This reduction is mainly visible outside the centre of the brain, indicating that it might be caused by the effect of $B1^+$ inhomogeneity on the nonselective 180° refocusing pulse required for slab-selective TSE [28]. Furthermore, it should be noted that to suppress out-of-slab FID artefacts, slab-selective TSE requires averaging of at least 40% of k-space with additional data acquired using the opposite phase of the refocusing pulse. This results in a scan time increase by at least the same factor.

In conclusion, saturation bands efficiently suppress most signal, but high fat signal and some background signals remain in the saturated area. Although selective excitation can suppress this remaining signal, it requires additional scan time and reduces the signal in (especially) low-$B1^+$ areas. For this reason, we did not deploy the SPACE readout sequence with a selective excitation preparation.

A.2.2 ROVir Coils

Region-optimized virtual (ROVir) coils [177] are a receive coil compression technique to calculate coil combinations aiming to retain maximum sensitivity in a specified region of interest, while suppressing the signal from a predefined interference region (i.e., the region outside the acquired slab). In ROVir, a subset of the calculated virtual coils can be selected to retain at least a certain percentage (I_{min}) of the sensitivity in the region of interest, while retaining as little sensitivity as possible in the interference region. The results presented in the original ROVir paper show excellent suppression of signal outside of a slab covering the brain (Figures 3-6 in Ref. [177]). Therefore, the use of ROVir for the suppression of signal outside of a specific slab seemed to offer a possible method for reducing the acquired DANTE-SPACE field-of-view.

A ROVir reconstruction algorithm was implemented in MATLAB and applied to a DANTE-SPACE acquisition using various combinations of signal and interference regions. The best results were generally achieved with a small signal region, a large interference region, and a sizeable gap between the two. Figure A.5 shows an example of one of the best performing realistic combinations. However, the results in Figure A.5b indicate that when, for example, using I_{min} = 85%, this requires the use of 28 virtual coils which gives 86% retained signal but leaves 35% of the signal in the interference region. This means that its use results in a substantial SNR reduction while still leaving around a third of the interfering signal, as is visible in Figure A.5c.

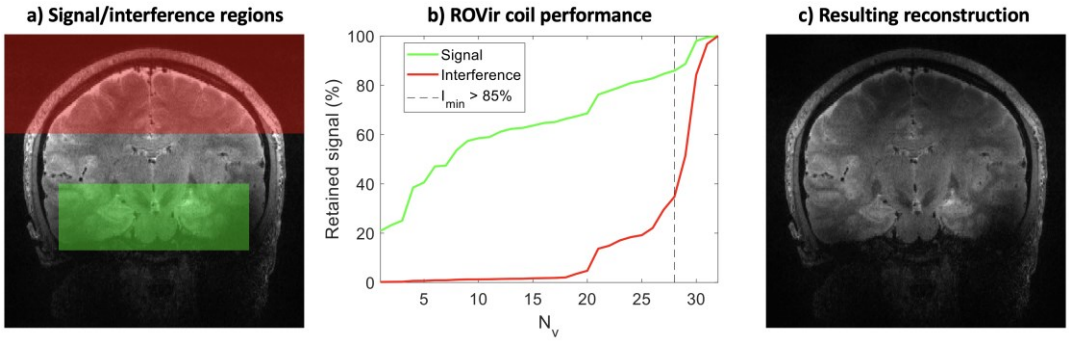

Figure A.5: Example ROVir implementation. Subplots show **(a)** the selected 3D signal and interference regions and **(b)** the retained signal and interference when using N_V out of the resulting 32 ROVir channels, and **(c)** the reconstruction using the first 28 ROVir coils (such that $I_{min} > 85\%$). Figures (a) and (c) are shown using the same colour bar range.

Based on these results, we concluded that the best way to reduce the field-of-view in the head-foot direction would be to use a combination of techniques, such as spatial saturation to remove most unwanted signal and ROVir to reduce the fat signal. An alternative option, which was not explored in this work, would be to also include spectral fat saturation pulses to reduce the remaining fat signal, although this could possibly affect the signal in lipid plaque components.

Acquiring DANTE-SPACE data with a smaller FOV using the approaches discussed here would reduce the data quality through the combination of the reduced signal when using ROVir coils, the $\sqrt{R}$ penalty, and possible remaining artefacts. Given the relatively low inherent contrasts of the DANTE-SPACE sequence, this could obstruct vessel delineation. Therefore, this thesis mainly focused on improving the VW contrasts. Further work could consider reducing the scan time using the approaches discussed here.

A.3 SPACE: Flip Angle Trains

The following SPACE flip angle train (in degrees) was used for all DANTE-SPACE acquisitions at 7T (starting with the 90° excitation pulse):

90.0, 87.7, 48.2, 38.0, 32.3, 29.2, 26.6, 24.9, 23.2, 21.9, 21.1, 22.1,
22.6, 23.2, 23.8, 24.6, 25.4, 26.3, 27.1, 28.1, 29.1, 30.2, 31.2,
32.4, 33.5, 34.7, 36.0, 37.3, 38.8, 40.3, 41.9, 43.7, 45.6, 47.6,
49.9, 52.4, 55.1s, 58.2, 61.6, 65.7, 70.3, 72.5, 73.6, 74.0, 74.2,
74.7, 75.1, 75.6, 76.0, 76.5, 77.0, 77.5, 78.1, 78.6, 79.3, 80.0,
80.7, 81.5, 82.3, 83.2, 84.3, 85.4, 86.6, 88.1, 89.6, 91.5, 93.5,
95.9, 98.7, 102.0, 105.9, 110.9, 117.3, 125.9, 139.1

And the following flip angles were used at 3T:

90.0, 100.9, 58.5, 46.6, 40.1, 36.6, 33.5, 31.3, 29.1, 27.3, 26.7,
27.5, 27.9, 28.6, 29.3, 30.2, 31.1, 32.2, 33.4, 34.7, 36.0,
37.4, 38.7, 40.2, 41.6, 43.2, 44.9, 46.7, 48.7, 50.8, 53.1,
55.6, 58.2, 61.3, 64.6, 68.4, 72.7, 77.6, 83.5, 90.4, 93.9,
95.0, 95.0, 95.2, 95.7, 96.0, 96.3, 96.7, 97.2, 97.6, 98.0,
98.5, 99.1, 99.6, 100.2, 100.9, 101.6, 102.4, 103.3, 104.2, 105.3,
106.4, 107.8, 109.2, 110.9, 112.8, 114.9, 117.4, 120.4, 123.9, 128.1,
133.5, 140.6

A graph comparing those two flip angle trains can be found in Figure 7.5.